Supraglacial landslides: improved detection, and their deposits as sources of bioavailable Fe

William David Smith

Thesis is submitted for the degree of

Doctor of Philosophy (PhD)

School of Geography, Politics & Sociology
Newcastle University
Newcastle upon Tyne
United Kingdom

January 2022

Declaration

Candidate's declaration

I, William David Smith, do hereby certify that this thesis, submitted for the degree of PhD, has been written by me, and that it is the record of work carried out by me, or principally by myself in collaboration with others as acknowledged, and that it has not been submitted in any previous application for any degree. Where work has formed part of jointly-authored publications, the contributions of the candidate and the other authors are explicitly indicated at the beginning of each chapter.

Abstract

Large landslides (rock avalanches [RA]) onto glaciers are thought to be increasing in frequency and magnitude due to feedbacks with both climate warming and permafrost degradation. However, there are no rapid, standardised detection methods to quantify these events. Understanding their frequencies and magnitudes is key to determining their glaciological and geochemical impacts from source to sink. As point sources of highly reactive, comminuted sediment they may be important delivery mechanisms for lithogenic nutrients such as iron (Fe). In this thesis, a new rapid, free-to-use tool; the Google Earth Engine supRaglAciaL Debris INput dEtector (GERALDINE), is presented, which can semi-automatically detect supraglacial RAs with 92% accuracy. This tool is applied to Glacier Bay National Park and Preserve, Alaska (~5000 km^2); a known slope-failure hotspot, to assess an existing inventory of 24 supraglacial rock avalanches that were identified between 1984 and 2016. GERALDINE analysed an order of magnitude more Landsat imagery to aid in the creation of a new inventory of 69 RAs between 1984 and 2020. The original inventory underestimated RA frequency by 53%, missing predominantly small events, resulting in an area/volume bias in current detections. RAs increased in magnitude and frequency in the last decade, their triggering clustered temporally between May-September, and they clustered spatially at high altitudes and around the modelled permafrost boundary, with one ridge producing 29% of all events. Additionally, 58% were deposited in accumulation zones resulting in sequestering of debris into englacial and possible subglacial transport pathways. The largest of these RAs; the Lamplugh RA, was sampled to analyse its contribution to glacial iron (Fe) cycling. Its bioavailable Fe content was lower than other glacial sources, due to crystallisation on the surface and a lack of pyrite available for oxidation within the source rock. However, a singular RA is a large, rapid, point-source delivery of Fe into the glacial domain, and over wider areas their spatial and temporal clustering results in seasonal pulses of Fe along key glacial pathways, making them previously overlooked components of glacial Fe cycles.

Acknowledgements

First of all, I would like to thank my supervisors Stuart Dunning, Jon Telling and Neil Ross. Without your tolerance of my incessant questioning and curiosity, in addition to your guidance, this thesis would not have been possible. Every meeting we have ever had, I have learnt something new, which has greatly improved the quality of this work. Stu, I have thoroughly enjoyed working with you and it has been great to get out on fieldwork to various places, even if I did forget the coffee on one very remote trip. Jon, I will forever be grateful for your invaluable help and patience in the laboratory. Neil, thanks for all your support and for teaching me how to finally use punctuation. All in all, it has been an absolute pleasure to get to know and work with all of you.

Secondly, I'd like to thank all the people who have helped me along the way in this project. This includes co-authors of papers, members of the Newcastle Geography department and technical staff. Of those I'd like to specifically extend my thanks to Dave Earley and Ana Contessa for help in the laboratory. In addition, thanks to Northumbria University, in particular Dave Thomas and Lesley Dunlop for allowing and teaching me how to use the X-ray Fluorescence spectrometer.

Thirdly, I must thank my brother Richard for his help on fieldwork, which you not only made great fun but also helped keep us all safe. I hope you enjoyed your fieldwork birthday and Iceland apologises for its freezing cold 'hot' spring. I would also like to thank everyone who has helped me along the way, in particular everyone in the GPS office, who I have wasted countless hours in the coffee room discussing a whole raft of topics, and my housemates who have made the last few years' good fun. In particular, thanks to Jake Collins-May for chatting absolute 'breeze' with me 24/7 and attending a plethora of surf trips. I would also like to thank Devin Harrison for showing me that even the most enthusiastic gravel expert can become disillusioned after 10 days of solid gravel. Also, a special thanks must go to Faith Willsher, for putting up with me over the last three years, and somehow providing endless pep talks.

Finally, I must thank my parents for their unconditional love, support and encouragement throughout. I would not be where I am today without you and I can never thank you enough for that. Whether it has been coming to visit you on holiday in the Lake District, walking the dog or going cycling, all of it has helped immensely.

COVID-19 impact statement

The COVID-19 pandemic has severely disrupted this PhD project. Laboratory work was due to commence in late March 2020, after samples had been prepared ready for analysis. Preparation had been undertaken; however, the week analysis was due to start, the first national lockdown commenced. The laboratory reopened in September, but access was only allowed on an alternating rota of two days one week and three days the following week. Sample preparation had to be undertaken once more. The sequential extraction methodology to extract different iron (Fe) fractions from my samples required a significant amount of refinement before it was suitable and reliable. This 2/3 day a week laboratory rota gave very little time to refine the sequential extractions. The extraction process required 4 consecutive days in the lab, as preparation had to occur (1 day), extractions had to be undertaken (2 days), and analysis of the extraction products on the atomic absorption spectrometer (AAS) had to be undertaken as quickly as possible i.e. the next day. Refinement of the method and a pilot study was completed in December 2020, at which point the AAS broke due to a gas line issue, and this was difficult to get fixed as it happened just before the Christmas break (17th December), and was further delayed due to the subsequent third national lockdown between January and March 2021. The AAS was up and running again in mid-February. With lockdowns and equipment breaking I had a total of ~3.5 months of consistent lab time in 12 months. The project was supposed to investigate four elements: Fe, Si, N and P, however, this was not feasible due to the lockdowns, so it was decided to reduce this to only include Fe analysis.

Contingency work was discussed with supervisors to ensure I still had the possibility to complete a PhD. This contingency work was undertaken for three months but has not been included in the thesis because the university did not provide adequate IT equipment to allow its completion. I was using a personal laptop, but this was insufficient and would not load certain critical programs i.e. QGIS. I requested a university PC in August 2020, but this was not received until the end of January 2021.

Table of contents

List of abbreviations

AAS	Atomic Absorption Spectrometer
ANOVA	Analysis of Variance
DEM	Digital Elevation Model
DI	Deionised
DTM	Digital Terrain Model
ECMWF	European Centre for Medium-Range Weather Forecasts
ELA	Equilibrium Line Altitude
ENSO	El Niño–Southern Oscillation
ETM+	Enhanced Thematic Mapper Plus
GEE	Google Earth Engine
GEEDiT	Google Earth Engine Digitisation Tool
GERALDINE	Google Earth Engine Supraglacial Debris Input Detector
GIS	Geographic Information System
GLBA	Glacier Bay National Park and Preserve
GPR	Ground Penetrating Radar
GPS	Global Positioning System
HDPE	High-density polyethylene
IFSAR	Interferometric Synthetic Aperture Radar
IPCC	Intergovernmental Panel on Climate Change
MEI	Multivariate El-Niño-Southern Oscillation
NDSI	Normalised Difference Snow Index
NOAA	National Oceanic and Atmospheric Administration
OLI	Operational Land Imager
OWL	Occurrence Window Length
PDO	Pacific Decadal Oscillation
PZI	Permafrost Zonation Index
QGIS	Quantum Geographic Information System
RA	Rock avalanche
RGI	Randolph Glacier Inventory
ROI	Region of Interest
SLC	Scan Line Corrector
SWIR	Short-wave Infrared
TIRS	Thermal Infrared Sensor

TM	Thematic Mapper
USGS	United States Geological Survey
UV	Ultraviolet
XRF	X-ray fluorescence

List of figures

Supplementary Figures

List of tables

Supplementary Tables

Chapter 1 - Introduction

1.1 Cryosphere and cryospheric hazards

The global cryosphere refers to all areas on Earth where water is found in its frozen state, incorporating glaciers, ice sheets, sea ice, snow cover, permafrost, and ground ice (Barry and Gan, 2011). It is a critical component of the global climate system, and is the largest source of fresh water, with the Greenland and Antarctic ice sheets accounting for 97 % of global freshwater resources (Barry, 2011). However, because the cryosphere is a product of a low-temperature climate regime; typically found at high latitudes and altitudes, it is vulnerable to global temperature increases (IPCC, 2019). This is particularly important because the globally averaged land and ocean surface temperature has risen by 0.85 °C between 1880 and 2012 (IPCC, 2019). High altitude and latitude areas are disproportionately affected by temperature increases (e.g. Pepin et al., 2015; Rangwala & Miller, 2012; Stjern et al., 2019), with high latitude areas susceptible due to a phenomenon known as polar amplification; a process defined as the ratio between polar warming and tropical warming (Pithan and Mauritsen, 2014; Goosse *et al.*, 2018; Stuecker *et al.*, 2018). This has caused dramatic alteration of the cryosphere, characterised by shrinking land ice (e.g. Bamber et al., 2018) and sea ice extents (e.g. Stroeve et al., 2012), permafrost degradation (e.g. Chadburn et al., 2017; Schuur et al., 2015) and annual snow cover extents declining (e.g. Hernández-Henríquez et al., 2015). These processes contribute to a number of macroscale, mesoscale, and, microscale impacts, with global impacts such as sea-level rise (e.g. DeConto & Pollard, 2016), further release of potent greenhouse gases (e.g. Schuur et al., 2015; Turetsky et al., 2020), and, reductions to the Earths albedo (e.g. Perovich & Polashenski, 2012; Riihelä et al., 2013), the latter two creating positive feedback loops that increase the speed of atmospheric warming (IPCC, 2019).

Destabilisation of the cryosphere due to climate change is causing a number of cryospheric hazards including but not limited to ice shelf collapse (e.g. Scambos et al., 2004), glacier collapse/avalanche (e.g. Faillettaz et al., 2015; Giordan et al., 2021; Kääb et al., 2018), glacier lake outburst floods (GLOFs) (e.g. Harrison et al., 2018), slope failures (e.g. Gariano & Guzzetti, 2016; McColl, 2012), flooding from snow and ice melt (e.g. Arp et al., 2020; Duan et al., 2020), and, the growth and evolution of thermokarst (Kokelj and Jorgenson, 2013). High altitude mountain areas are hotspots for this activity (Ding *et al.*, 2021), with terrestrial temperatures rising by 0.3°C per decade in comparison to the global average of 0.2°C per decade (IPCC, 2019). 10 % of the global population live within close proximity to high mountain regions, therefore these hazards also have considerable socio-economic costs (IPCC, 2019).

Catastrophic mass flows, which involve mass movements of glacial ice, rock avalanches, ice-rock avalanches, glacial debris flows and outburst-generated flows (Evans, Delaney and Rana, 2021) encompass the common threats to ecosystems, human populations and infrastructure in these high mountain regions. These events occur suddenly, they are rapid (mean velocity ≥5 m s^{-1}), and, mobile (i.e. low volumes can produce exceptionally long runouts), and typically involve and incorporate earth materials, and water in different states (i.e. ice, snow and liquid water) (Evans, Delaney and Rana, 2021). It is common for catastrophic mass flows to be interconnected, with one process frequently triggering other processes, increasing event magnitudes and as a consequence, environmental and economic damage, this is known as a 'hazard cascade' (Evans, Delaney and Rana, 2021). For example, glacial ice catastrophic mass flows such as those documented in the Caucasus Mountains (Huggel *et al.*, 2005), and the Aru Range in the Western Tibetan Plateau (Kääb *et al.*, 2018), both of which were fatal, involved a variety of interconnected factors. Two of the three hypotheses for the Kolka Glacier collapse in the Caucasus Mountains in 2002, involve mass input of sediment from slope failures, causing collapse of the Kolka Glacier, releasing >130 M m^3 of ice and debris, that travelled 19 km down-valley, before evolving into a rapid debris flow that travelled a further 15 km (Huggel *et al.*, 2005; Evans *et al.*, 2009). Similarly, GLOFs are often triggered by catastrophic mass flows (Evans and Delaney, 2015; Haeberli, Schaub and Huggel, 2017) such as landslides; mainly rock and ice avalanches, causing overtopping or failure of the lake dam (Clague and O'Connor, 2015; Faillettaz, Funk and Vincent, 2015). These events are frequently documented because 36% result in societal impacts, with >12,000 recorded deaths, and damage to infrastructure, such as hydropower electricity generation, and agricultural land (Carrivick and Tweed, 2016). However, recent research suggests they are more common than our current records suggest due to under-detection in remote regions (Kääb *et al.*, 2021). The interconnected nature of catastrophic mass flows suggests that if just one of these types of events becomes more common, it may increase the frequency of other catastrophic mass flow events.

All of these hazards predominantly resulting from cryosphere destabilisation result in the mobilisation of vast amounts of sediment and water. Movement of sediment and water are key components in determining mountain landscape biogeochemistry (Burt and

Pinay, 2005; Hilton and West, 2020) and subsequently mountain ecosystems (Ren *et al.*, 2019), however, limited research exists exploring these feedbacks. Of these hazards, slope failures in the form of landslides have received the most research attention because they are not unique to cryosphere environments and they are increasing in frequency globally, due to climate warming (Gariano and Guzzetti, 2016). However, even in non-glacial environments, research into landslide impacts on mountain biogeochemistry is inadequate. Preliminary research suggests that slope failures are important components of the carbon cycle, mobilising both fossil and non-fossil particulate organic carbon into fluvial systems (Hilton, Galy and Hovius, 2008; Clark *et al.*, 2016; Croissant *et al.*, 2021). This carbon is mobilised in 'pulses' when multiple landslides are triggered by earthquakes, before it is exported by physical sediment processes, or degraded by heterotrophic respiration, the balance between which determines whether landslides promote the release or storage of carbon (Croissant *et al.*, 2021). Another critical component of landslides is they comminute large amounts of sediment (e.g., Knapp and Krautblatter, 2020). This vastly increases the surface area of debris that can be subjected to weathering processes, which is critical for nutrient release e.g., phosphorous, (Wu *et al.*, 2013) and overall solute fluxes in mountain ecosystems (Del Vecchio *et al.*, 2018).

Deposition of a landslide onto a glacier complicates its impact on mountain biogeochemical cycles. First of all, glacially deposited landslides are unlike their non-glacial counterparts in that they are characterised by exceptionally long runouts (Sosio *et al.*, 2012) which promote thinner deposits. Depending on the deposition location, these deposits can remain undisturbed on glacier surfaces for decades, or they can be rapidly advected into the ice (Uhlmann *et al.*, 2013; Dunning *et al.*, 2015). These different debris transport pathways will determine their biogeochemical impacts over time. Secondly, glaciers are a unique biome, home to an ecosystem adapted to living under cold, low-nutrient conditions (e.g. Anesio *et al.*, 2017). It is unknown how a landslide deposited into this biome would impact the unique ecosystem that it hosts and if any of the biogeochemical effects seen by non-glacial landslides i.e., impacts on the carbon cycle, would still be present after its sediment has been exported from the glacier. It may be the case that other biogeochemical reactions that occur on the glacier, will consume and/or alter any resulting solute fluxes from the landslide, therefore preventing their export or utilisation in downstream ecosystems. However, before we can begin understanding the biogeochemical effects of landslides onto glaciers their frequency needs to be accurately quantified. This will allow their catchment-scale biogeochemical significance to be determined and aid our understanding of their impacts over time, due to a hypothesised increase in their frequencies caused by warming atmospheric temperatures (Coe, 2020).

Evidence shows that supraglacially deposited landslides are increasing in size and mobility, due to warming temperatures (Coe, Bessette-Kirton and Geertsema, 2018) but overall, minimal research has investigated the magnitudes and frequencies of these slope failures (e.g. Uhlmann *et al.*, 2013; Coe, Bessette-Kirton and Geertsema, 2018; Bessette-Kirton and Coe, 2020). This is in sharp contrast to those in terrestrial unglaciated landscapes (Tanyaş *et al.*, 2017; Froude and Petley, 2018), of which there are national databases (Martino, Prestininzi and Romeo, 2014; Rosser *et al.*, 2017). The modelling and observational evidence shows that warming atmospheric temperatures have the ability to increase landslide frequency, because they weaken and/or trigger slope failures through two main mechanisms: thermal and hydrologic stress e.g. permafrost degradation (e.g. Gruber and Haeberli, 2007; Stoffel, Tiranti and Huggel, 2014; Chiarle *et al.*, 2015; Ravanel and Deline, 2015; Paranunzio *et al.*, 2016; Patton, Rathburn and Capps, 2019), and redistributing slope stresses due to glacial retreat and downwasting (Grämiger *et al.*, 2017; McColl and Draebing, 2019). However, our current methods for detecting these events and any climatic-driven frequency increases are limited due to their remote occurrence, insensitivities to smaller events (Ekström and Stark, 2013), and the time required to analyse entire satellite imagery archives, made more difficult by persistent cloud cover in mountain environments (Coe, Bessette-Kirton and Geertsema, 2018; Bessette-Kirton and Coe, 2020). These archives provide unprecedented amounts of information, both spatially and temporally, which has not previously been exploited to create current glacial landslide inventories. This could result in numerous unidentified events in existing inventories, preventing accurate analysis of climate-driven uplifts in frequencies, and accurate quantification of sediment and nutrient fluxes. This biases our knowledge of the frequency and magnitudes of these events in remote glaciated areas. Yet these areas are hotpots of climate warming (IPCC, 2019) and landslides can display a possible signal of this warming (Coe, 2020).

This thesis aims to rectify any under-detections, by creating the most complete inventory of supraglacially deposited landslides (mainly rock avalanches), to assess their magnitudes and frequencies, and explore how the resulting deposits can input a limiting nutrient into the glacial and extra-glacial environment. This will be achieved through one overall aim and multiple objectives.

1.2 Research aims and objectives

The overall aim of this project is to:

Quantify the under-detection of the frequencies and magnitudes of supraglacial landslides and assess their potential to be sources of bioavailable Fe to extra-glacial environments.

To achieve this aim the project is split into a number of objectives outlined below.

Objective 1: Create a tool to identify landslide deposits on glacier surfaces

The spatial and temporal frequencies and magnitudes of landslides onto glaciers are currently unknown, except for the largest events (Huggel, 2009) and limited small-scale studies (e.g. Coe et al., 2018). There are currently three methods to detect landslides onto glaciers: eye-witness reporting, seismic detection, and, manual analysis of satellite imagery. Eye-witness reporting only works when humans are within close proximity, or their livelihoods are somewhat affected by these events (Deline, Hewitt, *et al.*, 2014); seismic detection can only detect large events that create a seismic signal ≥ 5.0 *M* (Ekström and Stark, 2013), therefore likely missing many slope failures in glacial environments; and, manual analysis of satellite imagery, which is time and resource consuming for a user (e.g. Coe et al., 2018). Vast data archives of satellite imagery, and the increasing accessibility of high performance cloud computing resources, have not previously been combined. A combination of the two would allow maximum exploitation of all data in short periods of time. This study will combine the two to allow better understanding of the spatial and temporal frequency of landslides onto glaciers.

Objective 2: Apply the tool to aid identification of supraglacial landslide deposits in Glacier Bay National Park, Alaska, to compare against the existing rock avalanche inventory

Glacier Bay National Park, Alaska, is characterised by extreme topography, ranging from sea-level to Mount Fairweather (4671 m a.s.l.) within just 24 km. The area has undergone rapid deglaciation since the Little Ice Age ~250 years ago, exposing areas of previously ice-covered terrain (Connor *et al.*, 2009). These characteristics coupled with ongoing climate warming, have made it a global hotspot for large landslides onto glaciers, with 24 documented events over the last 40 years (Coe, Bessette-Kirton and Geertsema, 2018). This inventory of 24 events is currently the best glacial landslide inventory available and features no seismically triggered events, enabling isolation of any climate signal on landslide occurrences. From these data these events are predicted to be increasing in size and mobility due to the degradation of high-altitude slope permafrost (Coe, Bessette-Kirton and Geertsema, 2018). The area is also the location of one of the largest supraglacially deposited landslides in modern times; the Lamplugh glacier rock avalanche, which occurred after an exceptionally warm Alaskan winter in 2016 (Dufresne *et al.*, 2019). The tool created in objective 1 will be applied over the area to create a benchmark to determine if glacial landslide frequencies are underestimated using existing methods.

Objective 3: Investigate the contribution of supraglacially deposited landslides to glacial and extra-glacial Fe availability

Glaciers and ice sheets are significant sources of limiting nutrients to extra-glacial environments, and subsequently play an important role in the global carbon cycle (see Wadham et al., 2019). Of these nutrients Fe has received the most research attention because a number of ice sheets and glaciers discharge into Fe-limited oceans i.e., Southern Ocean and the Gulf of Alaska (e.g., Martin and Fitzwater, 1988; Martin, 1990). This fertilisation stimulates blooms of photosynthetic organisms e.g., phytoplankton, which can drawdown atmospheric carbon dioxide (e.g., de Baar *et al.*, 1995; Gerringa *et al.*, 2012). From a glacial perspective, Fe export has been explored through the geochemical composition of glacial flour and subglacial meltwater, principally deemed to be a product of subglacial weathering and/or microbial processes (e.g. Hawkings *et al.*, 2014, 2016, 2017). However, no research has focused on the geochemical contribution from large supraglacial debris inputs, such as landslides, despite supraglacial debris being a dominant control on the geochemistry of supraglacial meltwaters on debris-covered glaciers (e.g. Bhatt, Takeuchi and Acevedo, 2016). Using relatively 'fresh' sediment samples collected from the Lamplugh glacier rock avalanche, the geochemical impact of this event will be estimated both spatially and temporally.

Chapter 2 - Literature Review

This literature review is structured to give a general overview of the current knowledge on the source-to-sink processes of rock avalanches onto glaciers, from failure and emplacement on a glacier, to export of glacial debris into the extra-glacial environment. Each individual results chapter has its own literature review relevant to that chapter.

2.1 Landslides

Landslides are a type of mass-wasting and involve the downslope movement of rock, earth or debris under the influence of gravity (Bolt *et al.*, 1975). Landslides can be categorised based on their movement types, and then sub-categorised by slope failure material; this concept was first outlined by Varnes (1978). A revised classification has recently been suggested by Hungr et al. (2014), to reflect 36 years of research into these processes and the updated geotechnical and geological terminology. Their proposed new classification features six movement types: falls, topples, slides, spreads, flows, and, slope deformation (Figure 1), in addition to seven materials, which can be sub-categorised to reflect characteristics such as strength and degree of saturation (Hungr, Leroueil and Picarelli, 2014). This new general classification system outlines 32 possible landslide types.

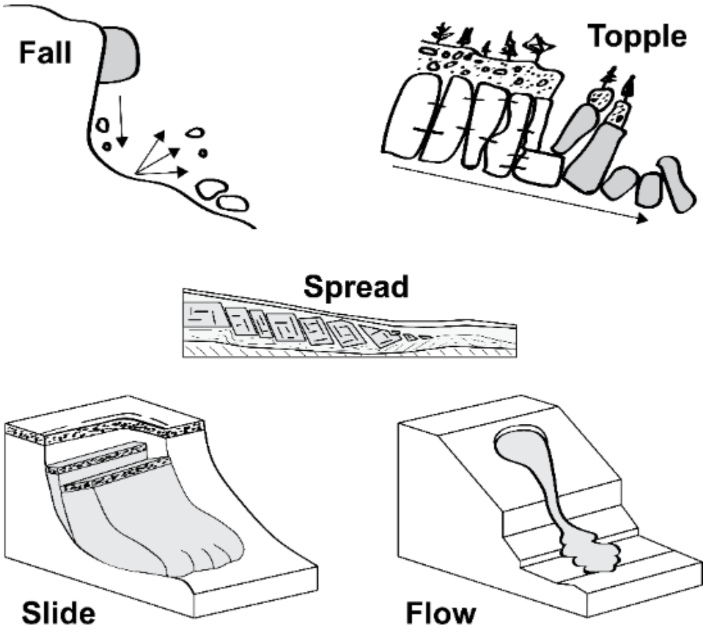

Figure 1: Movement types as described by Hungr, Leroueil and Picarelli (2014). Scale of each failure can vary from a < 4 m to >100 m. Adapted from Cruden and Varnes (1996).

Glaciated high mountain areas are hotspots for slope activity and therefore experience a variety of landslide types (Hewitt, Clague and Deline, 2011). Mass-wasting is often the most important form of erosion in these areas (Korup, 2005) but rates vary over space and time (Grämiger *et al.*, 2017, 2018, 2020). The types of landslides that are delivered to glacier surfaces vary from low-magnitude, high-frequency rock falls to high-magnitude, low-frequency deep-seated failures. Rock falls and rock slides dominate directly above glaciers due to warming atmospheric temperatures causing ice surface lowering, exposing rock to atmospheric temperature variability (Hartmeyer *et al.*, 2020). Rock falls involve detachment of individual or surficial blocks from a rock wall (Luckman, 2013), which fall, roll and bounce, undergoing minimal fragmentation during transportation (Hungr, Leroueil and Picarelli, 2014). Rock slides are larger and have numerous definitions dependent on the type of slide/rupture surface e.g. rotational, planar, wedge, compound, and irregular, but are essentially a single or contiguous mass of bedrock, that has slid over a rupture surface, due to it overcoming shear stress (McSaveney and Davies, 2007). These smaller events contribute debris to glacier surfaces on a year-round basis, resulting in the gradual formation of glacier debris covers (e.g. Kirkbride and Deline, 2013). However, if the bedrock failure mass of a slope failure is large enough to initiate fragmentation during transportation, they can evolve into other types of landslides e.g. debris slides and rock avalanches (RAs). This mass disintegration of source material, creates a flow-like motion that separates them from all other landslide types, particularly in terms of their unpredictability and long-runouts (Li *et al.*, 2021). These low-frequency high-magnitude RAs have rapid, large-scale impacts on a glacier and its behaviour (Deline, Hewitt, *et al.*, 2014) e.g. the Kolka-Karmadon RA (Haeberli *et al.*, 2004; Huggel *et al.*, 2005; Evans *et al.*, 2009).

Although formal categorisation and definitions of landslide types have been defined, the reality of accurately categorising landslide types in the field or in satellite imagery is difficult. The identification boundaries between different landslide types such as rock falls, rock slides and rock avalanches (RAs) are fluid and depend on a number of factors e.g. lithology, fall height, runout length and material entrainment. In addition, landslides can often start and end as a different type due to kinematic changes during flow i.e. a "slide" may end as a "flow" (Hungr, Leroueil and Picarelli, 2014). This is particularly true of landslides onto glaciers, which entrain large amounts of ice and snow, altering their transportation and depositional behaviour (Huggel *et al.*, 2005; Sosio *et al.*, 2012; De Blasio, 2014). This makes accurately categorising a landslide in these regions difficult. Despite this, research often uses landslide deposit size to categorise landslide type i.e. small rock falls <1000 m^3 (e.g. Hartmeyer *et al.*, 2020) and RAs >1 Mm^3 (Deline, Hewitt, *et al.*, 2014). However, estimating the size of these events is difficult without constant rock face monitoring and accurate pre and post-event digital elevation models, particularly for large RAs that scour and entrain glacial ice (Bessette-Kirton, Coe and Zhou, 2018). Due to this entrainment, smaller landslides often have deposits that are visually identical to RA deposits, despite having a volume <1 Mm^3. Size and process categories should therefore only be seen as vague guides to categorising their type. Overall, Hungr, Leroueil and Picarelli (2014) recommend that a researcher should decide the landslide type, and their classification should reflect their particular research focus (Hungr, Leroueil and Picarelli, 2014).

2.2 Rock avalanches

RAs are defined as bedrock slope failures that originate as an intact rock-mass (Hsü, 1975; Hungr *et al.*, 2001). They are "extremely rapid (> 5 m s^{-1}), massive (10^6 m^3), flow-like motions of fragmented rock from a large rock slide or rock fall" (Hungr, Leroueil and Picarelli, 2014, p. 180). In contrast to other slope failures, they are characterised by large fall heights (> 1000 m) and excess runouts (> 5 km) particularly on glaciers (Sosio *et al.*,

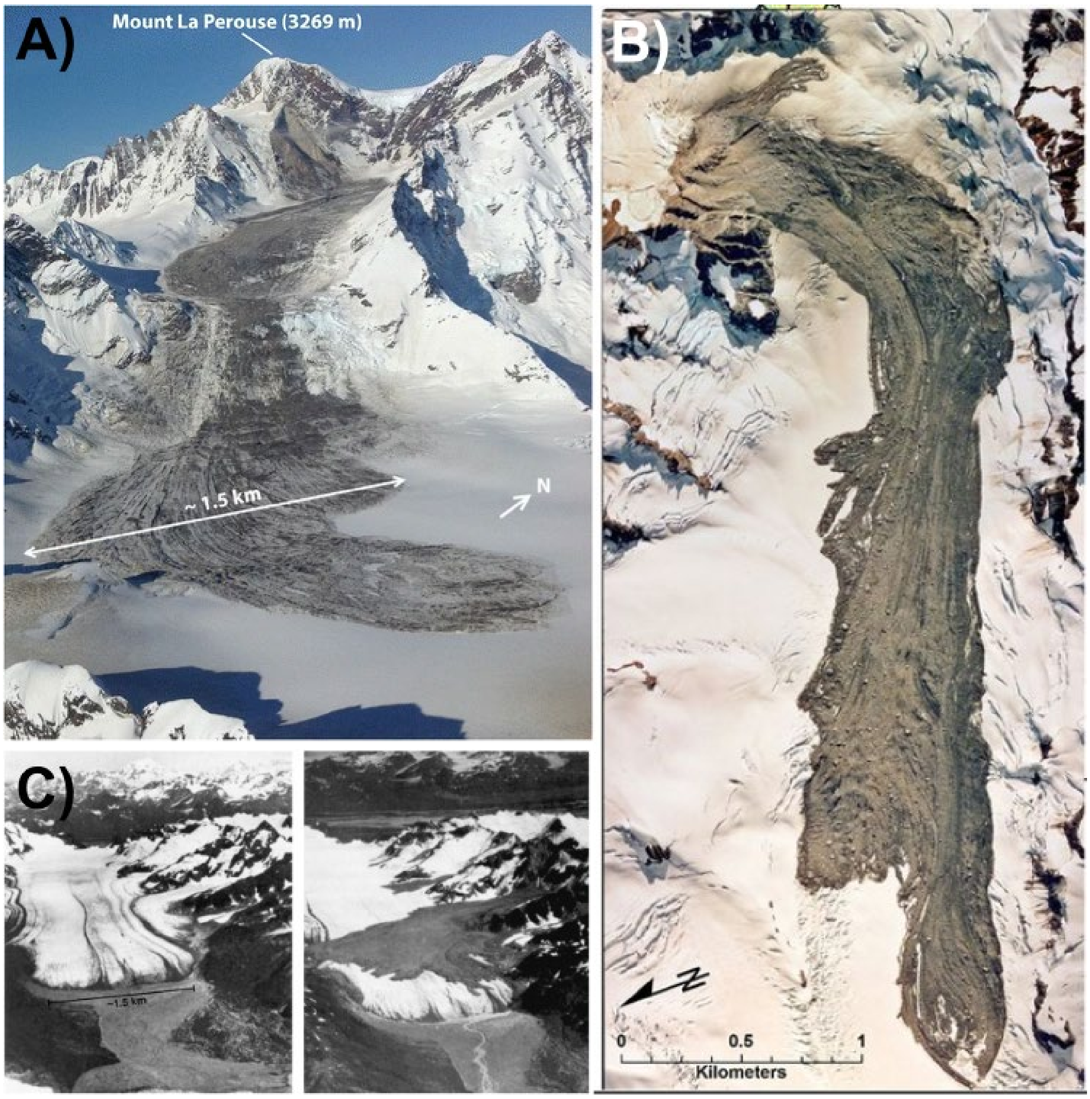

Figure 2: Examples of supraglacial RAs A) 2014 La Perouse RA (source: Coe et al., 2018), B) 1997 Mt. Munday RA (source: Delaney and Evans, 2014), and C) Before and after the 1964 Sherman glacier RA (source: Reznichenko et al., 2011).

2012). Their large headscarps, in addition to their large, thin deposits consisting of highly comminuted rock, often leave a clear imprint on the landscape (Figure 2). Rock avalanche events can be split into three consecutive phases before their movement terminates: failure/detachment (phase 1), disintegration (phase 2), and flow (phase 3) (Knapp and Krautblatter, 2020).

2.3 Rock avalanche failure

Phase 1 of a RA event can be categorised into preconditioning factors, preparatory factors, and triggering factors (Crozier and Glade, 2005; McColl, 2012). Preconditioning being any factor that is an intrinsic characteristic of the rock type i.e. lithology, structure, strength and quality, and does not change over time. Preparatory factors are those which do weaken the slope over time, but do not initiate movement. Triggers are the final processes that initiate slope movement, altering the slope from marginal stability to actively unstable. A combination of these processes is required for any slope activity, and some processes can be both preparatory and triggering factors. Here the processes directly associated with cryospheric environments, which are key due to projected increases in atmospheric temperatures (IPCC, 2019), are discussed. For a complete review of all factors influencing slope stability see McColl (2015) and McColl and Draebing (2019).

2.3.1 Preconditioning factors

Preconditioning factors are the inherent properties of the rock, which are determined by lithology. All lithology has different strengths and weaknesses that make it more or less susceptible to failure, due to its ability to resist the stresses acting upon it (GAPHAZ, 2017). The general strength of the rock, its deformability, coupled with the extent of bedding, foliation, joints and faults, and their orientations, control overall slope stability (McColl, 2012). In turn, this determines slope geometry and on a larger scale regional topography (Ott, 2020). Certain lithologies lend themselves to smaller more frequent failures, and others lend themselves to larger less frequent failures (Fischer *et al.*, 2012). The history of the rock mass is also important in determining its strength, for example, rocks subjected to multiple glaciations are weaker (Augustinus, 1995; Grämiger *et al.*, 2017). Preconditioning factors are therefore likely influenced by both preparatory and triggering factors during past glaciations.

2.3.2 Preparatory and triggering factors

A combination of mechanical, thermal and seismic mechanisms are needed to prepare and trigger rock slope failure. However, often it is difficult to attribute any single event to a particular cause as they often have no obvious trigger (e.g. Lipovsky *et al.*, 2008). Some rock slopes just fail due to the degradation of slope stability over time (McSaveney, 2002; Eberhardt, Stead and Coggan, 2004; Lipovsky *et al.*, 2008). The key cryospheric preparatory and triggering processes are described below.

2.3.2.1 Glacial factors

Mechanical preparatory processes are most common during glacial cycles (McColl, 2012). During glaciations a glacier will erode any substrate it is in contact with, causing over-deepened valleys with steep, undercut flanks. These longer, steeper valleys cause greater shear and self-weight stresses within slopes, reducing stability, but not to the point of failure (McColl, 2012). Erosion during glaciation can also expose existing faults and planes of weakness within the rock, which when ice is removed, can cause failure. Ice removal through downwasting has also been suggested as a cause, through a de-buttressing effect (Ballantyne, 2002b), however, this has been disputed (McColl, Davies and McSaveney, 2010). The brittle strength of ice, prevents high strain rates in the adjacent bedrock slope, reducing the chances of catastrophic failure (McColl, Davies and McSaveney, 2010). An exception to this rule is that slow moving gravitational creep and slope deformation is possible if the strain rate of the slope is higher than that of the ice flow (McColl, Davies and McSaveney, 2010). Multiple catastrophic failures have been proceeded by deep-seated gravitational slope deformation into the ice (Holm, Bovis and Jakob, 2004).

During deglaciation the removal of ice removes any lateral support (and the structural, thermal and hydrologic stability that comes with it (Haeberli, Wegmann and Mühll, 1997; McColl, Davies and McSaveney, 2010; Shugar, Rabus and Clague, 2010; Nagai *et al.*, 2013)) and exposes valley flanks to weathering (Viles, 2013), and climatic fluctuations that vary on sub-daily time-scales. Additionally, the release of stress due to ice-mass removal can generate near-surface rock fractures, weakening slopes and preparing them for failure (McColl, 2012). In the European Alps, half of RA and rockfall events occurred in areas associated with recent deglaciation (Fischer *et al.*, 2012). Modelling of repeat glaciations and the accompanying processes of ice loading and unloading, suggests that the majority of rock mass damage occurs during the first glaciation, because in successive glaciations damage accumulation in an already weakened slope is minor (Grämiger *et al.*, 2017).

2.3.2.2 Permafrost

Thermal rock slope properties and their role as a preparatory and triggering factor for rock slope instabilities, in particular the effects of permafrost degradation, are key in a warming climate (IPCC, 2019). Thermal stresses are complex as they can operate over

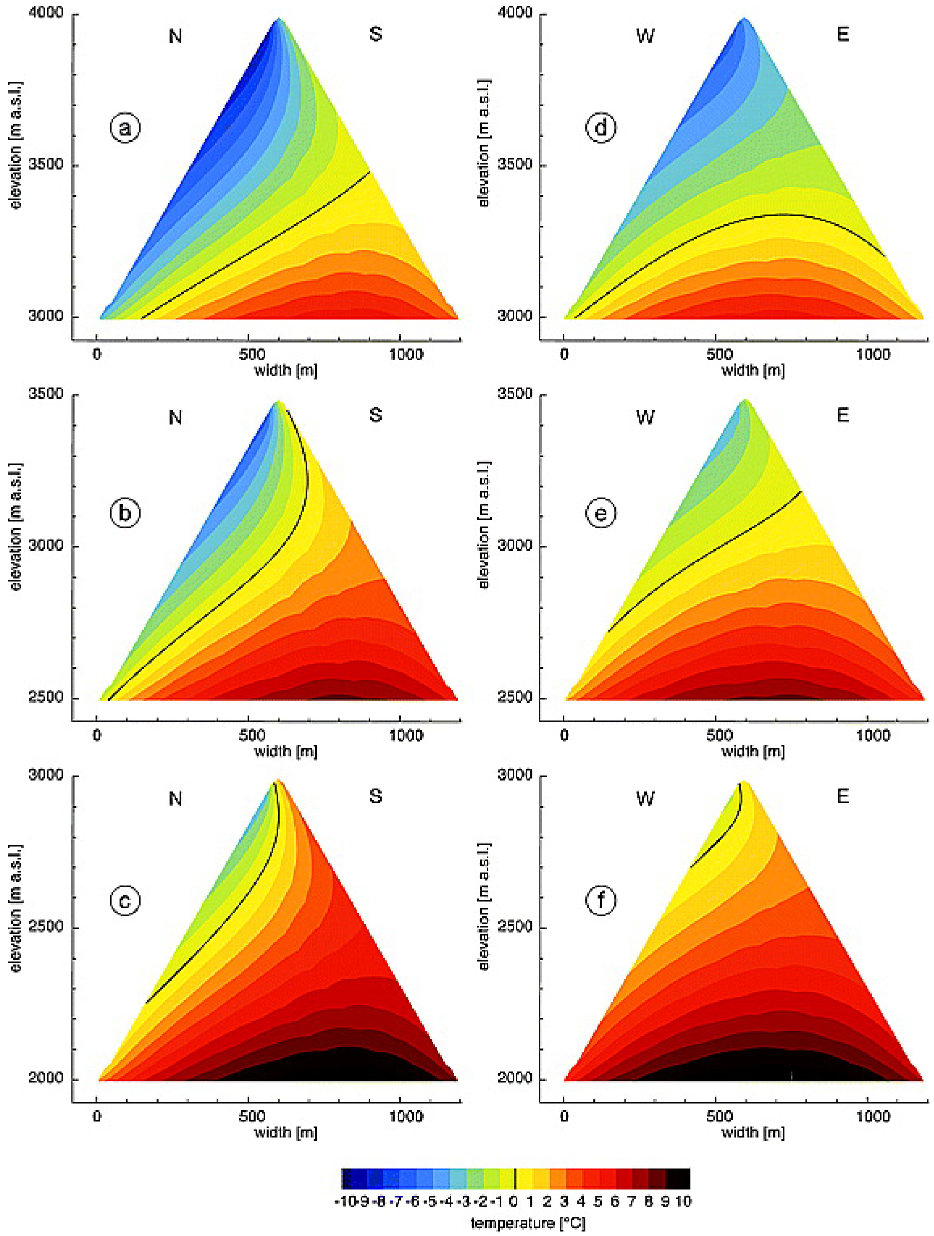

Figure 3: Modelled subsurface temperature distribution for six artificial ridges with 60° slopes. Black line represents the freezing level (0 °C isotherm), and therefore the permafrost boundary. Plots a-c represent north and south facing slopes, and d-f represent east and west facing slopes, throughout three different altitudinal ranges. (source: Noetzli et al. 2007).

the full temporal and spatial spectrum, modifying mechanical properties of the slope enough to induce instabilities (Krautblatter, Funk and Günzel, 2013; Viles, 2013).

Permafrost is officially defined as ground that remains below 0°C for two or more years (Everdingen, 1998) and is principally found in high latitudes and at high altitudes (Gruber, 2012). The perennially frozen component of permafrost is sandwiched between a seasonally thawed 'active layer' at the surface and unfrozen ground at depth. Due to this reliance on sub-zero temperatures it is particularly susceptible to climate change, however, it reacts with variable delay (Gruber, 2012). Permafrost within bedrock acts as a glue, increasing the strength of the rock to both compressive and tensile stresses, with larger negative temperatures equalling greater strength (Mellor, 1973). It also prevents destructive factors such as deep water penetration into the rock, due to it acting as an aquiclide, and it prevents freeze-thaw processes (Woo, 2012). However, during both formation and degradation it acts as a preparatory and triggering factor for slope failure.

A favourable ground thermal regime is required for formation, and this is controlled by ground surface temperature, ground characteristics and geothermal heat flux (Noetzli, 2008). In high mountain topography, complex thermal variations can dramatically alter permafrost location over small spatial scales (Noetzli *et al.*, 2007). Three-dimensional permafrost evolution modelling of idealised slopes in the northern hemisphere, shows the permafrost 0° isotherm, is at a higher elevation on the south-facing aspects of rock slopes, as opposed to northern aspects due to the differences in surface temperatures (Figure 3) (Noetzli *et al.*, 2007). Formation involves the freezing of moisture within bedrock cavities, fissures and fractures at 0 °C, and on much smaller scales within the pores of the rock at -0.1 to -1.5 °C (Deline *et al.*, 2014; Krautblatter, 2009). This is however, dependent on local lithology and degree of saturation (Krautblatter *et al.*, 2010; Draebing and Krautblatter, 2012). It exploits and creates weaknesses within naturally fractured bedrock. This occurs during the freezing of water within the bedrock, overcoming rock strength and overburden, initiating frost cracking activity. Frost cracking can operate either through the volumetric expansion of freezing water, or by ice segregation, which involves the temperature gradient induced suction of unfrozen water through rock pore spaces, towards freezing sites forming and growing ice lenses and layers (Murton, Peterson and Ozouf, 2006; Girard *et al.*, 2013). Rock damage is greater during sustained freezing than during cyclical freeze-thaw activity, and occurs down to temperatures of -15 °C (Girard *et al.*, 2013).

Permafrost degradation involves erosion of the frozen water within the bedrock. In steep topography insolation, aspect, exposure and snow cover all play important roles in its degradation (Gruber and Haeberli, 2007). Warming can penetrate from multiple angles, making peaks, ridges and spurs particularly susceptible to faster and deeper degradation (Gruber and Haeberli, 2007). Degradation involves variations in the ice temperature and geometries of bedrock, altering its mechanical properties. Degradation can induce a decrease in uniaxial compressive and tensile strength of the rock (Mellor, 1973; Dahlström, 1992; Dwivedi *et al.*, 1998; Ning *et al.*, 2003), initiate and grow shear planes (Krautblatter, Funk and Günzel, 2013) and weaken ice-filled joints (Davies, Hamza and Harris, 2001; Mamot *et al.*, 2018). This can modify hydraulic permeability, potentially increasing hydrostatic pressure within previously ice-sealed fractured rock (Krautblatter, Funk and Günzel, 2013), impacting the hydrological regime downslope (Haeberli, Wegmann and Mühll, 1997). Permeability is important because the increased availability of liquid water from melt of the bedrock permafrost, or from the surface via snow and ice melt, or precipitation, can percolate into bedrock permafrost. This is effective at transferring latent energy that can warm deep rock fractures, and it is unlikely to freeze unless impounded, increasing its degradation potential (Hasler *et al.*, 2011). Liquid water can further alter permeability and mechanical strength changes, subsequently causing a restructuring of the stress field (Deline, Gruber, *et al.*, 2014).

Frost weathering processes are important preparatory factors as described above, however, one process; freeze-thaw, is a known trigger for small rock slope failures (Deprez *et al.*, 2020). Freeze-thaw is a process that exerts cyclical pressure on bedrock. Pressure increases during freezing due to thermomolecular pressure gradients drawing water inside, it then decreases when ice thaws and pressurised water is expelled (Murton, Peterson and Ozouf, 2006). Multiple studies by Matsuoka and collaborators have found freeze-thaw to be a key cause of crack widening in spring and autumn (Matsuoka *et al.*, 1997; Matsuoka, 2001, 2008). Freeze-thaw failures can occur in two possible ways; from a build-up of stress on the material over time, or instantaneously by exceeding the material tensile strength (Deprez *et al.*, 2020).

Despite our understanding of these processes it is difficult to attribute any rock slope failures to permafrost degradation (Legay, Magnin and Ravanel, 2021). Evidence for such processes typically comes from correlation of enhanced slope activity during heatwaves. For example, in the European Alps during the 2003 and 2015 heatwaves, an exceptionally large number of rockfalls were reported, particularly on permafrost slopes (Gruber, Hoelzle and Haeberli, 2004; Ravanel, Magnin and Deline, 2017). In addition, the elevation of slope failure scars is at the lower permafrost limit (Ravanel and Deline, 2011; Fischer *et al.*, 2012), the temperature of permafrost has risen since 1987 (Harris *et al.*, 2003) and insulating snow cover has decreased (Matiu *et al.*, 2021). Rock-permafrost is also migrating upslope due to rising temperatures, with warm permafrost (> -2 °C) on southern-facing, steep alpine slopes in the Alps, now existing at 3300 m a.s.l. and higher (Magnin *et al.*, 2017). This is likely to trigger slope failures at increasing altitudes in the future (Gruber, Hoelzle and Haeberli, 2004). RAs have also been attributed to degrading permafrost in coastal south-east Alaska over the last 40 years (Coe, Bessette-Kirton and Geertsema, 2018; Bessette-Kirton and Coe, 2020). In the St Elias National Park, there is a distinct seasonality with the majority of RAs occurring in the summer months between April and October, when temperatures are at their highest (Bessette-Kirton and Coe, 2020).

2.3.2.3 Seismicity

Seismic activity is a common preparatory and triggering factor for rock slope failures in high mountain glacial areas (e.g. Jibson *et al.*, 2006; Uhlmann *et al.*, 2013). Seismic shaking weakens slopes making them more prone to failure (Voight, 1978; Eisbacher and Clague, 1984). This may cause the slope to reach a critical threshold from which further seismicity causes failure, or failure may be triggered by another triggering process (Voight, 1978; Eisbacher and Clague, 1984). Slopes triggered by earthquakes typically have inclinations > 25° and topographic prominences > 150 m (Keefer, 1984).

Relationships between the frequency of slope failures and magnitude of earthquakes have been determined, with clustering around areas characterised by the strongest ground acceleration (typically the epicentre), and then diminishing with increasing distance from the epicentre (Keefer, 1984, 2002; Meunier, Hovius and Haines, 2008). However, in highly erosive, geologically active glacial environments, they only account for a relatively small number of landslides in comparison to other triggers. For example, Liu, Wu and Gao (2021) created an inventory of landslides onto glaciers for the entirety of High Mountain Asia, and only four landslides out of a total of 131 were associated with earthquakes. Similarly, Jibson *et al.* (2006) evaluated RAs triggered by the M 7.9 Denali earthquake in 2002 and questioned why the frequency and concentration of slope failure events was lower than expected. They concluded that the earthquake was lacking high-frequency energy and acceleration to trigger the expected ~ 80,000 landslides as predicted by Keefer (2002), resulting in event frequency an order of magnitude lower.

Over glacial cycles simulations suggest that the loading and unloading of the earth's crust also influences the seismicity in a region (McColl, Davies and McSaveney, 2012). An ice mass may act as a damper for seismic motion, reducing its ability to weaken slopes or trigger their failure (McColl, Davies and McSaveney, 2012). When this ice mass has been removed, and, in combination with the deeper valleys created by glacial erosion, this enhances the topographic amplification effect (McColl, Davies and McSaveney, 2012). Topographic amplification refers to the increased peak ground acceleration during an earthquake at or near ridge crests, and, is responsible for clusters of slope failures at these locations (Meunier, Hovius and Haines, 2008). Earthquakes can induce systematic damage on a rock mass, opening a number of discontinuities, which can in turn amplify shaking in subsequent seismic events (Moore *et al.*, 2012).

2.4 Rock avalanche disintegration and flow

After failure and detachment (Phase 1) has occurred, disintegration (Phase 2) of the failed rock mass begins. Little is known about this phase of an event, because *in situ* measurements are impossible (for full review see Knapp and Krautblatter, 2020). Currently it is thought that the rock mass initially moves as a coherent block, with shearing occurring along its base, due to friction with the underlying ground substrate. This process is termed static disintegration and is driven by gravity. Once cohesion of the failed rock mass is overcome/lost, dynamic disintegration begins to occur because of the higher velocity. Dynamic disintegration involves rapid comminution of the block, due to grain collisions, and these collisions are driven by motion, causing the now comminuted rock mass to develop into a granular flow (Pollet and Schneider, 2004; Knapp and Krautblatter, 2020). This is phase 3. Granular flows involve a high concentration of particles, where particle-particle and particle-boundary interactions and momentum exchange and energy dissipation are key (for full reviews see Delannay *et al.*, 2017 and Li *et al.*, 2021). The result of this flow is a highly pulverised and comminuted rock mass, with grain size distributions encompassing house-sized boulders down to <1 µm grains (McSaveney and Davies, 2007; Shugar and Clague, 2011; Reznichenko *et al.*, 2012; Davies and McSaveney, 2013). Unlike other granular flows, a RA is unique in that there is no turbulence, preventing individual clasts from moving freely through the mass. A RA is more like a viscous fluid in this respect (Deline, Hewitt, *et al.*, 2014). This creates unique flow patterns that are visible in surface structures after the flow has terminated (Dufresne, Bösmeier and Prager, 2016).

RA flow onto a glacier complicates the flow physics further, with the incorporation of snow and/or ice (Pudasaini and Mergili, 2019). These solid phases (snow/ice) transform to liquids, due to the amount of energy created. This i) fluidises the flow, turning a solid-like dry RA into a fluid-like debris flow, ii) reduces the shear resistance of the flowing material, due to compression of snow/ice and the production of meltwater through frictional heating, increasing pore pressures and basal fluid saturation, and, iii) increases basal lubrication (Pudasaini and Krautblatter, 2014). The ice/snow content of a RA can vary, for example, the Mount Meager RA had < 1 % ice content (Guthrie *et al.*, 2012), whereas the Lyell glacier RA had a 90 % ice content (Gordon, Birnie and Timmis, 1978).

2.4.1 Frictionally-produced meltwater

Using equation 1, Sosio *et al.* (2012) estimated the frictional heat and the subsequent meltwater production from the earthquake-triggered Sherman glacier RA in 1964, suggesting the production of 86.2 ± 5.9 kg m^{-2} of equivalent water (Sosio *et al.*, 2012).

$$J = e\tau v = e\rho gh \cos\beta \tan\varphi_b v \tag{1}$$

Where J is the downward dissipation proportional to the velocity, e is the fraction of heat directed downward but can account for any of the heat that is locally dissipated resulting in ice melting, τ is the Coulomb frictional shear resistance, v is the flow velocity, ρ and φ_b are the density angle and friction angle of the flowing mass, g is the gravitational acceleration and h is the thickness of the flowing debris. Melting efficiency depends upon the contact area between the debris and the ice, between which heat exchange can occur. This is dependent upon the void ratio of the mobile debris (~25-30 % decreasing with depth in the debris to ~5 % (McSaveney, 1975; Hungr, 1981)) and on ice indentation (A_C), which is proportional to the applied load (F^N), where H is material hardness (50 MPa for ice at -5 °C (Barnes and Tabor, 1966) (equation 2).

$$A_C = \frac{F_N}{H} \tag{2}$$

Their estimate for the Sherman RA was based on a number of modelling results and assumptions: i) τ is entirely dissipated as heat and does not include losses from deformation, fragmentation, collisions, lateral dispersion and momentum exchange with the basal substrate; ii) the energy flux (e) was equally divided both into the flowing rock avalanche debris and into the ice over which it travelled; iii) the ice and air content of the debris was assumed to be 50 % and 20 % respectively; iv) the friction angle was 30° - typical for sandstone, and; v) the debris porosity varied between 5 and 25 %. Like any modelling, assumptions have to be made for parameters that are not directly measurable, however, the temperature of the snow and glacial ice over which the Sherman RA travelled was not considered. This RA occurred in late winter (March 27th) 1964, where the ice and snowpack is likely several degrees below freezing. Frictional energy will therefore not solely be used for the phase change from snow/ice to liquid water, it will also be used to raise the temperature of the snow/ice to 0 °C from which a phase change can occur. The quantity of frictionally-produced meltwater estimated by Sosio *et al.* (2012) is therefore likely an overestimate but is the current best estimate for any glacial RA. Despite these drawbacks, the Sherman glacier RA is typical of a glacial RA >1 Mm^3, with a number of attributes that make it a good representative of large RAs (Deline, Hewitt, *et al.*, 2014). This makes its calculated quantity of frictionally-produced meltwater a good estimate for large RAs in high-mountain glaciated regions.

2.5 Supraglacial rock avalanche mobility

A number of mechanisms have been proposed over the years attempting to explain the cause of long runouts that characterise large RAs, among them volume (Heim, 1932), slope and flow thickness (Legros, 2002), mechanical (Davies, 1982) or acoustic fluidisation (Collins and Melosh, 2003), dynamic fragmentation (Davies and McSaveney, 1999, 2009) water lubrication (Legros, 2002) and air lubrication (Shreve, 1968), although air lubrication has been deemed unrealistic due to the pressure required and air leakage through the debris (Erismann and Abele, 2001).

Glacial RAs often have far greater runouts than their non-glacial counterparts (Sosio *et al.*, 2012; De Blasio, 2014; Deline, Hewitt, *et al.*, 2014; Pudasaini and Krautblatter, 2014), suggesting path material is the dominant control on RA mobility (Sosio *et al.*, 2012; Aaron and McDougall, 2019). This is important for two reasons; i) glacial ice has low basal resistance and; ii) the incorporation/entrainment of snow and ice, which melts through frictional heating, fluidising the flow (as described in section 2.4). This is the main difference between a glacial and non-glacial RA. As such, the amount of snow and ice entrained into the flow, coupled with the roughness of the icy surface over which it travels, determines its mobility. Although less important relative to the quantities of frictionally-produced meltwater, the moisture content of the failed rock mass can also play a role, through the incorporation of permafrost in cleft systems or pore spaces (Schneider *et al.*, 2011).

RA mobility is often measured using the coefficient of friction, which represents the conversion of gravitational energy into kinetic energy (De Blasio, 2014). As well as being influenced by RA volume, ice and water content, and low-friction surfaces, this coefficient is influenced by topography, which can constrain or promote flow (e.g. Schneider *et al.*, 2011; De Blasio, 2014). Commonly, a proxy is used to represent the friction coefficient by dividing the total vertical height (*H*) i.e. difference between the maximum source zone height and the minimum deposit height, by the total horizontal distance (*L*) i.e. distance from the source, to the deposit terminus (e.g. Sosio *et al.*, 2012). This typically yields a value between 0 and 1, the lower the value, the more mobile the RA. However, if a RA fall height is greater than its horizontal travel distance, values can exceed 1, for example. where the runout is constrained by topography. For a model RA consisting of dry fragmented rock, where resistance to motion is governed by the friction angle, a H/L value of 0.6 should be expected (Heim, 1932). This *H/L* ratio is not constant and has been suggested to decrease with landslide volume (e.g. Lucas, Mangeney and Ampuero, 2014). Glacially deposited RAs feature some of the lowest *H/L* values of all RAs (Deline, Hewitt, *et al.*, 2014), with values as low as 0.11 (Huggel *et al.*, 2005; Deline, Hewitt, *et al.*, 2014). This indicates they travel with reduced friction in comparison to those running out onto other substrates such as snow, sediment, and bedrock (Sosio *et al.*, 2012; De Blasio, 2014; Aaron and McDougall, 2019).

The geomorphology of a RA deposit can provide clues about the RA propagation and flow, which are otherwise almost impossible to measure. De Blasio (2014) proposed a mechanism to explain glacial RA mobility and their reduced friction coefficient, by

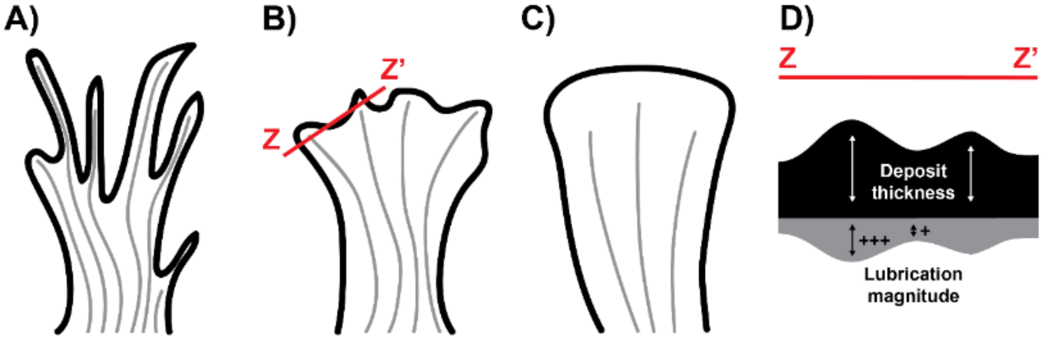

Figure 4: Different deposit typologies as suggested by De Blasio (2014). A) Typology 1, B) Typology 2, and C) Typology 3. D) Represents how the differences in deposit thickness influence the digitations of RAs flowing on glaciers. Modified from De Blasio (2014).

creating a model to investigate the mechanics of a rock mass sliding on ice. Key to their model was that RA friction is determined by the effect of rock ploughing of the ice surface, except under rare circumstances where the rock is softer than the ice. Due to this rock ploughing they hypothesise that two main stages occur: stage 1 involves the delivery of rocky blocks to the ice, sliding over and ploughing the ice surface. This ice cover envelops the basal rock debris, and frictional melting lubricates this ice cover, with sliding now occurring between wet icy surfaces. The second phase is characterised by resistance only coming from ice-ice interactions as opposed to ice-rock interactions, creating a natural basal lubricating layer. This reduced friction coefficient at the bed promotes rapid sliding and high mobility. The thickness of the rock debris during deposition also determines the shape of the deposit once it terminates. Thinner deposits are characterised by a less coherent mass with digitations (finger-like structures) at the terminus of the deposit, that De Blasio (2014) term 'typology 1'. Thicker deposits are characterised by a coherent lobate appearance termed 'typology 3'. A 'typology 2' deposit features smaller digitations and is more lobate than a deposit of typology 3 (Figure 4) (De Blasio, 2014). The low friction basal substrate, combined with the open, unconfined surfaces of glaciers promotes this deposit spreading (Deline, Hewitt, *et al.*, 2014). Flume experiments agreed with De Blasio (2014) in that meltwater significantly influenced the deposition morphology of the deposit (Yang *et al.*, 2019). They also determined ice contents > 30 % significantly increased runout distance, but ice contents > 80 % decreased runout length (Yang *et al.*, 2019). Mathematical modelling of these events is still in its infancy, but promising steps have been taken (Pudasaini and Krautblatter, 2014; Sansone, Zugliani and Rosatti, 2021). Developments in this area will allow us to understand and predict the hazards that these long runouts can pose.

2.6 Rock avalanche frequencies

As detailed above, supraglacially deposited RAs have profound environmental effects from source to sink, so it is important to understand their magnitudes and frequencies. In mountain environments RAs are typically high magnitude, low frequency events (Tebbens, 2020). Over long time scales slope stability is highly variable both spatially and temporally, and closely follows cycles of glaciation and deglaciation (Pánek, 2019). RA frequency has been found to be greatest immediately after deglaciation, before decreasing to a more constant rate, that can be maintained over thousands of years (Ballantyne and Stone, 2013). Studies of long term RA trends are important for analysing triggers and how current climate warming will influence slope stability (Pánek, 2019). Evidence indicates that RAs are more frequent in glacial environments, than in nearby ice-free valleys (McSaveney, 2002; Geertsema *et al.*, 2006; Hewitt, 2009). This is likely because cryospheric factors are key to preparing and triggering RAs above glaciers (see section 2.3.2). However, because mountain environments are under constant tectonic strain and experience high-magnitude seismic events (Burbank and Anderson, 2011), coupled with their susceptibility to static and cyclic fatigue (McColl, 2015) and exceptional erosion rates (Montgomery and Brandon, 2002), any climatic upturns in RA frequencies are difficult to discern (Coe, 2020).

RAs onto glaciers are normally recorded as large one-off events, such as the Kolka-Karmadon RA (Huggel *et al.*, 2005; Kääb *et al.*, 2021), or they are recorded as clusters, triggered simultaneously by a high-magnitude, low-frequency earthquake (Jibson *et al.*, 2006). This is evident in the databases collated by Schneider *et al.* (2011) and Deline *et al.* (2015), the latter of which collated all known events >1 Mm^3 since 1950 (Figure 5). It has therefore previously been difficult to understand the background frequencies of these events, as no consistent temporal records are available. Glacial RA inventories do exist (e.g. Whitehouse and Griffiths, 1983), but not with high spatial and temporal resolution. These inventories therefore only include events that are still recognisable in the landscape and have not lost their diagnostic features to erosion (e.g. Uhlmann *et al.*, 2013). This leaves large gaps in our understanding of annual and decadal trends and prevents accurate

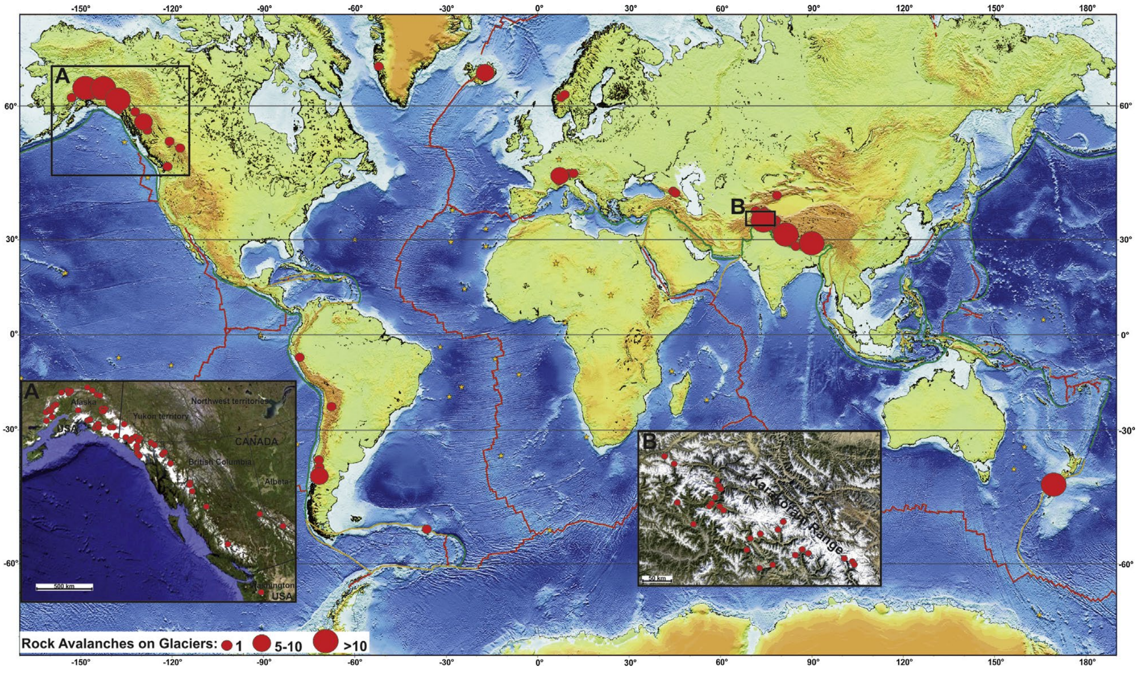

Figure 5: Distribution of rock avalanches (>1 Mm^3) onto glaciers worldwide. A) Northwest North America, B) Karakorum Range. (source: Deline et al. 2014).

analysis of climatic influence on rock slopes in glaciated regions. Nevertheless, over the last decade, three inventories have been created for southeast coastal Alaska. These were created by utilising the Landsat imagery archive dating back to 1972, giving high spatial and temporal resolution for RA identification. Uhlmann *et al.* (2013) created the first inventory of 123 RA deposits on glaciers in the Chugach Mountains, to assess their contribution to sediment fluxes. Coe, Bessette-Kirton and Geertsema (2018) created an inventory in Glacier Bay National Park, due to a cluster of exceptionally large events since 2012. This inventory was used to assess climatic upturns in frequency, size and mobility, with significant increases found for the latter two. Similarly, Bessette-Kirton and Coe (2020) created an inventory in the St Elias mountains, that consisted of 220 RAs, in just a 3700 km^2 region. From this they drew similar conclusions to those of the Glacier Bay dataset of Coe, Bessette-Kirton and Geertsema (2018), with increasing RA frequency between 2013 and 2016, due to uncharacteristically high air temperatures. In addition to these Alaskan RA inventories, other inventories have been created, but none which specifically look at landslides onto glaciers, just landslides associated with glacial activity (e.g. Liu, Wu and Gao, 2021).

These limited studies have allowed assessments of climatically driven upturns in RA frequency, particularly in Alaska where <5 events in the Glacier Bay and St Elias inventories were triggered by earthquakes. However, despite using the expansive Landsat imagery collection, we have to question the reliability of these inventories because of their methodology. All three studies acknowledge the limitations of manually identifying these RAs from just one or two satellite images per year. However, basing analysis on data that is not representative of the long-term RA rates in an area is problematic. It is known that RAs can only be visible on the surface for short time periods (Dunning *et al.*, 2015), so how many RAs have these studies missed? If this is a substantial amount, the frequency, magnitude, and mobility of RAs over time are likely misinterpreted. Additionally, RA relationship with climate trends may weaken, and their contribution to catchment sediment budgets may be significantly under-estimated. While these studies provide a good first step towards understanding the frequencies and magnitudes of these events under a changing climate, a lack of a standardised identification technique hinders comparisons and robust conclusions. Their clustering around coastal Alaska is also problematic for understanding larger scale trends. This has led for calls to create ‘bellwether’ sites: ~5000 km^2 areas, where inventories can be created, and RA frequencies monitored, to understand the impacts of climate change on these hazards (Coe, 2020).

2.7 Rock avalanche deposit characteristics

2.7.1 Deposit volumes

The failure volumes of RAs are commonly defined as >10^6 m^3 (Deline, Hewitt, *et al.*, 2014), however, failure volume and final deposit volume are often different, owing to the entrainment of material, particularly glacier ice, and compaction of the deposit (e.g. Bessette-Kirton, Coe and Zhou, 2018). Often RAs are detected from 2D satellite imagery (e.g. Uhlmann *et al.*, 2013) and therefore, volume cannot be derived from this information, only deposit areal coverage. Instead you need accurate pre and post event digital elevation models, which are often unavailable, to estimate volume, but this is also difficult for events deposited on glaciers due to ablation and scour of the glacier surface (Bessette-Kirton, Coe and Zhou, 2018). To circumnavigate this problem, volume-area scaling relationships have been derived for glacial RAs (Sosio *et al.*, 2012) (Figure 6), however, they perform poorly due to the unique nature of each event. For example, the Lamplugh RA has the best estimation of volume of any glacial RA, calculated by analysis of multiple digital elevation models, and crude modelling in areas of positive and negative elevation changes (Bessette-Kirton, Coe and Zhou, 2018). This estimated the volume of the deposit at 69.9 ± 7.9 Mm^3 of rock and snow/ice. In comparison, using the volume-area scaling relationship of Sosio *et al.* (2012) (volume = 2.6 x $area^{0.86}$), gives a volume estimate of 35.7 Mm^3; almost half the volume calculated using superior methods. Application of this volume-area scaling relationship over large RA inventories would result in significant underestimates of RA sediment fluxes.

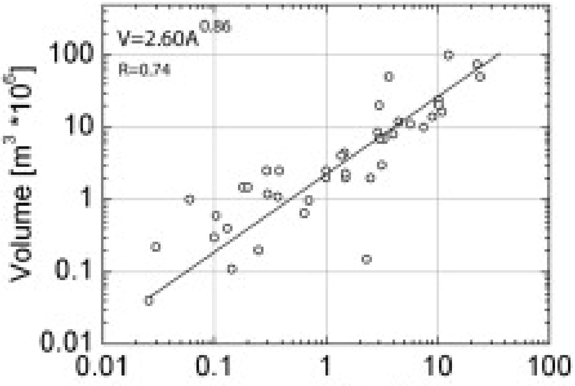

Figure 6: Empirical relationship between RA area and detached volume derived from 42 glacially-deposited RAs (source: Sosio et al., 2012)

2.7.2 Deposit thickness

The structure and character of a RA deposit is dependent on the original bedrock properties (Dufresne, Prager and Bösmeier, 2016) and the travel path (Aaron and McDougall, 2019). The deposit geometry and thickness is determined by flow characteristics (as described in section 2.5) and by the surface topography over which it travels, with slopes causing both extension and compression of debris, and larger obstacles causing splitting of the deposit into separate lobes (Deline, Hewitt, *et al.*, 2014). Flow of RA debris onto and over a glacier results in deposits that are thinner and longer than a RA of identical volume that flows over a non-ice substrate (Evans and Clague, 1988; Lipovsky *et al.*, 2008; Sosio *et al.*, 2012; De Blasio, 2014; Delaney and Evans, 2014). Glacial deposits are typically only a few metres thick on average, but vary between < 1 m and > 20 m (Deline, Hewitt, *et al.*, 2014). Thicknesses are, however, difficult to

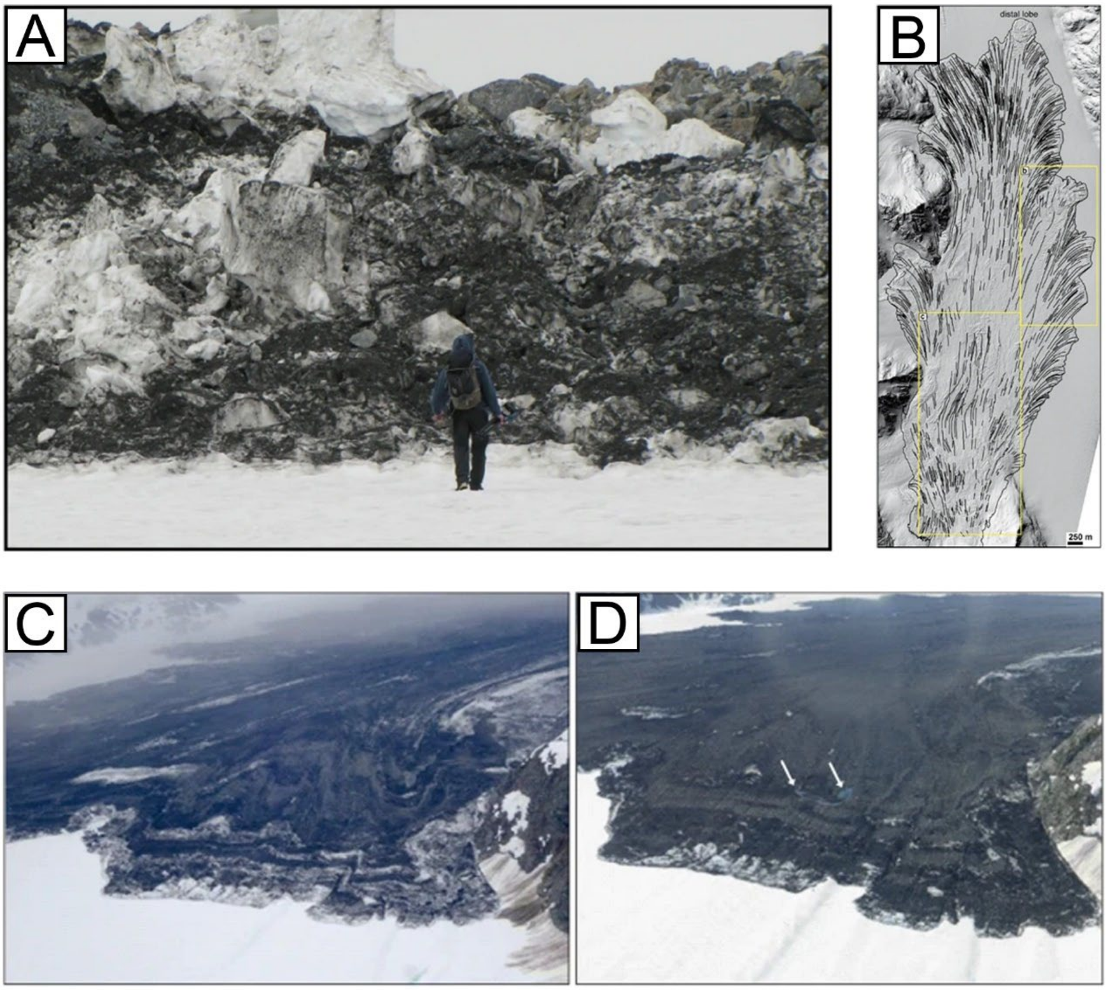

Figure 7: Lamplugh RA, A) bulldozed frontal-distal ridge with high snow/ice content. Geologist for scale. B) Flow lines, C) Photograph from the day of the RA, note snow/ice content of lobate distal rim, D) Photograph 6 days after the RA, note snow/ice melt out and ponds on deposit surface (white arrows). Photos from Dufresne et al. (2019).

derive and are often point measurements. The 1991 Mt. Aoraki RA was originally believed to be ~1.2 m thick on average (McSaveney, 2002), yet a ground-penetrating radar survey of the deposit later revealed thicknesses were 5-10 m (Reznichenko, Davies and Alexander, 2011).

2.7.3 Deposit sedimentology and features

Typically a non-glacial RA deposit will have two main vertical horizons: the top boulder carapace and the body facies (Dufresne, Bösmeier and Prager, 2016; Dufresne, 2017). Although sometimes a basal facies and a transitional facies is also present (Dufresne, Bösmeier and Prager, 2016; Dufresne, 2017). This structure implies widespread inverse grading of the deposit. However, thin supraglacial RAs do not often have a distinct carapace (Jibson *et al.*, 2006; Delaney and Evans, 2014; Dufresne *et al.*, 2019). Often a deposit is matrix-rich with no clear structure (Delaney and Evans, 2014). Surficial features are normally evident with pseudo-fluidal structures such as lobate forms, longitudinal ridges and flowbands, pseudo-viscous rims and frontal-distal ridges (Hsü, 1975; Dufresne and Davies, 2009; Shugar and Clague, 2011; Dunning *et al.*, 2015). In addition to pressure ridges and debris cones (alternatively known as 'molards' or 'hummocks') (Paguican, van Wyk de Vries and Lagmay, 2014). Lobes form at the deposit

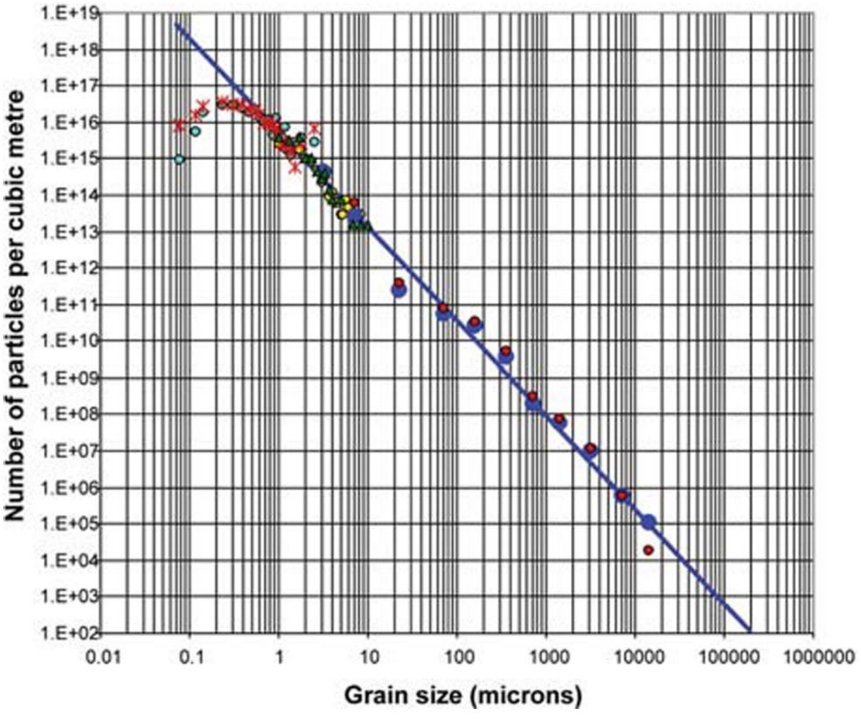

Figure 8: Grain size distribution of 1991 Mount Cook/Aoraki RA and 1992 Mount Fletcher II RA. Grain counts following a power-law relationship, which breaks down at smaller sizes. (source: Davies and McSaveney, 2007).

edge when flow is unobstructed (Figure 7A, C, D) (Shugar and Clague, 2011; Dufresne *et al.*, 2019). These are typically full of snow/ice from entrainment and bulldozing (Dufresne *et al.*, 2019). The origins of these lobes can be tracked using structural surface features such as perpendicular flowbands (Figure 7B), indicating direction of travel (Shugar and Clague, 2011; Dufresne *et al.*, 2019). Surficial linear/curvilinear structures are also present at the deposit surface indicating areas of compression and extension (Dufresne *et al.*, 2019). These features tell us about the RA process, and have been found to not reflect the underlying pre-event glacier surface (Dufresne *et al.*, 2019), unless they travel over moraines (Shugar and Clague, 2011).

Lithology, failure volume and runout play a critical role in determining supraglacial RA deposit grain-size distribution (Deline, Hewitt, *et al.*, 2014). Grain size distributions often follow a power-law relationship, meaning the distributions are fractal across most grain size ranges, implying scale invariance (Figure 8) (Crosta, Frattini and Fusi, 2007; McSaveney and Davies, 2007). This is to be expected for comminution by fragmentation processes (Turcotte, 1986) and can indicate both RA origin and processes. However, below 0.6 μm this fractal distribution breaks down, and decreases in grain size abundance are observed (Figure 8) (McSaveney and Davies, 2007), likely due to sub-micron fragments clinging to larger grains (Belousov, Belousova and Voight, 1999). There may therefore be a limit at which a grain can maintain independence, and not adhere to other particles. Despite this breakdown of the fractal relationship at sub-micron sizes, RA grain size distributions are dominated by fine material (Deline, Hewitt, *et al.*, 2014). Observations of a supraglacial RA in New Zealand found that 99.5 % of particles (by number) were < 10 μm (McSaveney and Davies, 2007), yet the mass of this fine fraction varies. In the Karakorum, over half the mass of a supraglacial RA deposit was made up of sub-granular particles (< 4 mm) (Hewitt, 2002a). Contrastingly, on the Black Rapids and Sherman Glacier RAs, in Alaska, the size fraction < 10 μm made up less than 5 % of the deposit mass but spatial variations were high (Shugar and Clague, 2011). Few other studies have investigated supraglacial RA deposit grain size distributions, but the limited information available implies that there is considerable variation, but all events produce a significant number of fine particles. However, these fine particles do not necessarily make up the bulk volume of the deposit, just the bulk particle frequency.

Accurate measurements of RA deposit grain size distributions are generally difficult to obtain, focusing on point measurements, because sampling the vertical thickness or representative volume of a deposit is difficult. In addition, this is complicated further by finer particles being composed of a number of even smaller submicron particles, termed 'agglomerates' (Reznichenko *et al.*, 2012). These particles are created during rapid, high-stress comminution, where fragmented particles cannot disperse, due to the confined conditions, and do not break down afterwards because of the high ratio of surface to inertial forces that prevent shear (Reznichenko *et al.*, 2012). These agglomerates appear very strong and can withstand typical sediment sieving and washing, making them good indicators of RA debris (Reznichenko *et al.*, 2012). This ability to withstand erosion and dispersion has made them useful for determining moraine formation mechanisms, which has subsequently brought about questions regarding the role of certain moraines as climatic indicators, as the agglomerates indicated they are of RA origin (Reznichenko *et al.*, 2012).

Large dust clouds created during phases 2 and 3 of a RA event are commonly overlooked with regards to sedimentology. This is likely because they are often only visible within the immediate aftermath of an event. Yet they can blanket areas much larger than the deposit themselves (Deline, 2001), often transported during the air blasts, that accompany large RAs (Deline, Hewitt, *et al.*, 2014). Deposition of this dust on glacier surfaces can lead to enhanced ablation due to it causing a decrease in surface albedo (Reznichenko *et al.*, 2010). Dufresne *et al.* (2019) managed to sample the dust that encircled the Lamplugh RA deposit in Glacier Bay National Park, Alaska, only a few days after emplacement. Grain size analysis using laser diffractometry revealed that it was dominated (> 86 %) by fine grains between 63 and 0.63 µm (Dufresne *et al.*, 2019). The maximum distance that this dust can travel, and the extraglacial effects it has on other ecosystems, are currently unknown. However, it is known that dust drives supraglacial algal blooms (McCutcheon *et al.*, 2021) and fertilises the ocean (Conway and John, 2014; Chen *et al.*, 2020), so it may be important for both glacial and extraglacial life.

2.8 Glacial debris transport pathways

The flux of glacial debris sourced from subaerial (i.e. RAs), aeolian and subglacial processes, varies both spatially and temporally due to a number of factors such as topography, lithology, hypsometry and climatic conditions (Antoniazza and Lane, 2021). The fate of this debris once in the glacial domain and the ability of a glacier to become debris-covered is inversely correlated with glacier mass balance (Kirkbride, 2000). Deposition location is the fundamental factor that determines its transport pathway and the length of time it remains in the glacial domain. Key to debris transport pathways is deposition above or below the equilibrium line altitude (ELA) (Figure 9) (Anderson and Anderson, 2016). Debris deposited in the accumulation area will be buried by snowfall and advected into the glacier, with the proximity of debris deposition to the ELA, determining how deep the debris will be advected into the glacier and the duration it remains englacially, and supraglacially once it re-emerges at the surface (Anderson and Anderson, 2016), where it can form medial and transverse moraines (Anderson, 2000; Moore, 2021). These englacial transport pathways are controlled by overall glacier stress conditions, and the resulting strain and velocity fields within the ice mass (Wirbel, Jarosch and Nicholson, 2018). Debris deposited below the ELA, in the ablation zone, will remain on the surface due to lower snowfall, higher melt rates and glacial ice flow dynamics. If debris deposition is high, ice ablation is high, and debris transport and export is inefficient, the ablation zone becomes debris covered, forming a debris-covered glacier (Kirkbride, 2011). Debris is a critical control on ice ablation, with thin debris layers enhancing melt and thick debris layers suppressing melt, with the critical debris thickness

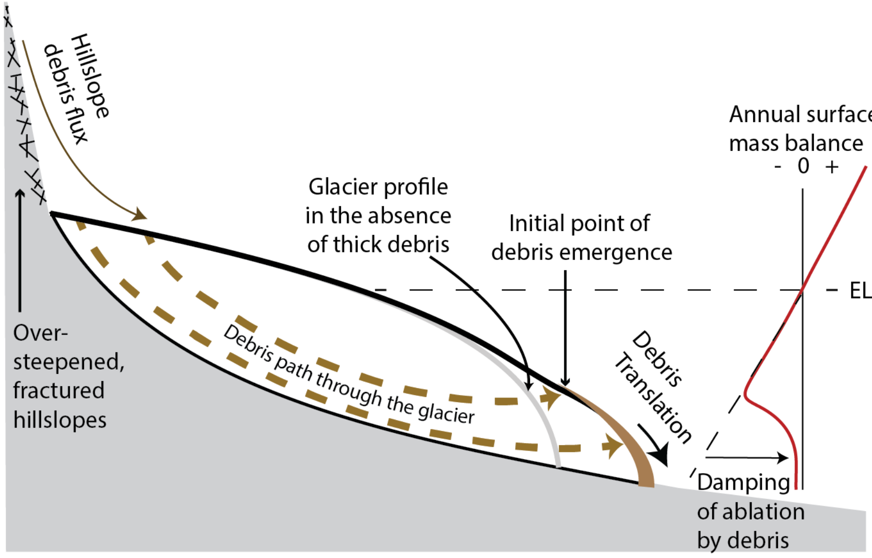

Figure 9: Schematic of the glacial debris transport system. (source: Anderson and Anderson, 2016).

determined predominantly by debris lithology (Østrem, 1959; Reznichenko *et al.*, 2010). However, the impact of an entire glacial debris cover on ablation rates is not as simple as thin debris enhancing melt and thick debris suppressing melt, as a number of debris-covered glaciers are retreating and downwasting as fast as their non debris-covered counterparts (e.g., Huo, Bishop and Bush, 2021). Despite these wide-scale spatial and temporal ablation impacts, a debris cover is universally acknowledged as a key control on the hydrological system of a glacier (e.g. Fyffe, Brock, Kirkbride, Mair, *et al.*, 2019; Miles *et al.*, 2020) and the distribution of ice (Benn *et al.*, 2012; Anderson *et al.*, 2021), both of which are important for debris export.

Hydrology is important for glacial debris transport because it can mobilise the small debris fraction (<4 mm) into supraglacial, englacial and subglacial drainage systems (Jennings, Hambrey and Glasser, 2014). This can occur either through direct interaction with active hydraulic components i.e., supraglacial streams, or through meltwater seepage of thicker debris layers where fines are preferentially translocated to the ice-debris interface (e.g. Eyles, 1979). The larger debris fractions are indirectly mobilised by hydraulic components through melt processes causing debris redistribution (e.g. Westoby *et al.*, 2020; Huo, Bishop and Bush, 2021). For example, ice-cliff backwasting can be enhanced by the supraglacial and englacial hydrological systems e.g. supraglacial ponds (Sato *et al.*, 2021), and backwasting causes redistribution and remobilisation of debris (Buri *et al.*, 2016; Huo, Bishop and Bush, 2021). This debris can be mobilised into supraglacial ponds (Buri *et al.*, 2016), resulting in long or short term storage depending on glacier dynamics and a lakes susceptibility to drain, or the debris will be flushed into active meltwater channels, travelling through the hydrological system before export (Jennings, Hambrey and Glasser, 2014). Ultimately, the more meltwater that is available to interact with the debris, the more likely debris is to be mobilised by meltwater processes, but this depends on debris coverage and thickness (Fyffe *et al.*, 2020). In areas of thin debris cover, where melt rates are high, an efficient drainage system can develop early in the melt season (Fyffe *et al.*, 2019). The entrained debris fraction from these thinner debris layers, may therefore undergo rapid export early in the melt season, in comparison to areas of thicker debris. Debris that does not get exported immediately may result in incorporation in subglacial ponds or subglacial till, where its export may be delayed any time between hours to years (for full reviews see Evans *et al.*, 2006; Cook and Swift, 2012). It may even reside subglacially until glacier recession, where it may reveal storage in a number of subglacial landforms such as tunnel valleys, eskers, bedrock channels, flutes, crag and tails and drumlins (Dowdeswell *et al.*, 2016). Longer delays in debris release increase in likelihood further down-glacier, particularly in heavily debris-covered areas, which are characterised by inefficient englacial and subglacial drainage systems as a result of hummocky topography and lower melt rates, with smaller supraglacial catchments dominating (Fyffe *et al.*, 2019). The key to debris export is particle size, with smaller particle sizes increasing the chances of export, as can be seen with glacial flour (< 63 μm; Benn, 2009) export in proglacial rivers (Hodson, Mumford and Lister, 2004; Barkdull *et al.*, 2021), lakes (Sommaruga and Kandolf, 2014) and the plumes at the terminus of marine-terminating glaciers (Dowdeswell *et al.*, 2015). A debris cover can also indirectly influence hydrology through its impact on the atmospheric boundary layer above it. For example, a debris cover is a heat source, driving convection and precipitation in the atmospheric boundary layer (Collier *et al.*, 2015). This precipitation would fall on clean ice and persist due to the cold temperature of the underlying ice, yet on a debris cover this snow may melt quicker due to the warmer debris cover, resulting in water percolation through the debris, subsequently increasing melt rates and mobilisation of fine-grained debris particles.

Debris cover impacts on ice distribution have similar impacts to hydrology, in that ice distribution can enhance and suppress debris mobilisation and export. On a localised scale, this can result in rock tables and the movement of larger clasts through the topple-walk mechanism (Anderson, 2000; Fyffe *et al.*, 2020; Moore, 2021). On a glacier-wide scale consistent debris inputs onto a glacier surface, coupled with the insulating effects of debris can create glaciers that are out-of-sync with a warming climate (e.g. Ferguson and Vieli, 2021). This insulating effect, delays both the volume and length response of a glacier (e.g. Ferguson and Vieli, 2021), altering both hypsometry and flow regime (Anderson and Anderson, 2016). A key characteristic of these changes is glacier length, which is primarily controlled by the rate of debris deposition and debris thickness but the location of debris deposition is a secondary control on glacier length (Scherler, Bookhagen and Strecker, 2011a; Anderson and Anderson, 2016). This is important for supraglacially deposited RAs, which influence the quantity, thickness and location of debris, although the extent of this influence is controlled by RA size. Glacier length is important for debris export as longer glaciers transport debris for longer time periods, although this is dependent on glacier velocity. Debris-covered portions of glaciers typically have lower glacier velocities (Scherler, Bookhagen and Strecker, 2011a; Anderson and Anderson, 2016). A reduction in glacier velocity, reduces subglacial erosion rates and can promote till accumulation at the bed (Delaney and Anderson, 2022). This not only inhibits subglacial debris export but englacial and supraglacial debris export. Changes in ice velocity fields also change the strain rates and subsequently the englacial debris transport pathways (Wirbel, Jarosch and Nicholson, 2018). Ultimately, slower ice velocities increase the amount of time debris spends in the glacial domain before export. Velocity decreases can become so profound that ice stagnation occurs (e.g. Thompson *et al.*, 2016; Garg *et al.*, 2022), and this stagnated ice can eventually become detached from the glacier altogether, where it can last for multiple years before the ice content melts out entirely, creating melt-out tills (Boulton, 1970; Schomacker, 2008).

2.8.1 Glacial RA deposit debris transportation and remobilisation

The transport pathways of supraglacially deposited RA debris are poorly constrained but are assumed to be almost identical to normal glacial debris pathways. Their effects on glaciers can, however, be more extreme than debris covers that have formed over time. This is due to their sudden mass input (and the weight this adds to a glacier), which can locally impact melt rates and surface slopes (Vacco, Alley and Pollard, 2010; Shugar *et al.*, 2012), and their potential to initiate glacier surges (Gardner and Hewitt, 1990; Hewitt, 2009), all of which influence a RA deposit debris transport pathway and duration.

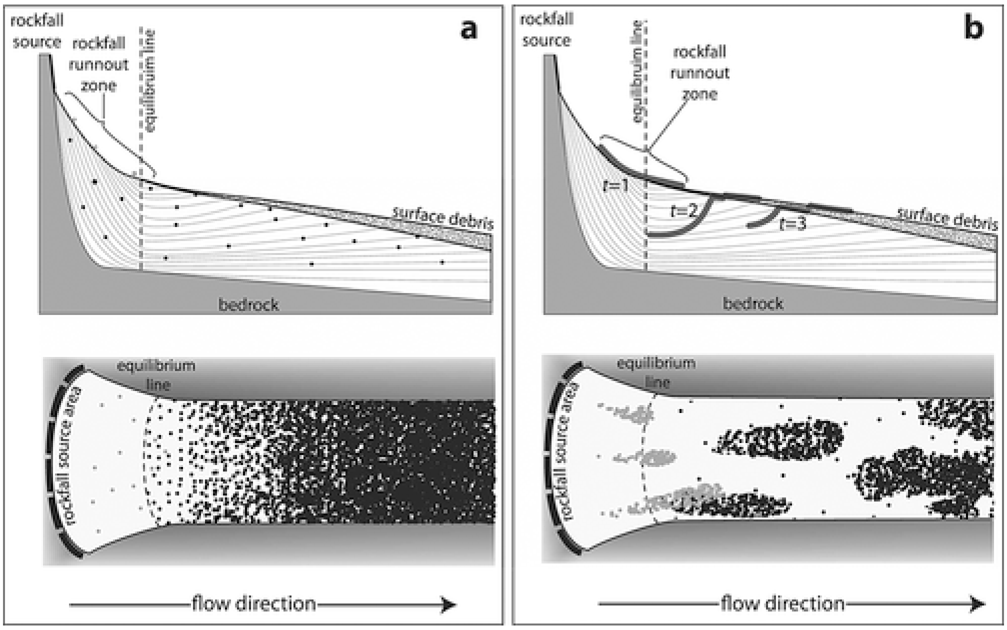

Figure 10: Diagrammatic explanation of rockfall debris deposition and transportation through glaciers in Antarctica A) high frequency, low magnitude rockfalls, B) higher magnitude, lower frequency rockfalls. (source: Mackay et al., 2014).

RA deposits deposited in the accumulation zone, which are advected into the ice get severely deformed during advection and transportation (Jennings, Hambrey and Glasser, 2014; Mackay *et al.*, 2014). Reappearance at the glacier surface after advection therefore shows almost no characteristic signs of these events, making them indistinguishable from an existing supraglacial debris cover (Goodsell, Hambrey and Classer, 2005; Kirkbride and Deline, 2013; Mackay *et al.*, 2014). However, in the dry valleys of Antarctica, ground penetrating radar (GPR) surveys have revealed that defined reflectors representing rockfall deposits are present englacially, with debris deposited at higher elevations travelling further and deeper into the glacier (Figure 10) (Mackay *et al.*, 2014). This is similar to what Dunning *et al.* (2015) found after the Mt. Haast RA in New Zealand in 2013, albeit the dry valley deposits were much older. If this is the case, and glacial flow lines are conducive to preservation of these RA deposit reflectors seen in GPR data, then deposits are potentially identifiable englacially before their re-emergence at the surface.

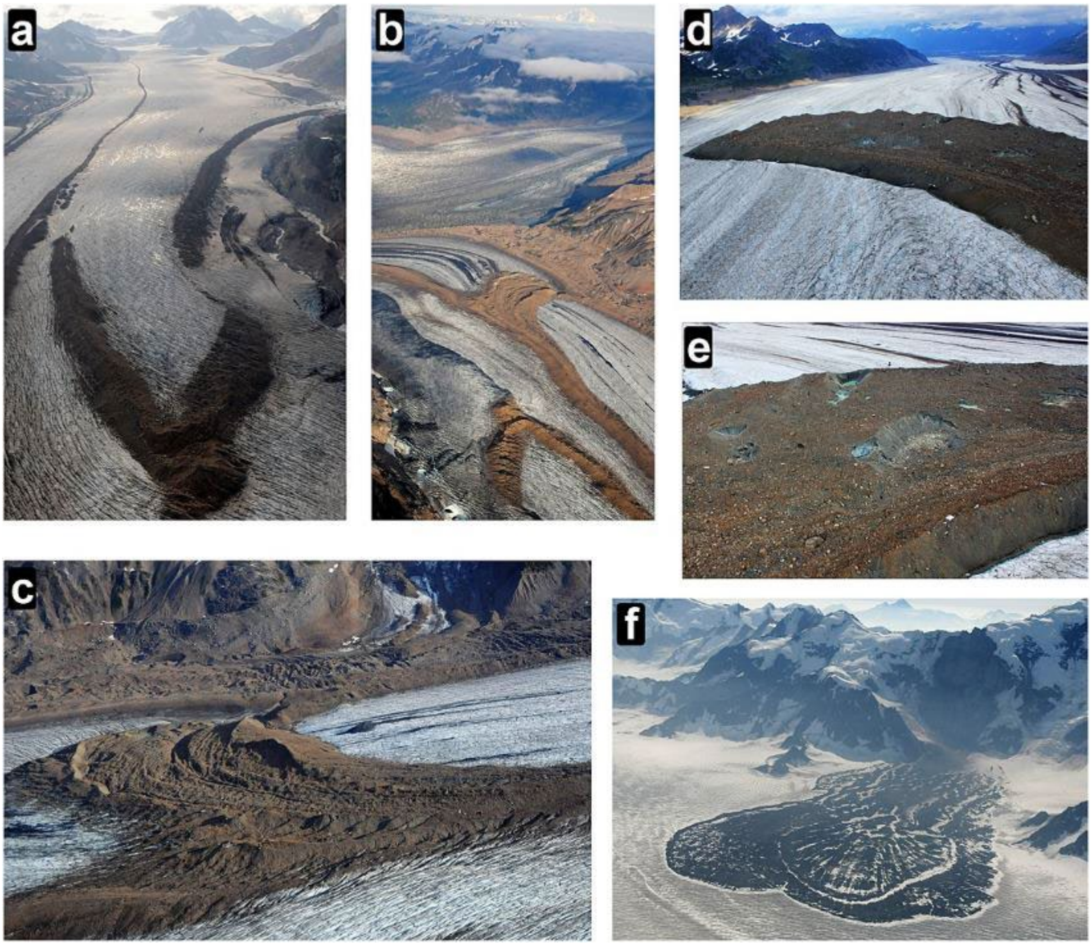

Figure 11: RA deposits altered by lateral strain gradients on glaciers in the Chugach Mountains Alaska (A-C), medial moraine derived from RA debris on Kieffer Glacier (D), Allen glacier RA deposit displaying ~60 m ice pedestal caused by differential melt (E) and lobate RA deposit on Allen Glacier (F) (source: Uhlmann et al., 2013).

RA debris deposited in the ablation zone of a glacier is passively rafted on the surface of a glacier, with the deposit often losing its lobate and elongated RA characteristics, due to deformation by ice flow (Uhlmann et al., 2013) (Figure 11). This is principally because ice at the lateral margins of a glacier commonly flows slower than ice in the centreline of a glacier, due to ice temperature, ice crystal orientation and interactions with the bed (Nielsen and Stockton, 1956; Hooke, 2019). During a RA deposits time on the surface of a glacier it undergoes modification through a number of processes. Initially, the snow and ice that it has entrained melts out, often causing the formation of ponds, and redistribution of the debris (Dufresne et al., 2019). Over time, a platform will gradually form beneath the RA, due to the insulating effect of the debris on the ice below, and the ablation of the surrounding ice (e.g. Reznichenko et al., 2010). These platforms are typically 5 – 50 m thick (Deline et al., 2015), with higher platforms rare, due to compensation by ice flow (Hewitt, 2009) and debris spilling down from the steep edge of the platform, due to ice backwasting, resulting in spreading and thinning of the deposit (Reznichenko, Davies and Alexander, 2011). Due to the heterogeneous nature of the debris thickness, hummocky topography forms, with debris undergoing constant reworking (Deline et al., 2015). Glacier flow and all that entails, such as compression, convergence, extension i.e. crevasses, can all influence the structure of the deposit after emplacement (Uhlmann et al., 2013; Deline et al., 2015). Finer materials are often disturbed and relocated by wind and meltwater, potentially removing them and resulting in a coarser deposit over time (Deline et al., 2015). Grains of all sizes may be further comminuted by these redistribution processes (Deline et al., 2015), and the freeze-thaw processes that occur post-deposition (Shugar and Clague, 2011). After prolonged exposure to these processes, deposits often lose their initial morphology, such as flow bands, however, newer flow bands can form, indicating ice flow speeds beneath the deposit (Figure 11) (Shugar and Clague, 2011; Uhlmann et al., 2013).

2.9 Glaciological implications of rock avalanche deposits

Over the long term, the input of a large debris mass, with a low albedo, onto a typically high albedo surface, results in changes to ablation on a glacier surface, with thicker debris reducing ablation and thinner debris promoting ablation (Figure 12) (Reznichenko *et al.*, 2010). This sudden change to ablation can alter glacier mass balance, causing the terminus to become out-of-sync with the climate, due to the insulating effect of a RA deposit (Figure 13), although this depends on RA deposition location. Modelling of the Black Rapids Glacier with and without the 2003 RA deposits present on the glacier surface suggests that these changes can result in increased ice flow velocity downstream of the RA deposits but decreased ice flow velocity upstream of the RA deposits (Figure 14) (Shugar *et al.*, 2012), which can lead to glacier terminus advance (Shugar, Clague and McSaveney, 2018). However, it is difficult to disentangle these effects from natural glacier surges (Hewitt, 2009; Kääb *et al.*, 2021). Deposit lithology plays a critical role in these processes, as this determines the thermal conductivity of the debris (Mihalcea, Brock, *et al.*, 2008). The effects of the mass input onto the glacier have also got to be considered, as this can lead to internal ice deformation and increased basal sliding (Jamieson, Ewertowski and Evans, 2015). However, often the mass input is insignificant in comparison to the seasonal weight loss and gains from accumulation and ablation (Hewitt, 2009). The effects of this mass input depend on the size of the glacier and the size of the RA. A small RA onto a large glacier is likely insignificant, but a large RA onto a small glacier, is likely to have far greater implications. In the case of the catastrophic Kolka-Karmadon low-angle glacier detachment in 2002, which resulted in the release of 130 x 10^6 m^3 of ice and rock, claiming ~135 lives, the glacier had been subjected to frequent mass loading (~10^6 m^3) by rock and ice falls in the months leading up to the event (Kotlyakov, Rototaeva and Nosenko, 2004). This caused bulging and widespread

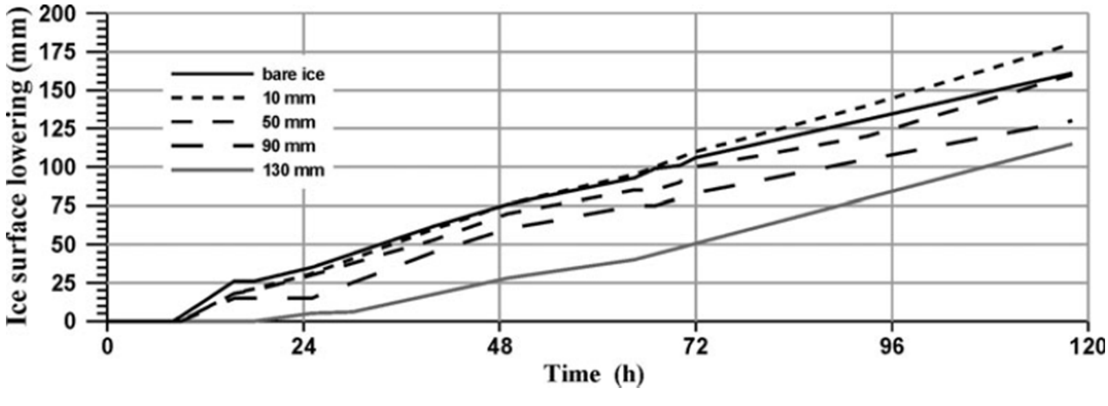

Figure 12: Debris thickness effect on ice surface lowering, for thicknesses 10, 50, 90 and 130 mm, in comparison to bare ice (source: Reznichenko et al. 2010)

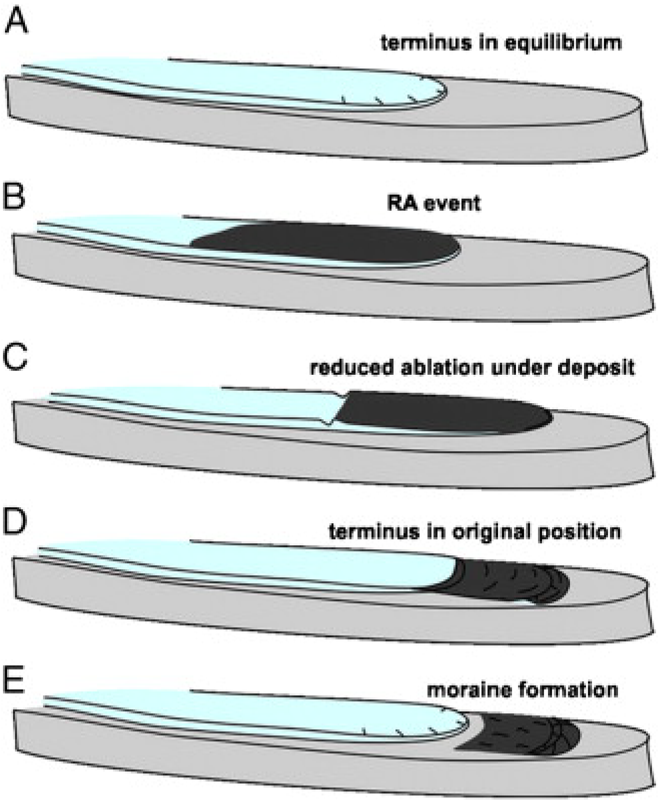

Figure 13: Conceptual model of a glaciers response to a RA deposited in the ablation zone (source: Reznichenko et al., 2011).

crevassing of the ice, and the creation of supraglacial ponds (Evans *et al.*, 2009). Both this loading by subaerial mass wasting and the instantaneous impact energy of a large (~20 Mm^3) rock/ice fall onto the glacier, have been suggested as separate causes of this collapse (Huggel *et al.*, 2005; Evans *et al.*, 2009). In addition to these glaciological effects, it has been postulated that supraglacial RAs can also increase subglacial water pressures. This is due to the mass input onto the glacier surface, and the creation and rapid subglacial drainage of frictionally-produced meltwater (Fountain *et al.*, 2005; Evans *et al.*, 2009). Key to these processes is the calculation of RA volume, which is difficult to estimate as described in section 2.7.1.

2.10 Rock avalanche debris export into the extraglacial environment

There is currently a lack of research into supraglacial RA deposit source to sink processes. This is, in part, because RA deposits are not always passively rafted on the surface of a glacier, so debris provenance is not always clear (see section 2.8). However, no matter what happens to a RA deposit, it will likely become part of an existing glacier debris cover, and/or be exported straight into the extraglacial environment. Uhlmann *et al.* (2013) were the first and only study to calculate glacial RA debris transport and export for more than a single deposit. They mapped 123 RA deposits on the surface of glaciers from 1979 to 2008. However, they did not account for RAs which are rapidly advected into the ice (Dunning *et al.*, 2015), likely resulting in significant underestimations of RA frequency. Additionally, to calculate deposit volume they assumed a uniform debris thickness of 2-3 m, which is difficult to validate based on our current knowledge of glacial

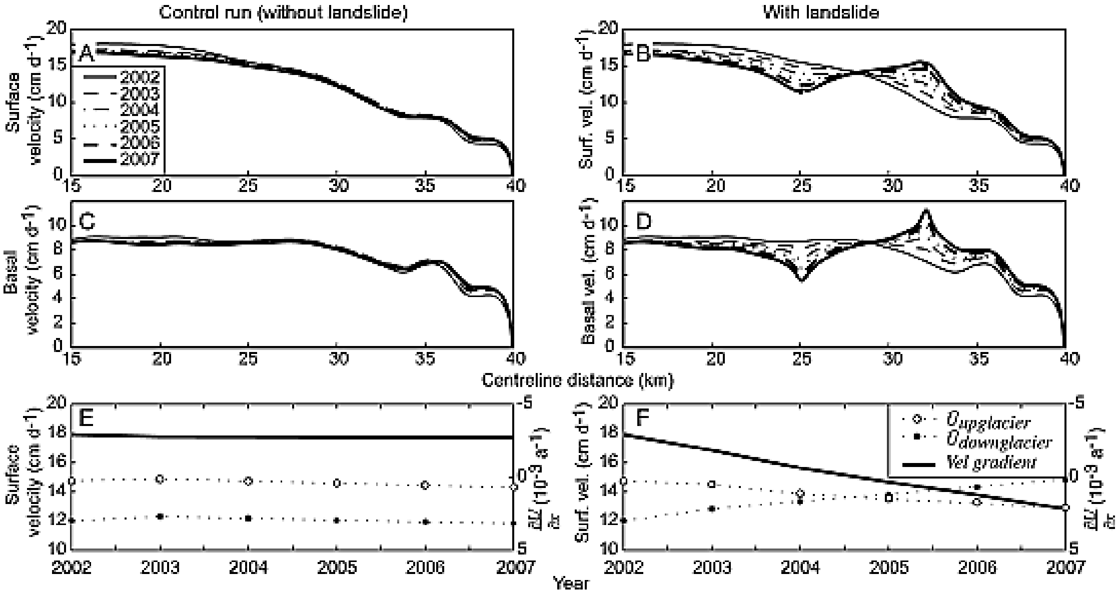

Figure 14: Modelled surface and basal ice velocities of Black Rapids Glacier, with the 2003 landslide and without a landslide to act as a control, using a full Stokes model (source: Shugar et al., 2012).

RA volumes (see section 2.7.1). Using this data they estimated sediment yields of 190 to 7400 t km^{-2} yr^{-1} of glacial RA debris export. This is equivalent to erosion rates of 0.5-0.7 mm yr^{-1} in the region, with earthquakes responsible for 73 % of this rate (earthquakes were responsible for 73 % of total RA volume). These export rates are comparable to fluvial sediment yields from similar sized catchments in mountain environments, and those of terminal locations at glaciers outside of Alaska (Korup, 2012). However, in their study area, sediment yields from supraglacial RAs were an order of magnitude lower than rates found at the terminus of Alaskan glaciers. This suggests a subglacial, englacial or ice-marginal source of debris dominates sediment export in this area of Alaska. Although the origin of this subglacial/englacial/ice-marginal debris may have been misclassified and the sediment packages may originate from subaerial erosion, the products of which were advected into the ice. Despite this limited research, it does suggest that RAs may be an important, previously overlooked contributor to glacial sediment export. This is backed up by studies of singular RA deposits, that have been calculated to be equivalent to multiple years of ‘normal’ glacial erosion or rockwall supply (Korup, 2012; Williams and Koppes, 2019), so even in areas of little RA activity, a single event may act as an important sediment pulse.

The environment this debris is exported into is key for further modification and storage. Release of sediment from land-terminating glaciers is crucial in landform genesis in the proglacial environment and the response of these landforms and the catchment as a whole to environmental change (Porter, Smart and Irvine-Fynn, 2019). Sediment transport connectivity by distinct landforms and landscape units is termed ‘geomorphic coupling’, and involves the aggradation and degradation of sediment by geomorphic processes across a landscape, forming sediment cascades, coupling sources to sinks (Burt and Allison, 2009). For marine-terminating glaciers, the source to sink journey is substantially shorter, but sediment export is key for biogeochemical processes (e.g. Hopwood *et al.*, 2014), and paleoenvironmental reconstructions (e.g. Simon, St-Onge and Hillaire-Marcel, 2012). The fluxes and storage of glacial sediment in extraglacial environments are therefore important for geomorphologists, and biogeochemists.

2.10.1 Export from land-terminating glacier

For a land-terminating glacier, export can occur by aeolian and hydraulic erosion of the finer fraction of the deposit, during its time on the surface, and then through melt out of the underlying ice, or transport off the end of the glacier, due to glacier down-wasting, ice velocity or glacier recession. The speed of this is determined by catchment size and climate, because this determines precipitation and water storage, and subsequently ice turnover rates (Benn *et al.*, 2014). For a sediment package of an identical size, a larger glacier is needed to transport the same amounts of sediment in a dry climate, in comparison to a wet climate, where a smaller glacier would be needed. This is due to the lower turnover rates of ice in arid climates. The rates of transportation and export of this sediment through the proglacial zone depend on glacial-fluvial coupling (Benn *et al.*, 2014). A coupled ice margin is dynamic and the coupling between glacial and proglacial sediment transport is efficient. In these zones moraine development and therefore sediment storage is limited, due to meltwater streams migrating across the glacier terminus. This promotes rapid export of debris through fluvial processes. In contrast, a decoupled ice margin is the result of low precipitation and subsequently low ice supply and therefore smaller glaciers, but debris supply remains high. In these areas glacial and fluvial transport is decoupled, meaning there is inadequate outwash. This promotes the aggradation of sediment into moraines and other such landforms in the proglacial forefield, which act as both temporary and more permanent storage (Carrivick *et al.*, 2013). They can also dam meltwater, forming proglacial lakes (Benn *et al.*, 2014; Carrivick and Heckmann, 2017) and these lakes can store debris as they are effective sediment traps (e.g. Geilhausen *et al.*, 2013). However, moraine dams are often weak and prone to failure (Neupane, Chen and Cao, 2019), causing large outburst floods that can mobilise large amounts of forefield debris (Carling, 2013). Erosion and export of sediment from proglacial forefields, can also be caused by high magnitude rainfall events (Warburton, 1990), and the finer debris fraction can be mobilised by aeolian processes i.e. katabatics, anabatics and föhn winds (Benn *et al.*, 2014). In contrast, proglacial forefields may be re-incorporated into the glacier, if surging occurs, restarting or delaying the sedimentation and export process (Antoniazza and Lane, 2021). Despite these erosion and export mechanisms in proglacial forefields, often sediment export is significantly lower than eroded sedimentary inputs, and this is known as the sediment delivery problem (for full review see de Vente *et al.*, 2007). This disparity is likely to increase in the future as more glaciers transition from a coupled glacial and fluvial system, to an uncoupled system, due to rising ELAs, as a result of warming atmospheric temperatures (IPCC, 2019).

For RA debris deposited into the proglacial forefield, this glacial-fluvial coupling will be key to RA sediment transport rates to lower elevations and larger river systems. At a coupled margin, sediment will be fluvially-exported, although the sheer amount of RA debris, will likely result in export taking decades, at which point, due to warming atmospheric temperatures, a glacier may become decoupled, so only a portion of the debris is exported. If a glacier is fluvially decoupled sediment will remain at the glacier terminus in moraines, much like has been hypothesised as the cause of the Waiho Loop (Alexander, Davies and Shulmeister, 2014).

2.10.2 Export from marine-terminating glacier

Marine-terminating glaciers often have a less visible supraglacial debris cover. This is often due to widespread crevassing, causing debris advection into the ice (Wirbel, Jarosch and Nicholson, 2018), or because subaerial processes are not dominant, and sediment is mainly derived from the bed i.e. in Antarctica (Winter *et al.*, 2019). Similar to debris transportation into and through the proglacial zone, climate also plays a key role in determining sediment discharge into marine environments. Debris export from glaciers in Polar Regions, where summer temperatures do not exceed freezing, is predominately through calving and incorporation in icebergs (Anderson, 1999; Domack and Powell, 2018). This debris fraction, believed to be negligible due to the clean ice surfaces of glaciers in these regions, has hitherto been underestimated (Winter *et al.*, 2019). In more temperate areas, where ice is at the pressure melting point and ablation dominates, the predominant mechanism for sediment export is through meltwater export, with iceberg rafted debris negligible (Domack and Powell, 2018). The key difference in marine environments is the lack of any sediment modification and storage, because export occurs into the ultimate sediment sink; the ocean.

2.11 Biogeochemical impacts of glacial sediment export

Export of sediment from glaciers is important on a global scale as they export large amounts relative to their discharge. For example, drainage from the Greenland Ice Sheet accounts for 1.1 % of the Earth's freshwater flux, but 8 % of global suspended sediment export to the ocean (Overeem *et al.*, 2017). The fine fraction of glaciofluvial sediment is the critical component, being attributed to a number of biogeochemical marine processes (Wadham *et al.*, 2019). This is principally because of its reactivity, due to a high surface-area-to-volume ratio (Gunnarsen *et al.*, 2019). Consequently, this has resulted in research suggesting glaciers are natural factories for lithogenic nutrients (Hawkings *et al.*, 2014, 2015, 2017), principally iron (Fe) (Hawkings *et al.*, 2014, 2018; Raiswell *et al.*, 2016), nitrogen (N) (Wadham *et al.*, 2016), silica (S) (Hawkings *et al.*, 2017) and phosphorous (P) (Hawkings *et al.*, 2016), and their implications for the global carbon cycle after export (Wadham *et al.*, 2019).

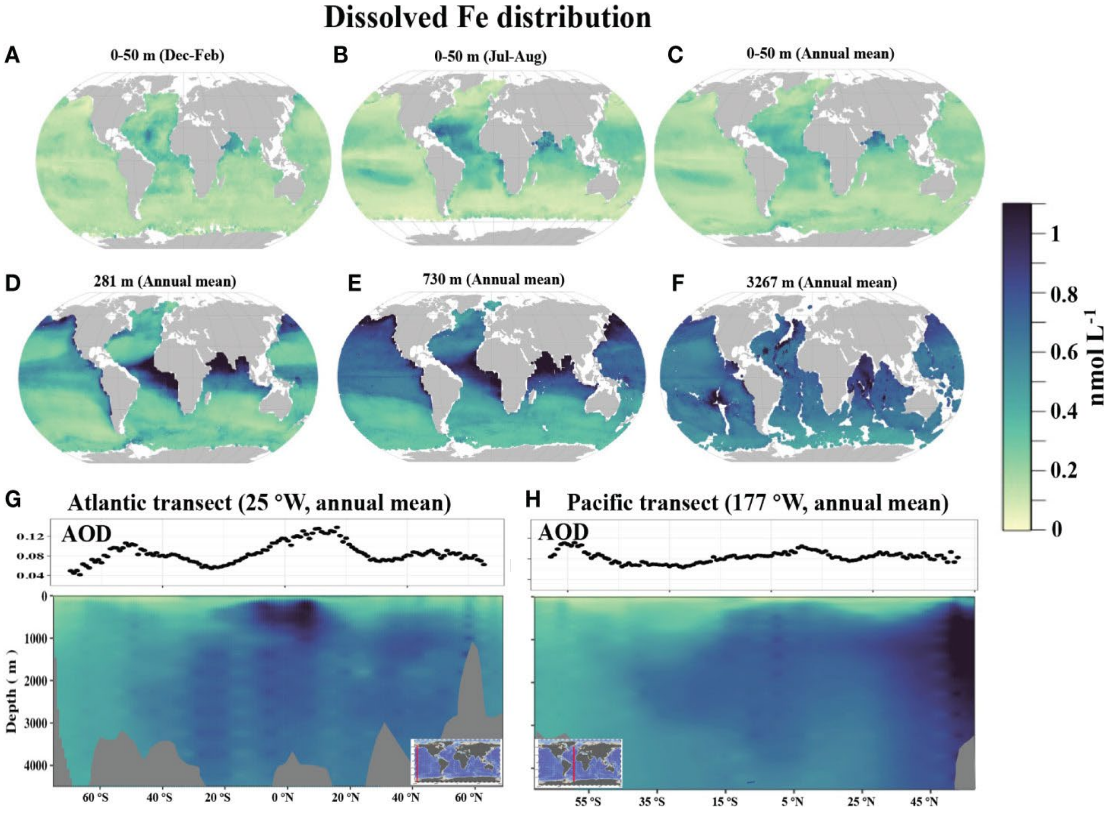

Figure 15: Modelled global Fe distribution in the photic zone between A) December and February, B) July and August, and C) annually. Modelled Fe distribution at varying depth horizons (D-F) and dissolved Fe concentrations at transects across the G) Pacific Ocean, and H) Atlantic Ocean. (source: Huang, Tagliabue and Cassar, 2022).

These nutrients are transported by meltwater into extraglacial environments where they can be utilised by microbial assemblages. Export of these lithogenic nutrients into oceanic environments has received considerable attention because a number of oceans that glaciers discharge into are nutrient-limited i.e. Antarctic glaciers and the Southern Ocean (e.g. Raiswell *et al.*, 2008; Gerringa *et al.*, 2012; Monien *et al.*, 2017; St-Laurent *et al.*, 2017), Greenlandic glaciers and the North Atlantic Ocean (e.g. Bhatia *et al.*, 2013; Hopwood *et al.*, 2016; Hawkings *et al.*, 2018), and Alaskan glaciers and the Gulf of Alaska (e.g. Hood and Scott, 2008; Crusius *et al.*, 2011; Schroth *et al.*, 2011, 2014).

Oceanic nutrient limitation refers to ocean productivity being limited by a lack of available nutrients. Ocean productivity is the key control on carbon partitioning between the atmospheric carbon reservoir, and the oceanic carbon reservoir, the latter of which is approximatively 60 times larger than the former (Berger, Smetacek and Wefer, 1989). The oceanic carbon reservoir is controlled by photoautotrophs, primarily phytoplankton, which account for the vast majority of marine primary production (Moore *et al.*, 2013). These photoautotrophs therefore play a critical role in global CO_2 sequestration, which is increasingly important with warming atmospheric temperatures (IPCC, 2019). However, in certain areas of the global ocean, their growth rates, populations and activity are limited by the availability of certain nutrients (Moore *et al.*, 2013). The two key limiting nutrients are iron (Fe) and nitrogen (N) although a number of other co-limiting nutrients also thwart productivity (Moore *et al.*, 2013). Of these two key limiting nutrients Fe is almost solely derived from glacial sediment and has been directly linked to phytoplankton blooms (e.g. Gerringa *et al.*, 2012), whereas the glacial nitrogen cycle is more complex, with N sources split between precipitation (snow and rain) (e.g. Hodson *et al.*, 2005; Telling *et al.*, 2012) and microbial activity of glacial sediments (Wadham *et al.*, 2016). Here we focus on Fe export from sedimentary sources because RAs may play a key role in this process.

2.11.1 Fe in the global ocean

Since the first vertical profiles of Fe were published in the 1980s (Gordon, Martin and Knauer, 1982; Martin and Fitzwater, 1988) Fe has become the most studied trace element in the ocean (Boyd and Ellwood, 2010). It has been estimated to control primary productivity in half of the world's oceans (Moore *et al.*, 2001). This makes Fe a key control on CO_2 drawdown and subsequently the global climate over multiple glacial cycles, with Martin (1990) terming this the "iron hypothesis". A number of studies since then have attempted to quantify Fe quantities in the global ocean (e.g. Johnson, Michael

Gordon and Coale, 1997; Measures *et al.*, 2008), with most recent estimates using a combination of observations and modelling indicating an overall Fe distribution that varies spatially, temporally and at depth (Figure 15) (Huang, Tagliabue and Cassar, 2022). Oceanic currents play a key role in bioavailable Fe concentrations because the longer Fe spends in the ocean, the more it ages, resulting in a decrease in its bioavailability due to adsorption, precipitation and aggregation (Wu *et al.*, 2001; Bergquist, Wu and Boyle, 2007). This is why the Pacific and Southern Oceans have lower concentrations than the Atlantic (Figure 15).

Fe has a predominantly lithogenic source, existing in three main redox states: Fe(0), Fe(II) and Fe(III). These all persist as solids in oxygenated environments but the most common forms are Fe(II) and Fe(III) (referred to as ferrous and ferric iron ions) (Raiswell *et al.*, 2018). Fe(II) is the most reactive and soluble form, and in oxygenated waters it oxidises to Fe(III), which is less soluble (Hawkings *et al.*, 2018), unless Fe(II) is stabilised by organic colloids (Breitbarth *et al.*, 2009). Despite Fe being the fourth most common element on earth, it is biologically scarce in the oceans, as it is believed to predominantly exist as nanoparticulate/colloidal Fe(III), resulting in low solubility, and this limits solid-liquid interactions and therefore its overall bioavailability (Raiswell and Canfield, 2012). Of the Fe that is dissolved, 99 % is strongly bound by organic ligands which further decreases its bioavailability (Gledhill and van den Berg, 1994; Rue and Bruland, 1995; Wu and Luther, 1995).

The release of Fe into the ocean occurs through the erosion of Fe bearing minerals, with Fe being transported to the ocean by fluvial and aeolian processes, iceberg rafted sediment and subglacial runoff, hydrothermal activity and recycling of ocean shelf sediments (Raiswell and Canfield, 2012). These sources supply the majority of Fe as

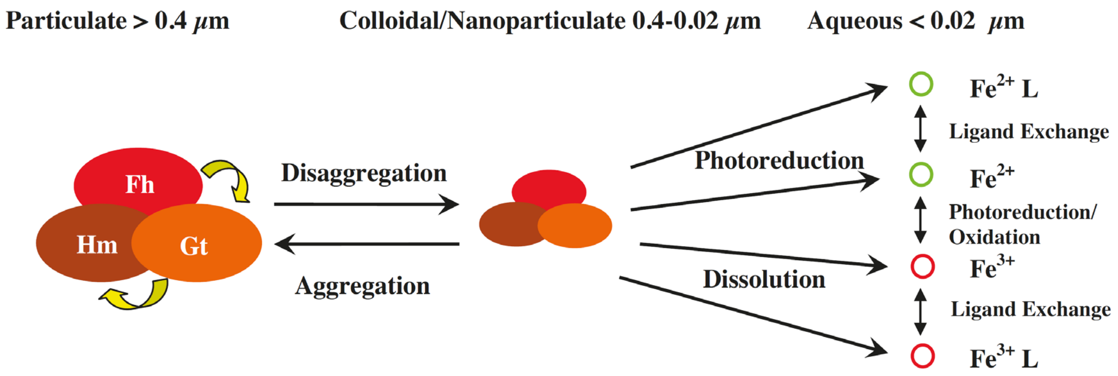

Figure 16: Surface seawater interactions and transformations between aqueous, colloidal/nanoparticulate and particulate Fe (oxyhydr)oxides. The yellow arrows represent the transformation of ferrihydrite to goethite and haematite. (source: Raiswell and Canfield, 2012).

(oxyhydr)oxides (>0.4 µm), instead of in its dissolved form (<0.4 µm) (Poulton and Raiswell, 2002), resulting in low aqueous Fe concentrations in the ocean. Cellular uptake of Fe requires it to be in its aqueous form but in Fe-limited areas, Fe (oxyhydr)oxides can be utilised (Figure 16). This is due to the transformation of particulate (oxyhydr)oxides into colloidal/nanoparticulate Fe through disaggregation, which can then subject it to photoreduction and dissolution, to transform it into an aqueous form (for full review see Raiswell and Canfield, 2012). Of the particulate species, ferrihydrite is the least stable but the most likely source of bioavailable Fe, however, it has a short half-life before it transforms into more stable forms i.e., goethite/haematite, depending on ocean temperature and pH, and interactions with foreign ions and organic matter (Schwertmann, Stanjek and Becher, 2004; Das, Hendry and Essilfie-Dughan, 2011).

2.11.2 Glacial Fe

The majority of research into glacial Fe export has focused on iceberg-rafted debris (Raiswell, 2011; Death *et al.*, 2014; Duprat, Bigg and Wilton, 2016; Raiswell *et al.*, 2016) and meltwater runoff (Schroth *et al.*, 2011; Gerringa *et al.*, 2012; Bhatia *et al.*, 2013; Hawkings *et al.*, 2014). Fe from these two sources is dominated by the highly reactive and bioavailable nanoparticulate (<0.1 µm) Fe(II) fraction, primarily in the form of ferrihydrite (Hawkings *et al.*, 2014, 2018; Raiswell *et al.*, 2016). However, variation between catchments/regions is stark, likely due to the total organic carbon content of glacial flour, which promotes its accumulation and release (Hopwood *et al.*, 2014). Analysis of this Fe(II) export from glaciated environments reveal that it is highly biolabile (Hawkings *et al.*, 2018) and is therefore easier for marine microbiota to mine and consume than Fe(III) (typical of nonglaciogenic Fe sources), (Shoenfelt *et al.*, 2017). In addition, the particle size fraction that is often measured for glacial Fe (<2 µm) (e.g. Hawkings *et al.*, 2018), should allow it to remain suspended in the euphotic zone after export, increasing the likelihood of it being biologically utilised. However, this depends on a number of conditions after export, which can promote/inhibit Fe utilisation, which are relevant for a number of other nutrients exported by glaciers.

2.11.3 Export of glacial nutrients into extraglacial environments

All nutrient export from glaciers into extraglacial environments is variable both spatially and temporally, with some following seasonal cycles and varying with meltwater discharge (Wadham *et al.*, 2016). The majority of research into glacial nutrient export has focused on marine-terminating glaciers, due to their direct export of meltwater and sediment into the ocean. This has resulted in marine-terminating glaciers being termed "macronutrient pumps" (Hawkings, 2021). The export of nutrients from marine terminating glaciers occurs through two main processes: meltwater discharge and iceberg calving, the latter of which can transport nutrients thousands of kilometres from its source (e.g. Wu and Hou, 2017).

Meltwater discharge directly exports nutrients into the immediate extraglacial environment at the glacier terminus stimulating phytoplankton blooms (e.g. Gerringa *et al.*, 2012; Arrigo *et al.*, 2017). However, the importance of direct nutrient export in meltwater is somewhat disputed and its effectiveness depends on a number of factors, such as the subglacial drainage system and the ice/ocean interface (for full review see Hopwood *et al.*, 2020; Hawkings, 2021). The upwelling of nutrient-rich deep ocean water, to the surface in buoyant meltwater plumes, may actually be more important for productivity (Hopwood *et al.*, 2020). This has been found by comparing the productivity of two Greenlandic fjord systems, one fed by a marine-terminating glacier, and the other by a land-terminating glacier (Meire *et al.*, 2017). Yet each individual fjord is different, with a number of factors influencing circulation and stratification patterns and subsequent nutrient dispersal (Meire *et al.*, 2017; Kanna *et al.*, 2018; Torsvik *et al.*, 2019). Sediment dispersal is also important in these situations, with concentrated sediment plumes having a negative effect on ecosystem productivity. This is because high suspended sediment concentrations reduce the euphotic depth, and therefore shrink the productive zone, although this 'sediment shading' can reduce UV radiation stress on microorganisms (Sommaruga, 2014). Similar to fresh meltwater plumes, sediment-laden icebergs can also induce surface mixing of ocean waters, albeit on a much smaller scale (Helly *et al.*, 2011; Carlson *et al.*, 2017). This mixing along with gradual deposition of entrained sediment through melt, has been observed to induce phytoplankton blooms far away their source glacier (Raiswell, Benning, Tranter, *et al.*, 2008; Schwarz and Schodlok, 2009; Duprat, Bigg and Wilton, 2016; Wu and Hou, 2017). In the future, the importance of both meltwater and solid ice discharge nutrient export pathways will be modified, due to changes in ice dynamics and surface melt (Choi *et al.*, 2021). This will have important implications for ocean fertilisation on both a local and global scale.

In contrast, research investigating nutrient export from land-terminating glaciers into proglacial lakes and rivers has received less attention, likely due to the more localised effects on aquatic ecosystems. In glacier-fed streams and lakes, glacially exported sediment and nutrients are key to determining the light availability, and the structure and composition of biological communities (Laspoumaderes *et al.*, 2013; Martyniuk, Modenutti and Balseiro, 2014; Rose *et al.*, 2014; Hotaling *et al.*, 2017; Barouillet *et al.*, 2019; Ren *et al.*, 2019). However, unlike nutrient export into the marine environment, Fe does not play a critical role in limiting freshwater aquatic ecosystems. Instead, carbon (C), N, and P are the critical nutrients exported from land-terminating glaciers which influence downstream aquatic communities (for full review see Ren *et al.*, 2019). In glacier-fed streams the C exported from glaciers is readily bioavailable for heterotrophic consumption, therefore controlling the abundance and structure of heterotrophic communities (Hood and Berner, 2009; Singer *et al.*, 2012; Fegel *et al.*, 2019) and N and P availability limit biofilm production and subsequently macroinvertebrates in streams (Ren *et al.*, 2019). In glacier-fed lakes, P and N availability limits both phytoplankton communities (Elser *et al.*, 2009, 2010; Slemmons and Saros, 2012), and bacterial communities at higher trophic levels (Mindl *et al.*, 2007). Export of nutrients into these environments therefore determines local aquatic ecology immediately downstream of the glacier terminus. Yet rapid changes in glacial ice cover are having significant impacts on the biogeochemistry of these ecosystems, with reduced glacial cover increasing the export of some nutrients, but decreasing others (Hood and Berner, 2009; Pryer *et al.*, 2020). Aquatic ecosystem fertilisation is not the only benefactor of glacial nutrient export though, with glacial flour found to be an effective fertiliser for plants (Gunnarsen *et al.*, 2019). Deposition of this in decoupled proglacial areas (see section 2.10.1), may therefore provide fertile ground for a plethora of fauna to colonise.

The origins of glacial nutrients are often overwhelmingly assumed to be subglacial, through subglacial erosion and then weathering and microbial reactions of this eroded sediment at the bed (e.g. Hopwood *et al.*, 2014; Hawkings *et al.*, 2017, 2018), but no study has ever considered the contribution of other debris sources i.e. supraglacial debris, except cryoconite (for full review see Cook *et al.*, 2016). There is no research on the effects of a glacial debris cover on glacial nutrient export, despite the subaerial weathering reactions that occur (Owen, Derbyshire and Scott, 2003) and the abundance of fine sediment (e.g. Hambrey *et al.*, 2008). However, the higher metal concentrations found in the geochemical meltwater signatures of rock glaciers suggest debris is a key control on nutrient export (Thies *et al.*, 2013; Ilyashuk *et al.*, 2014; Fegel *et al.*, 2016). RA deposits could therefore be a key component of nutrient delivery into, and export from, glacial domains. They not only produce an abundance of fine sediment, delivered with an abundance of frictionally-produced meltwater during RA flow (see section 2.4) that could wash a substantial amount of fine material to the bed of a glacier, but their debris can also remain supraglacially for long periods, subjecting it to chemical weathering reactions and solute release. It is therefore important to determine whether fine RA material is geochemically similar to other glacier debris released from glaciers i.e. glacial flour, and could therefore have similar fertilising effects upon release into the extraglacial environment.

Chapter 3 - GERALDINE (Google Earth Engine supRaglAciaL Debris INput dEtector) – A new tool for identifying and monitoring supraglacial landslide inputs

Published in **Earth Surface Dynamics**, December 2020

Authors: William D. Smith[1], Stuart A. Dunning[1], Stephen Brough[1,2], Neil Ross[1], Jon Telling[3]

1. School of Geography, Politics and Sociology, Newcastle University, Newcastle upon Tyne, UK.
2. Department of Geography and Planning, School of Environmental Sciences, University of Liverpool, UK.
3. School of Natural and Environmental Sciences, Newcastle University, Newcastle upon Tyne, UK.

Citation: Smith, W. D., Dunning, S. A., Brough, S., Ross, N., and Telling, J.: GERALDINE (Google Earth Engine supRaglAciaL Debris INput dEtector): a new tool for identifying and monitoring supraglacial landslide inputs, Earth Surf. Dynam., 8, 1053–1065, https://doi.org/10.5194/esurf-8-1053-2020, 2020.

Author contributions: William Smith developed the tool and wrote the manuscript. Stuart Dunning made substantial contributions to the conception and functionality of the tool, as well as manuscript editing. Stephen Brough, Neil Ross and Jon Telling provided useful guidance on tool functionality and contributed to the manuscript. The supplementary information for the manuscript is included in Chapter S1.

Abstract

Landslides in glacial environments are high-magnitude, long runout events, believed to be increasing in frequency as a paraglacial response to ice-retreat/thinning, and arguably, due to warming temperatures/degrading permafrost above current glaciers. However, our ability to test these assumptions by quantifying the temporal sequencing of debris inputs over large spatial and temporal extents is limited in areas with glacier ice. Discrete landslide debris inputs, particularly in accumulation areas are rapidly 'lost', being reworked by motion and icefalls, and/or covered by snowfall. Although large landslides can be detected and located using their seismic signature, smaller ($M \leq 5.0$) landslides frequently go undetected because their seismic signature is less than the noise floor, particularly supraglacially deposited landslides which feature a "quiet" runout over snow. Here, we present GERALDINE (Google earth Engine supRaglAciaL Debris INput dEtector): a new free-to-use tool leveraging Landsat 4-8 satellite imagery and Google Earth Engine. GERALDINE outputs maps of new supraglacial debris additions within user-defined areas and time ranges, providing a user with a reference map, from which large debris inputs such as supraglacial landslides (> 0.05 km^2) can be rapidly identified. We validate the effectiveness of GERALDINE outputs using published supraglacial rock avalanche inventories, then demonstrate its potential by identifying two previously unknown, large (>2 km^2), landslide-derived supraglacial debris inputs onto glaciers in the Hayes Range, Alaska, one of which was not detected seismically. GERALDINE is a first step towards a complete global magnitude-frequency of landslide inputs onto glaciers over the 38 years of Landsat Thematic Mapper imagery.

3.1 Introduction

There are currently >200,000 glaciers worldwide covering >700,000 km^2, of which 8.2% are less than 1 km^2 (Herreid and Pellicciotti, 2020), excluding the Greenland and Antarctic ice sheets (RGI Consortium, 2017). Recent estimates suggest supraglacial debris only covers 7.3% of the area of these glaciers (Herreid and Pellicciotti, 2020), up from 4.4% estimated by Scherler et al. (2018). However, for many glaciers supraglacial debris plays a critical role in controlling a glaciers response to climate change, due to its influence on surface ablation and mass loss (e.g., Benn et al., 2012; Mihalcea et al., 2008a, 2008b; Nicholson and Benn, 2006; Østrem, 1959; Reznichenko et al., 2010). Extensive debris coverage can alter the hydrological regime of a glacier (Fyffe *et al.*, 2019), with the potential to increase/decrease downstream freshwater availability (Akhtar, Ahmad and Booij, 2008), and can play a key role in controlling rates of glacier thinning and/or recession, subsequently contributing to sea level rise (Berthier *et al.*, 2010). This supraglacial debris control is thought to be particularly important in the context of negative glacier mass balance, with retreating glaciers being characterised by expanding debris cover extents (Scherler, Bookhagen and Strecker, 2011b; Kirkbride and Deline, 2013; Tielidze *et al.*, 2020). The expansion of supraglacial debris cover is due to: (i) glaciological and climatological controls such as thrusting and meltout of sub- and en-glacial sediment onto the surface (e.g., Kirkbride & Deline, 2013; Mackay et al., 2014; Wirbel et al., 2018); (ii) debris input from surrounding valley walls through bedrock mass movements (Porter *et al.*, 2010; Deline, Hewitt, *et al.*, 2014); (iii) dispersion of medial moraines (Anderson, 2000); and, (iv) remobilisation of debris stores, particularly lateral moraines (Van Woerkom *et al.*, 2019). The relative contributions of 'glacially' derived sediment, which may in fact be the re-emergence of glacially modified mass movements (Mackay *et al.*, 2014), as compared to direct subaerial inputs, is highly variable and there is complex coupling between hillslopes and glaciers that varies with relief (Scherler, Bookhagen and Strecker, 2011a). However, recent evidence from the Greater Caucasus region (Eurasia) suggests that supraglacially deposited rock avalanches (RAs), attributed to processes associated with climate change, are a key factor in increasing supraglacial debris coverage (Tielidze et al. 2020). Magnitude-frequency relationships suggest these low frequency, high magnitude events have a disproportionate effect on sediment delivery (Malamud *et al.*, 2004; Korup and Clague, 2009). One of these large events mobilises enough debris to dominate overall volumetric production and delivery rates of debris, exceeding that of the much higher frequency but lower magnitude events. Here, we focus on supraglacial landslide deposits (>0.05 km^2). Such deposits are commonly associated with RAs, which are defined as landslides: (a) of high magnitude (> 10^6 m^3); (b) perceived low frequency; (c) long runout; and (d) where there is disparity between high present-day rates of slope processes above ice (Allen, Cox and Owens, 2011; Coe, Bessette-Kirton and Geertsema, 2018) and expected rates based on theories of lagged paraglacial slope responses (Ballantyne, 2002a; Ballantyne, Wilson, *et al.*, 2014).

In formerly-glaciated landscapes, dating of RA deposits has shown a lag in the response of paraglacial slope activity with respect to the timing of deglaciation (Ballantyne, Sandeman, *et al.*, 2014; Pánek *et al.*, 2017). Events cluster in deep glacially eroded troughs and inner gorges at relatively low elevations in the landscape (Blöthe, Korup and Schwanghart, 2015). Numerical modelling has shown how considerable rock-mass damage is possible during the first deglaciation cycle (Grämiger *et al.*, 2017) and some of the largest inventories highlight a close association between the former glacier limits and the source zones of RAs, particularly in the vicinity of glacial breaches (Jarman and Harrison, 2019). However, almost all of our knowledge of past events relies on the presence of in-situ RA deposits. Due to erosional and depositional censoring such deposits are heavily biased to ice-free landscapes where preservation potential is higher, although these are still unlikely to constrain true magnitude-frequencies unless rates of geomorphic turn-over are low (Sanhueza-Pino *et al.*, 2011). In supraglacial settings, landslides, where topography allows, travel much further than their non-glacial counterparts due to the reduced friction of the ice surface (e.g., Sosio et al., 2012). Rapid transportation away from source areas also occurs because of glacier flow. This removes the simplest diagnostic evidence of a subaerial mass movement – a linked bedrock source area and debris deposit. Without the associated deposit, bedrock source areas are easily mistaken for glacial cirques (Turnbull and Davies, 2006). Fresh snowfall or wind redistribution of snow can rapidly cover a RA deposit that is many kilometres square in area (Dunning *et al.*, 2015). If this occurs within the accumulation zone the deposit is essentially lost to all surface investigation and non-ice-penetrating remote sensing and ground-based techniques until its eventual re-emergence in the ablation zone, after potentially considerable modification by transport processes. If a RA is deposited in the ablation zone, surficial visibility may be seasonal, but through time surface transport will disrupt the initially distinctive emplacement forms (Uhlmann *et al.*, 2013). This supraglacial debris loading represents a glacier input (Jamieson, Ewertowski and Evans, 2015) and can alter glacier mass balance, influence localised melt regimes (Hewitt, 2009; Reznichenko, Davies and Alexander, 2011), and glacier velocity (Shugar *et al.*, 2012; Bhutiyani and Mahto, 2018), leading to speed-ups and terminus positions asynchronous with current climatic conditions. Sometimes this leads to moraines that are out of phase with climate, due to the reduction in surface ablation and surging (or the slowing of a retreat) caused by large landslide inputs (Hewitt, 1999; Tovar, Shulmeister and Davies, 2008; Shulmeister *et al.*, 2009; Vacco, Alley and Pollard, 2010; Reznichenko, Davies and Alexander, 2011).

Currently, the detection of large supraglacially deposited landslides – other than through the most common form of ground-based detection, eye-witness reporting – is through the application of optical satellite imagery. This is a labour and previously computationally intensive process, often involving the downloading, pre-processing and manual analysis of large volumes (gigabytes) of satellite imagery. Manual imagery analysis to identify supraglacial landslide deposits and RAs has principally been applied in Alaska. This technique enabled detection of 123 supraglacial landslide deposits in the Chugach Mountains (Uhlmann *et al.*, 2013), 24 RAs in Glacier Bay National Park (Coe, Bessette-Kirton and Geertsema, 2018), and more recently, 220 RAs in the St Elias Mountains (Bessette-Kirton and Coe, 2020). These studies acknowledge that their inventories are incomplete/underestimates due to analysis of summer imagery and an inability to detect events that are rapidly advected into the ice. These are critical drawbacks preventing accurate magnitude-frequency relationships from being derived, but analysis of more imagery over larger areas is unfeasible due to time and computational requirements. Studies of this kind are also typically in response to a trigger event e.g., earthquake or a cluster of large RA events (e.g., Coe et al. (2018) in Glacier Bay National Park), spatially biasing inventories into areas with known activity. They therefore provide a snapshot in time, with no continuous record. Methods are needed which are accessible, quick and easy to apply and require no specialist knowledge, to re-evaluate magnitude-frequencies in glacial environments. Currently, the only method capable of identifying a continuous record of such events, is seismic monitoring (Ekström and Stark, 2013). Seismic detection utilises the global seismic network to detect long-period surface waves, characteristic of seismogenic landslides. Seismic methods have identified some of the largest supraglacially deposited RAs in recent times (e.g., Lamplugh glacier RA; Dufresne et al., 2019) which are compiled in a database (IRIS DMC, 2017), and, when combined with manual analysis of satellite imagery, gives information on duration, momenta, potential energy loss, mass and runout trajectory. However, landslides are challenging to detect using seismic methods and event positional accuracy is limited to a 20 – 100 km radius, due to the lack of high frequency waves when compared to earthquakes, further inhibited by the low frequencies and long wavelengths of dominant seismic waves worldwide (Ekström and Stark, 2013). This also results in an inability to detect landslides that are relatively low in volume, due to their weak seismic fingerprint ($M < 5.0$) and causes underestimation of landslide properties (e.g., event size and duration) because their runouts are seismically "quiet", likely due to frictional melting of glacier ice (Ekström and Stark, 2013). Despite these difficulties, current studies seem to indicate an increase in the rates of rock avalanching onto ice in rapidly deglaciating regions such as Alaska and the Southern Alps of New Zealand, where the majority of recent (aseismic) RAs are associated with glaciers. This increase has been linked to climate warming (Huggel, Clague and Korup, 2012) and potential feedbacks with permafrost degradation (Allen, Gruber and Owens, 2009; Krautblatter, Funk and Günzel, 2013; Coe, Bessette-Kirton and Geertsema, 2018). These links, coupled with the availability of high spatial and temporal resolution optical satellite imagery, have demonstrated the need for systematic observations of landslides in mountainous cryospheric environments (Coe, 2020). Five 'bellwether' sites have been suggested for these purposes: the Northern Patagonia Ice Field, Western European Alps, Eastern Karakorum in the Himalayas, Southern Alps of New Zealand and the Fairweather Range in Alaska (Coe, 2020).

The large archives of optical imagery, coupled with the recent boom in cloud-computing platforms, now provides the perfect combination of resources, which can be exploited to identify supraglacially deposited landslides on a large scale. Since the launch of Landsat 1 in July 1972, optical satellites have imaged the Earth's surface at increasing temporal and spatial frequency. Six successful Landsat missions have followed Landsat 1, making it the longest continuous optical imagery data series, revolutionising global land monitoring (Wulder *et al.*, 2019). Analysis-ready Landsat data is available for Landsat 4 (1982-1993), Landsat 5 (1984-2012), Landsat 7 (1999-present) and Landsat 8 (2013-present), providing 38 years of data at a 30 m spatial resolution and a 16-day temporal resolution. These data are categorised into three tiers: (1) Tier 1 data that is radiometrically and geometrically corrected (< 12 m root mean square error); (2) Tier 2 data which is of lower geodetic accuracy (> 12 m root mean square error); and (3) Real Time imagery, which is available immediately after capture but uses preliminary geolocation data and thermal bands require additional processing, before being moved to its final imagery tier (1 or 2) within 26 days for Landsat 7, and 16 days for Landsat 8. Traditionally, it has been difficult to exploit these extensive optical imagery collections such as Landsat, without vast amounts of computing resources. However, in the last decade, cloud computing has become increasingly accessible. This allows a user to manipulate and process data on remote servers, removing the need for a high-performance personal computer. Google Earth Engine (GEE) is a cloud platform created specifically to aid the analysis of planetary-scale geospatial datasets such as Landsat and is freely available for research and education purposes (Gorelick et al., 2017).

Here, we utilise Google Earth Engine (GEE), and the Landsat data archive of 38 years of optical imagery, to present the Google earth Engine supRaglAciaL Debris INput dEtector (GERALDINE). A free-to-use tool to automatically delimit new supraglacial debris inputs over large areas and timescales, which then allows for rapid user-backed verification of inputs from large landslides specifically. GERALDINE is designed to allow quantification of the spatial and temporal underreporting of supraglacial landslides. We describe the methods behind GERALDINE, verify tool outputs against known supraglacial rock avalanche inventories, and, finally demonstrate tool effectiveness by using it to find two new supraglacial landslides, one of which cannot be found in the seismic archives.

3.2 Methods

GERALDINE exploits the capability and large data archive of GEE (Gorelick *et al.*, 2017), with all processing and data held in the cloud, removing the need to download raw data. By default, it utilises Tier 1 Landsat imagery (30 m pixel resolution) that has been converted to top-of-atmosphere spectral reflectance (Chander, Markham and Helder, 2009), from 1984 – present, incorporating Landsat 4, 5, 7, and 8. GERALDINE also gives the user the following options: (i) to utilise Tier 2 Landsat imagery; and, (ii) to utilise Real Time Landsat imagery. Tier 2 imagery is valuable in regions where Tier 1 imagery is limited, e.g., Antarctica where there is a lack of ground control points for imagery geolocation. Real Time imagery is useful for rapid identification of landslide locations if a seismic signal has been detected but an exact location has not been identified. Landsat imagery is used in conjunction with the Randolph Glacier Inventory (RGI) version 6.0 (RGI Consortium, 2017). The RGI is a global dataset of glacier outlines excluding those of the Greenland and Antarctic ice sheets, digitised both automatically and manually based on satellite imagery and local topographic maps (Pfeffer *et al.*, 2014). RGI glacier boundaries are delineated from images acquired between 1943 and 2014, potentially introducing errors into analysis due to outdated boundaries (Scherler, Wulf and Gorelick, 2018; Herreid and Pellicciotti, 2020) (see Chapter S1 section 1.1). However, this database represents the best worldwide glacier inventory available and shrinking ice as the dominant global pattern means the tool is occasionally running over ice-free terrain with null results rather than missing potential supraglacial debris inputs. Any updated version of the RGI will be incorporated when available. Additionally, the RGI can be replaced by the user with shapefiles of the Greenland and Antarctic ice sheets (v1.1 line 536 and 543), if analysis is required in these regions, or higher resolution (user defined) glacier outlines, if the RGI is deemed insufficient.

3.2.1 Overview of processing flow

GERALDINE gathers all Landsat images from the user-specified date range and all the images in the year preceding this user-specified date range, within the user-specified region of interest (ROI), creating two image collections within GEE. Users should note that smaller ROIs and annual/sub-annual date ranges increase processing speed, with processing slowing considerably with >800 Landsat images (~160-1500 GB of data). The software clips all images to the ROI, applies a cloud mask, and then delineates supraglacial debris cover from snow and ice. GERALDINE acquires the maximum debris extent from both image collections, creating two maximum debris mosaics, then subtracts these mosaics and clips them to the RGI v6.0 (or user defined area if not using RGI) to output a map. This map highlights debris within the user-specified time period that was not present in the preceding year, which we term 'new debris additions'. This map is viewable within a web browser as a layer in the map window. However, as it is calculated 'on-the-fly' (Gorelick et al., 2017), large areas can be slow to navigate. All files can be exported in GeoJSON (Georeferenced JavaScript Object Notation) format for further analysis, including to verify if detections are discrete landslide inputs. This is recommended for large ROIs. An overview of the workflow is presented in Figure 17 and the detail for each step described in Sections 3.2.2–3.2.4.

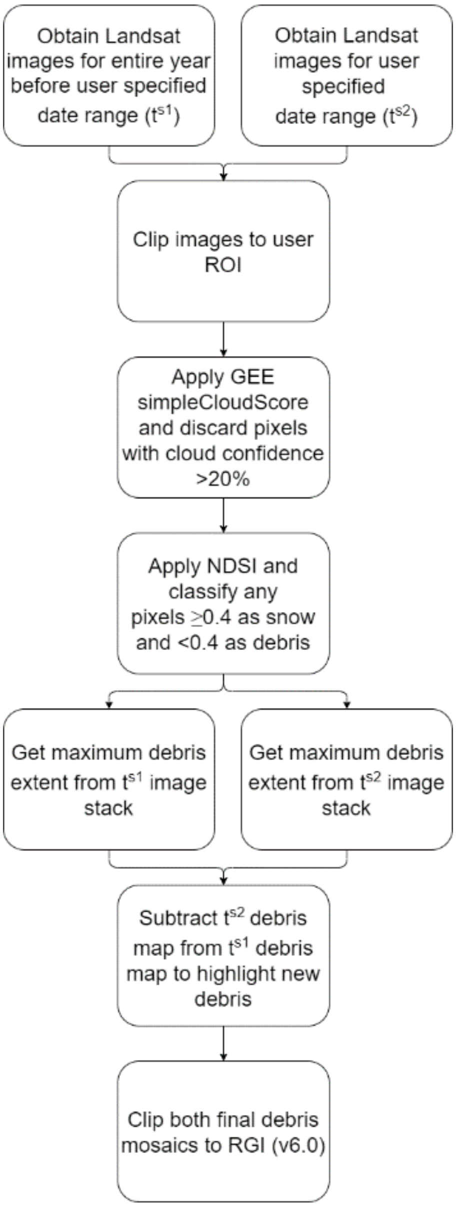

Figure 17: Processing flow of GERALDINE.

3.2.2 Cloud masking

GERALDINE masks cloud cover using the GEE built-in 'simple cloud score' function (Housman et al. 2018). This pixel-wise cloud probability score allows fast and efficient identification of clouds, suitable for large-scale analysis (Housman, Chastain and Finco, 2018) and has been previously applied and well-justified for use in glacial environments (Scherler, Wulf and Gorelick, 2018). A 20%

threshold is applied to every image, thereby excluding any pixel with a cloud score >20% from the image. We quantitatively evaluated this threshold to ensure optimum tool performance (see Chapter S1 section 1.2). Cloud shadow is not masked as it was found to have a minimal effect on the tool delineating debris from snow/ice whilst greatly increasing processing time.

3.2.3 NDSI

The Normalised Difference Snow Index (NDSI) is a ratio calculated using the green (0.52-0.6 λ) and SWIR (1.55-1.75 λ) bands. It helps distinguish snow/ice from other land cover (Hall, Riggs and Salomonson, 1995) and excels at detecting ice where topographic shading is commonplace (Racoviteanu *et al.*, 2008), due to high reflectance in the visible range and strong absorption in the SWIR range. GERALDINE applies the NDSI to all images and a threshold of 0.4 is used to create a binary image of supraglacial debris (<0.4) and snow/ice (≥0.4). This threshold has been utilised by studies in the Andes (e.g., Burns and Nolin, 2014) and Himalaya (e.g., Zhang et al., 2019), but optimum thresholds often vary between 0.5 (Gjermundsen *et al.*, 2011) and 0.2 (Keshri, Shukla and Gupta, 2009; Kraaijenbrink *et al.*, 2017). We justify our 0.4 threshold based on Scherler et al. (2018) who deemed it optimum for the creation of a global supraglacial debris cover map using Landsat images. We advise users to use this default threshold but if this appears sub-optimum in a user defined region of interest (ROI), the threshold can be fine-tuned in the code (v1.1 line

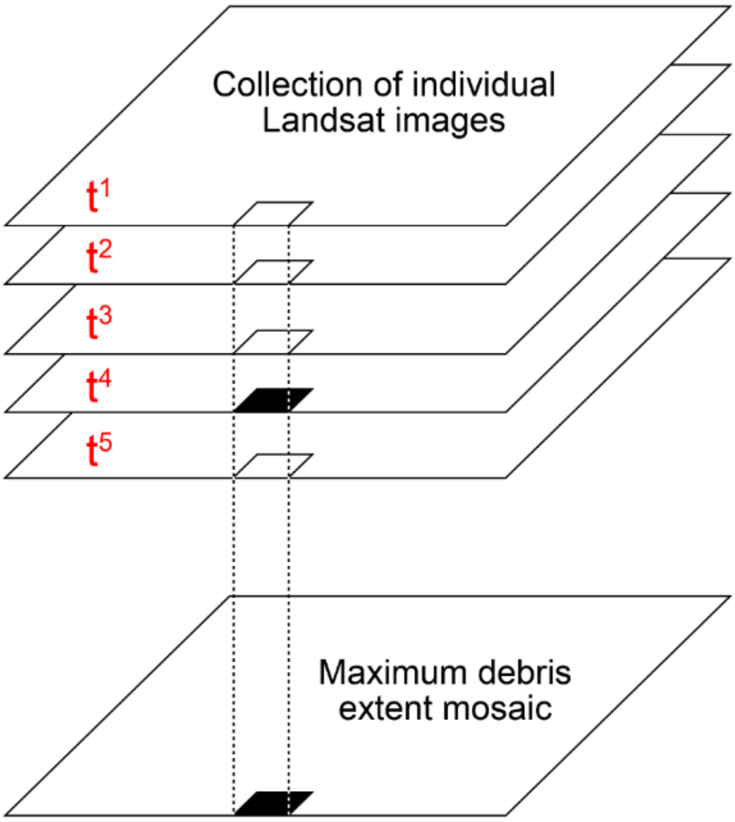

Figure 18: Reducer diagram - GEE stacks all images in the collection and undertakes pixel-wise analysis of debris cover, to create a mosaic of maximum debris cover extent. If just one pixel in the image stack is debris, then the corresponding pixel in the maximum debris mosaic will be debris. White pixels represent snow/ice, black pixels represent debris.

244 and 254). We utilise NDSI instead of newer band ratio techniques (e.g., Keshri et al., 2009) and more complex algorithms (e.g., Bhardwaj et al., 2015) to ensure transferability between Landsat TM, ETM+ and OLI TIRS sensors as we wish to harness the full temporal archive.

3.2.4 Retrieving maximum debris extent

To attain a maximum debris extent, GERALDINE reduces each image collection to an individual image using a pixel-based approach (Figure 18). Every binary image (supraglacial debris: 0, snow/ice: 1) in each image collection is stacked, with pixels in the same geographic location stacked sequentially. If any pixel in the temporal image stack is debris, the corresponding pixel in the final mosaic will be a debris pixel, creating a maximum debris extent mosaic. GERALDINE is therefore debris biased due to this processing step (Figure 18). Calculated maximum debris extent mosaics for both the user-defined time period and previous year are differenced, the output being new debris additions. Both the previous year maximum debris extent, and new debris addition mosaics, are displayed for user analysis within the GEE interactive development environment, and easily exportable to Google Drive (included as part of sign-up to Google Earth Engine).

3.2.5 Validation

A two-part validation was undertaken to assess the effectiveness of GERALDINE outputs for allowing a user to rapidly identify supraglacially deposited landslides: a detection validation (i.e. can the user confirm a supraglacially deposited landslide has occurred from a GERALDINE output?), and an area validation (i.e. how much of the area of the supraglacial landslide deposit has GERALDINE detected?). Although areal detection is not the main purpose of the tool, greater area detection would ultimately help the user with identification of supraglacially deposited landslides. Validation was performed against the already-defined RA databases of Bessette-Kirton and Coe (2016), Deline et al. (2014), Uhlmann et al. (2013) and the Exotic Seismic Events Catalog (IRIS DMC, 2017). To provide validation, RAs had to occur after 1984 (onset of Landsat TM era) and had to deposit debris predominantly onto clean-ice areas of glaciers in the RGI. Forty-eight events out of a total of 325 met these criteria, their locations distributed across the European Alps, Alaska, New Zealand, Canada, Russia and Iceland (Fig. S5).

GERALDINE was run for the year of the event using Landsat Tier 1 imagery; the new debris vector output file was exported into a GIS and after an initial qualitative step to see if the user would flag the RA from the GERALDINE output, the area of the deposit it detected was calculated within the GIS. We utilised the select by location tool in QGIS, to select any pixels/pixel clusters within/intersecting an outline of the RA manually-digitised from a Landsat image using the Google Earth Engine Digitisation Tool (GEEDiT) (Lea, 2018). We clipped selected pixels to the manually digitised RA outline and calculated the area of these selected pixels. The tool-detected area was then compared against the area of the manually digitised RA outline. These two steps allow for an assessment of GERALDINE's ability to highlight new debris inputs, and if this changes over the Landsat era.

3.3 Results and Discussion

3.3.1 Validation

Of the 48 validation RAs, the user was able to correctly identify 44 of these events from GERALDINE output maps, a true positive detection accuracy of 92 %. False negatives all pre-date 1991 (Figure 19), giving 100% successful user identification post-1991. These false negatives can be explained by reduced (and insufficient in this case) Tier 1 Landsat image availability pre-Landsat 7 within the GEE data catalogue, inhibiting GERALDINE from highlighting the RA as new debris. We note that if just one image featured the RA, GERALDINE would highlight the deposit as new debris due to its bias towards debris detection (see section 3.2.4). However, a true 100 % detection rate for supraglacial landslide deposits on glaciers is unlikely, due to some deposits running out over existing debris cover, and some having high snow/ice content or entraining large amounts of snow/ice during events, which can be common for landslides deposited supraglacially. This high snow/ice content can mask them as snow/ice during NDSI delineation from debris, inhibiting detection. However, events of this kind also pose significant difficulty for user delineation with original optical imagery. GERALDINE works best when a number of images in the image stack represent maximal debris cover in the preceding year, reducing false positives for the timespan of interest i.e. flagging old debris as new debris, due to a lack of old debris exposure in the previous year. This is particularly applicable to small (<0.5 km^2) glaciers, where the overall significance of a single pixel increases. The debris bias of GERALDINE ensures true negative detection is also extremely high, but this high true negative detection is why user verification of new debris outputs is needed, because they are flagged as new debris but display no supraglacial RA characteristics i.e. lobate and elongated (Deline, Hewitt, *et al.*, 2014). To a user familiar with glacial and landslide processes, the differences in GERALDINE outputs between true positives/negatives and false positives/negatives are clear when running the tool to find RA inputs.

GERALDINE RA areal accuracy increases over time from 19 % in the Landsat 4/5 era, to 71 % with the current Landsat 7/8 constellation (Figure 19), with the latter period characterised by increasingly modern sensors with greater spectral and temporal resolution. Low areal accuracy in the Landsat 4/5 era is once again a product of the GEE data catalogue having limited imagery for certain years in glaciated areas, reducing the ability of GERALDINE to detect the entire area of new debris additions. Areal accuracy increases after the failure of Landsat 4 in December 1993, at which point Landsat 5 is the sole data collector of imagery at a frequency of every 16 days. Despite this single functioning satellite, the tool detects all eight validation events and on average 59 % of the deposit areas between 1993 and the activation of Landsat 7 in 1999. The dual Landsat

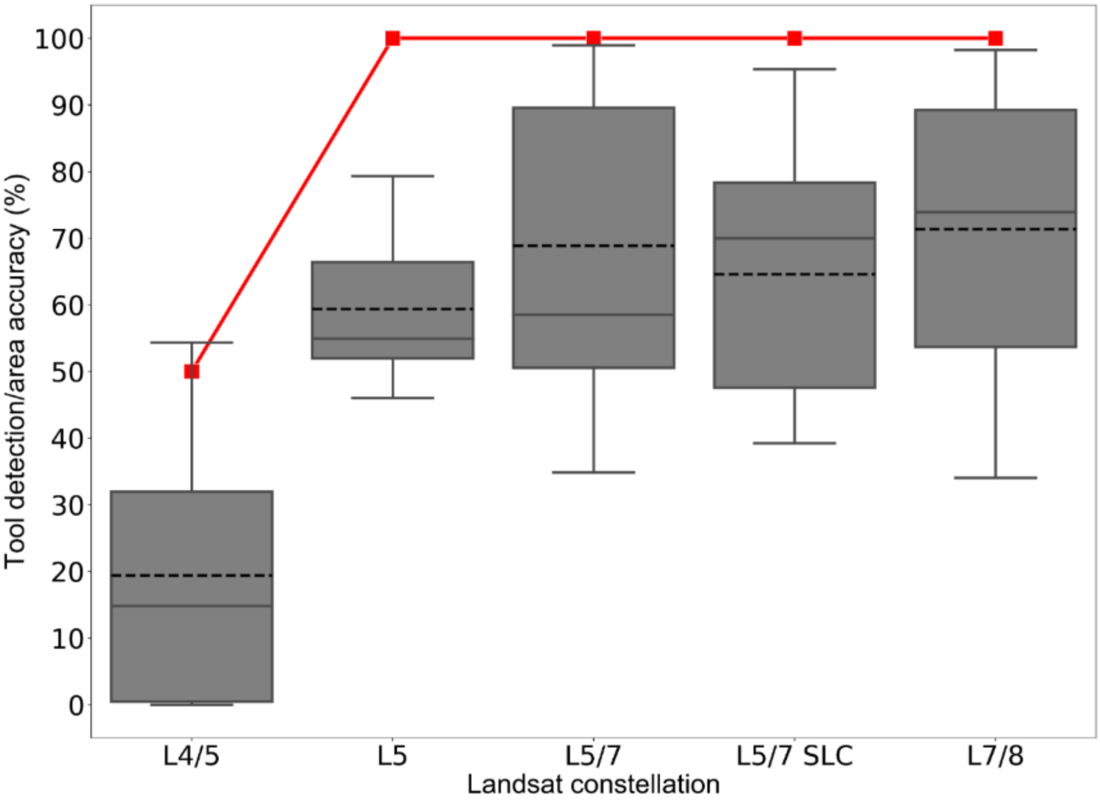

Figure 19: GERALDINE rock avalanche (RA) detection accuracy (red line) and RA area accuracy (boxplots) with different Landsat constellations over time. L4/5 (1984-1993) – 8 validation RAs, L5 (1993-1999) – 8 validation RAs, L5/7 (1999-2003) – 9 validation RAs, L5/7 SLC (Scan Line Corrector failure) (2003-2013) – 11 validation RAs, and L7/8 (2013-present) – 12 validation RAs. Dashed line represents mean, solid line median, box represents upper and lower quartiles, whiskers represents min and max area accuracies.

5/7 constellation increases tool area accuracy further to 69 %. However, a decrease in mean area accuracy is evident after the failure of the Landsat 7 Scan Line Corrector in May 2003 (Markham *et al.*, 2004), decreasing tool areal accuracy by 4 %, due to images missing up to 20-25 % of data per image in the stack (Hossain *et al.*, 2015). We find that a number of Landsat 7 scenes also feature stripes of no data, pre-dating the scan line corrector failure, and can inaccurately cause ‘stripes’ of new debris in tool outputs. The current Landsat 7/8 constellation has the highest accuracy for detecting the area of RAs at 71 %. The smallest new debris addition we used for validation was 0.062 km^2, of which GERALDINE detected 71 % of the area, so we have confidence in detection greater than 0.05 km^2, equating to ~56 Landsat pixels. Even with GERALDINE performing well, additional refinement and/or full automation of landslide deposit identification would be an interesting, and priority, area for further investigation. We also envisage development with other higher resolution and higher repeat satellites e.g., the Sentinel 2 and Planet Lab constellations. However, we found that current cloud mask algorithms for these data are not sufficient for accurate global glacial debris delineation.

GERALDINE is frequently affected by the RGI dataset causing over/under-estimation of previous year debris extents and new debris additions. For example, at tidewater glaciers that have undergone retreat since their margins were digitised, the tool often detects clean ice and debris at the tongue. This is dependent on the presence of ice mélange (NDSI classification as ice/snow) and dark fjord water (NDSI misclassification as debris) in imagery (see Chapter S1 section 1.1). In addition, we found an instance where a supraglacial landslide deposit had been misclassified as a nunatak (60°27'23.7"N, 142°33'35.7"W) and therefore this section of the glacier is erroneously missing from the RGI dataset altogether, preventing tool detection, but this is likely a single case. Topographic shading and/or bright illumination of debris cover can at times cause pixels to be masked from Landsat scenes due to misclassification as cloud (see Chapter S1 section 1.2); however, if the tool is run over a sufficiently long period, this will not influence new debris detection. GERALDINE can also not detect landslide debris deposition onto an existing debris cover. Therefore, if a landslide consists of multiple failures, a GERALDINE output map would only detect one event, with the deposit extent being the combined total of all failures. In this case, it would be highly beneficial to combine GERALDINE with seismic detection to help delineate the number of failures that occur.

3.3.2 New Supraglacial Landslide Input Detection Example

The Hayes Range, Alaska has a history of large supraglacial debris additions (e.g., Jibson et al., 2006), but no events have been documented in the last decade, in contrast to a recent dense cluster in the Glacier Bay area of Alaska (Coe, Bessette-Kirton and Geertsema, 2018), which formed part of the validation dataset. To test this, we ran GERALDINE for 2018 to highlight new debris additions on glaciers in the Hayes Range (Figure 20a). GERALDINE used a total of 228 Landsat images for analysis; 107 to determine the 2017 debris extent and 121 to determine the 2018 debris extent. Landsat tiles vary from 200 MB to 1000 MB when compressed, so, if we assume an average tile is 500 MB, a user would require 114 GB of local storage, a large bandwidth internet connection to download

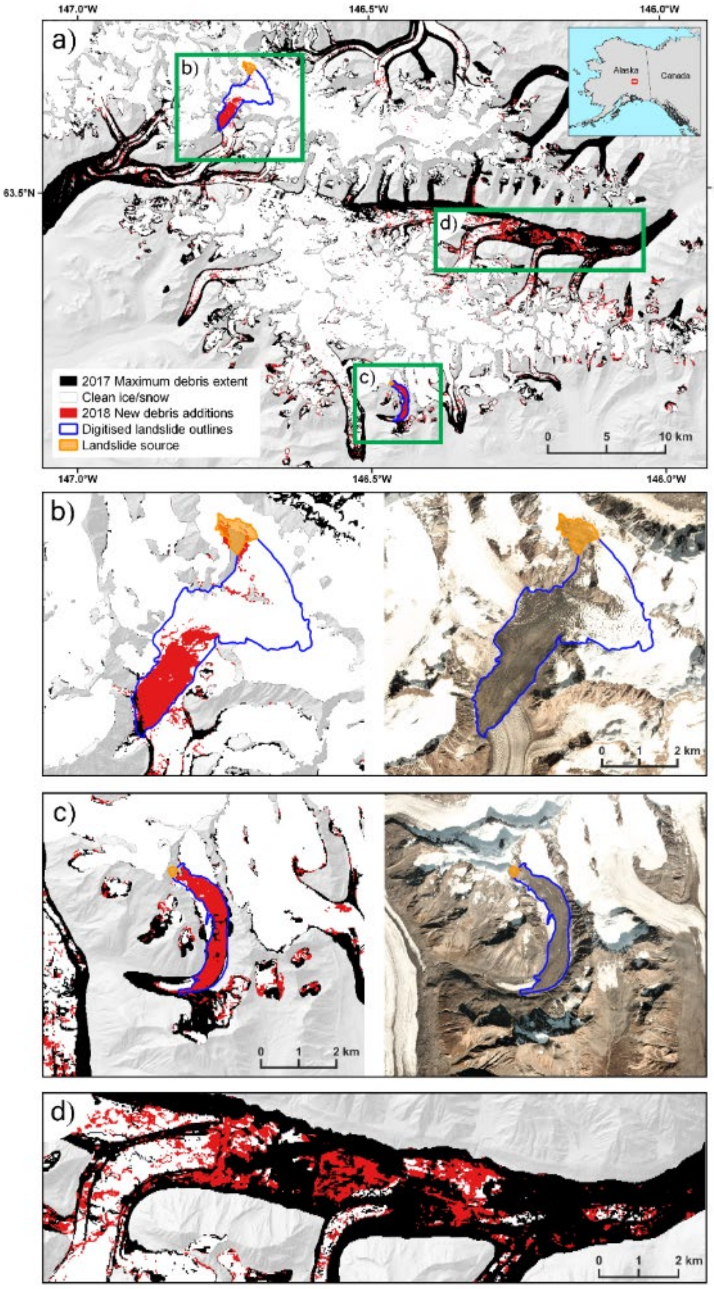

Figure 20: a) 2018 new debris additions in the Hayes Range, Alaska. RA outlines digitised using Landsat imagery and the GEEDiT tool (Lea, 2018). Inset map denotes location of Hayes Range. b) GERALDINE output of Mt Hayes landslide extent and corresponding image courtesy of Planet Labs, Inc. (31/07/2018). c) GERALDINE output of landslide extent on a small valley glacier east of Maclaren glacier and corresponding image courtesy of Planet Labs, Inc. (13/09/2018). d) Erroneous 2018 tool detection of Black Rapids glacier RA deposits, which were deposited as a cause of the 2002 Denali earthquake (Jibson et al., 2006). Green boxes signify areas of interest and correspond to magnified areas of b), c) and d), respectively. IFSAR DTM background from the Alaska Mapping Initiative (doi: 10.5066/P9C064CO)

(which comes with an associated carbon cost), and, a PC capable of processing these data. GEE required none of these requirements and completed analysis in under two minutes, extracting information from every available cloud-free pixel, to maximise use of the imagery. The new debris output map produced was 6.5 MB, and contained all relevant 'new' debris information from 2018. The output map highlighted two large supraglacial landslide deposits, which occurred between 1 January 2018 and 31 December 2018. These were manually verified and the potential window of event occurrence identified using satellite imagery within GeeDiT (Lea, 2018). The larger of the two deposits is from a slope collapse on the southern flank of Mt Hayes (4216 m) (63°35'11.7"N, 146°42'50.0"W), with emplacement determined between 10 and 25 February 2018 (Figure 20b). This supraglacial landslide was also detected using the seismic method (Ekström and Stark, 2013 see section 3.1), and confirmed as occurring on 12 February 2018 (Goran Ekström, personal communication, 2019). The resulting debris deposit covered 9.4 km^2 of the surface of the Susitna Glacier (digitised from Planet Labs Inc. imagery from 31/07/2018). The tool detected 27.5 % of the area of this deposit, due to emplacement predominantly in the accumulation area, with the upper half of the deposit rapidly covered by snow after the event. The second, smaller supraglacial landslide deposit occurred between 4 and 7 July 2018, on an unnamed glacier to the east of Maclaren Glacier (63°20'21.9"N, 146°26'36.1"W) (Figure 20c). GERALDINE detected 78 % of this 1.9 km^2 supraglacial debris input, which transformed the glacier from 16 % debris covered to 51 % debris covered, and will have important implications for glacier melt regime, velocity and response to atmospheric drivers. Unlike the larger supraglacially deposited landslide from Mt Hayes, this event was not automatically detected using seismic methods (Goran Ekström, personal communication, 2019), suggesting that its seismic signature was lower than the seismic detection limit ($M < 5.0$) (Ekström and Stark, 2013). Therefore, there is a high potential to detect all events using GERALDINE, and then provide time-location filters to seismic records to retrospectively quantify force histories and precise timings of events not flagged automatically as a landslide.

We note that new large debris inputs are partially highlighted on the Black Rapids Glacier for 2018 (Figure 20d), but these 'new' additions were actually deposited in 2002 during the Denali earthquake (Jibson *et al.*, 2006; Shugar and Clague, 2011; Shugar *et al.*, 2012). We assign this discrepancy to minimal cloud-free imagery during summer (a time when deposits are uncovered by snow melt), preventing the tool from highlighting their full summer extent, and causing underestimation of the 2017 debris cover. To a human operator, however, it is clear these debris additions are erroneous because ‘new’ debris is patchy, with 2017 debris extent and snow/ice preventing detection of a homogeneous deposit. If GERALDINE is run annually for multiple years, the user will be able to determine the emplacement date for these earlier supraglacial landslide deposits.

3.3.3 Tracking new debris transportation

A secondary use of GERALDINE is tracking existing supraglacial landslide deposits. These deposits are transported down-glacier by ice flow, although often the initial emplacement geometry is characteristically deformed and spread due to differential ablation and ice motion (Reznichenko, Davies and Alexander, 2011; Uhlmann *et al.*, 2013). GERALDINE can give an indication of deposit behaviour and movement by highlighting ‘new’ debris, at the lateral and down-glacier end of the deposit, as it moves between image captures (Figure 21). Differencing the distance of this new debris from the previous year’s deposit extent can give an approximation of lateral spreading and glacier velocity over the user-specified time period, the latter of which is often unknown at the temporal resolution of Landsat and complex to calculate in high mountain regions (Sam *et al.*, 2015).

To demonstrate the evolution of a RA through time, we ran GERALDINE for 2012, 2013, and 2014 for the Lituya Mountain RA in Alaska. This RA occurred on 11 June 2012 and was deposited onto a tributary of the John Hopkins glacier (Geertsema, 2012). The upper portion of the deposit was sequestered into the ice after its deposition in 2012, as is common of debris inputs in glacier accumulation areas (Dunning *et al.*, 2015). However, the deposit toe remained visible on the surface, likely because it was below the snow line. We estimate the down-glacier transport velocity of this RA by tracking and measuring the movement of the deposit toe, to measure the displacement of the deposit leading edge. Using this method, estimates of down-glacier transportation of the deposit leading edge between 2012 and 2013 are ~575 ± 30 m, and ~328 ± 30 m between 2013 and 2014 (Figure 21), the latter in agreement with glacier velocity calculated by Burgess et al. (2013) between 2007 and 2010 (250 – 350 m a^{-1}), and ITS_LIVE velocity from 2013 (300-400 m a^{-1}) (Gardner et al., 2018; Gardner et al., 2019). We suggest that the higher RA deposit velocities between 2012 and 2013 are a result of the immediate response of the glacier to reduced ablation rates directly beneath the debris, causing an ice-pedestal to form, from which debris is redistributed through avalanching off the pedestal sides, expanding debris coverage (Reznichenko, Davies and Alexander, 2011). We note other areas are flagged as ‘new debris’ in 2013 and 2014. These are typically where glacier downwasting has occurred exposing more of the valley walls, or where there has been temporal evolution of the debris cover e.g., glacier flowline instabilities. These flow instabilities can cause double-counting of debris when larger time windows are specified (see Herreid and Truffer, 2016). Both processes subsequently cause false classification as ‘new debris’. However, neither glacier downwasting nor evolution of the debris cover

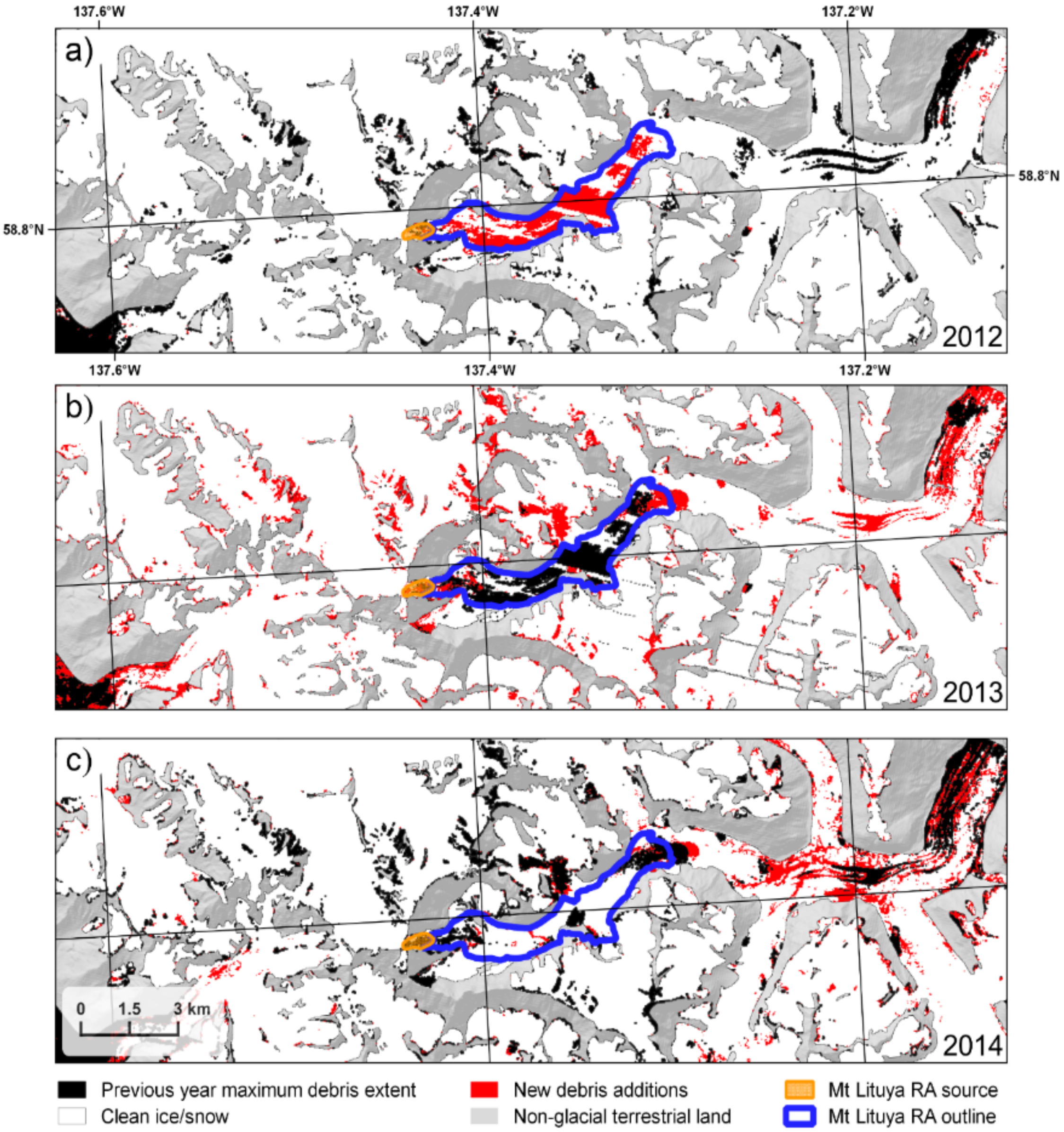

Figure 21: Deposition and behaviour of Lituya RA, John Hopkins Glacier Alaska (58°48'54.3"N, 137°17'40.9"W) detected by GERALDINE when run for a) 2012, b) 2013, and c) 2014. Landsat 7 scan line corrector issue visible in lower right section of 2013 image (B). IFSAR DTM background from the Alaska Mapping Initiative (doi: 10.5066/P9C064CO).

display supraglacial landslide characteristics, so it is highly unlikely that a user would mistake them for one.

3.4 Conclusion

GERALDINE is the first free-to-use resource that can rapidly highlight new supraglacial landslide deposits onto clean ice for a user-specified time and location. It can aggregate hundreds of Landsat images, utilising every available cloud-free pixel, to create maps of new supraglacial debris additions. Using the output maps produced, GERALDINE gives an objective starting point from which a user can identify new debris inputs, eliminating the time-intensive process of manually downloading, processing and inspecting numerous satellite images. The method allows user identification of mass movements deposited in glacier accumulation zones, which have very short residence times due to rapid advection into the ice. This is a process that has not previously been quantified. We demonstrate its effectiveness by verifying it against 48 known, large, supraglacially deposited rock avalanches that occurred in North America, Europe, Asia, and New Zealand. GERALDINE outputs helped identify 92% of all 48 events, with 100% successful identification post-1991 when image quality and availability increases. We showcase how GERALDINE does not suffer from the traditional disadvantages of current manual and seismic detection methods that can cause supraglacial landslides to go undetected, by identifying two new supraglacial landslides in 2018, in the Hayes Range of Alaska. One of these events was not detected using existing methods, therefore, the frequency of large supraglacial debris inputs is likely historically underestimated. We suggest users should apply GERALDINE at standardised time intervals in recently identified ‘bellwether sites’ in glaciated high mountain areas undergoing rapid change i.e. Greenland, Alaska, Patagonia, the European Alps, New Zealand Alps and the Himalaya, to investigate annual rates of these large debris inputs. GERALDINE can become part of the repertoire of tools that enable glacial landslides/rock avalanches to be identified in the past, present, and future. It will improve remote detection and characterisation of these events, to help quantify and evaluate their frequency, spatial distribution and long-term behaviour in a changing climate.

Chapter 4 - Revising rock avalanche magnitudes and frequencies in glacial environments

Chapter 4

This chapter has been accepted in **Geomorphology**.

Authors: William D. Smith[1], Stuart A. Dunning[1], Neil Ross[1], Jon Telling[2], Erin K. Jensen[3], Dan H. Shugar[4], Jeffrey A. Coe[5] and Marten Geertsema[6]

1. School of Geography, Politics and Sociology, Newcastle University, Newcastle upon Tyne, UK
2. School of Natural and Environmental Sciences, Newcastle University, Newcastle upon Tyne, UK
3. Department of Geology and Geophysics, University of Utah, Salt Lake City, UT, United States
4. Water, Sediment, Hazards, and Earth-surface Dynamics (waterSHED) Lab, Department of Geoscience, University of Calgary, Calgary, Canada
5. Geologic Hazards Science Center, U.S. Geological Survey, Golden, CO, United States
6. British Columbia Ministry of Forests, Lands, Natural Resource Operations and Rural Development, Prince George, BC, Canada

Citation: Smith, W. D., Dunning, S. A., Ross, N., Telling, J., Jensen, E. K., Shugar, D.H., Coe, J.A. and Geertsema, M.: Revising rock avalanche magnitudes and frequencies in glacial environments, Geomorphology.

Author contributions: William Smith did all the analysis and wrote the manuscript. Stuart Dunning, Neil Ross, Jon Telling, Erin Jensen, Dan Shugar, Jeffrey Coe and Marten Geertsema all contributed to manuscript editing. The supplementary information for the manuscript is included in Chapter S2.

Abstract

The frequency of large supraglacial landslides (rock avalanches) occurring in glacial environments is thought to be increasing due to feedbacks with climate warming and permafrost degradation. However, it is difficult to (i) test this; (ii) establish cause–effect relationships; and (iii) determine associated lag-times, due to both temporal and spatial biases in detection rates. Here we applied the Google Earth Engine supraglacial debris input detector (GERALDINE) to Glacier Bay National Park & Preserve (GLBA), Alaska. We find that the number of rock avalanches (RAs) has previously been underestimated by 53 %, with a bias in past detections towards large area RAs. In total, GLBA experienced 69 RAs during 1984-2020, with the highest frequency in the last three years. Of these, 58 % were deposited into the accumulation zone and then sequestered into the ice within two years. RA sources clustered spatially at high elevations and around certain peaks and ridges, predominantly at the boundary of modelled permafrost likelihood. They also clustered temporally, occurring mainly between May and September when air temperatures were high enough to initiate rock-permafrost degradation mechanisms. There was a chronic background debris supply from RAs, with at least one RA occurring in all but nine years; however, a debris rich period during 2012-2016 was driven by three large RAs delivering 44 % of all (1984-2020) debris (by area). Comparable investigation of slope-failures in other remote currently glaciated regions is lacking. If RA rates are similar elsewhere, especially the bias towards emplacement onto/into accumulation zones, their contribution to glacial sediment budgets has been globally underestimated.

4.1 Introduction

Glaciers are fed with debris by the full range of landslide processes from small scale rock falls to large scale failures such as rock avalanches (Deline et al. 2014, 2021). Rock avalanches (RAs) are high magnitude, perceived low frequency, predominately bedrock slope failures that generate volumes of material typically > 10^6 m^3 (Dufresne et al. 2016). RA sediment supply is as highly fragmented debris emplaced as a point source, perhaps equivalent to many years of 'normal' chronic and more spatially distributed supply from valley walls. For example, the debris volume of the Lyell Glacier supraglacial RA in South Georgia, was estimated to be equivalent to 93 years of 'normal' supraglacial supply (Gordon et al. 1978). RA surface morphology typically shows common geomorphic and semi-diagnostic features so they can be remotely identified (Hewitt 1999; Shugar and Clague 2011). RAs occur in areas of high relief and in many landscapes have been shown to be highly effective erosive agents, generating substantial sediment fluxes and extensive valley fills (Korup et al. 2010). They are ultimately a key component in determining landscape geomorphology and sedimentary budgets (Korup et al. 2004; Korup 2005, 2012; Uhlmann et al. 2013). Determining their magnitude and frequencies in glacial environments through time is potentially an important, yet largely unquantified, flux to glacial debris supply (Ekström and Stark 2013) and mountain erosion above downcutting ice. Establishing this flux is important due to the control of debris supply on glacier melt (e.g., Reznichenko et al. 2010), glacier velocity (e.g., Shugar et al. 2012), and the export of limiting nutrients like silica and iron into extra-glacial ecosystems (e.g., Death et al. 2014; Hawkings et al. 2014, 2017).

Relief, slope angle, and active tectonics are known contributors to RA hotspots in glacial environments (e.g., Jibson et al. 2006; Coe et al. 2018). Recent research has suggested that the frequency of RAs in these environments, outside of those clusters linked to earthquakes, is increasing due to the pressures of climate warming on permafrost, and, as glaciers retreat, the exposure and contested idea of de-buttressing of high-relief slopes (e.g., Huggel et al. 2012; Ravanel et al. 2017; Dai et al. 2020; Chiarle et al. 2021). However, many RAs may also be explained by accumulating rock slope stresses over multiple glacial cycles (Grämiger et al. 2018). Establishing the true magnitude-frequency of RAs and any paraglacial forcing is therefore complex (McColl 2012; Ekström and Stark 2013; Grämiger et al. 2017). In non-glacial and/or formerly glaciated environments the rate of detection through time can also be linked to deposit size and the rate at which the deposits diagnostic features are eroded or modified (Sanhueza-Pino et al. 2011), as well as being reliant on correct identification of landslide provenance, rather than a glacial origin (Hewitt 1999). However, even in highly erosive/active environments, diagnostic features that reveal former RAs can persist; in fluvial environments some RA dams can cause knickpoints identifiable in the geological record (Korup et al. 2010; Fan et al. 2020). In glacial environments, however, detections of past supraglacial RAs are primarily limited to the time they are visible on the glacier surface, or imaged in the ice column using geophysical methods (Dunning et al. 2015). RAs deposited in glacier accumulation zones can be rapidly covered by fresh or windblown snow, and ingested into the ice (Dunning et al. 2015), with as yet unknown persistence as a recognisable, single event deposit within the glacier as it moves. Those deposited in the ablation zone remain visible, but their deposits can: (i) deform through differential ice motion (Shugar and Clague 2011); and (ii) redistribute due to contrasting ablation rates at the boundary between clean ice and the thicker, melt-reducing deposit (Reznichenko et al. 2011; Uhlmann et al. 2013). Within or on debris-covered glaciers, RA identification is predominantly only possible through geomorphic analyses or lithological differences (Deline 2009; Shugar and Clague 2011; Deline et al. 2014). When supraglacial and englacial RAs emerge as pro-glacial/terminus deposits, they arguably contain unequivocal evidence of past RA processes (Reznichenko et al. 2012) but require extensive sampling campaigns and microscopic sedimentological analyses to determine their origin and age. Our current understanding of past supraglacial RA frequencies and importance is therefore temporally biased and insufficient (Ekström and Stark 2013). This makes any postulated climatic-driven upturn in frequencies difficult to establish in an environment that may be the most sensitive to climate warming-driven changes (Coe 2020). Incorporating these size (larger events are easier to identify) and visibility (landslides in some dynamic environments are quickly lost (Dunning et al. 2015; Higman et al. 2018)) biases into inventories provides unrealistic estimates of the frequencies of supraglacially deposited RAs. The data available indicate that RA size and frequency are increasing (Schlögel et al. 2011; Coe et al. 2018; Hibert et al. 2019; Bessette-Kirton and Coe 2020) (Kyrgyz Tien Shan and Glacier Bay, Alaska, respectively), but that it is likely that severe underestimates of slope activity exist in large components of mountainous landscapes (Hibert et al. 2019).

Detection of contemporary RAs in glacial environments has typically occurred in three main ways: eye-witness reporting (Deline et al. 2014), seismic detection (Ekström and Stark 2013), and manual analysis of optical satellite imagery (Bessette-Kirton and Coe, 2016; Uhlmann et al. 2013). Eye-witness reports of events are low, particularly in remote glacial areas, unless societal/economic damage has occurred (e.g., Hubbard et al. 2005; Schneider et al. 2014; Cox et al. 2015). Seismic detections can locate events and give exact timing and information on emplacement dynamics, but both long period (e.g., Ekström and Stark 2013) and high frequency (e.g., Zimmer and Sitar 2015; Dietze et al. 2017; Fuchs et al. 2018) seismic wave detection techniques for identifying slope-failures have their limitations. Long-period seismic waves only identify those with a strong seismic signal (magnitude (M) >5.0) and often with a ~100 km^2 radius location accuracy (Ekström and Stark 2013). High-frequency seismic wave detections of landslides are complicated by numerous non-landslide sources for high-frequency waves, making identification difficult and time-consuming (Hibert et al. 2019). Manual analysis of satellite imagery is resource-intensive and can be time-consuming for the operator if a regional scale, multi-temporal investigation is being undertaken. This results in a frequently adopted approach whereby images with minimal cloud cover between spring and autumn (where these seasons are distinct) are analysed (Bessette-Kirton and Coe, 2016) as detection chances are high with minimal new snow fall. However, this temporally restricted approach can overlook RAs occurring throughout the year that can then be sequestered into glacial ice rapidly after emplacement (Dunning et al. 2015). Detection of the La Perouse RA in Glacier Bay National Park & Preserve (GLBA), Alaska (Coe et al. 2018), is a good example of this. This RA occurred in late winter (16/02/2014) and entrained a large amount of snow and ice. This made the contrast between it and the surrounding ice low, and as a result the entire deposit was only clearly visible in four Landsat images before it was sequestered. The upper half of the deposit was sequestered within a month, the deposit toe was visible until November 2014. If the deposit did not straddle the equilibrium line altitude (ELA), and had been emplaced entirely above, it is unlikely it would have been detected by manual image analysis. Coe et al. (2018) acknowledge that they may miss autumn/winter events, or, erroneously date them to the following spring if they reappear.

Due to the limitations of existing detection techniques, comprehensive supraglacial RA inventories are rare, often with focus on just one RA (e.g., Cox et al. 2015), or multiple RAs triggered by an earthquake (i.e., an event inventory, e.g., Jibson et al. 2006). Recently a regional cluster of large RAs was detected in GLBA using manual mapping of time-series Landsat imagery with the purpose of creating a baseline from which changes in supraglacial landslide, frequency, magnitude and mobility could be determined, and possibly linked to climate change. Bessette-Kirton and Coe (2016) created this 1984-2016

RA inventory using 104 Landsat images (at least one image between May-October per year) of 30-m resolution, finding a total of 24 RAs ranging from 0.1 km^2 to 22.2 km^2 using optical contrast of debris to snow and characteristically lobate RA emplacement forms. Coe et al. (2018) used this dataset to analyse magnitude, mobility, and frequencies of the mainly spring and summer detected RAs and to investigate potential triggers. The events were found to 'cluster' temporally, with the three clusters showing increasing size and mobility over time: 1984-1986, 1994-1995 and 2012-2016. Examination of potential causes controlling the timing and sizes of RAs in GLBA revealed increasing air temperatures and the subsequent degradation of rock-permafrost as the most likely processes for triggering RAs.

It has been known for many years that bedrock permafrost containing ice-filled joints contributes to maintaining slope stability (e.g., Bjerrum and Jorstad 1968). Prolonged warm events such as the 2003 and 2015 heatwaves in the European Alps provided strong evidence for permafrost warming as a trigger for rock slope failures, as these summers were also characterised by an exceptional number of rockfalls from permafrost slopes (Gruber et al. 2004; Ravanel et al. 2017). Legay et al. (2021) simulated bedrock temperature for 209 rockfalls (2007-2015) and statistically compared their locations to 209,000 random artificial events at observed rockfall locations in the Mont Blanc massif. Results confirmed that warm permafrost areas (i.e., > -2 °C) are prone to slope failures, indicating this temperature is a critical threshold to trigger instabilities. The role of permafrost degradation in triggering far larger, deeper, rock-slope failures and rock avalanches is less easily resolved. The often remote and spontaneous nature of slope failures means it is difficult to definitively prove permafrost degradation as a final trigger for slope failures (Legay et al. 2021) – permafrost warming at depth is a long-term response and likely more insensitive to shallow, seasonal warming variability that has been shown to trigger smaller failures (Ravanel et al. 2017). However, work in Norway has been able to link the onset and deformation history of large rock-slope failures that may perhaps transition into RAs to degrading permafrost (Hilger et al. 2021). Coe et al. (2018) link the GLBA RAs to the combined effects of both short term (months) and long-term (millennia) warming as the simplest explanation for their observed increases in triggering. In the European Alps and Norway, both monitoring and modelling have shown that degrading permafrost over multiple timescales can be linked to current observations of decreasing slope stability and/or increasing creep rates in large deep-seated bedrock failures. Some of these failures may have initiated several thousand years ago, and, some can fail suddenly as rock avalanches (Mamot et al. 2021; Hilger et al. 2021), with the initial precursory long-term creep towards this final failure unknown or only identified in back analyses. The numerical modelling work of Mamot et al. (2021) highlights two major points relevant for our work, i) a non-linear response of stability to warming, with increased displacements (absolute and relative) when approaching the melting point of ice, ii) for steep (>50°) slopes the factor of safety falls below 1 when warmed from -4 °C to between -3 and -0.5 °C, temperatures closely linked to lower permafrost boundaries and documented landslide release zones (Coe et al. 2018; Fischer et al. 2012; Ravanel et al. 2010).

Our current understanding of bedrock permafrost degradation mechanisms involves decreasing uniaxial compressive strength and subsequently tensile strength (> -10 °C) (Mellor 1973; Dahlström 1992; Dwivedi et al. 1998; Ning et al. 2003), initiation and growth of shear planes (> -5 °C), which are then controlled by ice-mechanics, increasing susceptibility to atmospheric temperatures (Krautblatter et al. 2013), and the weakening of the stiffness and strength of ice-filled joints (> -1.5 °C) (Davies et al. 2001; Mamot et al. 2018). Advective heat transfer by water percolation is also a key control on the morphology of ice-filled joints (Hasler et al. 2011), and percolating water can increase hydrostatic pressures in ice-sealed fractures (Krautblatter et al. 2013). Determining the role of hydrostatic pressures in slope failures is difficult, however, due to a lack of in-situ monitoring and coupled thermo-hydromechanical models (Krautblatter et al. 2012). However, modelling (e.g., Matsuoka and Sakai 1999; Deline et al. 2011; Frauenfelder et al. 2018) and statistical analysis of climate variables (Allen and Huggel 2013; Luethi et al. 2015; Paranunzio et al. 2016) provide strong evidence that this is the case.

Few events are recorded in glacier accumulation zones, which are usually backed by higher, colder slopes than ablation zones. To determine with any confidence that RA occurrence in relation to permafrost, mobility, or other changing environmental variables, we need complete inventories. Currently, a question that could be asked is: Is the lack of known accumulation zone RAs a function of limited occurrence, or, of limited detections? The balance between accumulation zone and ablation zone RA sources can allow us to make inferences about the required conditions above glaciers to trigger RAs. In addition, if RAs are underreported in accumulation zones, they potentially have a more important role in generating englacial and subglacial sediment than is currently attributed to basal erosion and entrainment.

Here we formally hypothesise that if accumulation zone RAs are under detected, then use of the Google Earth Engine supraglacial debris input detector (GERALDINE) (Smith et al. 2020) will correct this issue. GERALDINE is a new, free-to-use, cloud-based tool that utilises the computing capabilities of Google Earth Engine (Gorelick et al. 2017) to eliminate the disadvantages of manual RA detection and streamline the detection process. We show the added value of GERALDINE with a reanalysis of the manually mapped (Bessette-Kirton and Coe, 2016) GLBA RA hotspot. We find and present a substantive difference in identified RAs between their inventory and our more complete GERALDINE inventory.

4.2 Methods

4.2.1 Detection

GERALDINE utilises an image stack using every cloud-free pixel of every available Landsat image within a user-defined area and timeframe of interest. Using these data, GERALDINE creates a simple map from which a user can identify and verify new supraglacial RA deposits > 0.05 km^2 (see Smith et al. (2020) for details of the tool). It cannot, however, detect RA debris deposited onto already debris-covered glacier ice, therefore preventing detection of events characterised by multiple failures, nor can it utilise cloudy imagery. It is therefore important to acknowledge that, even with GERALDINE, RA detection rates are likely to be underestimates. We ran GERALDINE annually between 1984 and 2020 using a study area identical to the one utilised by Bessette-Kirton and Coe (2016) and Coe et al. (2018). In total, 1853 Landsat images were analysed by GERALDINE (for breakdown of annual and monthly image frequency and average scene cloud cover see Figure S 6), with 1393 of these images analysed over the same period as Bessette-Kirton and Coe (2016), in contrast to the 104 they utilised. All output maps with automatic debris detections were manually analysed along with the Landsat scenes to verify RA deposit detections, based on commonly agreed characteristics: lobate and elongated, and discrete source area association (Deline et al. 2014). We refer to all landslide deposits as RAs in this study, despite most newly identified events being relatively small in areal extent (i.e., 71 % were < 0.5 km^2), due to the characteristics described above. Despite this abundance of smaller RAs, our dataset is directly comparable to that of Bessette-Kirton and Coe (2016) because we only identify one RA that was smaller (0.097 km^2) than their smallest RA deposit (0.11 km^2). Any RA candidates that were not part of the Bessette-Kirton and Coe (2016) inventory were verified, digitised, and their time window of occurrence was identified using the Google Earth Engine Digitisation Tool (GEEDiT) (Lea 2018). To do this, we specified the location and the year of the RA within GEEDiT, which then returned all the Landsat images that fit these criteria. Then, we analysed each image to determine the window of occurrence, before digitising the deposit, and exporting it into a geographic information system (GIS). Minimum and maximum elevations of each RA deposit and aspect of the headscarp were calculated using the Interferometric Synthetic Aperture Radar (IFSAR) digital elevation dataset (5 m resolution) collected in summer 2012 (USGS, 2018) as per Bessette-Kirton and Coe (2016).

Landslides were manually mapped in their entirety using GEEDiT, with polygons including both the source and deposit to ensure continuity between our dataset and that of Bessette-Kirton and Coe (2016). Source zones in GLBA are often small (in two dimensions (2D)) in comparison to the deposits due to the exceptionally steep rock-wall sources. It is also difficult to accurately delineate the boundary between source and deposit zone due to the glaciated nature of the region, providing minimal contrast between the different RA zones without an accurate post-event digital elevation model (DEM) (Bessette-Kirton et al. 2018).

4.2.2 Magnitude frequency

We calculated the magnitude-frequency relationship of our RA inventory using the method of Tanyaş et al. (2018). This is done by binning RAs based on their deposit size and plotting these bins against the corresponding frequency-density values to create a frequency-area distribution curve (Tanyaş, Allstadt and van Westen, 2018). For the GLBA RA inventory, we do not report the landslide-event magnitude (*mLS*) parameter as per Tanyaş et al. (2018) method because our RAs were not triggered by a singular event at a defined point in time (e.g., earthquake). Typically, the frequency-area distributions of medium and large landslides are characterised by a power-law relationship (e.g., Malamud et al. 2004). To assess the validity of the power-law fit to our data, a *p*-value indicating hypothesis plausibility was calculated using the method of Clauset et al. (2009). This method was also used to assess uncertainties by Tanyaş et al. (2018).

4.2.3 Rock avalanche relationship with temperature

To assess RA relationship with temperature, we used 2-m, above-ground, monthly-mean (derived from mean daily temperatures) temperature data from the ERA5-Land reanalysis

(Muñoz Sabater, 2019). This dataset is an improvement of the land component of the ERA5 reanalysis dataset (Hersbach *et al.*, 2020), which is created using observations of atmospheric conditions, predominantly from satellites. These data are used as an input into the European Centre for Medium-Range Weather Forecasts (ECMWF) integrated forecasting system (Cy41r2). ERA5-Land has a spatial resolution of 0.1 × 0.1 degrees (Muñoz Sabater, 2019), which equates to pixel sizes of about 11.1 × 5.8 km in the study region. Each cell uses the average elevation of the Shuttle Radar Topography Mission 30-m DEM as altitude, and is corrected using a daily lapse rate derived from ERA5 (Muñoz-Sabater *et al.*, 2021). RAs occurred in 21 of the ERA5-Land cells. To retrieve temperature, we used the ERA5-Land cell that the RA source occurred within, and the date the RA was first visible in Landsat satellite imagery, as the date of occurrence, or the actual event date if known (four RAs). This window of occurrence (gap between the image where the RA was not visible and was visible) averages 39 days, but varies between 7 and 272 days (Table S 2). The nature of RAs in the study area is that RAs are typically only visible over their summer of occurrence and are then buried by winter snowfall and/or advected into the ice indefinitely, as documented elsewhere (Dunning *et al.*, 2015). As a result, we have confidence that our visible dates are close to their actual occurrence dates (generally within 30 days) and are therefore suitable for assessing temperature relationships using monthly-mean average temperatures. For RAs that occur on the first day of the month, this is imperfect, but for RAs that occur at the end of the month, this works well. There is therefore no perfect solution to this issue due to the format of the ERA5-Land data. Temperature anomalies were calculated by extracting monthly temperature data from the corresponding ERA5-Land cell within which the RA occurred, averaging these data between the years of 1984 and 2020 as a reference window, and then subtracting the RA occurrence month's temperature from this average. For example, a RA that occurred within ERA5-Land cell 14 in June 2015 would have all June temperatures for cell 14 averaged, and then the June 2015 cell 14 temperature would be subtracted from this average. This gives a positive value if the RA occurrence month's temperature was above average and a negative value if the temperature was below average.

In addition to the ERA-5 temperature data, we used the 30 arc-second (~1 km grid) global permafrost zonation index (PZI) (Gruber, 2012) to investigate the relationship between RAs and permafrost likelihood. This dataset was derived by modelling the established relationships between air temperature and permafrost occurrence using the NCAR-NCEP reanalysis (Kalnay *et al.*, 1996) and CRU TS 2.0 (Mitchell *et al.*, 2004). The permafrost zonation index output is a qualitative map of permafrost likelihood spanning from permafrost existing in only the most favourable conditions, to permafrost existing in almost all conditions.

4.2.4 Earthquakes as a trigger

We used an identical method to Coe et al. (2018), which is a modified version of Keefer (1984) and Jibson (2013), to determine if any RAs were caused by earthquakes, instead of using newer methods (e.g., Havenith et al. 2016). This is because the newer methods require detailed information on lithology and antecedent rainfall conditions, which we do not have for GLBA. We downloaded data for all >*M* 4.0 earthquakes within 100 km of the study area, from the USGS Earthquake Catalog (https://earthquake.usgs.gov/). Only

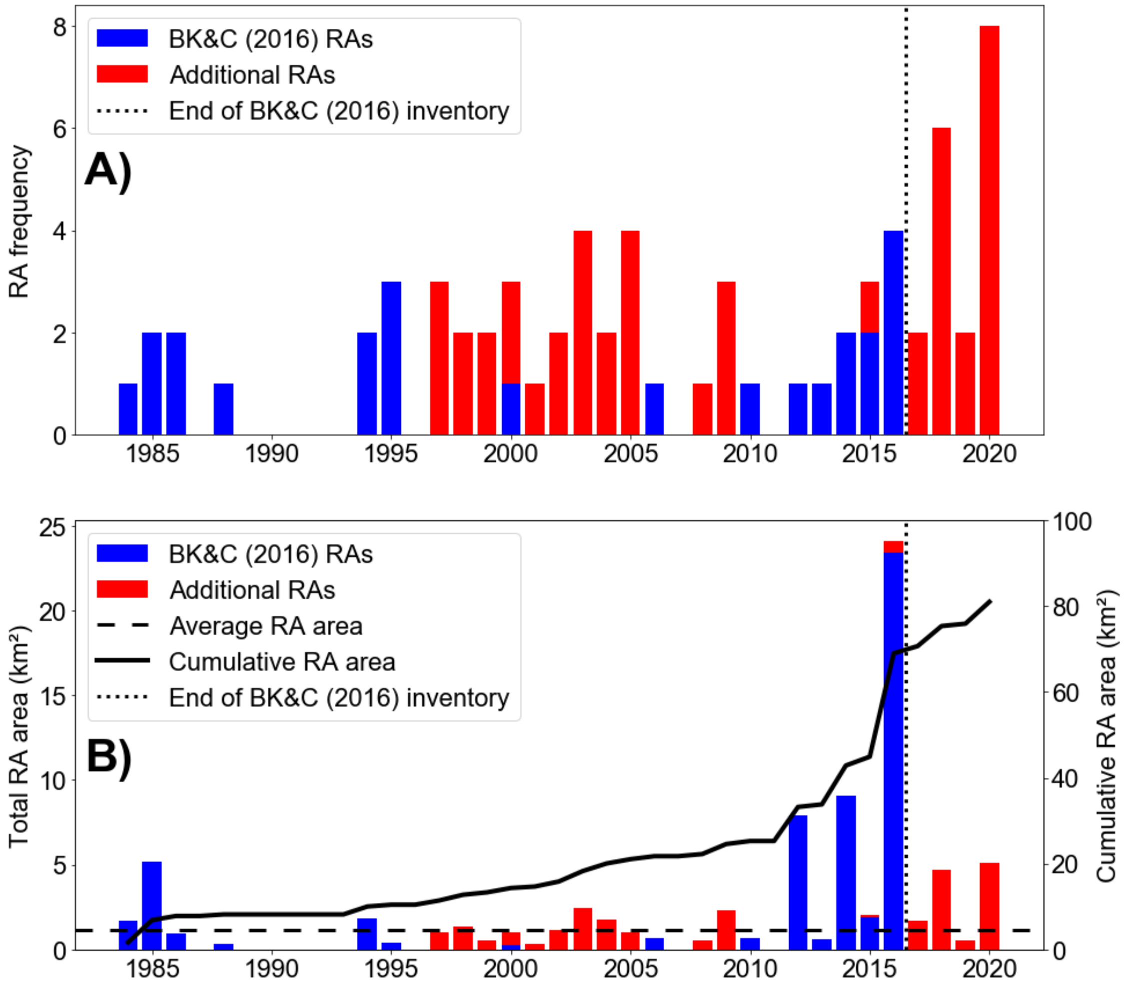

Figure 22: A) Frequency of rock avalanches in Glacier Bay National Park & Preserve, Alaska, between 1984 and 2020, from the original Bessette-Kirton and Coe (BK&C 2016) database and the additional RAs found in this study. B) Total annual rock avalanche deposit area and cumulative total from 1984 to 2020. Average RA area (1.16) read from the Total RA area (km^2) axis.

earthquakes >*M* 4.0 were selected because earthquakes under this threshold are characterised by an insignificant area over which they can trigger mass movements (Keefer, 1984; Jibson, 2013).

4.3 Results

4.3.1 Frequency and size

Using GERALDINE, 27 RAs were identified between 1984 and 2016 that were not included in the original inventory created by Bessette-Kirton and Coe (2016) (Figure 22A, 23A, and Table 1). This equates to a 53 % underestimation of the number of RAs using manual detection. Of the 27 additional RAs identified, 21 occurred in accumulation areas. In addition, 26 of them were recorded in just a 14-year period between 1997 and 2009 (Figure 22A). This fills in the majority (57 %) of the 'quiet' time periods where no RA events were previously identified (Coe, Bessette-Kirton and Geertsema, 2018). Instead of clusters of RA activity, we find that a consistent RA frequency characterises the region during our study window. Our new inventory shows that only nine of the 33 years analysed featured no RA activity, with just one quiet period between 1989 and 1993. However, this quiet period had the lowest image availability over the study period, so RAs may have occurred, but inadequate images prevented detection (Figure S 6). With the additional RAs we identified between 1984 and 2016, average frequency for this time period increases from 0.7 to 1.5 RAs yr^{-1}. Updating the inventory to include 2017-2020 identifies an additional 18 RAs. In this 4-year period, 2020 experienced the highest RA event frequency of the entire 37-year period, with eight RAs (8 RAs yr^{-1}). Including these four additional years increases the average annual RA frequency to 1.9 RAs yr^{-1}. RA frequency never exceeded four events per year until 2018 and 2020, when we see six and eight events, respectively. In total, 69 RAs were detected between 1984 and 2020 (Table 1).

Bessette-Kirton and Coe (2016) estimated the total RA deposit area between 1984 and 2016 at 55 km^2; however, we find an additional 13.3 km^2 of RA debris coverage over this time period, a 19 % underestimate (Figure 22B and Table 1). An additional 12 km^2 of RA debris coverage was identified between 2017 and 2020. Using this updated RA debris coverage (80.3 km^2), this equates to 0.04 % of the GLBA glaciated area (a total of 2037 km^2) at some point being covered by RA debris between 1984 and 2020. The largest previously unidentified RA we were able to identify within the Bessette-Kirton and Coe

(2016) study period occurred in 2004 and had a deposit area of 1.5 km^2. The 27 additional RAs we found between 1984 and 2016 covered an average area of 0.49 ± 0.33 km^2, in comparison to the Bessette-Kirton and Coe (2016) RA inventory, which covered an average area of 2.29 ± 4.65 km^2 (Table 1). Combining both datasets for 1984-2016 revises

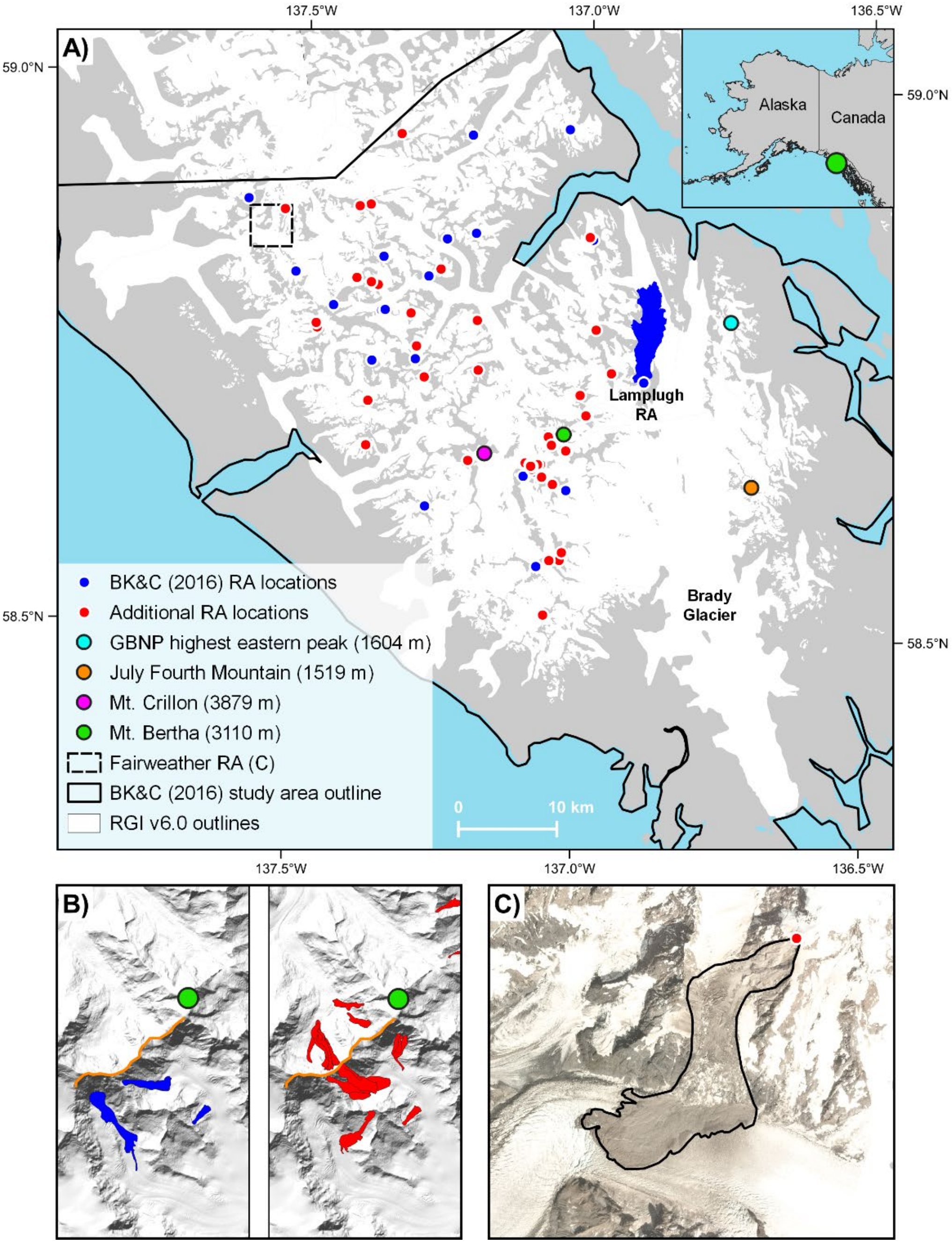

Figure 23: A) Rock avalanche (RA) source locations for the Bessette-Kirton and Coe (BK&C 2016) database and the additional RAs found using GERALDINE. Lamplugh RA deposit (22 km^2) shown in dark blue. The study area of Bessette-Kirton and Coe (2016) follows the coastline. B) Concentrated cluster of RAs around a ridgeline (orange line) between Mt. Bertha and Mt. Crillon identified by Bessette-Kirton and Coe (2016) (blue) and this study (red), and C) 2018 Fairweather Glacier RA image courtesy of Planet Labs Inc. (29-07-2018).

Table 1: Comparison summary statistics for the Bessette-Kirton and Coe (BK&C 2016) RA inventory and the updated RA inventory presented here (this study).

	Number of RAs	**Mean annual frequency**	**Total area (km^2)**	**Mean size (km^2) (± st. dev.)**	**Mean *H/L* (± st. dev.)**
BK&C (2016) (1984-2016)	24	0.73	54.98	2.29 ± 4.65	0.36 ± 0.13
This study (1984-2016)	27	0.82	13.33	0.49 ± 0.35	0.53 ± 0.16
This study (2017-2020)	18	4.5	11.99	0.67 ± 0.81	0.47 ± 0.11
All RAs (1984-2020)	69	1.86	80.29	1.16 ± 2.87	0.45 ± 0.15

the average RA deposit size to 1.34 ± 3.29 km^2. Although the updated inventory indicates that RA frequency is consistent as opposed to clustered (Coe, Bessette-Kirton and Geertsema, 2018), the supply of debris is less uniform, with a significant pulse of debris between 2012 and 2016. This is principally due to three large RAs: the 2012 Lituya, 2014 La Perouse, and 2016 Lamplugh RAs. The debris from these three events covered areas of 7.94 km^2, 5.45 km^2, and 22.19 km^2 respectively, totalling 44 % of all supraglacial RA deposit coverage (Figure 23B). Areal coverage of all RA deposits from 2012-2016 accounted for 63 % of all RA deposit areal extents over the 33-year 1984-2016 period (Figure 23B) and 54 % between 1984 and 2020. The largest single post-2016 event covered 3.4 km^2 of the Fairweather Glacier in the northwest of GLBA (Figure 23C). Including the RA events of 2017-2020, overall average RA size decreases to 1.16 ± 2.9 km^2 (Table 1), due to 72 % of events 2017-2020 being < 0.5 km^2. Although no exceptionally large events were identified that were comparable to the large RAs that occurred in 2012 (Lituya), 2014 (La Perouse), and 2016 (Lamplugh), each year from 2017-2020 (excluding 2019) experienced an RA larger than the mean RA size (1.16 km^2). However, this indicates that 2016 marked the end of the period identified by Coe et al. (2018), where RAs > 5 km^2 were increasing in frequency since 2012. None of the additional RAs in this study were > 5 km^2, and we have instead infilled the inventory with harder to detect 'small' (< 0.5 km^2) events. In contrast to the 2012-2016 period, the years with the highest RA frequencies (2018 and 2020) are not characterised by the largest debris areal coverage due to a lack of large events.

The magnitude-frequency relationship for our updated RA inventory shows that a typical power-law relationship is not a robust fit for these data (Figure 24). A p-value close to 1 indicates good power-law fit; however, our dataset produces a p-value of 0.323. Above RA sizes 3×10^6 m^2, the power-law relationship decays and underestimates RA area, whereas the cutoff value, where the inventory no longer follows the power-law relationship at the smaller RA sizes, is high at 284,614 m^2. A power-law relationship can therefore only describe a small subset of this new inventory. It must be noted that our power-law fit is, in effect, only attempting to span what we have classified as RA, which as a landslide process sits at the low frequency – high magnitude end of more complete event or historical inventories. The scaling exponent (β) of the 'best' power law fit to these data, which is used to show the dominance of either small-frequent or large-rare events is low (1.9787) in relative terms in comparison to other landslide databases (Tanyaş, Allstadt and van Westen, 2018), indicating larger events are greater debris contributors than small events (Hergarten, 2003). This is primarily driven by the three large (> 5 km^2) RA events that occurred during 2012-2016.

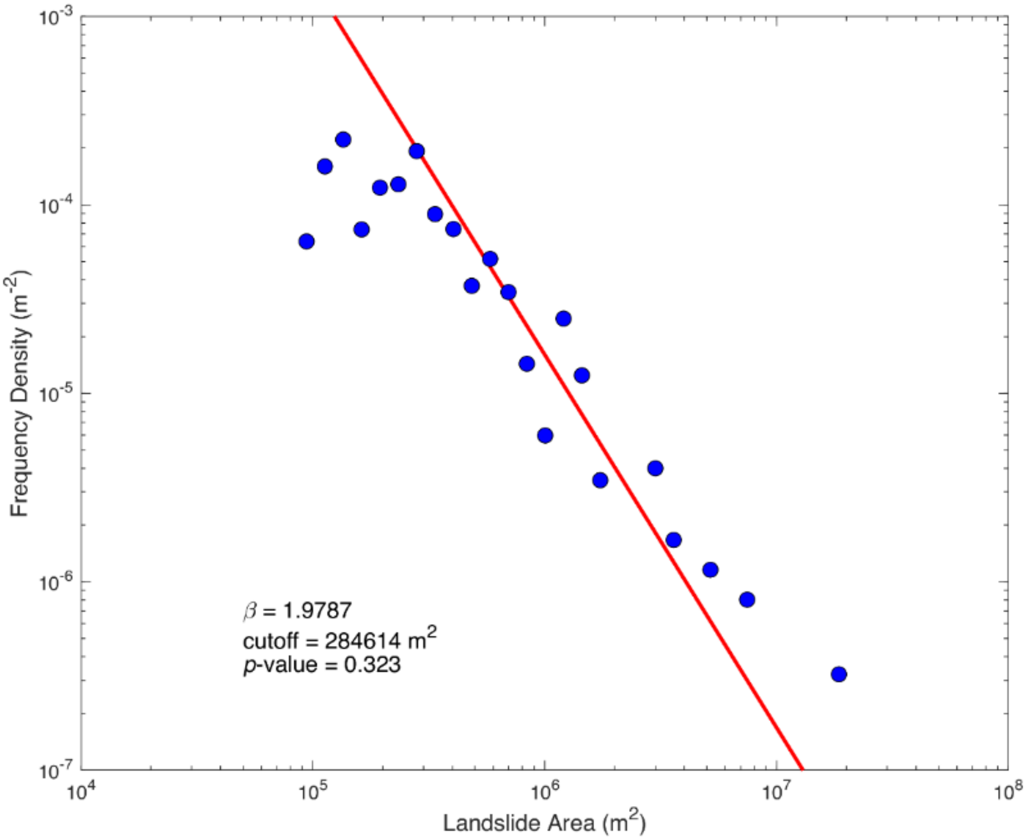

Figure 24: Magnitude frequency relationship of all rock avalanches identified in Glacier Bay National Park using a modified version of Tanyas et al. (2018).

4.3.2 Spatial distribution

Our new inventory of 69 RA events that occurred between 1984 and 2020 in GLBA displays spatial clustering in the western half of the national park (Figure 23A), where topography has greater relief (Figure S 7). This indicates that manual identification did not neglect any specific areas, because neither the original inventory nor the updated inventory presented here find RAs in the eastern region. Consistent with the dataset of

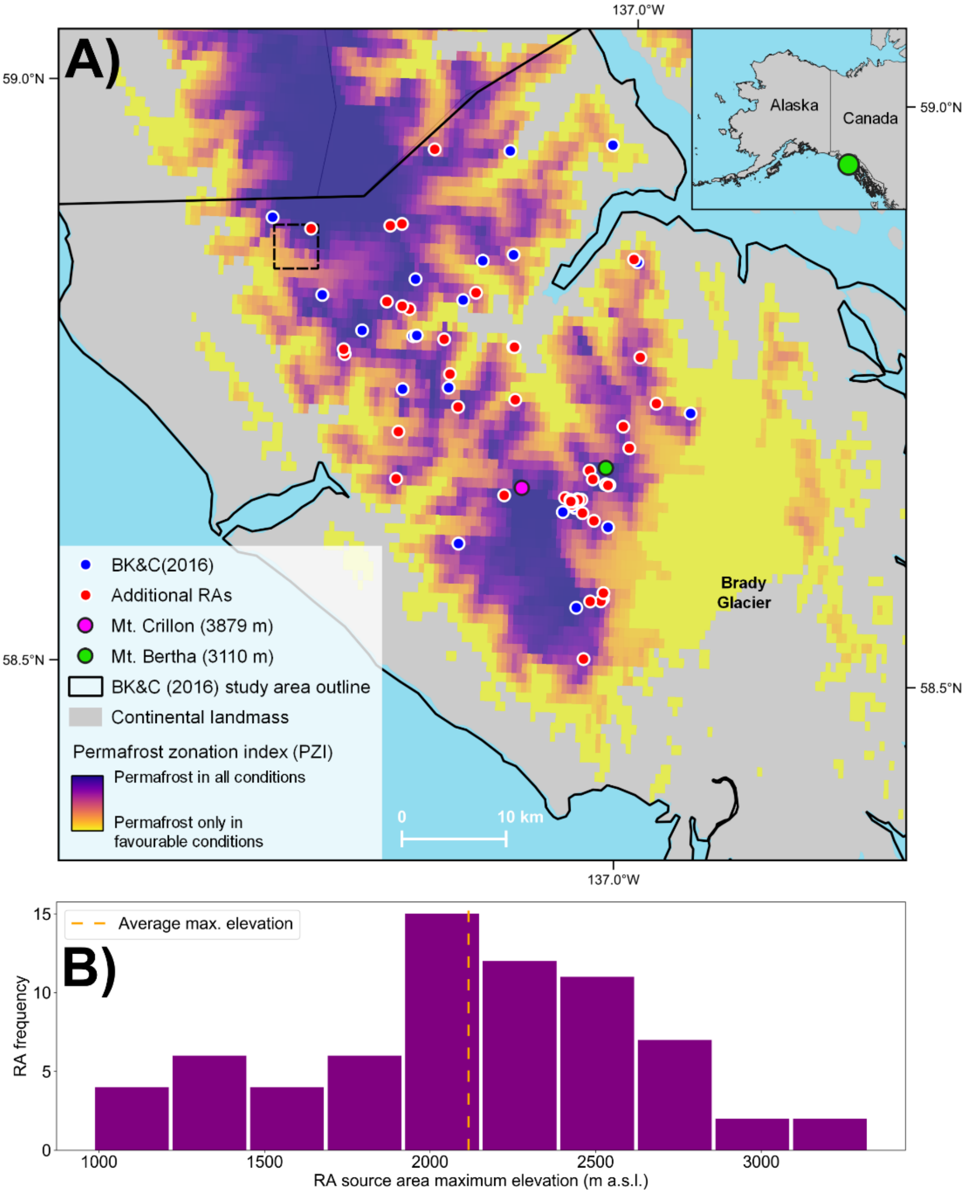

Figure 25: A) RA locations from the Bessette-Kirton and Coe (BK&C 2016) database and the additional RAs identified in this study, in relation to the Permafrost Zonation Index (PZI) of Gruber (2012). The PZI is the likelihood of permafrost occurring in any given location. B) Histogram of RA source maximum elevations.

Bessette-Kirton and Coe (2016) and the analysis by Coe et al. (2018), all additional RAs identified in this study are distributed around the modelled transition of permafrost likelihood, from ‘occurrence in all conditions’ to ‘only under favourable conditions’ (Gruber, 2012) (Figure 25A). No RAs are deposited onto glaciers in the eastern region of GLBA around the Brady icefield: a region with permafrost only likely under very favourable conditions, or not at all (Figure 25A). This correlates with RA source area maximum elevation, with most events initiated at elevations around ~2000 – 2500 m above sea level (a.s.l.) (Figure 25B). Even the highest peaks of the eastern area do not

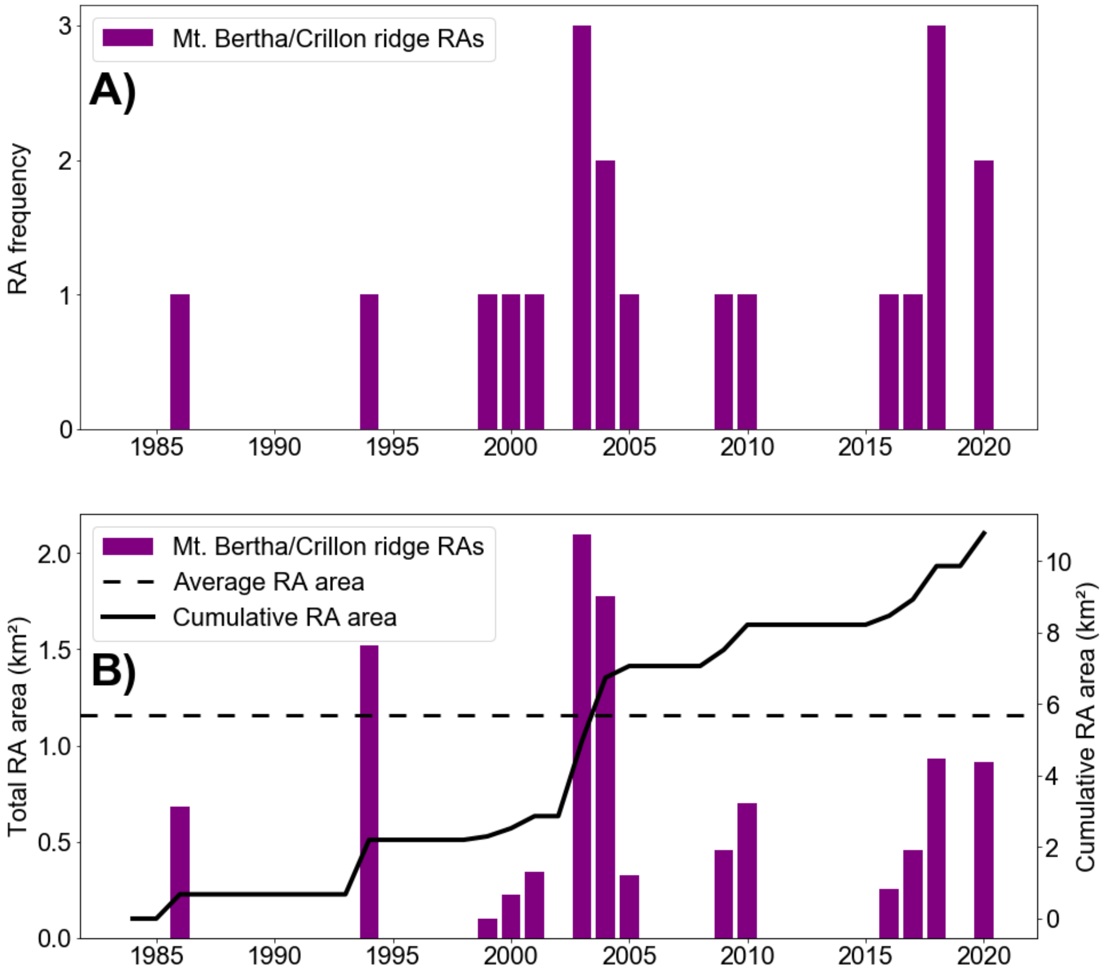

Figure 26: Frequency (A) and area (B) of RAs occurring between Mt. Crillon and Mt. Bertha. Average RA area (1.16) for the complete RA inventory (all 69 events) read from the Total RA area (km^2) axis.

reach these altitudes (all peaks < 1604 m a.s.l), perhaps providing a climatic/topographic threshold to RA occurrence. However, this eastern area is characterised by large areas of dirty ice and/or debris cover around the lateral edges of glaciers making identification with GERALDINE difficult due to the minimal contrast between new RA debris and existing supraglacial debris (Smith *et al.*, 2020). In this case, the manual analysis of satellite images is more reliable, but still difficult (Bessette-Kirton and Coe, 2016).

In addition to RA association with the modelled permafrost boundary in GLBA, a spatial cluster of 16 previously undetected RAs were identified between Mt. Crillon (Lat: 58.662778, Long: -137.171944) and Mt. Bertha (Lat: 58.682028, Long: -137.039167) (Figure 23B and Figure 26) over the study period. This is in addition to the four already documented (two of which failed from the same source and were almost identical in terms of their runout extent at the mapping scale of Figure 23). This cluster represents ~29 % of all RA events, and 13 % of the area of RA deposits. The years 2003 and 2018 marked the most active years, with three RAs apiece (Figure 26A). The 2003 events result from what appears to be the partial collapse of the southwestern ridge that runs between Mt. Crillon and Mt. Bertha, the deposits of which covered a combined area of 2.08 km^2. This ridge was the site of nine of the additionally identified events and two events documented by Bessette-Kirton and Coe (2016). The Geologic Map of Alaska (Wilson et al., 2015) indicates no unique lithologic/structural differences or any (known) fault lines that may cause this heightened activity, although we have not undertaken a detailed analyses of the topographic/geomorphic drivers and differences.

Aspect also appeared to be a controlling factor on the susceptibility of slopes to RAs, with 28 % of events occurring on north facing slopes (340-20°) (Figure 27A) and 20 % occurring on south facing slopes (160-200°). Normalising RA slope aspect by all slope aspects in the study area (Figure S 8), shows that north facing slopes were still dominant with regards to failure, and east facing slopes (90-120°) featured a higher prevalence of events proportionally (Figure 27B). No large events (> 3 km^2) occurred on the dominant active slope aspects (north and south facing). These trends mirror those found by Coe et al. (2018) despite our study increasing the number of identified events by 53 % over the same time frame. A similar aspect trend was also observed during the 2003 heatwave in the European Alps (Gruber, Hoelzle and Haeberli, 2004).

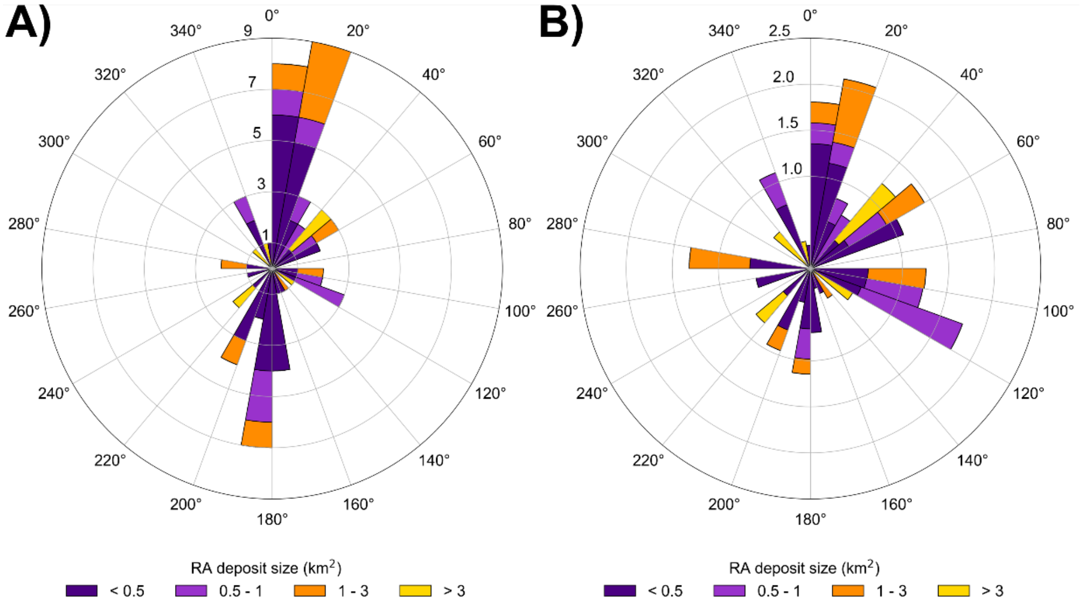

Figure 27: A) Frequency of rock avalanche source area aspects categorised into 20° bins, B) Rock avalanche area aspects normalised using all slope aspects in Glacier Bay National Park.

4.3.3 RA sequestration

Of the 69 RAs found between 1984 and 2020, 58 % of RAs were sequestered into the ice within two years, 8 % were partially sequestered, and 20 % were not sequestered and remain on the surface. The remaining 14 % included RAs that occurred in 2020, so there has been insufficient time to determine whether they will be visible the following year, and two RAs from 1984 and 1986 that we could not identify from the Bessette-Kirton and Coe (2016) dataset. Of these 2020 RAs, two (RA ID 66 and 67) are likely to stay visible due to partial/complete deposition below the snowline in their respective locations, while the remaining six were sequestered. Of the 27 additional RAs we found that were not identified in the original inventory, 21 were sequestered within two years.

4.3.4 Mobility

A key point raised by Coe et al. (2018) was the increase in RA mobility over time. RA mobility is calculated by dividing the total fall height of the RA (highest elevation of the source area and lowest elevation of the deposit), by the maximum runout distance of the RA (source to deposit terminus), which is referred to as *H/L*. This metric is a crude proxy for the friction angle/travel angle (Heim 1932; Davies and McSaveney 2013; Sosio et al. 2012), with 0.6 a common threshold applied for rock avalanche like motion. Using the updated inventory, we calculated *H/L* (Figure 28) and found no significant upward trend ($p = 0.66$ using the Mann-Kendall test) in RA mobility over the 1984-2020 time period, four years longer than the original Bessette-Kirton and Coe (2016) inventory. Our new inventory has a mean *H/L* value of 0.45, compared to 0.36 estimated by Coe et al. (2018) (Table 1). We attribute this to the identification of several smaller RAs, decreasing average RA size from 2.29 ± 4.65 km^2 to 1.16 ± 2.9 km^2 (Table 1). Smaller RAs are well known to have higher *H/L* values than larger events (Sosio *et al.*, 2012; Aaron and McDougall, 2019), although this relationship is complex (Evans and Delaney, 2015). RA mobility is less than previously believed in the region and lower than other databases of glacial RAs. Deline et al. (2015) gathered data from 56 supraglacially deposited RAs worldwide and found an average *H/L* of 0.28, whereas Bessette-Kirton and Coe (2020) identified 220 RAs in the St. Elias Mountains of Alaska, and found an average *H/L* of 0.37. The GLBA average is more comparable to that of Bessette-Kirton and Coe (2020). This is because they did not exclude events due to a size/mass threshold, with an average RA size of just 0.6 km^2, whereas the database of Deline et al. (2015) is made up of RAs with volumes > 10^6 m^3. However, the derivation of volume from area is poorly constrained with few quantitative examples to account for the complex patterns of erosion, entrainment and compaction that preclude simple source zone differencing (Bessette-Kirton et al. 2018), from which the Deline et al. (2015) inventory predominantly relies upon.

4.3.5 Potential causes of rock avalanche occurrence

Coe et al. (2018) proposed increasing atmospheric temperatures and subsequent rock-permafrost degradation as the likely cause of increasing RA size in the study area. However, they acknowledged that the exact processes that cause degradation and destabilisation are unknown, and the slopes are likely pre-conditioned through accumulating elastic crustal strain, glacial thinning, and increased precipitation. With the addition of 45 RAs to the existing inventory, our results are also spatially coincident with the modelled boundary/transition of permafrost favourability (in the period 1961-1990) created by Gruber (2012) (Figure 25A). However, the permafrost zonation index (PZI) of Gruber (2012) is a global dataset with necessary simplifications and higher resolution permafrost models/data would offer a considerable advance in further quantifying any links between permafrost and RA events. Future improvements to local or global permafrost products will allow the RA dataset presented here to be reanalysed.

To look at possible air temperature controls we use the higher resolution ERA5-Land reanalysis, 2-m height, monthly product, temperature data (Muñoz Sabater, 2019) (Figure

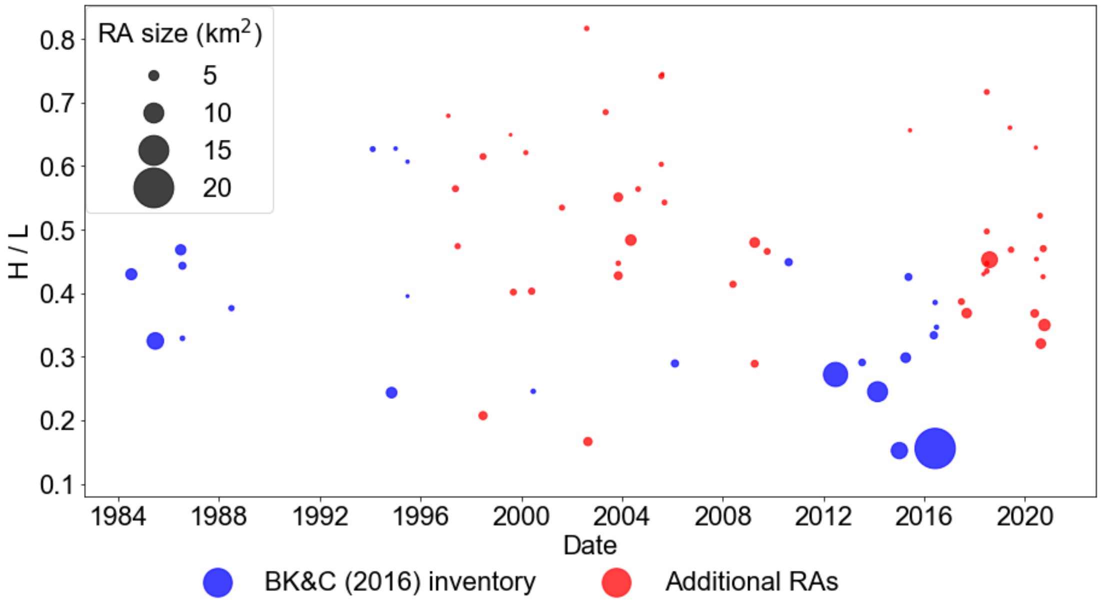

Figure 28: Ratio of fall height (H) to travel distance length (L) for all rock avalanches (RA) identified by Bessette-Kirton and Coe (BK&C 2016) and the additional RAs identified in this study, in Glacier Bay National Park during 1984-2020. Marker size represents RA size.

29 and Figure 30). Mean monthly temperatures across ERA5 cells in GLBA and RA monthly frequency (Figure 30) show a strong seasonal control on occurrence. RA derivation from 37 years of data using GERALDINE gives us confidence that this is real rather than a seasonal detection bias, however, Landsat image frequency in November, December, and January is notably lower (Figure S 6B), and this may play a role in preventing some RA identification during these months. All but two RAs were first visible in imagery between May and September when average monthly temperatures are consistently above -1.5 °C. This seasonality in RA occurrence has been found in other areas of Alaska (Bessette-Kirton and Coe, 2020) and the addition of our 45 (albeit often smaller) RAs shows that this seasonality of triggering is not size or detection biased. The two RAs identified outside of the May-September period, the La Perouse RA (February

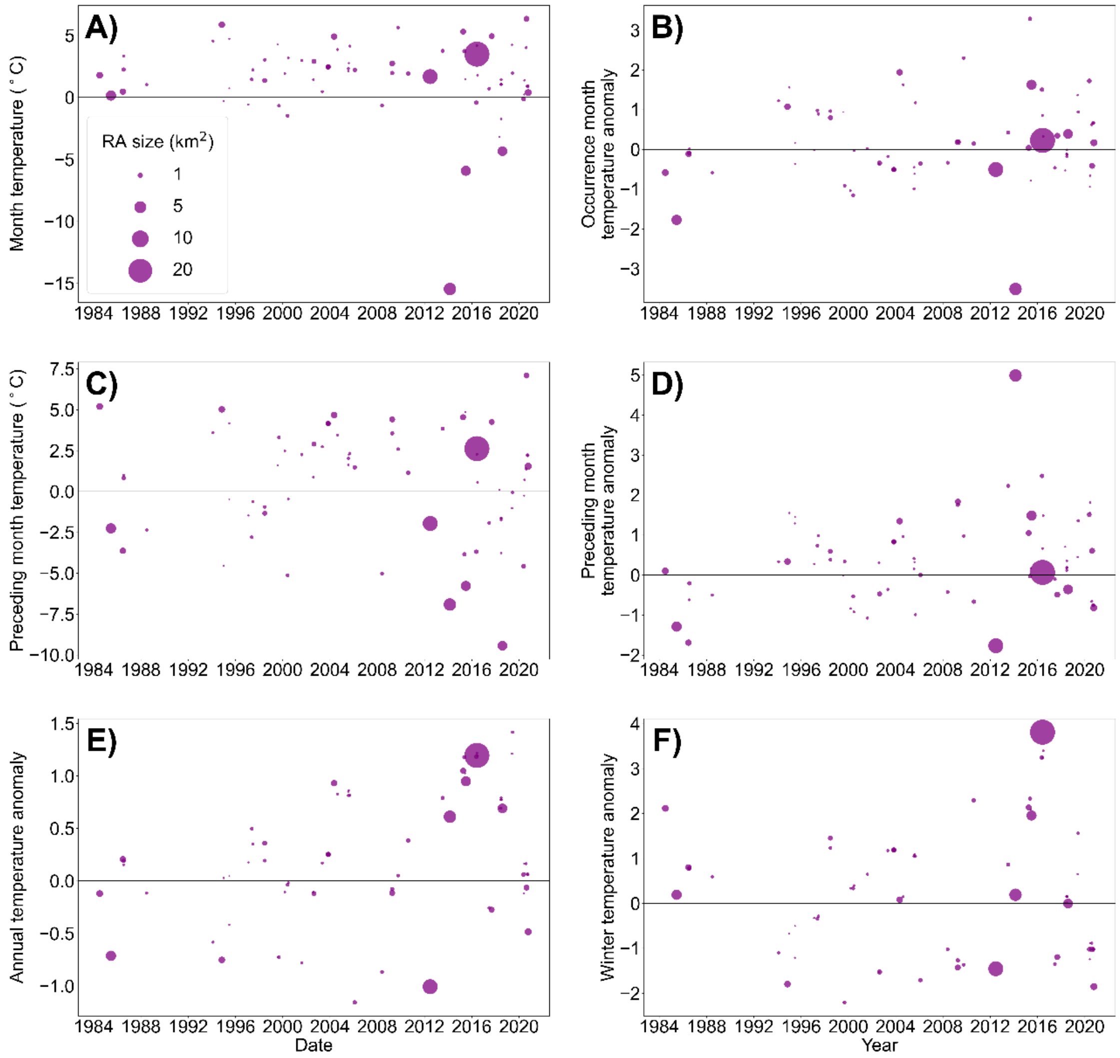

Figure 29: ERA5-Land temperatures for each rock avalanche A) month of occurrence temperature, B) month of occurrence temperature anomaly, C) preceding month of occurrence temperature, D) preceding month of occurrence temperature anomaly, E) annual temperature anomaly, and, F) winter (December, January, February) temperature anomaly.

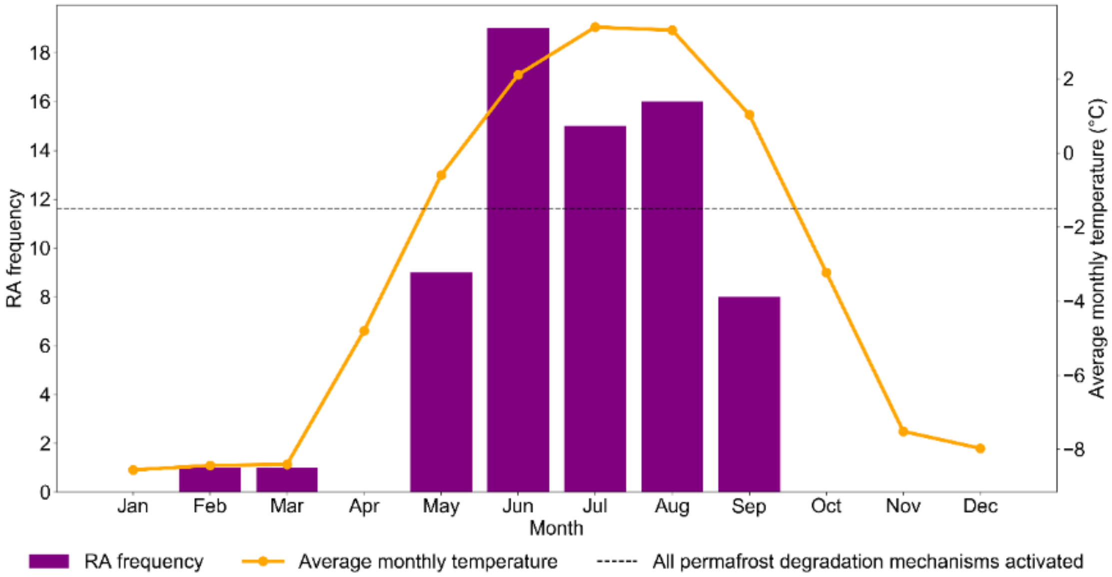

Figure 30: Monthly rock avalanche frequency (assigned as the image month in which the RA is first visible) and average monthly temperature from ERA5-Land temperature data using the cells in which RAs occurred within, in Glacier Bay National Park & Preserve during 1984-2020.

2014) and the Orville-Wilbur RA (March 2015), have not previously been assigned a trigger (Coe, Bessette-Kirton and Geertsema, 2018; Hibert *et al.*, 2019). It is possible that other RAs did occur in these months but were not identified in this study, with lower Landsat image frequency over winter (Figure S 6B), and this may play a role in preventing RA identification during these months. However, our confidence in this seasonality is high because we evaluated 37 years of data on an annual basis using a debris biased approach (GERALDINE). In terms of absolutes, RAs between 1984-2020 are being detected in months with GLBA average temperatures between ~ -4°C and +3 °C. We can improve the granularity somewhat using the ERA5 cells (22) covering GLBA assigned to each RA source zone and the temperature anomalies (Figure 29). Only 12 RAs occurred during a month with an average temperature below 0 °C (Figure 29A), and only five occurred during a month with an average temperature below -1.5 °C; the temperature at which all rock-permafrost degradation mechanisms are active, as outlined in the introduction. However, 2 m air-surface temperature is not rock surface temperature, especially where aspect strongly controls solar radiation receipt (e.g., Lamp et al. 2017). Rock surface and air temperature are also not representative of temperatures at the depths that RA shear planes may be located. However, RAs on north-facing slopes dominate our inventory (Figure 27A), and their dominant temperature control is air temperature (e.g., Salzmann et al. 2007; Noetzli et al. 2007; Noetzli and Gruber 2009). Deep seated RA shear planes likely respond to longer term warming rather than shallow permafrost thaw, but, recent work has shown correspondence between degrading permafrost (and precipitation) and both the onset, and, deformation rate of rock-slope failures in Norway (Hilger et al. 2021). In comparison to the monthly average temperature in which RAs were identified, 28 RAs experienced temperatures below 0 °C in the month preceding failure (Figure 29C). Of these 28 RAs, 18 occurred during a month with an average temperature >0 °C, directly following a month during which the average temperature was <0 °C, indicating a temperature rise through the temperature zone of maximum permafrost rock-slope destabilisation. Temperature anomalies for both RA occurrence month (Figure 29B) and preceding month (Figure 29D), show no clear association with failure, indicating the temperature of the month of failure is the key factor.

Calculated annual temperature anomalies for each RA show no clear relationship with RA occurrence (Figure 29E), with an average anomaly of 0.244. Similarly, winter (December-February) temperature anomalies are also not a clear indicator of RA occurrence, averaging 0.198 (Figure 29F). We do not rule out temperature anomalies at any time of year as a trigger for RAs, as it is highly likely that above average temperatures trigger RAs, as found elsewhere (e.g., the European Alps; Gruber et al. 2004), but they cannot explain all RAs in the GLBA inventory.

On a larger scale, the Pacific Decadal Oscillation (PDO) and El-Niño-Southern Oscillation (ENSO) have a strong influence on temperature and precipitation in Alaska (Fleming and Whitfield, 2010; Wendler, Gordon and Stuefer, 2017), switching from positive (warmer and wetter) to negative (cooler and drier) phases (Papineau, 2001; Fleming and Whitfield, 2010). Switches to positive PDO and ENSO phases have been attributed to recent increases in glacier mass loss and thinning in Alaska (Hugonnet *et al.*, 2021; Jakob *et al.*, 2021). We utilised the PDO index data from NOAA (2021) and the Multivariate El-Niño-Southern Oscillation (MEI) data (Wolter and Timlin, 2011) to assess RA relationship with these large-scale climatic influences. Although increased temperatures and subsequent glacier thinning are both known to cause increased rock slope activity (Deline, Hewitt, *et al.*, 2014), in accordance with the analysis of Coe et al. (2018), we determined no correlation between RA occurrence and PDO and ENSO behaviour (Figure S 9).

We rule out earthquakes as a cause of RAs because only one >*M* 4.0 earthquake occurred in the region that: (i) corresponded to a RA window of occurrence (RA ID 30), and (ii) occurred within the landslide trigger zone. This was an *M* 5.6 earthquake on 27/05/1999, which should have a landslide trigger zone of ~400 km^2, according to the relationship between area affected by landslides and earthquake magnitudes (Keefer, 1984, 2002). Although we rule out earthquakes as a dominant triggering mechanism, the study area experienced 14 earthquakes >*M* 4.0 over the study period (1984-2020). The area is also undergoing high rates of post-glacial isostatic uplift at ~24 mm y^{-1}, due to the loss of over 3030 km^3 of ice in the past 300 years (Larsen *et al.*, 2005). Seismicity and redistribution of rock slope stress therefore remain likely contributing pre-conditioning factors for slope instabilities (Ballantyne, 2002b).

4.4 Discussion

4.4.1 Why is GERALDINE detection better?

The manual analysis method of Bessette-Kirton and Coe (2016), which involved selecting a minimum of one cloud-free Landsat image acquired annually between May and October and visually analysing it for RA deposits using different band combinations (104 images analysed in total) has long been considered the most reliable approach, and we chose the inventory for additional evaluation due to its high quality. We have shown that this was outperformed by GERALDINE. GERALDINE outputs target likely deposits for manual validation, which allowed the detection of several smaller RA deposits in GLBA over the same time period (1984-2016) as the Bessette-Kirton and Coe (2016) inventory, with the average deposit size of additional RAs being 0.49 km^2, in comparison to the average RA deposit size (2.29 km^2) of the original inventory (Table 1). We suggest the smaller area additional detections identified from GERALDINE are because larger deposits are easier to detect both visually and using seismic methods (Ekström and Stark, 2013). We further investigate the under-reporting of RAs in the Bessette-Kirton and Coe (2016) inventory by comparing the minimum elevation of RA deposits to look at sequestration/spatial bias (Figure 31). The Bessette-Kirton and Coe (2016) inventory did not detect RAs that occurred at all elevation bands, and above 1600 m a.s.l., only one small RA deposit (deposit ID 24 at 0.7 km^2) was identified in the original inventory, whereas we identified 14 additional RA deposits (Figure 31). This under-reporting at higher elevations is likely due to the difficulties of detection when RAs are deposited into glacier accumulation zones where they are visible for a shorter period of time / appear in less images. This is due to a higher likelihood of precipitation falling as snow (and wind redistribution of this snow), and subsequent sequestration into the ice and englacial transport system. In contrast, deposition of RA material at lower elevations in glacier ablation zones ensures they are visible on the surface for longer, and likely annually for many years, aiding manual detection. However, we also found four additional RAs detected below the ELA of the largest glacier in GLBA: Brady Glacier (~745 m a.s.l in 2013; Pelto et al. 2013) (Figure 31). Three of these deposits were deposited onto the John Hopkins Glacier, two of which (deposits ID 32 and ID 47) were deposited onto a branch flowing at ~800 m a^{-1}, and the remaining (deposit ID 50) deposited onto a branch with a velocity of ~350 m a^{-1}. These fast velocities cause rapid modification of 'diagnostic' RA deposit characteristics, and rapid incorporation into medial and lateral moraines, making manual detection difficult, particularly from the limited cloud-free imagery in GLBA as per Bessette-Kirton and Coe (2016). The remaining RA deposit occurred in a steep narrow valley, where it could easily be mistaken as a bare rock slope on a 2D Landsat image. An added benefit of GERALDINE is that it allows for the rapid analysis of many more images than are practical using manual methods (greater than an order of magnitude more in this case). This situation likely resulted in additional detections compared to the original study.

The results of this study prove GERALDINE is a valuable tool for RA detection, particularly in areas where debris cover is more intermittent (due to the detection challenges posed by debris deposition onto already debris covered glaciers; see Smith et

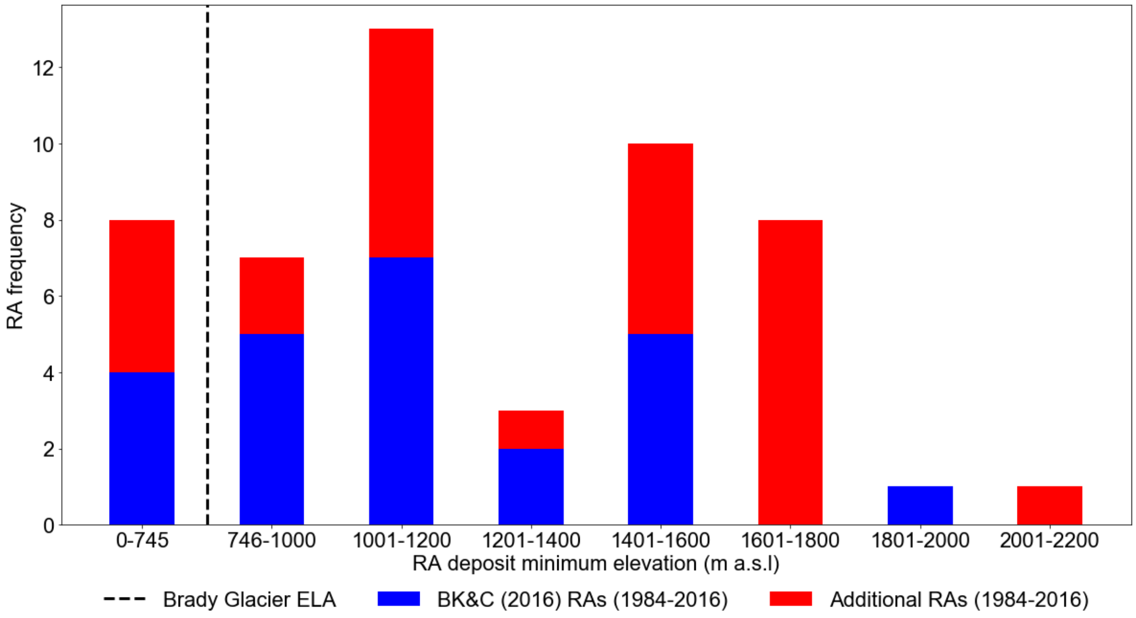

Figure 31: Minimum elevation of all RA deposits identified by Bessette-Kirton and Coe (BK&C 2016) and the additional RAs identified in this study, that occurred between 1984 and 2016, in relation to the Brady Glacier equilibrium line altitude (ELA) identified by Pelto et al. (2013).

al. (2020)). We recommend it is applied alongside other detection tools, such as seismic inversion (Ekström and Stark, 2013), in other high mountain glaciated regions, particularly the 'bellwether' sites identified by (Coe, 2020), to allow investigation of spatial and temporal trends in RA occurrence on a global scale, with GERALDINE able to work backwards within the long timeseries of Landsat imagery.

4.4.2 Temporal, spatial and areal RA trends

Our new inventory has filled in many of the years in which no RA activity was previously documented, showing RAs in GLBA are a more chronic / consistent supplier of debris and do not cluster temporally (Coe, Bessette-Kirton and Geertsema, 2018). RAs are responsible for a 'background' rate of debris delivery onto glaciers in GLBA, with a 'spike' in debris delivery during years of exceptionally large RAs that input a disproportionately high amount of debris into the glacial domain and dominate the historical inventory, in the 2012-2016 period. This background consistent supply of debris through rock-slope failures in GLBA has not previously been recognised (Coe, Bessette-Kirton and Geertsema, 2018) but has been found elsewhere over a longer time period (1950-2008) and a larger study area (~25,000 km^2) in the Chugach Mountains, Alaska (Uhlmann *et al.*, 2013). Similarly, in the St. Elias Mountains, RA frequency is constant and considerably higher than we find in GLBA (6 RAs per year as opposed to 1.9 per year in this study) over a smaller study area (3700 km^2) (Bessette-Kirton and Coe, 2020). However, RAs >5 km^2 were not documented in the St. Elias Mountains, and only three were documented in the Chugach Mountains, indicating the three that occurred in GLBA in just 4 years represent an exceptional period of large debris supply. In addition to the three large RAs we document between 2012 and 2016 in GLBA, on the 17/09/2022 another large RA (7.17 km^2 deposit area) was deposited onto the Lamplugh glacier, and partially ran out over the 2016 Lamplugh RA deposit (Petley, 2022). We know of no other glacial areas worldwide with such a high documented prevalence of large RAs over the last 40 years. We find the highest RA frequencies between Mt. Crillon and Mt. Bertha in GLBA, which experienced 29 % of all RAs recorded (Figure 26). Likewise, Bessette-Kirton and Coe (2020) documented that > 50 % of the RAs occurring in the St. Elias mountains initiated from source areas that failed repeatedly. This was attributed to lithology and tectonic setting (Bessette-Kirton and Coe, 2020). However, the extreme topography in these regions, rising from sea level to > 4000 m a.s.l. within 25 km, is characterised by numerous peaks and ridges, which are particularly susceptible to permafrost degradation as the warming can penetrate from multiple sides (Noetzli et al.

2007). Each area experiencing multiple failures over multiple years likely has a unique cause, but set within regional and global drivers of change that may be moving slopes towards their ultimate thresholds. It is unknown what combinations of conditions causes these areas to ‘switch on,’ and, once that (in)stability threshold has been crossed, if they will ever ‘switch off’ due to, for example, exhaustion or self-stabilisation of their sources, as has been hypothesised in paraglacial environments (Ballantyne, 2002b). For the Bertha-Crillon ridge (Figure 28) two clusters, 1999-2005 and 2016-2020 qualitatively appear to show a ramping up of event frequency-area. RA frequency in GLBA as a whole shows no clear signal of change when we include our detections alongside the previous inventory (Figure 22 and Figure 28). The three large RAs between 2012 and 2016 were exceptional in areal extent, and perhaps mobility (which is linked to volume). These large events disproportionately impact long-term debris area patterns (Figure 22B), although a number of smaller events also exhibited similar mobility (Figure 28). These large events are superimposed on a possible upward trend in debris coverage, after the three large events it is the frequency of moderate size events that drive this trend.

Our new inventory is unique in that it is derived from all available Landsat data, ensuring a level of completeness not previously available, and in the case of GLBA, the inventory is not affected by earthquake-triggered RAs, therefore, it represents the best currently available assessment of the background rates of RAs onto glaciers – with the caveat that past earthquakes will have affected rock-slope stability long-term. By utilising this more complete inventory we analysed the magnitude-frequency relationship (Figure 24) in which a weak power-law fit is observed – we cannot statistically say these data are best described by a power law. As is the case with most inventories, there is a point at which smaller event sizes deviate (‘roll over’) from the power-law (for full review, see Tebbens 2020), yet we also see this occurring at larger sizes as a ‘roll under’; they are more common than the power law fit suggests. We attribute this deviation at larger event sizes to the increased mobility (and subsequently areal coverage via spreading) of glacially deposited RAs in comparison to their non-glacial counterparts for a given volume (Sosio *et al.*, 2012). It has also been found that using data collected over time to derive frequency-area relationships can be problematic, particularly if large landslide frequencies have increased, shifting the distribution tail upwards (Schlögel *et al.*, 2011). Deviations at smaller event sizes are frequently attributed to smaller events going undetected (Tebbens, 2020), and we cannot detect events < 0.05 km^2 due to method limitations (Smith *et al.*, 2020). However, the causes of this rollover point are debated and recent research indicates that it may be accurate due to the change in physical processes occurring at small and large scales, due to variations such as lithology (Tebbens, 2020). In GLBA, small (<0.5 km^2) events are likely short runout, low spread, rock topples and rock falls, producing no homogenous deposit on the ice surface. We have witnessed events that leave a small, thin dust covering on the ice surface more akin to a debris fan, with snow/ice still universally visible beneath due to their minimal thickness. However, we do not categorise these as RAs, as their appearance and mobility are dramatically different from a RA deposit, and therefore we exclude them from the inventory. Size bias is also affected by image frequency. It is not possible to identify whether large failures are in fact a collection of smaller failures. Dusfresne et al. (2019) showed using seismic records that the largest RA in GLBA, the 2016 ‘Lamplugh’ event, was two discrete events separated by 2 hours (21 km^2 and 3.4 km^2 extents).

4.4.3 Warming triggers

We cannot conclusively show RAs in GLBA are triggered by a rise in atmospheric temperature and subsequent rock-permafrost degradation, but it is likely a contributing factor over a range of timescales. The dominant seasonal trend (May-September) of RA occurrence in GLBA, also found farther north in the St. Elias Mountains (Bessette-Kirton and Coe, 2020), coupled with the average temperatures of these months, rising atmospheric temperatures in the region as a whole, and a close association with the modelled boundary/transition of permafrost favourability (Gruber, 2012), indicate temperature-related destabilisation mechanisms are likely key for RA generation in GLBA. As previously noted by Coe et al. (2018), the exceptionally large RAs in 2012, 2014, and 2016, all took place during a multi-year period of record-breaking warm winter and spring temperatures. The seasonal triggering temperatures for our RA inventory (Figure 29 and Figure 30) are within the destabilisation temperatures (> -4°C, with the strongest effects as 0 °C is approached) modelled by Mamot et al. (2020), although the authors caveat that transferability is strongest for slopes similar to the model setup. The Gruber (2012) permafrost model output we use is a low-resolution product, which does not take into account slope aspect nor the topographic nuances that determine permafrost on steep, mountain slopes (e.g. Etzelmüller et al. 2022). In addition, it was created using mean annual air temperature data from 1961-1990, so, it represents an outdated, probably over-estimated permafrost extent, and is only directly applicable to RAs that occurred between 1984 and 1990 in our inventory. There is a pressing need for a high-resolution permafrost map in the area, to help discern the role permafrost degradation on RA preparation and/or triggering, and to assess the role of shallow warming in the onset of deeper seated RA failures.

Despite the limitations of the Gruber (2012) permafrost zonation product, the dominance of north-facing slopes as RA source areas in GLBA further supports permafrost degradation mechanisms. North facing slopes experience much less inter-annual temperature variability and subsequent permafrost thaw depth than their south-facing counterparts, due to their limited exposure to shortwave radiation (Gruber, Hoelzle and Haeberli, 2004). Current warming is amplifying these temperature variations and modelled future warming indicates further increased sensitivity (Noetzli *et al.*, 2007; Salzmann *et al.*, 2007). This is because north-facing slopes will be subject to stronger shortwave radiation during summer months, increasing their susceptibility to ground-surface temperature changes, increasing thaw depth and subsequent chance of failure (Noetzli *et al.*, 2007; Salzmann *et al.*, 2007). A similar trend of high rockfall incidence at the continuous/discontinuous permafrost boundary has been found in other high mountain areas, e.g., New Zealand and European Alps (Allen, Cox and Owens, 2011; Fischer *et al.*, 2012). This is consistent with the hypothesis that rock-permafrost degradation is the most likely cause of rock slope failures in the region (Coe, Bessette-Kirton and Geertsema, 2018). The predicted increases in atmospheric temperatures over the coming century and subsequent increased permafrost degradation (IPCC, 2019) is expected to weaken slope stability further in GLBA, consequently increasing the size and frequency of RA events.

4.4.4 Glacial sediment budgets and extra-glacial impacts

The 53 % RA number and 19 % RA deposit area underestimation in GLBA, an area where RA activity is well documented, raises questions regarding the completeness of other RA inventories such as those of Uhlmann et al. (2013) and Bessette-Kirton and Coe (2020). If these existing glacial RA inventories, created using manual analysis of satellite imagery, also underestimate RA frequency by over 50 % and RA area by ~20 %, as found in this study, rates of debris supply onto/into glaciers from RAs are likely much higher than previously quantified. If this pattern holds true for other similarly active, high elevation glacial environments with (currently) known RA clusters, for example New Zealand's Southern Alps, parts of the Himalaya, Tien Shan, and Pamir, it would result in significant global underestimates of glacial sediment fluxes from subaerial mass movements. Given that we quantify ~60 % of subaerial supraglacial RAs emplaced above the ELA, much of the sediment flux from RAs will, on deposition/removal from the glacier transport system, be considered part of the glacial sediment flux. Uhlmann et al. (2013) noted the (extreme) sediment yields at Alaskan glacial snouts were an order of magnitude below their quantified longer-term subaerial landslide fluxes; our data indicate that a portion of this ‘glacial’ debris originates from frequent supraglacial landslide additions travelling englacially. Separating out the contribution of subaerial RA to both supraglacial and englacial environments, and establishing if the original RA provenance can be deduced from englacial and emergent debris are key outstanding research challenges. Prior to this, more robust area-volume scaling relationships would be beneficial to move from what can be quantified in 2D imagery to volumetric fluxes.

The fate of this under-estimated debris is also unknown. If high rates of RA sequestration are also found elsewhere in Alaska and in other glaciated regions, we question how much debris is locked up in glaciers and how this will affect proglacial and extraglacial environments in the future. Many large Alaskan glaciers discharge into the ocean, and glacial debris is known to be rich in bioavailable iron (Hawkings *et al.*, 2018). The export of glacial debris to the oceans can have fertilising effects (Raiswell, Benning, Davidson, *et al.*, 2008; Hawkings *et al.*, 2014; Raiswell *et al.*, 2016), so the subaerial glacial contribution to the iron-limited Gulf of Alaska (e.g., Coyle et al. 2019) may be greater than previously believed.

4.5 Conclusion

Our review of an existing glacial rock avalanche (RA) inventory in Glacier Bay National Park & Preserve, Alaska, between 1984 and 2016, with a new semi-automatic detection method (GERALDINE), provides evidence of a large (53 %) underestimation of the number of glacial RAs and RA area (19 %). Of those that were missed, the majority were small RAs that occurred across all elevation bands. RAs did not cluster temporally, as indicated by the previous inventory (Bessette-Kirton and Coe, 2016); instead over the 37-year period we investigated (1984-2020), a background rate of debris was delivered by RAs. This debris delivery did, however, increase substantially between 2012 and 2016, due to three large (> 5 km^2) RAs before returning to pre-2012 levels. Despite GERALDINE allowing the detection of numerous smaller events, these three large events between 2012 and 2016 remained the greatest debris contributors, contributing 44 % of overall debris areal extent. The new inventory identified spatial clustering in the study area, with one ridgeline producing 29 % of all 69 RAs identified. Additionally, slope aspect played a key role in RA occurrence, with 28 % of events occurring on north-facing slopes (340-20°).

In contrast to previous analysis, we find no evidence for an increase in RA mobility over the study period and attribute this to our ability to detect smaller events. Analysis of RA triggering mechanisms indicates rock-permafrost degradation and temperature change to be the key drivers of these slope failures, with close association between the fringes of permafrost favourability and RA source location. In addition, the seasonality of RA occurrence is predominantly limited to the months of May – September. The only months where atmospheric temperatures are above the limit at which most rock-permafrost degradation-induced slope instabilities can be expected within and near the active-layer of the permafrost. The fate of all RA debris is quantified with 58 % of deposits sequestered within two years, and 8 % partially entrained and sequestered, providing the first estimate of RA sequestration rates on glaciers. This has important implications for glacial sedimentary budgets, which may be globally underestimated in areas with highly active slope processes. Here we have corrected what appears to be an areal bias in manual detections by using an automated tool, GERALDINE. This tool is a valuable resource to aid and update our understanding of glacial RAs, their magnitude and frequencies, links to climatic drivers, and their contribution to glacial sediment fluxes past, present, and future. Our updated and expanded inventory showcases how an area known for its high glacial RA activity is even more active than previously realised. It is important to quantify whether this activity is unique to the region, or whether other glacial areas across the world experience similarly high rates of debris delivery from large slope-failures.

Chapter 5 - Supraglacial rock avalanches as a source of Fe for glacial and extraglacial ecosystems: a Lamplugh rock avalanche case study

Chapter 5

This chapter is being prepared for publication.

Authors: William D. Smith[1], Jon Telling[2], Stuart Dunning[1], Neil Ross[1]

1. School of Geography Politics and Sociology, Newcastle University, Newcastle upon Tyne, UK
2. School of Natural and Environmental Sciences, Newcastle University, Newcastle upon Tyne, UK

Citation: Smith, W.D., Telling, J., Dunning, S.A. and Ross, N. Supraglacial rock avalanches as a source of Fe for glacial and extraglacial ecosystems: a Lamplugh rock avalanche case study.: In prep.

Author contributions: William Smith collected the samples, undertook the laboratory and data analysis and wrote the manuscript. Jon Telling provided guidance in the laboratory. Stuart Dunning helped collect the samples. Jon Telling, Stuart Dunning and Neil Ross all contributed and edited the manuscript.

Acknowledgements: The Mount Everest Foundation and the Gino Watkins Memorial fund provided supplementary funding for sample collection.

Abstract

Glaciers and ice sheets play an important role in the production and export of nutrients into extra-glacial ecosystems, but these are assumed to be sourced from snowpacks and supraglacial and subglacial ecosystems. The role of supraglacial debris has been neglected, yet large supraglacial debris inputs, in the form of rock avalanches (RA) are increasing in frequency, due to temperature related destabilisation of slopes. These events deliver vast amounts of freshly pulverised sediment to a glacier surface. Here we assess the ability of the Lamplugh Glacier RA, to deliver iron (Fe) into the glacial domain. RA lithology controls the RA deposit Fe content, and grain size distribution controls the amount of this Fe that is potentially bioavailable Fe (oxyhydr)oxides e.g. ferrihydrite. Finer grain sizes have higher concentrations of bioavailable Fe, and we postulate that this finer fraction is potentially lost immediately after deposition, due to flushing of this fine fraction into the glacier hydrological system by frictionally-produced meltwater. This interaction with frictionally-produced meltwater also likely depletes bioavailable Fe stocks, due to its pH being conducive to dissolution of ferrihydrite. Over time this finer fraction is further depleted by aeolian erosion and 'sieving' of the debris during remobilisation. In conjunction, results show that depletion of bioavailable Fe similarly occurs over time, as the debris is passively transported supraglacially, ageing into more stable, aged, crystalline forms of Fe i.e. goethite and hematite. Although total Fe concentrations for the Lamplugh RA were similar to previously recorded glacial ice and aeolian dust rates, the amount of this Fe that is extractable is low. However, our samples have not yet undergone similar modification and transportation, which are likely important mechanisms determining Fe speciation. Overall, in 2018, two years after RA debris deposition, we estimate the Lamplugh RA contained 0.034 ± 0.012 Gg of potentially bioavailable Fe. This will gradually decrease over time into less bioavailable forms during passive supraglacial transportation, until export in ~100 years. With glacial RAs increasing in size and frequency in Alaska, they may become an increasingly important component of glacial Fe cycling.

5.1 Introduction

Glaciers and ice sheets are biogeochemical reactors that create, transport and export nutrients (Hodson *et al.*, 2008, 2015; Sharp and Tranter, 2017; Hopwood *et al.*, 2020). The majority of these biogeochemical processes occur in the supraglacial and subglacial domains (Hodson *et al.*, 2008; Wadham *et al.*, 2010), the products of which are exported into extraglacial environments (e.g. Raiswell *et al.*, 2008; Hopwood *et al.*, 2014; Hawkings *et al.*, 2015, 2018). Reactions between glacial meltwaters and finely ground rock flour release phases of bioavailable nutrients from bedrock (Wadham *et al.*, 2019). A number of these products are important for supplying aquatic life with key nutrients such as silica, phosphorous and iron (Fe) (e.g. Hawkings *et al.*, 2014, 2015). Analysis of glacial meltwater chemistry and sediment load, as well as solid ice discharge have therefore received increasing attention over the last decade due to climate driven increases in meltwater discharge (Raiswell *et al.*, 2006, 2016, 2018; Raiswell, Benning, Tranter, *et al.*, 2008; Raiswell, 2011; Bhatia *et al.*, 2013; Death *et al.*, 2014; Hawkings *et al.*, 2014, 2015, 2016, 2017, 2018; Hopwood *et al.*, 2014; Lawson *et al.*, 2014; Wadham *et al.*, 2016, 2019; Meire *et al.*, 2016; Monien *et al.*, 2017).

Fe is a key lithogenic nutrient that is derived from processes occurring in glacial environments (Raiswell *et al.*, 2006; Raiswell, Benning, Tranter, *et al.*, 2008; Bhatia *et al.*, 2013; Death *et al.*, 2014; Monien *et al.*, 2017; Hawkings *et al.*, 2018), and its extraglacial delivery is important despite its very low concentrations, particularly in Antarctica, due to it discharging into the Fe-limited Southern Ocean (Monien *et al.*, 2017). Fe fluxes from ice sheets and glaciers are comparable to fluxes from large rivers (Hawkings *et al.*, 2020). The terrestrial origin of Fe is closely linked to subglacial grinding of bedrock and subsequent rock-water interactions (Hopwood *et al.*, 2014). Principally, Fe is sourced from bedrock by a number of microbially mediated weathering reactions that include silicate dissolution, sulphide oxidation and iron reduction (Tranter *et al.*, 2002; Foreman *et al.*, 2007; Nixon *et al.*, 2017). These reactions also determine its speciation, but determining speciation of dissolved Fe is difficult, so it is often crudely approximated using size fractionation (Hawkings *et al.*, 2014; von der Heyden and Roychoudhury, 2015; Raiswell *et al.*, 2018). This categorises >1.0 µm as particulate, 0.1-1.0 µm as colloidal, and 0.02-0.1 µm as nanoparticulate. The most important of these fractions with regards to bioavailability is the soluble fraction. This fraction is determined as all aqueous Fe, including both ionic species; Fe^{3+} and Fe^{2+}, and all their complexes with organic and inorganic ligands, plus all Fe that passes through a 0.02 µm filter

(Raiswell *et al.*, 2018). However, certain forms of particulate Fe (oxyhydr)oxides such as fresh ferrihydrite have also been shown, experimentally, to be bioavailable (Wells, Zorkin and Lewis, 1983; Rich and Morel, 1990; Kuma and Matsunaga, 1995; Nodwell and Price, 2001). These sediment-bound forms are typically the most abundant (Statham, Skidmore and Tranter, 2008; Hawkings *et al.*, 2014; Hodson *et al.*, 2017; Raiswell *et al.*, 2018). Export of soluble and particulate Fe in meltwater and ice-rafted debris has been found to have fertilising effects in the ocean (e.g. Raiswell, Benning, Tranter, *et al.*, 2008; Death *et al.*, 2014). This is primarily due to the uptake of Fe by phytoplankton in the euphotic zone (e.g. Ducklow, 1999), and this has implications for the glacial carbon cycle (Finkel *et al.*, 2010). However, other marine microbial communities at all depths of the water column also uptake Fe (Tortell *et al.*, 1999), and use it in enzymes and for processes such as photosynthesis (Sunda, Swift and Huntsman, 1991; Timmermans *et al.*, 2001, 2005).

Despite knowing that the majority of bioavailable Fe exported from glacial catchments is sediment-bound (Statham, Skidmore and Tranter, 2008; Hawkings *et al.*, 2014; Hodson *et al.*, 2017; Raiswell *et al.*, 2018), no one has investigated the role of glacial debris cover in Fe budgets, despite debris covers often originating from large slope failures characterised by an abundance of comminuted rock (Deline, 2005, 2009; Diolaiuti *et al.*, 2012; Deline, Hewitt, *et al.*, 2014). Large slope failures in glacial environments are typically rock avalanches (RA); a type of deep-seated bedrock failure with volumes >10^6 m^3, vertical drop heights >1000 m, horizontal travel distances >5 km, and speeds >25 m s^{-1} (Deline, Hewitt, *et al.*, 2014). Smaller, more frequent failures, such as rock falls and topples, also affect glaciers but they are not of sufficient size to induce rapid, large-scale comminution of debris, and do not have such large-scale consequences (Deline, Hewitt, *et al.*, 2014). In glacial environments RA triggers are mainly associated with earthquakes (e.g. Jibson *et al.*, 2006; Jibson, 2013) and warming atmospheric temperatures causing failure associated with the degradation of bedrock permafrost (Gruber, Hoelzle and Haeberli, 2004; Gruber and Haeberli, 2007; Noetzli *et al.*, 2007; Deline, Gruber, *et al.*, 2014; Coe, Bessette-Kirton and Geertsema, 2018; Bessette-Kirton and Coe, 2020). Once a rock mass has failed, gravity rapidly accelerates the detached mass, which then begins to disaggregate through shear, with differential movement of blocks crushing the original rock mass. Further disintegration occurs due to loss of rock mass internal cohesion, creating a ‘granular flow’ (for full review see Knapp and Krautblatter, 2020). Granular flow over glacial ice promotes exceptionally long debris runouts, in comparison to non-glacial counterparts (Sosio *et al.*, 2012). This has been attributed to low-friction (Evans and Clague, 1988), fluidisation of the rock mass akin to a debris flow (McSaveney, 1978), and increased saturation at the base of the flow (Geertsema *et al.*, 2006). Modelling results of the 1964 Sherman Glacier RA suggests ice melting from frictional heating effectively reduced the basal friction angle by 35 % (Sosio *et al.*, 2012), and frictional melting of ice produced melting of 86.2 ± 5.9 kg m^{-2}, equivalent to 9-10 cm of surface lowering (Sosio *et al.*, 2012). This indicates large quantities of meltwater production and interaction during and immediately after RA deposition. Once RA movement terminates, a specific surface morphology becomes apparent. RAs typically have a surface carapace consisting of larger clasts, with a combination of distinct lithological and/or flow bands, clast orientations, clast imbrication (overlapping), collisional features, and a raised distal rim (Deline, Hewitt, *et al.*, 2014) but some are matrix-rich with no clear structure (Delaney and Evans, 2014). Highly fragmented debris with grain sizes <1 μm is found beneath this carapace (McSaveney and Davies, 2007; Davies and McSaveney, 2013; Dufresne, 2017). In New Zealand, the grain size distribution of RAs immediately after deposition have been found to be dominated (99.5%) by particles <10 μm (McSaveney and Davies, 2007). However, this varies depending on lithology (Shugar and Clague, 2011), RA volume, and runout (Deline, Hewitt, *et al.*, 2014). It is particularly difficult to quantify grain sizes <10 μm because these very fine particles adhere to the surface of larger grains and aggregate into agglomerates (Reznichenko *et al.*, 2012). Quantifying the volume of all RA debris is important for catchment sediment budgets, but deposition onto ice makes quantification of RA volume difficult due to the loss (scour and ablation), gain and entrainment of ice and snow (Bessette-Kirton, Coe and Zhou, 2018). However, this unique loss and gain of the basal substrate does allow deposit categorisation into detailed zones based on the degree of loss and gain and subsequent debris thickness (Bessette-Kirton, Coe and Zhou, 2018). This method of categorisation typically provides more detail than visual RA deposit inspection (Dufresne *et al.*, 2019).

Export of RA debris has predominantly been investigated in the context of moraine formation (e.g. Alexander, Davies and Shulmeister, 2014), yet these events may play a critical role in the export of fine sediment. Investigation of this fine sediment export may challenge the view that fine glacial sediment is predominantly sourced from subglacial bedrock erosion through crushing and grinding (Deline, Hewitt, *et al.*, 2014). Previous investigation in south-central Alaska determined that sediment yields from supraglacial landslides are an order of magnitude below sediment yields measured at the terminus of some Alaskan glaciers, indicating dominance of subglacial and ice-proximal sources (Uhlmann *et al.*, 2013). However, sediment yields will vary spatially and temporally, and hotspots for supraglacial RAs (Coe, Bessette-Kirton and Geertsema, 2018; Bessette-Kirton and Coe, 2020), will likely contribute a much greater proportion to overall sediment yields. It is also likely that supraglacial RAs are more frequent than previously realised due to under-detection (Smith *et al.*, 2020), and this needs to be considered when evaluating sediment yields from glacial environments.

Evaluating the processes that occur during a supraglacially deposited RA suggests they provide abundant interactions between finely comminuted rock material and meltwater. These are the ideal conditions for the exposure/production and export of Fe into the glacial domain, and subsequently extraglacial environments, where it will have important implications for Fe fluxes and ecosystem productivity. Here we investigate the spatial and temporal variability in Fe content of the largest identified supraglacial RA in the last decade, to determine whether RAs can play a previously unrecognised role in Fe cycling and export in glacial environments.

5.2 Methods

5.2.1 Study area and sample collection

The Lamplugh glacier RA (58°46'57.2"N 136°53'04.0"W) occurred on 28 June 2016, in Glacier Bay National Park and Preserve, Alaska; an area with a history of large slope failures (Coe, Bessette-Kirton and Geertsema, 2018) (Figure 32). It was deposited onto the Lamplugh Glacier, an outlet glacier of the Brady Icefield, that discharges into the West Arm of Glacier Bay. The RA covers approximately 21 km^2 of the Lamplugh glacier, with a length of 10.5 km, and a width of ~3.5 km (Dufresne *et al.*, 2019). Its volume was calculated at 69.9 Mm^3; 51.7 Mm^3 of which was intact rock, with the remaining 13.2 Mm^3 derived from scouring and entrainment of snow and ice (Bessette-Kirton, Coe and Zhou, 2018). Debris thickness ranges from 11.1 m to 2.6 m, varying with each RA zone (Bessette-Kirton, Coe and Zhou, 2018). The RA source area was a north-facing bedrock ridge, on an unnamed peak standing at ~2100 m a.s.l. giving a total descent of 1620 m from source to toe (Dufresne *et al.*, 2019). Geological mapping by Wilson et al. (2015) indicates the source zone is part of the Kelp Bay Group, consisting of phyllite, quartzite, greenschist, greenstone, greywacke, and greywacke semischist. No trigger has been assigned to the failure but recent evidence suggests permafrost degradation in bedrock as a likely pre-conditioning factor, driven by warming atmospheric temperatures in the region (Coe, Bessette-Kirton and Geertsema, 2018).

The mapped RA deposit was categorised into six distinct zones based on depletion or accumulation of material by Bessette-Kirton, Coe and Zhou (2018): source area (zone A), post-event rockfall (zone B), scour (zone C), internal toe (zone D), interior transport zone (zone E), and, distal rim (zone F). We extracted five samples from each of the four accessible main zones (20 samples total): scour (zone C), internal toe (zone D), interior transport zone (zone E) and distal rim (zone F), on 24th and 25th June 2018 (Figure 32 and Figure 33), using a map and compass to navigate to each RA zone (for full fieldwork report see Appendix). We extracted ~500 g of fine (maximum 20 mm diameter grain size) RA material into a sterile 1 L HDPE Nalgene bottle at each sampling location with a plastic trowel, cleaned with glacial meltwater between samples. These samples were then

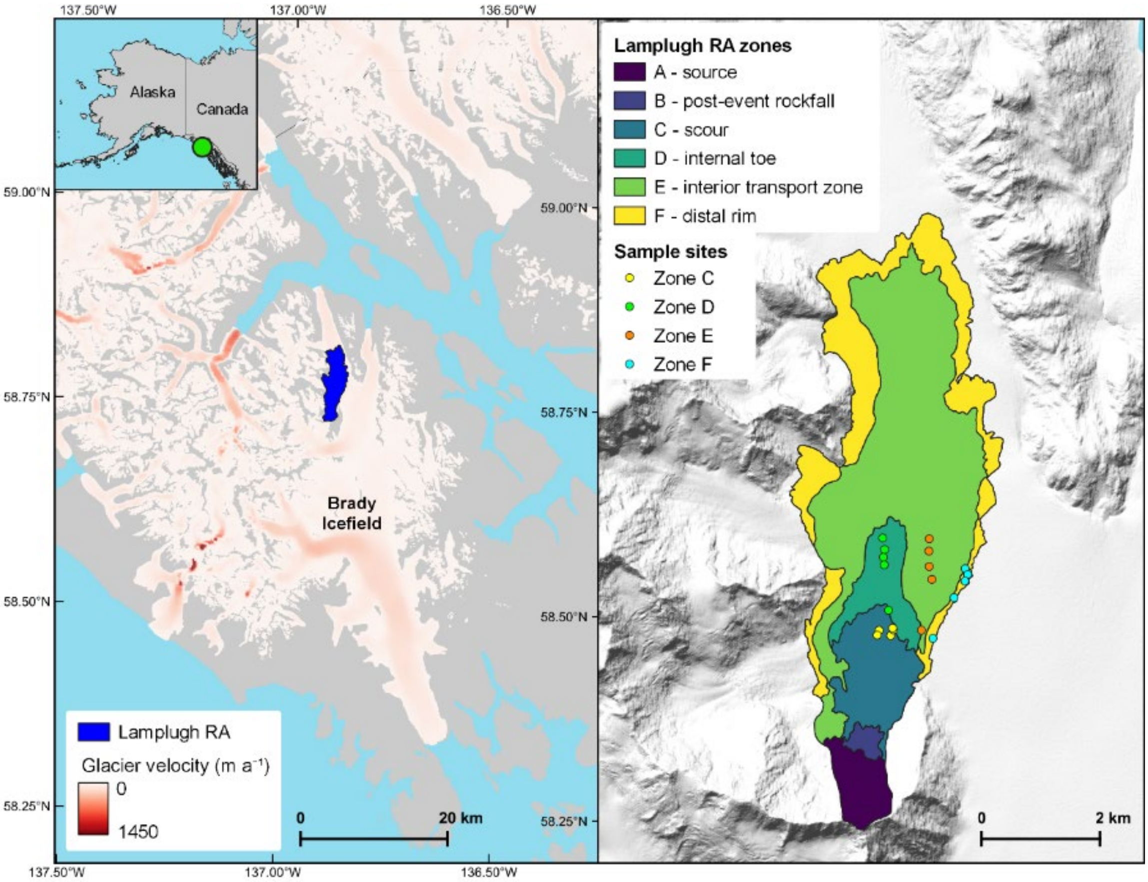

Figure 32: Lamplugh Glacier RA location within Glacier Bay National Park and Preserve, Alaska (left). ITS_LIVE glacier velocity (1985-2019 average) (Gardner et al., 2018, 2019) clipped to the glacier outlines of the Randolph Glacier Inventory v6.0. Inset map depicts the location of the Lamplugh RA (green circle) in Alaska. Lamplugh RA zones as determined by Bessette-Kirton et al. (2018), and the associated sample sites for each zone (right).

frozen until analysis in 2021. Additionally, we collected clasts of representative geology at two locations in each zone. These were stored in sealed plastic bags at room temperature until analysis. A post-sampling re-zoning of the rock avalanche deposit was

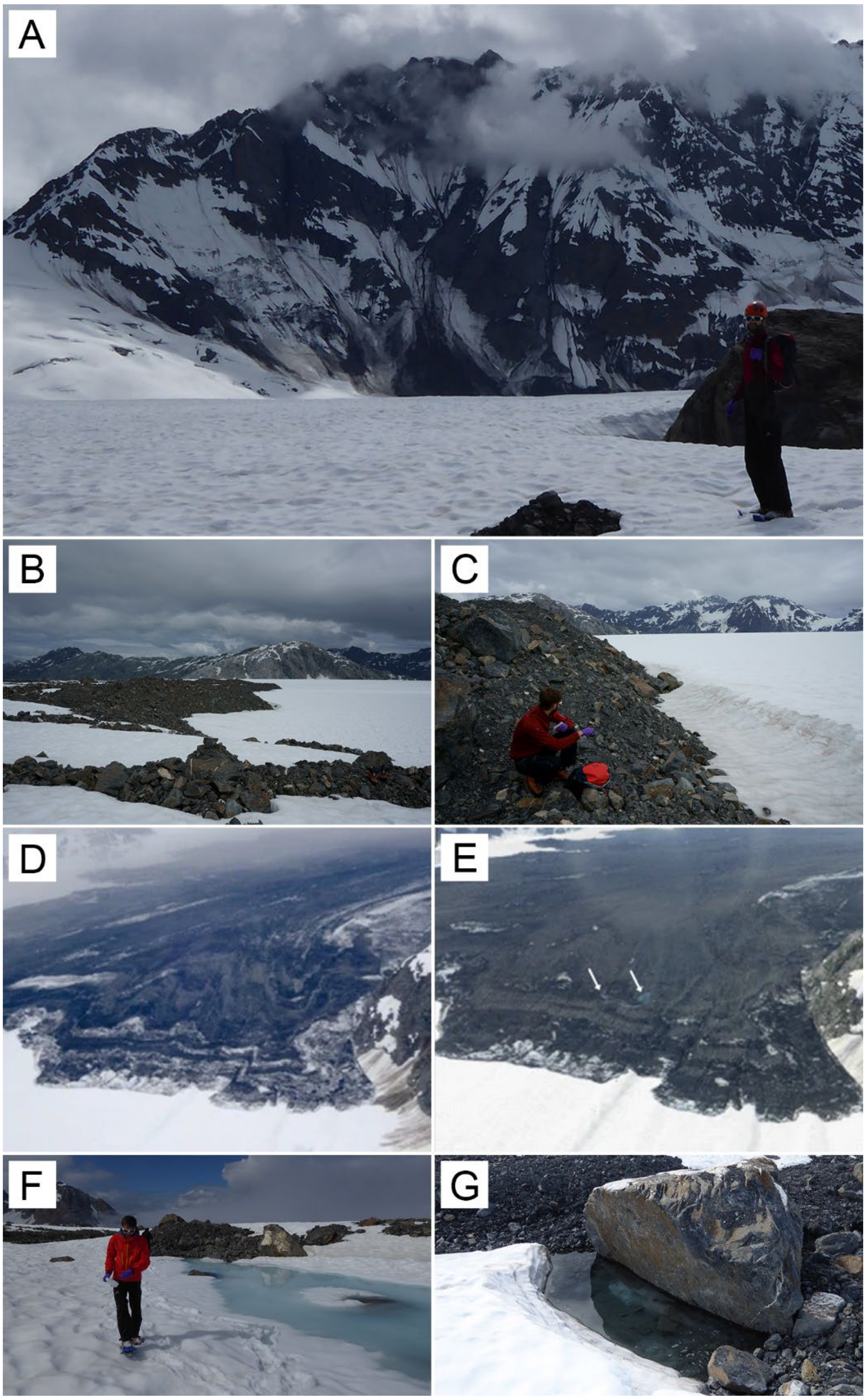

Figure 33: Lamplugh RA A) Source zone, B) and C) Distal rim sampling sites, D) and E) Photos of the distal rim on the day of the event and 6 days later, respectively from Dufresne et al. (2019). Note the melt out of snow/ice and melt ponds (shown by white arrows in E), F) and G) Meltwater ponds during onset of melt season during field season June 2018.

undertaken by Dufresne *et al.* (2019) based on morphology and associated features, reducing the zone count to five: main deposit, raised margin, runup, fallback and the secondary deposit. The main deposit, raised margin and secondary deposit of Dufresne *et al.* (2019) corresponds to the zones sampled in this study.

5.2.2 Clast crushing and grain size distribution

Clasts of representative lithology extracted from the Lamplugh RA deposit enabled us to recreate a 'time zero'. Unlike the finer RA material that we collected, clasts crushed in the laboratory were not subjected to any atmospheric influence, or interaction with snowpack and/or glacial ice melt. The 25 clasts collected contained three lithologies: schist (Sch), greenschist (GSch), and quartz (Q), with schist being dominant (>90 %), and quartz only apparent in small veins. Clasts of each lithology were initially broken into smaller blocks using a hammer, with the hammer head protected by multiple polyethylene bags to prevent any Fe contamination. Smaller blocks were then placed into a Retsch S1 automatic agate ball mill, for two different durations (2 or 30 minutes) to simulate production of different grain sizes, at an intensity of 60 %. Two crushing durations allowed us to assess the influence of grain size on extractable Fe content (see methods section 5.2.3). The crushing process of a ball mill vs a RA contrasts in that a ball mill relies on impact and attrition to crush grains, whereas the dominant comminution method of a RA is shear motion (Knapp and Krautblatter, 2020). This difference in crushing mechanisms means a ball mill cannot replicate a RA in the creation of fine-grained material. Other instruments can better replicate rock shearing processes, such as a ring shear, but they all rely on using metal apparatus which would potentially introduce additional Fe into fine-grained samples, so they were discounted in this study in favour of an agate ball mill. Nevertheless, a ball mill is effective in producing fresh fine material which can be used as a control for fresh RA material.

Grain size distributions of all samples (RA fines and crushed rock) were quantified using laser diffraction on a Mastersizer 3000 (Malvern, UK) with Hydro EV attachment. All samples were sieved through a 1 mm polypropylene sieve, before analysis. Stirrer speed was set to 2470 rpm to prevent sedimentation of suspended particles, and samples were sonicated for 10 seconds before readings were taken to ensure no clumping. A refractive index of 1.555, absorption index of 0.01, and, density of 1 g^{-1} cm^{-3} was used. Five replicates of each sample were used, and five measurements were taken for each replicate. Results were analysed using GRADISTAT v9.1 (Blott and Pye, 2001).

5.2.3 Wet chemical extractions

A sequential ascorbate (FeA) (Raiswell *et al.*, 2010) and dithionite (FeD) (Raiswell, Canfield and Berner, 1994) wet chemical extraction was performed on all samples. This method extracts amorphous and nanoparticulate iron (Fe) (oxyhydr)oxides (e.g. highly reactive ferrihydrite (FeA), that has been shown experimentally to be bioavailable (Wells, Zorkin and Lewis, 1983; Rich and Morel, 1990; Kuma and Matsunaga, 1995; Nodwell and Price, 2001)), and more crystalline (oxyhydr)oxides (i.e. aged ferrihydrite, schwertmannite, lepidocrocite, goethite, and hematite) (FeD). Frozen samples were dried at room temperature for ~2 weeks, sieved through a 1 mm polypropylene sieve, and then 10-40 mg (mean = 30.8 mg) of sieved sample was weighed into a 15 mL centrifuge tube. The FeA extractant was then prepared in bulk using 500 mL deoxygenated DI water and consisting of 0.17 M tri-sodium citrate, 0.6 M sodium bicarbonate, made up to pH 7.5 with ascorbic acid, as per Hawkings *et al.* (2018). 10 mL of FeA extractant was added to each sample. Samples in the FeA matrix were placed horizontal on an orbital shaker and shaken at 300 rpm for 24 hours and then filtered through 0.45 µm sterile mixed cellulose ester membrane filters. The residual sediment was then shaken for two hours in 10 mL of dithionite extractant consisting of 0.29 M sodium dithionite, 0.35 M acetic acid and 0.2 M sodium citrate (Raiswell, Canfield and Berner, 1994), with pH adjusted to pH 4.8 using hydrochloric acid, and then filtered through 0.45 µm mixed cellulose ester membrane filters. The resulting solutions were analysed within 24 hours on an air-acetylene flame Perkin Elmer AAnalyst 400, with matrix matched standards. Blank corrections were negligible.

5.2.4 Total Fe x-ray fluorescence

To analyse the total Fe (TFe) content of each sample we used x-ray fluorescence spectrometry. All 20 RA samples (<1 mm) and five replicates of each of the three crushed lithologies (schist, greenschist and quartz) were run. Homogenous pellets were created by fusing sediment samples with Cereox BM-0002-1 (Fluxana, Germany) binder at a 10:1 sediment to binder ratio. To ensure homogeneity once fine sediment and binder were combined, they were shaken for 15 seconds at a frequency of 25 Hz on a Retsch MM200. Fused sample and binder was pressed into a pellet measuring 32 mm diameter and 2 mm thick, under 9 tonnes of pressure in a manual press. Pellets were run on a SPECTROSCOUT ED-XRF analyser, calibrated using soil samples. The spectrometer underwent periodic 300s iCAL calibrations (Intelligent Calibration Logic) before each batch of samples.

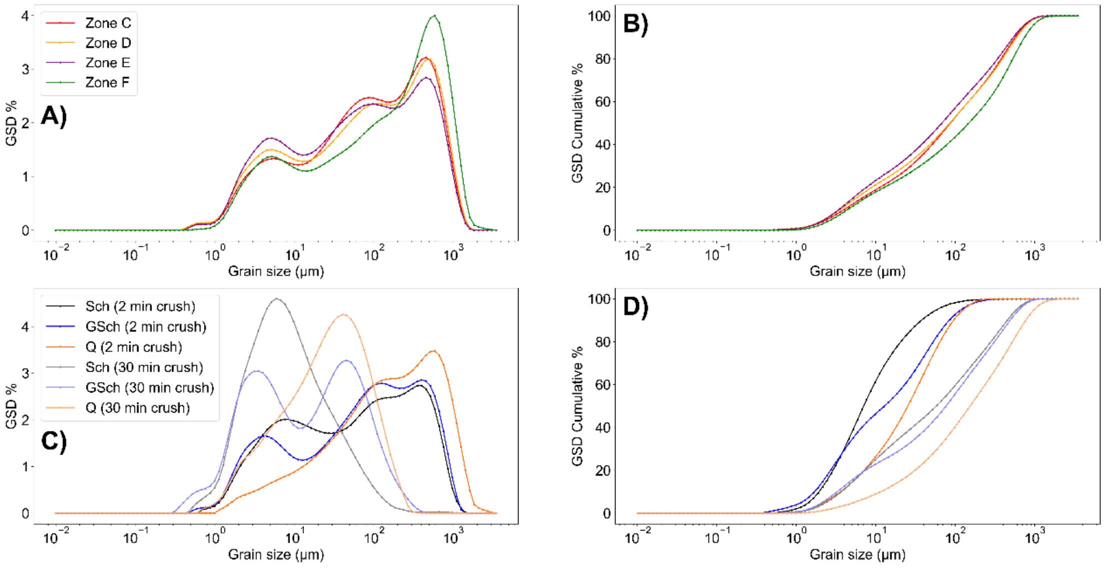

Figure 34: The grain size distributions (<1 mm) and cumulative grain size distributions of Lamplugh RA fines (A and B) and, crushed rock extracted from the Lamplugh RA (C and D).

5.3 Results

5.3.1 Grain size distributions

Analysis of the < 1 mm grain size distribution of Lamplugh RA zonal debris, revealed that all zones shared a similar grain size distribution, with increasing particle size predominantly displaying increasing abundance (Figure 34A). However, small decreases in abundance were seen at grain sizes of 10^1 and 10^2 μm. Zone F was characterised by a higher abundance of larger particles, with grain sizes ~10^3 accounting for 4 % overall, as opposed to ~3 % for all other zones. All zones were composed of very poorly sorted sands (sorting: 4 to 16) (Table S 3). The grain size distributions were polymodal, fine-skewed (skewness: -1.3 to -0.43) and platykurtic (kurtosis: 1.7 to 2.55) (Table S 3).

Crushed rock displayed contrasting grain size distributions to Lamplugh RA fines, which we infer is principally because of different rock crushing mechanisms (ball mill grinding vs. rock avalanche crushing/shearing) (Figure 34). All three lithologies displayed broadly similar grain sizes when crushed for 2 minutes (Figure 34A and Figure 34B), but quartz (Q) was fine-skewed (skewness: -1.3 to -0.43) as opposed to being symmetrical (skewness: -0.43 to 0.43) like schist (Sch) and greenshist (GSch) (Table S 3). Additionally, all samples were very poorly sorted, fine-skewed, except schist, which had a symmetrical distribution (skewness: -0.43 to 0.43), and platykurtic, except quartz, which was mesokurtic (kurtosis: 2.55 to 3.7).

Crushing for 30 minutes produced grain sizes for all rock types with greater variability than those which had undergone 2 minutes of crushing (Figure 34C and Figure 34D). Crushed schist displayed one clear peak, with the maximum percentage of grains found at 6 µm, making up 4.6 % of all grain sizes. Similarly, the grain size distribution of quartz featured a singular peak but at a greater grain size in comparison to schist, with the

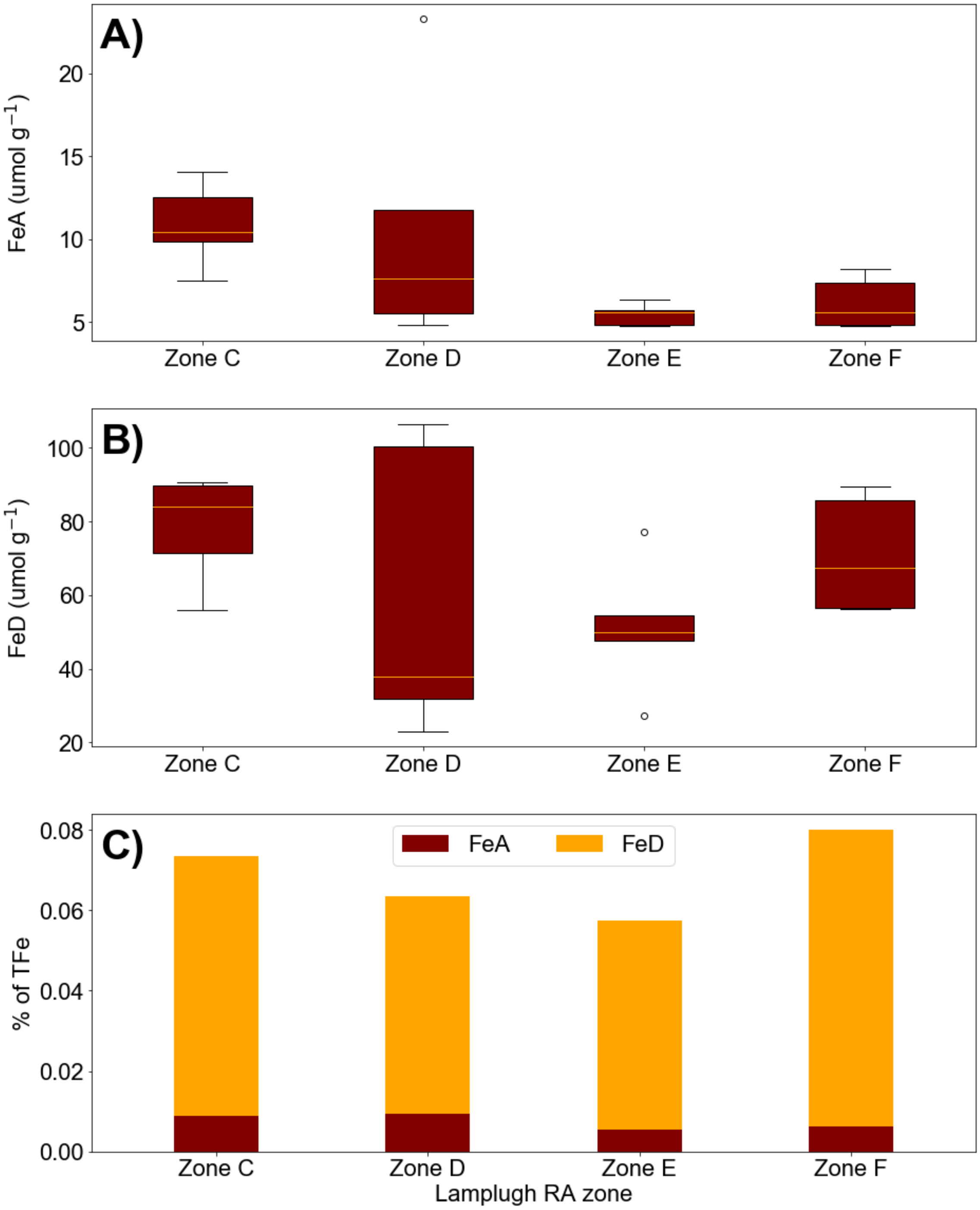

Figure 35: Lamplugh RA fine material (<1 mm) A) extractable FeA, B) extractable FeD, and C) all extractable Fe as a percentage of total Fe, for each sampled RA zone. Boxes represent upper and lower quartile, orange line represents median, whiskers represent the range, and dots represent outliers.

maximum grain size abundance found at 40 μm. The greenschist grain size distribution was characterised by a bimodal distribution, with peaks at 3.5 and 45 μm, and also contained the finest grain sizes of all samples, with particles as small as 0.3 μm. Overall, crushing for 30 minutes produced a larger overall percentage of smaller particles than crushing for 2 minutes (Figure 34D). Samples crushed for 30 minutes were poorly sorted (sorting: 2 to 4), except greenschist, which was very poorly sorted, and distributions were symmetrical, except quartz, which was fine-skewed, and platykurtic, except schist, which was mesokurtic (Table S 3).

5.3.2 Lamplugh RA fines Fe

All zones featured a high concentration of total Fe (Table S 4), however, total Fe was highest at zone C and decreased with distance from the RA source. Between-zone variations in total Fe were found to not be statistically significant ($p = 0.06$) using a one-way ANOVA test. FeA extractable bioavailable ferrihydrite varied across all RA zones (Figure 35A), however, like total Fe, a one-way ANOVA showed no statistically significant variations between zones ($p = 0.1$). Zones C and D were characterised by the highest overall concentrations averaging 10.8 ± 2.5 μmol g^{-1} and 10.6 ± 7.6 μmol g^{-1} respectively. Zone E and F samples were approximately 50 % lower, with average concentrations of 5.4 ± 0.6 μmol g^{-1} and 6.2 ± 1. 6 μmol g^{-1} respectively. FeD extractable Fe was over an order of magnitude greater than minimum FeA concentrations averaging between 51.3 ± 17.8 μmol g^{-1} for zone E and 78.4 ± 14.6 μmol g^{-1} for zone C. Greater variability was also evident across all samples (Figure 35B), however, like total Fe and FeA concentrations a one-way ANOVA showed no statistically significant variations between zones ($p = 0.3$). Neither of the extractable fractions made up a large proportion of the total Fe in samples (Figure 35C), with combined totals of just 0.073 %, 0.063 %, 0.057 %, and 0.08 % for zones C through to F. However, TFe was high for all zones varying between 8.3 % and 4.9 %, with zone averages decreasing with increasing distance from the source from zone C (6.8 %) to zone F (5.39 %) (Table S 4). FeD extractable Fe dominated the ratio of FeA:FeD for all samples, with FeA only making up a maximum of 15% (Figure 35C).

5.3.3 Crushed rock Fe

Crushed rock samples showed an overall clear trend with regards to all extractable Fe (FeA and FeD), with samples that had undergone crushing for longer, and therefore had smaller particle sizes, having larger amounts of extractable Fe (Figure 36). This is likely down to increased surface area from which Fe can be extracted (Horowitz and Elrick, 1987). Greenschist had the highest concentration of FeA extractable Fe, regardless of crushing time and particle size (Figure 36A and Figure 36B). Schist and quartz had lower quantities of FeA than greenschist but their concentrations were similar with averages of 6.1 ± 1.6 and 6.7 ± 2 μmol g^{-1} for samples crushed for 2 minutes, and 18.7 ± 3.4 and 9.5 ± 1.9 μmol g^{-1} for samples crushed for 30 minutes, respectively. FeD extractable Fe showed an identical trend to that of FeA, with greenschist characterised by higher concentrations in comparison to schist and quartz lithologies (Figure 36C and Figure 36D). Extractable Fe as a percentage of overall Fe was low (Figure 36E and Figure 36F), similar to RA fines from different zones (Figure 35C). As a ratio of FeA:FeD it was clear that greenschist, and, to a lesser extent schist samples, are FeD dominated (Figure 35E).

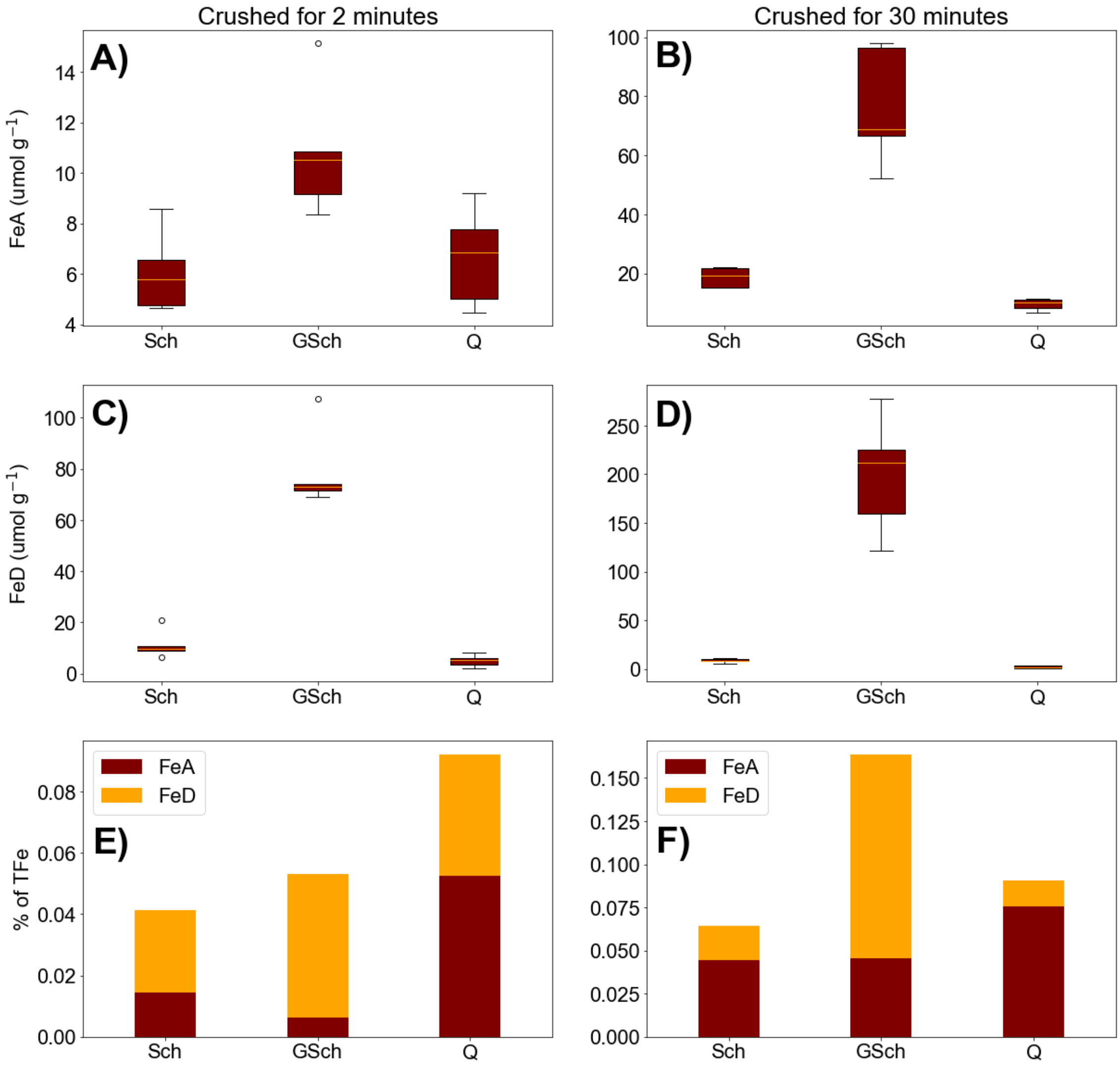

Figure 36: Lamplugh RA crushed clast (<1 mm) extractable FeA, FeD, and extractable Fe as a percentage of total Fe for rocks crushed for 2 minutes (A, C, and D), and 30 minutes (B, D, and F), respectively. Boxes represent upper and lower quartile, orange line represents median, whiskers represent the range, and dots represent outliers.

In contrast, quartz lithology had a higher proportion of FeA extractable Fe as opposed to FeD (Figure 36E and Figure 36F). Although greenschist had higher concentrations of FeA and FeD, it made up a smaller percentage of TFe (Figure 36E and Figure 36F) because stark differences were found for TFe content of crushed rock (Table S 4). Greenschist had the highest overall percentage Fe at 9.4 % weight, and quartz the lowest at 0.7 %, with schist at 2.4 % (Table S 4). In comparison, rock crushed for 30 minutes showed FeA:FeD ratios that were FeA dominated (Figure 36F), excluding greenschist, but FeA made up a larger proportion of TFe overall in comparison to the same lithology crushed for only 2 minutes (Figure 36E). Although the Fe content of greenschist was high relative to the other lithologies (Table S 4, Figure 36E and Figure 36F), its Fe concentration and abundance within the deposit were not high enough to have a disproportionate effect on deposit Fe concentrations.

5.4 Discussion

5.4.1 What processes control the grain size of RA deposits?

Our grain size data for Lamplugh RA fines is in-keeping with other glacial and extraglacial RA deposits (e.g. Deline *et al.*, 2015; Dufresne and Dunning, 2017). Grain sizes did not display large spatial variations, likely due to the RA deposit material being dominated by one lithology (Dufresne *et al.*, 2019). The supraglacial dust deposited by the RA beyond the Lamplugh deposit, is however, much finer, with the 0.63 – 63 μm size fraction dominating (Dufresne *et al.*, 2019). However, this dust disappears through erosion and burial by snowfall soon after RA deposition and this fraction only makes up a small percentage of our grain sizes at <2 %. This raises questions as to why these smaller size fractions are not more dominant in the RA deposit itself, as they were evidently produced during failure and deposition, and our rock crushing proves that Lamplugh lithology will produce these grain size fractions. In addition, Lamplugh is one of the largest recorded glacial RAs, with a drop height of 1617 m, and larger drop heights are negatively correlated with median grain sizes (Locat *et al.*, 2006; Marc, Turowski and Meunier, 2021). The absence of fines may, in part, be due to our sampling bias of the top 10 cm of the deposit, where these finer grains may have been removed either through wind redistribution, or, by what we term 'sieving' of the deposit over time. For glacial deposits this 'sieving' is likely key, and we postulate that it occurs in two main mechanisms: deposit redistribution and flushing. Deposit redistribution may occur through differential melt between the adjacent ice and the RA debris (Reznichenko, Davies and Alexander, 2011), and differential melt within the debris due to varying debris thicknesses (e.g. Reznichenko *et al.*, 2010). This mobilisation of debris has been quantified by studies on debris covered glaciers (Westoby *et al.*, 2020) and is likely to induce size-segregation of particles, where the largest(smallest) grains gradually work themselves towards the top(bottom) of the deposit. This is a well-known phenomenon that is colloquially known as the ‘Brazil nut effect’ (Gajjar *et al.*, 2021). On the other hand, flushing involves repeated loading of the deposit by snow, which then melts and flushes finer RA debris grains through the deposit. This may also occur with precipitation in the summer months and year-round on non-glacial RAs. Additionally, a similar mechanism may occur during supraglacial deposition when meltwater is created, due to friction at the ice-debris interface (Deline, Hewitt, *et al.*, 2014), flushing a substantial portion of RA fines into the hydrologic system. This mechanism may have been unknowingly evidenced by Hewitt (1988) who sampled fine RA material from the Bualtar Glacier RA, finding that all samples contained ‘exotic’ minerals from other lithological bands. This suggests fine material had diffused through the RA deposit. The key to quantifying this process is sampling of RAs immediately after deposition, as was done for the 1991 Mt. Aoraki RA in New Zealand, where 99.5 % of grains were <10 µm (McSaveney and Davies, 2007), and then sampling again on an annual basis, to determine if the fine fraction is depleted over time. To our knowledge the Mt. Aoraki RA is the only glacial RA that has been sampled immediately after deposition; sampling often occurs weeks, months or years after, where this size fraction may have disappeared.

5.4.2 Bioavailable Fe in Lamplugh RA zones

The debris in each zone of the Lamplugh RA has undergone increasing modification and interaction with snow/ice and meltwater, the further away it is from the source. We note that there are no statistically significant differences between zones, but FeA concentrations do decrease with increasing distance from the RA source. The influence of grains sizes can be discounted because all zones had similar grain size distributions. However, RA zones furthest from the source (E and F) were characterised by accumulation and depletion of material (Bessette-Kirton, Coe and Zhou, 2018), and therefore prolonged interaction with snow/ice and frictionally-produced meltwater during deposition (Figure 33D,E). In contrast, the debris in zone C; a scoured zone, and to a lesser extent, zone D, will have undergone relatively minor interaction with snow/ice, as it would have been the last to deposit. Glacial ice meltwater pH (between 6 and 9; Hawkings *et al.*, 2015) correlates well with optimum pH for dissolution of bioavailable ferrihydrite (Yu *et al.*, 1999), suggesting this could be a likely cause of any FeA disparities between zones. Meltwater interaction from seasonal snowmelt (as shown in Figure 33F,G), and precipitation does not seem to have similar capabilities for depleting the debris stocks of FeA or FeD over time, as the difference between the overall percentages of extractable Fe (FeA + FeD) from RA fines and crushed rock is minimal. This may be due to the increased acidity of snowmelt and rainwater, with Alaskan snow pH values varying between 4.5 and 6.8 (Douglas and Sturm, 2004), and the solubility of ferrihydrite decreasing with increasing acidity (Yu *et al.*, 1999). The pH of snow does however, correspond well with dissolution of schwertmannite (Yu *et al.*, 1999); an Fe mineral that is extracted in the FeD stage of extraction. It may well be that this small fraction of extractable schwertmannite (Raiswell *et al.*, 2010) is slowly depleted every year through snowmelt. However, the aging of fresh ferrihydrite (FeA) into more stable, aged, crystalline minerals i.e. hematite and goethite over time (Schwertmann and Taylor, 1972; Schwertmann and Fischer, 1973; Cornell and Schwertmann, 2003; Raiswell *et al.*, 2018) more than compensates for its removal.

Comparison between FeA and FeD data for RA fines and for freshly crushed rock did reveal changes to the bioavailability of Fe over time. The FeA:FeD ratio in RA fines is characterised by a lower proportion of FeA, making up between 8 and 15 % of extractable Fe, whereas, for crushed rock this varies between 12 and 83 %. This is also likely to result from the aging of fresh ferrihydrite (FeA) into more stable, aged, crystalline minerals (Schwertmann and Taylor, 1972; Schwertmann and Fischer, 1973; Cornell and Schwertmann, 2003; Raiswell *et al.*, 2018) and can be accelerated by weathering (Waychunas, Kim and Banfield, 2005). However, aging is slower at lower temperatures (Shaw *et al.*, 2005; Yee *et al.*, 2006), potentially prolonging the bioavailability of RA debris on glacier surfaces, in comparison to RAs in temperate environments. The RA deposit is also covered for more than six months of the year by snow, slowing this aging process but also slowing any weathering reactions. These FeA:FeD ratios also indicate that finer grain sizes increase the amount of extractable ferrihydrite that is potentially bioavailable, similar to findings from glacial flour (Hopwood *et al.*, 2014). Therefore, a RA characterised by finer grain sizes, due to either lithology or failure and flow mechanisms, will theoretically have a higher concentration of bioavailable FeA. If as suggested above, a RA loses its finer debris fraction soon after deposition, this could result in an initial pulse of fine-grained sediment, with high Fe bioavailability into the hydrological system during and immediately after RA emplacement. Fe quantities will, however, be determined by lithology, with pyrite-rich rocks being key to the production of potentially bioavailable ferrihydrite, due to pyrite oxidation (Raiswell *et al.*, 2018).

5.4.3 Comparison of the Lamplugh RA deposit with other glacial Fe sources

Lamplugh RA fines were approximately two orders of magnitude lower than average iceberg, glacial ice and atmospheric dust values collated by Raiswell *et al.* (2016), for FeA and FeD as a percentage of weight (Table 2). Additionally, the total amount of extractable Fe from Lamplugh RA fines, as a percentage of total Fe, was similarly between two or three orders of magnitude lower than that of iceberg, glacial ice and atmospheric dust values. Breaking this down and comparing to samples used to create these averages and the Lamplugh RA fines had a similar total Fe percentage as glacial flours from Greenland, Norway, the Alps and Antarctica (Hopwood *et al.*, 2014). The percentage of Lamplugh TFe that was extractable Fe (oxyhydr)oxides was, however, two orders of magnitude lower than glacially produced flours despite the samples from Antarctica having a similar lithology (Hopwood *et al.*, 2014). The size fraction used for glacial flour was <63 µm (Hopwood *et al.*, 2014), in comparison to our <1 mm size fraction, and we know from our rock crushing data and extractions that finer size fractions have more extractable Fe (Figure 35). FeA concentration was inversely correlated to size fraction in our study, similar to glacial flours (Hopwood *et al.*, 2014). However, the FeD content of glacial flours was found to not change with flour grain size fraction (Hopwood *et al.*, 2014), yet we find this depends on lithology, with smaller size fractions decreasing extractable FeD for schist and quartz. In contrast, for greenschist the smaller size fractions increase extractable FeD. In addition, to the data from Raiswell *et al.* (2016) (Table 2), Raiswell *et al.* (2018) added further samples to the averages and included meltwater samples, however, our Lamplugh RA data is still approximately two orders of magnitude lower than these averages as a percentage of sediment dry weight (wt. %). Multiple different factors are likely the cause of this, particularly the lithology of local bedrock and the conditions that the sediment is subjected to. Our results from rock crushing indicate none of the lithologies that make up the Lamplugh RA deposit have a high percentage of extractable Fe, in comparison to other quantified sources. Rocks with a low pyrite content are often cited as reasons for low amounts of ferrihydrite, due to a lack of pyrite available for oxidation (Raiswell *et al.*, 2018). We note that our samples were collected and frozen until analysis and freezing of samples causes the formation of aggregates which makes it difficult for ascorbate to penetrate the matrix, slowing down dissolution and impeding extractions (Raiswell *et al.*, 2010). De-watering of samples can also impede extractions due to aggregation promotion (Raiswell *et al.*, 2010) and samples will have undergone multiple wetting/drying cycles on the surface. Our results may therefore be underestimates of bioavailable Fe in the Lamplugh RA deposit. They do, however, correspond well with our crushed rock samples, which were not stored frozen.

Deposition of RA debris on a glacier surface is just the beginning of the debris journey. Once deposited, RA debris will be subjected to physical, biological, and chemical weathering. In the supraglacial, englacial and subglacial environment, the rates of these will vary depending on the pathway of the debris. For example, debris within ice can undergo freeze-thaw cycles that concentrate ions, facilitating dissolution of Fe (oxyhydr)oxides, and then (re)precipitate these oxides (Raiswell *et al.*, 2018); UV radiation can reduce Fe (oxyhydr)oxides in ice-hosted sediments (Kim *et al.*, 2010); and subglacial environments host Fe reducing bacteria (Nixon *et al.*, 2017). All these processes may facilitate concentration of bioavailable Fe (oxyhydr)oxides, resulting in greater amounts of FeA during export from the glacial system.

5.4.4 Deposit Fe contribution

The source of the Lamplugh RA has been calculated as failure of 51.7 Mm^3 of material (Bessette-Kirton, Coe and Zhou, 2018). We convert this to weight using the average density of the dominant RA lithology (schist) (see Chapter S3 section 3.1), giving a total RA weight of 146.3 ± 4.2 Gg. For the purposes of calculating overall Fe content, the fine fraction (<1 mm) is the most important, and by number is the most abundant (McSaveney and Davies, 2007). However, for glacial RA deposits this fine fraction by volume accounts for a maximum of 50 % (Hewitt, 2002a). Assuming 50 % of deposit weight (73.15 Gg) and the average RA deposit FeA concentration from all zones (8.26 μmol g^{-1}), our results show that when our samples were extracted in 2018, the Lamplugh RA

Table 2: Composition of Lamplugh RA zone and crushed rock samples, in comparison to icebergs, glacial ice and atmospheric dust from Raiswell et al. (2016). Number of samples in brackets.

	wt% FeA			wt% FeD			(FeA + FeD) / FeT	
Sample	Low	Mean	High	Low	Mean	High	Low	High
Zone C (5)	0.0004	0.0006	0.0008	0.0031	0.0044	0.0051	0.0005	0.0009
Zone D (5)	0.0003	0.0006	0.0013	0.0013	0.0033	0.0059	0.0003	0.0012
Zone E (5)	0.0003	0.0003	0.0004	0.0015	0.0029	0.0043	0.0003	0.0008
Zone F (5)	0.0003	0.0003	0.0005	0.0031	0.0040	0.0050	0.0006	0.0010
Sch2 (5)	0.0003	0.0003	0.0005	0.0004	0.0006	0.0012	0.0003	0.0007
GSch2 (5)	0.0005	0.0006	0.0008	0.0039	0.0044	0.0060	0.0005	0.0007
Q2 (5)	0.0002	0.0004	0.0005	0.0001	0.0003	0.0004	0.0005	0.0014
Sch30 (5)	0.0008	0.0010	0.0012	0.0003	0.0005	0.0006	0.0005	0.0008
GSch30 (5)	0.0029	0.0043	0.0055	0.0068	0.0111	0.0155	0.0010	0.0022
Q30 (5)	0.0004	0.0005	0.0006	0.0001	0.0001	0.0002	0.0006	0.0012
Icebergs (51)	0.03	0.076	0.194	0.2	0.377	0.715	0.0630	0.201
Glacial ice (16)	0.015	0.03	0.06	0.042	0.091	0.196	0.0130	0.059
Atmospheric dust (15)	0.018	0.038	0.081	0.428	0.868	1.76	0.2400	0.52

deposit stored 0.034 ± 0.012 Gg of potentially bioavailable ferrihydrite, and 0.266 ± 0.09 Gg of more crystalline Fe (oxyhydr)oxides. The assumption that 50 % of the RA deposit weight is fine-grained is at the maximum end of the spectrum, however, we argue that every RA is unique in the number of fines that are produced, so any value used would be an assumption. Here we want to explore the maximum potential impact of a glacial RA. The amount of fine material in a RA deposit would be dynamic over time, with aeolian and hydraulic erosion removing fine particles but also breaking down larger clasts and creating new particles, in combination with other processes such as frost-shattering. It is unlikely that any RA deposit has had its fine fraction accurately quantified due to these processes, plus measuring techniques often rely on point-sampling, which is unrepresentative of an entire RA deposits sedimentological makeup. In addition, the fine fraction is likely to be sieved to the base of the RA, as indicated by the ‘exotic’ fines in the lithological bands of the Bualtar Glacier RAs (Hewitt, 1988), which would cause underestimation from point-sampling strategies that do not sample the entire vertical RA deposit profile (see section 2.7.3 for further discussion). Furthermore, although the fines are the predominant source of FeA, there will still be an abundance of FeA locked up in the larger clasts, yet their smaller surface area in comparison to an assortment of fines with the same mass, inhibits its release. Although this estimate of bioavailable Fe is towards the maximum end of the spectrum, to put it in context, 1778 Lamplugh RAs would be needed per year to equal the lower bound of bioavailable Fe export from Antarctica (0.06 Tg - Hawkings *et al.*, 2014). Substituting in the FeA concentrations from the crushed rock data indicates that if the RA was made up entirely of fine-grained greenschist, then the deposit could store 0.312 Gg of ferrihydrite. In contrast, if the deposit was made up entirely of schist comminuted to larger grain sizes, it could store just 0.024 Gg.

5.4.5 Transport to the extraglacial environment

The fine-grained fraction of the RA deposit that is potentially flushed into the glacier after RA deposition, may increase the bioavailable Fe content of nutrient-poor glacial meltwater. This will, however, be dependent on the ferrihydrite staying in its bioavailable form during transportation. In an idealised world this meltwater would be unimpeded on its journey through/beneath the glacier and exported within hours or days into the extraglacial environment. This rapid export of highly comminuted RA fine material would be the most important contribution of a supraglacially deposited RA to Fe budgets extraglacially. However, the hydrology of each individual glacier is unique and has its own associated lag times between meltwater input and output, often depending on the seasonality of the drainage system, the presence of any hydraulically isolated zones (Seaberg *et al.*, 1988; Willis, Sharp and Richards, 1990; Mair *et al.*, 2002; Cowton *et al.*, 2013; Miles *et al.*, 2019), and the basal substrate (Hart *et al.*, 2022). In winter the drainage system is inefficient with high water pressures, resulting in prolonged residence times of meltwater at the bed and low surface velocities (e.g. Rada and Schoof, 2018). In spring, during the onset of the melt season, the increased meltwater input leads to higher water pressures and subsequently increased surface velocities (e.g. Bartholomew *et al.*, 2011), whereas in summer, the water pressure subsides due to the evolution of a more efficient channelised drainage system, resulting in lower velocities once more. The time of year that a RA is deposited will therefore influence the export time of the initial sediment-rich meltwater pulse. If the pulse occurs in winter, its export time will be prolonged and diffuse, but throughout summer it will be fast. Any pulse that occurs during the onset of the ablation season may be delayed but once an efficient drainage system has developed it will be rapidly exported. However, the pulse may be indistinguishable from the seasonal meltwater peak that occurs during this time (e.g. Crumley *et al.*, 2019). In addition, during meltwater transport through the glaciers hydrological system, the sediment may fall out of suspension and be incorporated into basal tills and other sedimentary landforms (see section 2.8). In this case only the soluble Fe will be transported into the extraglacial environment. Yet it is possible that storage at the bed could increase the bioavailability of Fe released from RA debris due to a number of subglacial microbially mediated weathering reactions (Tranter *et al.*, 2002; Foreman *et al.*, 2007; Nixon *et al.*, 2017).

In areas that experience frequent supraglacial RAs, such as south-east Alaska (Coe, Bessette-Kirton and Geertsema, 2018; Bessette-Kirton and Coe, 2020), ‘pulses’ may occur on a sub-annual basis, yet it is unknown what percentage of this Fe could be attributed to overall glacial Fe export and its importance in the extraglacial environment; in this case the Gulf of Alaska. Soluble Fe is the most bioavailable form, but the particulate form is also important where communities are Fe limited (see Chapter 2, section 2.11). If a sediment-rich meltwater plume occurred at a glacier terminus (originating from a RA meltwater pulse), within a short time period after RA deposition, this would have fertilising effects. However, the utilisation of this Fe may be impeded by the sediment reducing the photic depth due to shading, reducing primary production (Sommaruga, 2014; Reisdorph and Mathis, 2015; Barouillet *et al.*, 2019). In Glacier Bay National Park and Preserve this has previously been attributed as a cause of low primary productivity (Reisdorph and Mathis, 2015). Therefore, ‘pulses’ of RA fines rich in bioavailable Fe may actually inhibit its utilisation by marine organisms. This is dependent on the efficiency of glacier hydrology and subsequent meltwater evacuation times. In Alaska, the majority of RA events occur in summer months (Bessette-Kirton and Coe, 2020 and Chapter 4), where supraglacial drainage is at its most efficient (Irvine-Fynn *et al.*, 2011), so export of sediment in RA meltwater ‘pulses’ will likely be rapid, which could inhibit Fe utilisation due to this shading effect. Although, as found in Chapter 4, a number of RAs occur at high altitudes, in the accumulation zone of glaciers. In this zone, meltwater transport to the subglacial environment is slow, often percolating through the snow pack, where it can refreeze if temperatures allow (Pfeffer, Meier and Illangasekare, 1991; Van Pelt, Pohjola and Reijmer, 2016). Meltwater that does not refreeze travels slowly through fractures and englacial conduits (which can collapse due to ice creep) before it reaches the subglacial drainage system (Gulley, Benn, Müller, *et al.*, 2009; Gulley, Benn, Screaton, *et al.*, 2009). Additionally, meltwater created at high altitudes has further to travel before it is exported, therefore increasing its chance of storage and the deposition of suspended sediment. In the case of the Lamplugh RA studied here, it ran out over, and was deposited on the ablation zone of the Lamplugh Glacier, entraining 13.2 Mm^3 of snow and ice (Bessette-Kirton, Coe and Zhou, 2018). Its deposition also occurred in late June (28th) 2016, so an efficient subglacial drainage system should have developed beneath the Lamplugh Glacier, as hydrographs of GLBA indicate (Crumley *et al.*, 2019). These conditions are ideal for rapid export of a sediment-rich meltwater pulse of bioavailable Fe into the John Hopkins Inlet of GLBA.

After the initial deposition and meltwater pulse, the RA deposit will remain in the glacial domain for a number of years while undergoing down-glacier transport either englacially (if deposited in the accumulation zone) or supraglacially (if deposited in the ablation zone, like the Lamplugh RA) (see Chapter 2 section 2.8). Export of the finer debris fraction may occur during this passive down-glacier transportation, by entrainment in meltwater, particularly from the seasonal melting of snow on the deposit (see section 5.4.1). Gradual export of this finer debris fraction would prevent reductions in photic depths, unlike ‘pulses’ of sediment after RA deposition but debris quantities are likely small, so their effect would be minimal. In addition, the aging of ferrihydrite will decrease the quantities of bioavailable Fe within this fine debris fraction over time. Eventually, any debris that has remained within the glacial domain during down-glacier transportation will reach the glacier terminus and will gradually be deposited into the extraglacial environment. Based on the Lamplugh RA deposit toe being ~8527 m from the Lamplugh glacier terminus after deposition in June 2016 and a glacier centreline velocity of 87 m a^{-1} (Gardner *et al.*, 2018, 2019), we estimate that the debris passively rafted supraglacially would take 98 years before it begins to be exported into the ocean. This does not account for terminus retreat and velocity changes as a result of thinning and/or retreat, as is evident in Glacier Bay National Park and Preserve since the Little Ice Age ~250 years ago (Larsen *et al.*, 2005; Mann and Streveler, 2008; Gaglioti *et al.*, 2019). In this time any fresh ferrihydrite (FeA) that was created during deposition will have undergone aging and stabilised into more crystalline forms that are not known to be bioavailable (Schwertmann and Taylor, 1972; Schwertmann and Fischer, 1973; Cornell and Schwertmann, 2003; Raiswell *et al.*, 2018). Export of this aged, crystalline Fe to the ocean is unlikely to have any 'fertilisation' effects on marine life, principally because the majority of debris will immediately sink to greater depths. However, any buoyant fine debris that has evaded prior export and is rich in aged, crystalline Fe (oxyhydr)oxides may become bioavailable once exposed to UV radiation, as this can increase the bioavailability of both crystalline and non-crystalline Fe (oxyhydr)oxides in seawater (Wells and Mayer, 1991). If the RA was deposited in the accumulation zone of a glacier and the debris had travelled englacially throughout the entirety of its down-glacier transport, this frozen englacial storage could potentially freeze the Fe in its bioavailable ferrihydrite form (Shaw *et al.*, 2005; Yee *et al.*, 2006). This could result in the export of a pulse of bioavailable Fe, years, decades, or even centuries after RA deposition.

In addition to glacial export, it is well known that oceans are fertilised by Fe sourced from dust that has been transported over vast distances (e.g. Crusius *et al.*, 2011). Exposure of fresh glacial sediment due to glacier retreat will lead to increases in dust storms and sediment yields from these environments, with far greater spatial range than nutrients transported through glacial meltwater discharge (Crusius *et al.*, 2011; Prospero, Bullard and Hodgkins, 2012; Bullard, 2013). A RA can deposit dust over ranges >100 km^2 during deposition (Gordon, Birnie and Timmis, 1978), and once emplaced may act as a dust source. Their role in creating and storing fine dust, which subsequently gets redistributed through aeolian processes, may therefore be more valuable than their inputs into the glacial hydrologic system. This would allow export of dust further afield, particularly into Fe-limited high-nutrient low-chlorophyll areas that glacial meltwater cannot directly impact. It is known from Dufresne *et al.* (2019) that the Lamplugh RA produced a considerable amount of very fine dust, that was quickly eroded, and this may have been transported into the Fe-limited Gulf of Alaska (Martin and Fitzwater, 1988; Boyd *et al.*, 2004). However, the low concentrations of bioavailable Fe we measure from the Lamplugh RA in comparison to atmospheric dust (Table 1) are likely to have negligible affects.

In Glacier Bay National Park and Preserve, at least one RA has occurred in 24 of the last 33 years, with frequency seemingly increasing over the last decade (see Chapter 4). This delivers a consistent point-source supply of highly comminuted debris into the glacial domain, which these results show will also deliver a supply of bioavailable Fe. This input of Fe has not previously been quantified and may provide an important delivery of a limiting nutrient to the glacial ecosystem and beyond (Hodson *et al.*, 2008; Anesio *et al.*, 2017). In addition, there is widespread lithologic variation across the park (Wilson *et al.,* 2015), some of which may be more conducive to higher quantities of extractable bioavailable Fe than measured in the Lamplugh RA. The majority of this debris is transported straight to the ocean, owing to the dominance of marine-terminating glaciers. However, as glaciers retreat in the area due to climate warming, proglacial lakes and forefields are becoming larger (Pelto *et al.*, 2013), potentially increasing the lag time between RA events and export of Fe to the ocean. Although Fe input into the ocean has been known to 'fertilise' marine ecosystems (e.g. Boyd *et al.*, 2007; Blain, Sarthou and Laan, 2008) the processes of aquatic life consumption are highly complex (see Hopwood *et al.*, 2020 for full review). Export of meltwater and debris into the ocean vs proglacial lakes and streams will have important implications for Fe speciation and bioavailability, as they are all characterised by unique biogeochemistry both spatially and temporally (Hodson, Mumford and Lister, 2004; Hood and Scott, 2008; Hood and Berner, 2009; Pierre *et al.*, 2019; Hopwood *et al.*, 2020). Increases in RA frequencies, coupled with glacial retreat in the area, are therefore likely to change the flux and chemical nature of Fe loads in these extraglacial environments, which will have important consequences for marine and freshwater ecosystems (Schroth *et al.*, 2011).

5.5 Conclusion

We present the first data investigating the Fe content of the largest supraglacial rock avalanche (RA) to have occurred in Alaska over the last decade. We find that deposit lithology and grain size distribution is a key determinant of Fe quantities, with an inverse relationship evident between grain size and quantity of potentially bioavailable Fe (oxyhydr)oxides. However, we theorise that the finest fraction is lost immediately after deposition, due to 'sieving' of the fine material through flushing by frictionally-produced meltwater during deposition, or debris redistribution during settling and shortly after deposition. In addition, we postulate that this interaction with frictionally-produced meltwater may deplete RA debris bioavailable Fe stocks. Debris in zones that have had prolonged interaction with frictionally-produced meltwater, had a lower concentration of potentially bioavailable Fe, although between-zone variations were not statistically significant. Initial deposition is likely to have the largest effect on export of potentially bioavailable Fe in both soluble and particulate forms, as we found no evidence to suggest depletion of Fe through gradual dissolution over time, only through its transformation into more stable, aged species that are not currently known to be bioavailable. The bioavailable Fe content of the Lamplugh RA is two orders of magnitude lower than those recorded from other glacial sources and aeolian dust. However, RA debris has not yet undergone the biogeochemical transformations that other quantified glacial sources have undergone in the subglacial environment. Overall, we calculate the Lamplugh RA deposit in 2018 contained approximately 0.034 ± 0.012 Gg of potentially bioavailable Fe. This will gradually deplete over time, due to aging into less-bioavailable forms during its supraglacial transport down-glacier, until it begins to be deposited into the extraglacial environment in ~100 years. RAs sourced from areas with Fe-rich lithology can deliver larger amounts of bioavailable Fe. The increasing frequency of large RAs due to warming atmospheric temperatures and the degradation of permafrost, may require re-evaluation of Fe fluxes in high relief maritime-proximal glacial environments

Chapter 6 - Discussion

In this chapter, the implications of all results chapters will be discussed and brought together to form a conceptual model of glacial rock avalanche (RA) Fe export. To summarise the results chapters: Chapter 3 satisfies Objective 1 and describes the free-to-use GERALDINE tool (Smith *et al.*, 2020), created to aid the detection of these events, using the entirety of the Landsat data archive. Chapter 4 satisfies Objective 2 and applies this tool to Glacier Bay National Park (GLBA), Alaska and finds that even in an area that has been studied extensively, the frequency and magnitudes of these events have been underestimated. The updated RA inventory created in Chapter 4 is the best currently available dataset of aseismic background RA rates, so climatic drivers are explored, with a key driver of these events likely to be rock-permafrost degradation. RAs are clustered spatially, with certain peaks and ridges failing multiple times. They also clustered temporally, occurring mainly between May and September when air temperatures were high enough to initiate rock-permafrost degradation mechanisms. Overall, they supplied a chronic background rate of sediment into the glacial domain, with only one multi-year period without any recorded RA events. Additionally, the majority (58%) of these RA deposits were sequestered/entrained into the ice within two years, suggesting glaciers in the region store a substantial quantity of debris. This stored RA debris is likely wrongly-attributed to other erosional processes after export to the ocean. Chapter 5 satisfies Objective 3 and uses samples from the largest RA to have occurred in GLBA; the Lamplugh RA, which occurred in June 2016, to assess the ability of these events to deliver Fe into the glacial environment. While the majority of this Fe is not in a form that is readily bioavailable, as it has aged into a more crystalline form between deposition and sampling in 2018, it was estimated to still contain 34 tonnes of bioavailable Fe. The pathway and time scales over which this Fe is exported are, however, currently unknown. Here, a conceptual model is proposed outlining and discussing how this Fe from RAs is exported into the extraglacial environment. Following this, key outstanding research questions are posed, and, ways to test them and validate/refute the working conceptual model are given.

6.1 RA Fe delivery, transport and export

6.1.1 Rock-slope detachment, disintegration and flow

As soon as a rock slope fails above a glacier, the Fe journey begins. The failure and detachment of a large mass from a rock slope rapidly descends under the force of gravity, while at the same time fragmenting from an intact (joint defined) rock mass, to multiple smaller blocks, to fine grained particles, due to a number of different processes that occur between detachment and deposition (for full review see Knapp and Krautblatter, 2020). The finer the material, the greater the availability of Fe, due to the creation of new particle surface area. The disintegration of material creates a granular flow, that can travel exceptionally long distances on glaciers (Sosio *et al.*, 2012) and entrain large quantities of snow and ice (e.g. Bessette-Kirton, Coe and Zhou, 2018; Dufresne *et al.*, 2019). Modelling shows the friction between the flow and the ice/snow creates an abundance (70 - 90 kg m^{-2}) of frictionally-produced meltwater (Sosio *et al.*, 2012; De Blasio, 2014). This meltwater is hypothesised to interact with the freshly comminuted sediment, causing dissolution of bioavailable Fe, and is likely to become saturated with the fine debris particles carried at the base of the flow. During transportation and after flow termination, it is likely this sediment-laden meltwater rich in bioavailable Fe will drain in the most efficient way; through moulins and crevasses (Figure 37; RA 1 and RA 2). However, it may also percolate through the snow/ice (Figure 37; RA 1) or the weathering crust (Cook, Hodson and Irvine-Fynn, 2016; Samimi and Marshall, 2017). Results from chapter 5 show that fresh material has the highest concentration of bioavailable Fe (ferrihydrite), therefore, this sediment-laden meltwater rich in bioavailable Fe, is theorised as the largest and most significant pulse of bioavailable Fe into the glacier from a RA event. However, local glacial conditions (discussed in the following sections), will determine the extent of this pulse, such as meltwater refreezing. In addition to this meltwater pulse, the dust cloud from the event will be dispersed over a larger area than the deposit, due to air blast transportation (Deline, 2001; Dufresne *et al.*, 2019). This cloud features very fine grains (Dufresne *et al.*, 2019) that could have a relatively high concentration of bioavailable Fe, depending on RA lithology and can be exported straight into the extraglacial environment without any glacial modification due to aeolian processes. Yet in some cases, a RA may be sourced from highly jointed weathered bedrock, where clouds of fines are sourced from the headwall. These RAs are potentially preconditioned to transporting fine material, but the old, existing fine material that resulted from headwall erosion, will not be comparable in its bioavailable Fe quantities, to the fine material created during the RA debris disintegration/comminution process, due to its prolonged atmospheric exposure on the headwall (at the RA source before failure). The fate of RA-created dust that does not get exported through aeolian processes and instead gets deposited on the glacier surface will depend on the deposit emplacement location and the time of year. However, it is likely to disappear from the glacier surface within days due to erosion and/or burial by snowfall. In the days following flow termination, if the ambient temperature permits (>0 °C), the entrained snow and ice will melt out (e.g. Dufresne *et al.*, 2019), 'flushing' the RA debris, which will ultimately carry more fine sediment into the glacier hydrological system.

Drainage of sediment-laden meltwater from the surface, in either the initial pulse, or subsequent flushing events, will travel englacially and/or subglacially, where it will likely undergo numerous weathering reactions, particularly if it interacts with the subglacial hydrologic system, where chemical weathering and Fe reduction is common (Wadham *et al.*, 2010; Graly *et al.*, 2014; Hawkings *et al.*, 2014; Nixon *et al.*, 2017; Henkel *et al.*, 2018). Microbial life exists both supraglacially and subglacially (e.g. Anesio *et al.*, 2017) so it cannot be ruled out that Fe may be depleted and utilised in these environments, or may even increase due to microbially mediated weathering reactions (Tranter *et al.*, 2002; Foreman *et al.*, 2007; Nixon *et al.*, 2017). However, RA Fe derived from fine particles (ferrihydrite) will be harder to utilise than soluble Fe sources, which are already likely to be sufficient because there are no documented glacial ecosystems that are Fe-limited. Alternatively, it may slowly deplete by its use as a terminal electron acceptor in anaerobic respiration (Mikucki *et al.*, 2009). After transport through the glacial hydrological system, export of RA Fe will then occur into the extra-glacial environment, either a proglacial forefield or straight into the ocean (often via fjord systems). There are numerous controls on the rate of this export, from both the initial pulse, to the rafting and final deposition of this RA debris into the extra-glacial environment. These controls vary from the type of glaciated environment the RA is deposited into, to the time and location in which it was emplaced. These controls are discussed in detail in the next sections. However, it is important to note that over time the bioavailable Fe is converted into more stable forms, therefore, the faster the debris is exported, the greater the percentage of bioavailable Fe that is delivered into the extraglacial environment.

6.1.2 Accumulation zone deposition and export

A RA deposited into the accumulation zone of a glacier is at a higher elevation and an increased distance from the glacier terminus in comparison to one deposited into the ablation zone (Figure 37; RA 1, Figure 38; RA 3). This results in a greater delay between deposition and export of debris and Fe, in particular the bioavailable fraction. To begin, a RA deposited in the accumulation zone is more likely to run out over a thick snowpack. Although the differences between RA runout over ice and snow have not been quantified,

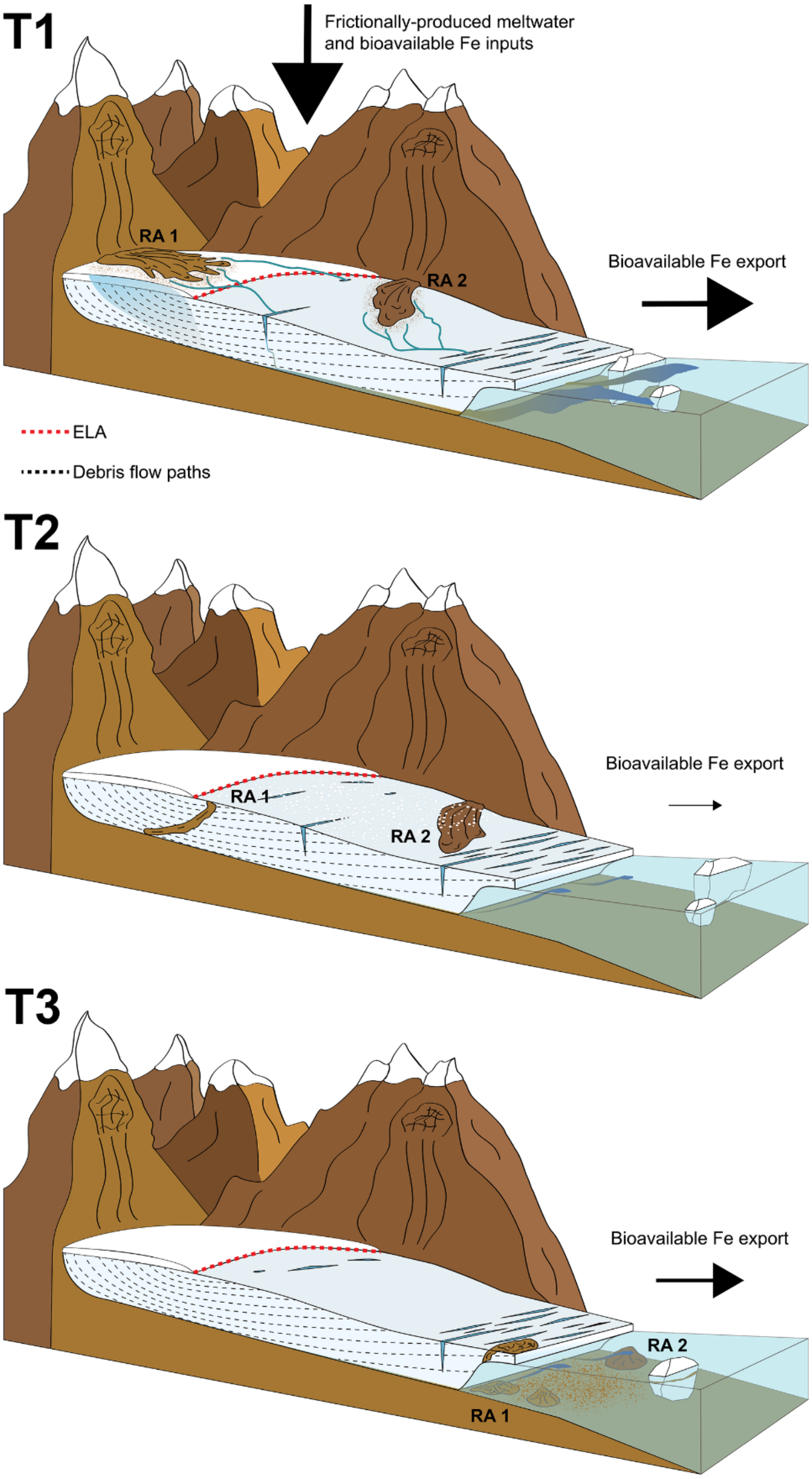

Figure 37: Schematic of deposition, transportation and export of RA debris and associated bioavailable Fe release over time on a marine-terminating glacier, for a RA deposited in a glacier accumulation zone (RA 1), and a RA deposited in a glacier ablation zone (RA 2). Glacier is a simplified version of the lower portion of a marine-terminating glacier, modelled on the Lamplugh glacier in GLBA.

it is theorised than runout over a snowpack should increase the amount of frictionally-produced meltwater created, as opposed to running out over bare ice, because it has a lower density (e.g. Booth *et al.*, 2013; Godio and Rege, 2015) and subsequently a higher surface area than ice (e.g. Domine, Taillandier and Simpson, 2007), promoting greater melt. Running out over a thick snowpack will also likely increase the amount of entrained material, as the lower density of snow should require less energy than ice to become

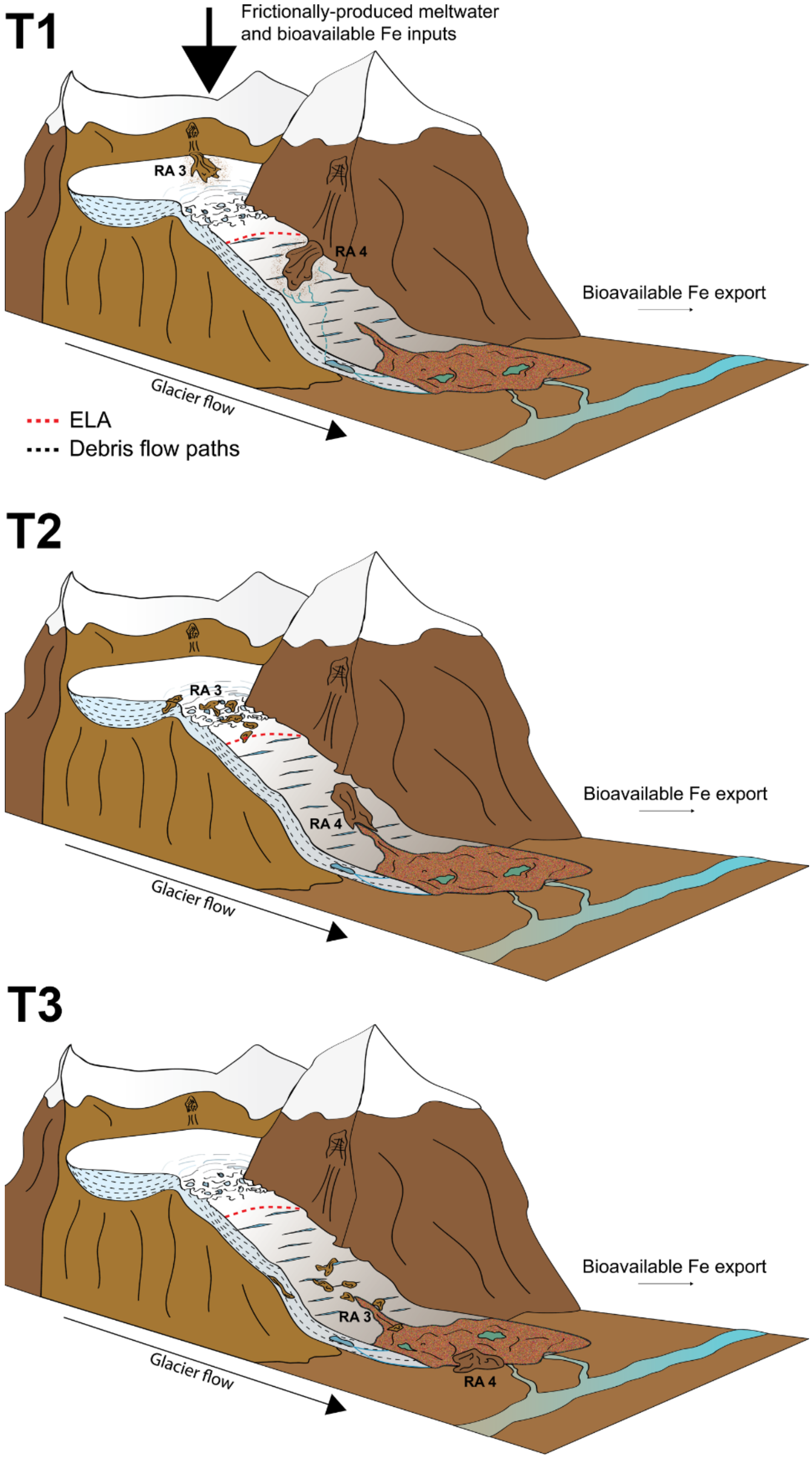

Figure 38: Schematic of deposition, transportation and export of RA debris and associated bioavailable Fe release over time on a debris-covered, land-terminating glacier, for a RA deposited in a glacier accumulation zone (RA 3), and a RA deposited in a glacier ablation zone (RA 4). The glacier itself is fed by a high-altitude icefield, before flowing over a bedrock lip, where an icefall is present, before becoming debris-covered at its terminus.

incorporated into the flow. The initial meltwater pulse should therefore be high from both frictionally-produced meltwater and the melt-out of snow/ice entrained in the deposit over the days following flow termination (Figure 39A). However, meltwater drainage in the accumulation zone is slower than the ablation zone, often occurring by water percolating through the snowpack, where it can refreeze (as would happen for RA 3 in Figure 38). If this meltwater pulse does make it to the bed, the accumulation zone hydrological system has a lower drainage density (Brykala and Arazny, 2000), which would delay export, resulting in a diffuse pulse. Export times will depend on the efficiency of the glacier hydrological system, which is dependent on the glacier thermal regime (Irvine-Fynn *et al.*, 2011) and the time of year, which is discussed in detail in section 6.1.4.

Once debris is deposited into the accumulation zone, it will be covered by snowfall and/or wind-blown snow over the following days, months and years (e.g. Dunning *et al.*, 2015). This will bury and sequester the debris into the ice. Once sequestered it will be advected through the glacier (Figure 37; T2, Figure 38; T2), following pre-determined flow-lines, due to the way ice flows from higher elevations to lower elevations (Kirkbride and Deline, 2013; Mackay *et al.*, 2014; Wirbel, Jarosch and Nicholson, 2018). This burial and incorporation into the glacial interior will essentially freeze the debris in time, preventing atmospheric interaction and weathering. However, it does not prevent the depletion of bioavailable ferrihydrite (Figure 39A) as freezing can cause aggregation (Raiswell *et al.*, 2010). Yet lower temperatures do promote slower crystallisation over time (Torrent, Guzman and Parra, 1982; Das, Hendry and Essilfie-Dughan, 2011), so the bioavailable fraction should be preserved relative to debris exposed on the surface, as hypothesised for debris in subglacial environments (Raiswell *et al.*, 2018). Nevertheless, crystallisation behaviour and rates are predominantly controlled by water interaction (Torrent, Guzman and Parra, 1982), so any percolating and refreezing meltwater that interacts with the englacially frozen debris will reduce the bioavailable Fe content of the debris. The pH of this water is also key, with complete crystallisation taking ~30 years at pH 6 and ~ 3 years at pH 8 (Schwertmann, Stanjek and Becher, 2004). In contrast, this percolating meltwater may aid the export of bioavailable Fe, as it may flush the fine debris particles into the glacier hydrological system, causing gradual export of the bioavailable fraction that has not yet undergone complete crystallisation. If the debris remains frozen and has minimal meltwater contact, it will prevent rapid reductions in Fe bioavailability due to crystallisation, in comparison to RA debris that remains in the supraglacial environment (i.e. a RA deposited in the ablation zone). Lithology of the debris will also determine crystallisation rates as the bioavailable ferrihydrite can be stabilised and rates of crystallisation further slowed by the presence of rare earth elements (Yang *et al.*, 2021), phosphates (Gálvez, Barrón and Torrent, 1999), silica and organic matter (Jones *et al.*, 2009). Overall, water interaction will depend on a glaciers hydrological system and lithology will be unique to the RA, so temporal estimates of crystallisation for englacially transported debris will be RA specific.

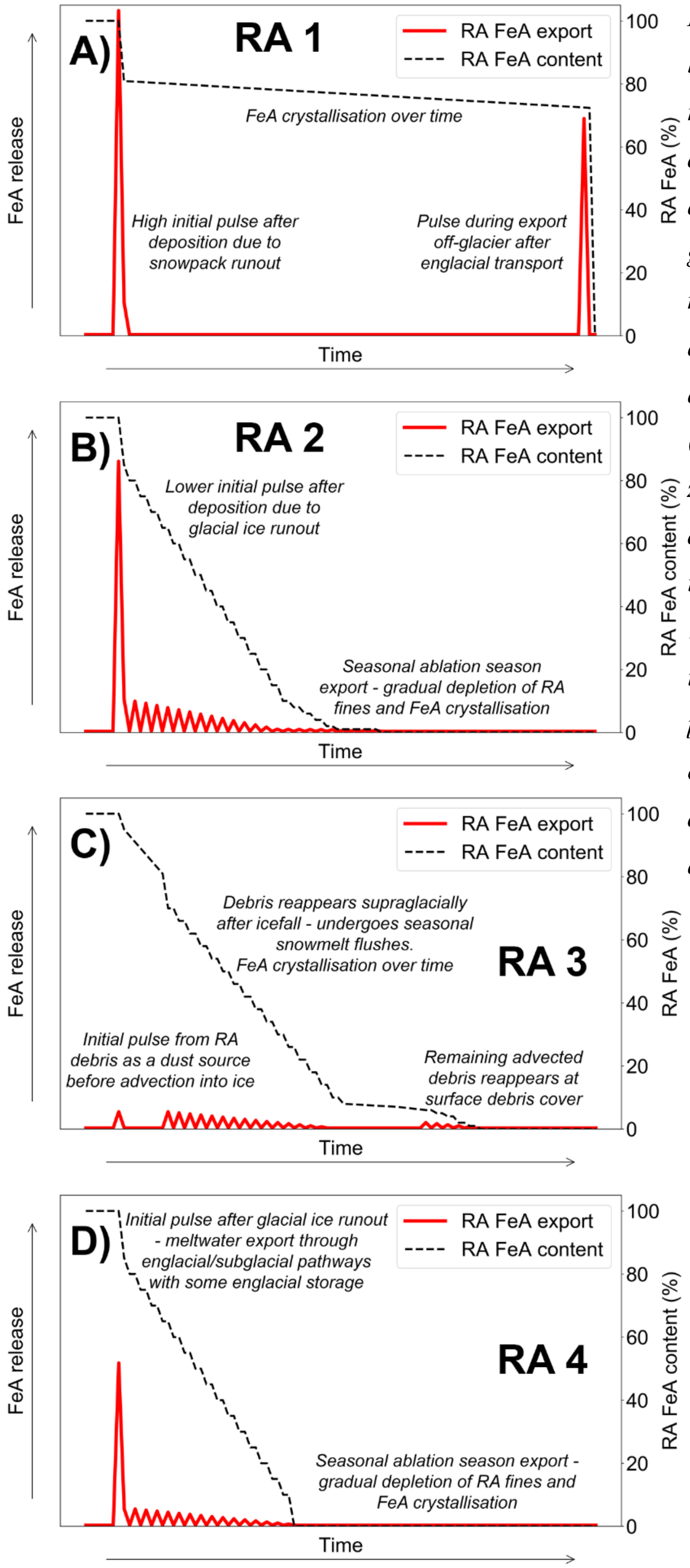

Figure 39: RA deposit bioavailable Fe (FeA) content and release over time for a RA deposited in the A) glacier accumulation zone (RA 1), and B) glacier ablation zone (RA 2) of a marine-terminating glacier with an efficient hydrological system, and C) glacier accumulation zone (RA 3) and D) glacier ablation zone (RA 4) of a land-terminating, debris-covered glacier, with an inefficient hydrological system. The amount of FeA is an illustration only to show the primary characteristics of its export. The exact amounts will depend on a multitude of factors and be unique to each event.

During englacial transportation the debris may not travel as a coherent deposit in its original sheet-like form, due to the internal deformation, extensional flow, thrusting, faulting and shearing of the glacier ice (Dunning *et al.*, 2015). Certain portions of the debris may become exposed in subglacial and englacial chambers. It may also be exposed to the atmosphere if crevasses open up and propagate down to the debris depending on the debris depth within the ice. For example, if a glacier flows over a lip and down a steep slope, the ensuing icefall will vertically mix the debris (Figure 38; RA 3, T2), like that seen for RAs occurring on Mount Cook, New Zealand (Dunning *et al.*, 2015). Exposure in any way would increase the rate of ferrihydrite crystallisation and subsequently reduce its bioavailability.

Once the debris begins to re-emerge at the surface, after advection through the ice, the time it is exposed on the glacier surface before export determines its effectiveness in delivering bioavailable Fe to extraglacial environments. If it remains in the ablation zone for many years, it will undergo seasonal flushing with snowpack melt, releasing a small fraction of bioavailable Fe each year, until it is depleted either through crystallisation into forms that are not known to be bioavailable or exhaustion of its Fe content through flushing, and therefore have no further impact (Figure 39B, C and D). However, if this debris is quickly exported into the extraglacial environment, due to glacial velocity and proximity to the terminus, it will still have a substantial quantity of bioavailable ferrihydrite. This will result in a second pulse of bioavailable Fe into the extraglacial environment, with the fine fraction having similar impacts as glacial flour (Figure 39A).

6.1.3 Ablation zone deposition and export

RA deposition below the equilibrium line altitude (ELA) in the ablation zone of a glacier will reduce the time between debris deposition and export, in comparison to an ablation zone RA (Figure 37; RA 2, Figure 38, RA 3). During RA flow and deposition, a RA in the ablation zone is more likely run out over glacial ice than snow, unless it occurs early in the melt season. As theorised in section 6.1.2, this will likely reduce the amount of frictionally-produced meltwater created and the amount of material entrained in comparison to an accumulation area RA, which runs out over a thick snowpack. This will reduce the initial pulse of sediment-laden meltwater from these events, relative to an accumulation area RA (Figure 39B). However, the drainage system in the ablation zone is likely to have greater efficiency than the accumulation zone (Irvine-Fynn *et al.*, 2011), so despite the reduced initial pulse, its export may be less diffuse, although this is dependent on meltwater pathways. Once the debris has been deposited it will remain supraglacial for its entire journey before export into the extra-glacial environment (Figure 37; RA 2, Figure 38, RA 4). This prolonged residence time on the glacier surface, in comparison to a sequestered accumulation area RA deposit, will subject it to higher temperatures (>0 °C) and seasonal interaction with meltwater and precipitation, causing the unstable bioavailable Fe in the debris, to gradually age, becoming more crystalline, and less bioavailable. With snowmelt and precipitation typically being acidic (pH 4 – 7) (e.g. Seip, 1980; Douglas and Sturm, 2004), complete crystallisation of the bioavailable ferrihydrite in the deposit should take >30 years (Schwertmann, Stanjek and Becher, 2004). However, the rate of crystallisation during multiple wetting/drying cycles and seasonal freeze-thaw cycles is unknown. If debris moisture does reach a minimum, it is known that ferrihydrite crystallisation rates are extremely slow when dry (Stanjek and Weidler, 1992). Although meltwater interaction will promote decreases in Fe bioavailability, in combination with aeolian processes it will also disturb and redistribute RA deposit fines over time. This will disperse the fine-grained material rich in bioavailable Fe, before it has aged into non-bioavailable forms, either directly into the extraglacial environment, or seasonally flush it into the glacier hydrological system before export (Figure 39B, C, D). This will occur on a seasonal basis, when the debris is exposed to the atmosphere and not covered by a snowpack.

Over time the supraglacial RA debris that remains on the surface and has not been exported by meltwater and aeolian processes, will be transported down-glacier due to glacier motion (Figure 37; T2, Figure 38; T2). During this transport debris may fall into crevasses or pass through an icefall, where much vertical mixing would occur (Dunning *et al.*, 2015). In this case it may become frozen in the ice and travel englacially (Figure 38; RA 3, T3), much like the debris in an accumulation zone RA. However, the majority of RA debris is likely to stay in the supraglacial environment. If the RA was deposited onto a debris-covered glacier, it would eventually become part of the supraglacial debris (Figure 38), where it could remain for long periods of time, resulting in complete crystallisation of ferrihydrite. In some cases such as the Miage Glacier RAs (Deline, Hewitt, *et al.*, 2014), a RA can be deposited onto the debris-covered portion of the glacier. In this scenario no frictionally-produced meltwater would be created, with meltwater interaction being limited to the supraglacial hydrological stores of meltwater within the debris cover i.e. streams and ponds. A lack of frictionally-produced meltwater would limit the initial Fe pulse, resulting in the dust cloud being the predominant source of initial Fe export. Over time, seasonal flushing of the debris may occur but beneath the debris-covered portion of the glacier, the drainage system is often inefficient (Fyffe *et al.*, 2019), so export of RA fines and bioavailable Fe will be slow, resulting in further aging and crystallisation of the debris and its meltwater export products.

The export of all remaining RA debris from the glacier terminus at the end of its glacial transportation will likely be insignificant if the debris has persisted on the surface for numerous years and the bioavailable Fe fraction has aged and crystallised. However, this is dependent on its deposition location proximity to the glacier terminus (i.e. the Taan fjord RA was deposited at the glacier terminus (Higman *et al.*, 2018), so Fe export would be fast) and on the glacier response to RA debris. RA debris deposition onto a clean ice glacier, has been found (debatably) to transiently increase glacier velocity (Shugar *et al.*, 2012). Therefore, the very presence of the debris on the surface, may decrease the time it takes to be exported, in comparison to estimates based on pre-emplacement velocities. Similarly, ice loss due to increasing atmospheric temperatures will reduce the size of glaciers (e.g. Sommer *et al.*, 2020). This may reduce the amount of time it takes to export material because of reductions in glacier length. However, reductions in glacier length may be offset by the decrease in glacier velocity that accompanies ice loss (e.g. Wu *et al.*, 2019).

Due to the processes outlined above the export of bioavailable Fe from an ablation area RA will be prolonged over multiple years in comparison to an accumulation area RA (Figure 38). However, this prolonged residence time at the surface will cause the unstable bioavailable Fe in the debris, to gradually age, becoming more crystalline, and less bioavailable. This will gradually diminish bioavailable Fe export from a RA deposit, until it essentially becomes inert as a bioavailable Fe source (Figure 38). This is unless emplacement location ensures rapid post-deposition debris export (i.e. within close proximity to the glacial terminus).

6.1.4 Seasonality

As discussed in chapter 4 the majority of RAs occur between the months of May and September, and in chapter 5 it is theorised that the greatest peaks in bioavailable Fe export occur in sediment-laden meltwater. The temporal evolution of glacier hydrological systems and supraglacial debris cover is therefore key both spatially and temporally to the export of nutrients. This May-September period where RAs predominantly occur, is the melt season for glaciers in the northern hemisphere, and subsequently a period where the glacier hydrological system undergoes significant changes, due to the increase in meltwater inputs (e.g. Irvine-Fynn *et al.*, 2011; Davison *et al.*, 2019). At the start of the melt season there is an abundance of meltwater at the glacier surface due to melt and under certain circumstances, the formation of superimposed ice, which prevents meltwater drainage to the bed (e.g. Wakahama *et al.*, 1976), forming supraglacial lakes and slush (e.g. Hodgkins, 2001). A RA running out over this saturated supraglacial environment would interact with more meltwater than a RA that occurs late in the ablation season, therefore potentially creating a greater pulse of sediment-laden meltwater rich in bioavailable Fe. The transportation speed of this meltwater through the glacier and into the extraglacial environment will however, be slower at the start of the season due to the inefficient, distributed glacier hydrological system (e.g. Fountain and Walder, 1998; Armstrong and Anderson, 2020), which may diffuse the sediment both spatially and temporally during export. Over time this evolves into an efficient channelized system, reaching maximum efficiency in late summer/early autumn (e.g. Fountain and Walder, 1998; Armstrong and Anderson, 2020). RA meltwater pulses will therefore be exported faster, the later in the melt season that the RA occurs, resulting in less diffuse sediment export. However, large meltwater inputs at the start of the melt season, such as the drainage of supraglacial lakes and winter snowpack melt, have been known to cause ‘hydraulic jacking’ of the ice mass, causing sudden release of meltwater (Kavanaugh and Clarke, 2001; Dow *et al.*, 2015). This is due to meltwater inputs exceeding glacier drainage system capacity, resulting in instabilities at the bed. If a RA can create enough frictionally-produced meltwater to overcome the drainage system capacity of its host glacier, the export of bioavailable Fe would be rapid. Rapid export prevents any significant changes to the structure and speciation of the RA-derived bioavailable Fe.

Although the speed of meltwater export is key to Fe export, in particular the initial frictionally-produced meltwater pulse, export speed is also highly dependent on meltwater storage within the glacier. For a RA that occurs at the start or end of the ablation season, or at a high altitude, when sub-zero temperatures are still likely, this frictionally-produced meltwater may refreeze at the surface or at the bed (Figure 38; RA 3, Figure 39C). This freezing may preserve the bioavailable Fe fraction, which would theoretically deplete slowly as it is frozen (Raiswell *et al.*, 2018), preventing any large-scale speciation changes and reductions in bioavailability. Once temperatures exceed 0 °C in the following days, or the following ablation season, and debris melts out, the bioavailable ferrihydrite fraction would therefore still be mostly present but its export would be dependent on the current status of the glacier hydrological system.

Meltwater storage that remains unfrozen could potentially have the opposite effect, causing faster aging and crystallisation of the bioavailable fraction. In some glaciers englacial drainage systems have low hydraulic gradients and sinuous meandering channels (Benn *et al.*, 2017) with englacial reservoirs (Miles *et al.*, 2019), which could store and delay the initial pulse (Figure 38; RA 3). Although much like the subglacial drainage system, the englacial drainage system can become more efficient with increasing meltwater inputs over the melt season from ablation and supraglacial pond drainage (Benn *et al.*, 2017; Narama *et al.*, 2017). The debris on debris-covered glaciers can also act as a meltwater store (Brock *et al.*, 2010; Irvine-Fynn *et al.*, 2017), in addition to supraglacial ponds, particularly the larger, more permanent ponds, which can receive meltwater inputs from streams and other ponds further up-glacier (Benn, Wiseman and Hands, 2001; Wessels, Kargel and Kieffer, 2002; Miles *et al.*, 2017). In these cases, any pulse that travels through the supraglacial debris of a debris-covered glacier, could be substantially delayed before it is exported into the extraglacial environment. Another factor influencing export time is storage within groundwater aquifer systems linked to the subglacial hydrological system (Andermann, Longuevergne, *et al.*, 2012), which can delay and dilute suspended sediment concentrations (Andermann, Bonnet, *et al.*, 2012; Andermann, Crave, *et al.*, 2012). Any storage of meltwater within any of these meltwater stores over longer time scales (weeks, months or years), will deplete the ferrihydrite content of fine RA sediment carried in suspension, through crystallisation and further weathering and result in diffuse extraglacial export. Storage and export delay will depend on the unique structure of the glaciers hydrological system, its seasonal evolution and the glacier thermal regime (Irvine-Fynn *et al.*, 2011).

6.1.5 Export into marine or proglacial environment

The environment debris is deposited into will be key for Fe cycling, whether this is a marine or proglacial environment (Raiswell *et al.*, 2018). In the marine environment, Fe delivery to potentially Fe-limited coastal waters depends on whether the glacier exports directly into the ocean, or into a large fjord system. Fjord systems complicate Fe delivery to coastal waters as they can act as sediment traps (Cowan *et al.*, 2010) and the salinity gradients, circulation patterns and estuarine processes all have potential to alter Fe speciation and delivery (Schroth *et al.*, 2014; Hopwood *et al.*, 2016, 2017). Fjord processes will become increasingly important as glaciers retreat and fjords get longer, becoming further detached from the ocean (e.g. Normandeau *et al.*, 2019). The export source is also key for marine Fe export; supraglacial meltwater is a minor contributor to overall discharge and Fe export (Hopwood *et al.*, 2020), however, if it is rich in fine RA material, it could be an important contributor, due to direct export into the photic zone. In contrast, subglacial meltwater export is potentially a negligible contribution (despite discharge often being far higher), in comparison to its effect on promoting the upwelling of nutrient-rich deep water (Hopwood *et al.*, 2020). It is likely that any fine RA sediment rich in bioavailable Fe travelling subglacially, would therefore never make it into the photic zone for utilisation, settling out at the seabed. However, this will depend on the water column depth that subglacial meltwater is released into. In addition to meltwater, debris export through solid ice discharge, in the form of icebergs with a high content of RA debris, will also transport bioavailable Fe to the ocean (Figure 37; RA 1, T3). This Fe will still have a high concentration of the bioavailable fraction, as it will have remained frozen since delivery. Icebergs are the largest source of Fe to the polar oceans (Hopwood *et al.*, 2019) and their transport away from coastal regions results in meltout of debris, releasing Fe to stimulate phytoplankton blooms (Smith *et al.*, 2007, 2013; Schwarz and Schodlok, 2009; Duprat, Bigg and Wilton, 2016; Wu and Hou, 2017).

Export of Fe-rich sediment from RAs into a proglacial environment may have less of an impact, than export into a marine environment (Figure 39C, D). This is dependent on glacial-fluvial coupling (see Chapter 2 section 2.10). For a coupled ice margin, RA debris export from its proglacial deposition location may be relatively fast by fluvial processes e.g., a proglacial river. During transportation in a proglacial river, Fe is depleted with increasing distance from the glacier terminus, due to Fe precipitation and stabilisation (Zhang *et al.*, 2015), so the Fe radius of influence after export may be small. In contrast, if a proglacial lake is present at the terminus, and RA debris is deposited into this lake, any bioavailable Fe may undergo crystallisation and depletion, and its export would be delayed and insignificant. However, in a Greenlandic proglacial environment, processes occurring in the proglacial lake were hypothesised to increase dissolved Fe in meltwaters (Bhatia *et al.*, 2013). This processing may increase the extraction of RA debris particulate Fe into its soluble form before export, although the chemical relationships for this are complex and glacier/lake specific.

If the extraglacial RA debris deposition location is at a decoupled ice margin, sediment is not transported in meltwater and will remain in the proglacial forefield, aging into more crystalline, less bioavailable forms. However, as outlined in chapter 5 section 5.4.5, this deposition into the proglacial forefield may act as a dust source, from which the Fe may be exported over much greater distances than simple marine deposition. This is particularly important for RAs deposited in the accumulation zone and advected into the ice for their entire down-glacier transportation (Figure 37; RA 1), because despite debris being in the glacial domain longer, the bioavailable fraction will likely have been preserved due it to being frozen in the ice. In contrast, RA debris deposited in the ablation zone, which has been passively rafted on the surface for >30 years, has lost its fine debris fraction and the Fe has crystallised into less bioavailable forms, will be an insignificant bioavailable Fe dust source (Figure 37; RA 2, Figure 38; RA 3 and RA 4). It is important to note that all hypothesise about RA Fe delivery, transport and export will be unique to each RA and their host glacier.

6.2 Glacial RA contribution to Fe fluxes in Glacier Bay National Park and beyond

In chapter 2, volume-area scaling relationships are criticised as being inaccurate and poorly constrained. However, there is currently no better way of determining the volume of multiple RAs over a large area. Here the volume-area scaling relationship for supraglacial rock avalanches derived by Sosio *et al.* (2012) is applied to the GLBA inventory presented in chapter 4. This allows estimation of the bioavailable Fe inputs from all RAs in the area. The total volume of all 69 RAs in GLBA using this method is estimated at 180.6 Mm^3. To convert this to mass, it was multiplied by the average density of the dominant Lamplugh RA lithology; schist (Table S 5), giving a total mass of 511 Gg of debris. To estimate the upper, middle and lower bounds of the bioavailable Fe content of this debris, it was assumed that 50 %, 25 % and 1 % of this debris was fine grained material (<1 mm), as per the upper (Hewitt, 2002b) and lower (Shugar and Clague, 2011) bounds found for glacial rock avalanches, although it is noted that the particle size distribution of RAs has likely never been adequately characterised for these purposes (as discussed in section 2.7.3). Each estimated mass was then multiplied by the average bioavailable Fe (FeA) concentration from the Lamplugh RA fines presented in chapter 5 (8.26 µmol g^{-1}). This provided estimates of 0.127, 0.06 and 0.003 Gg of bioavailable Fe brought into the glacial domain by RAs, for a total RA debris mass with assumed fine particle (<1 mm) masses of 50 %, 25 % and 1 % fines, respectively.

It is important to note that a number of assumptions are carried through these calculations, providing multiple sources of uncertainty that propagate to the end estimates. For example, the Lamplugh RA deposit Fe concentration is an underestimate (as shown in comparisons between freshly ground rocks of the same lithology in Chapter 5), as sediment was exposed and aged on the surface for two years before Fe quantification. The bioavailable Fe content of fresh RA sediment would need to be measured in a number of different RA lithologies in GLBA to provide a better understanding of initial Fe quantities that are delivered into the GLBA glacier domain. Although assuming all RAs are of the same lithology is the only way in this thesis to estimate Fe inputs from RAs, it is clear from the geology in GLBA that a number of RAs failed from peaks of different lithology (see GLBA geology map by Wilson *et al.* 2015) and chapter 5 shows that lithology is critical to Fe concentrations. The estimates calculated here do however indicate that RAs play an unrealised role in delivering Fe into the glacial domain, that may previously have been assigned to other processes.

Elsewhere in Alaska, where deposits are more frequent (Bessette-Kirton and Coe, 2020), the contribution of Fe from RAs could be higher, although this is dependent on source lithology. RA frequency and magnitude is key to the quantities of Fe, with episodic larger RAs creating larger point supplies of the fine-grained material rich in bioavailable Fe, whereas frequent smaller RAs deliver a constant chronic supply. Neither is truly a distributed supply, it is spatially clustered, so a small number of route ways/flux gates will dominate Fe fluxes. These constraints for large and small RAs are all satisfied during earthquakes, which can trigger multiple glacial RAs simultaneously over large areas (Jibson *et al.*, 2006). These clusters of RAs will input large amounts of debris rich in Fe, over multiple glaciers and over a wide area, therefore the initial pulse described in section 6.1.1, could be significant, if the conditions are conducive to quick meltwater export and glaciers export directly into the ocean. On a global scale, glacial RA frequencies and magnitudes need to be determined, but with lithology varying across high mountain regions (Ott, 2020), some regions may be exporting disproportionally high (or low) Fe pulses into the glacial domain.

To summarise, if the conceptual model was scaled up in space and time, it would scale with the frequency and magnitudes of RAs, with the caveat being RA lithology. In hot years where RAs are more frequent, there would be an increase in the number of Fe-rich pulses into the glacial domain. On a seasonal scale, RAs are linked to rock-permafrost degradation, so the majority of pulses would be during the ablation season when temperatures are high enough to activate all rock-permafrost degradation mechanisms. However, the export of these pulses would depend on the glaciers' hydrological efficiency. In addition, the majority of RAs occur on tributary glaciers at high elevations, so export times are longer, but sequestering of deposits somewhat preserves the bioavailable fraction by delaying degradation into stable forms. RAs are therefore a previously unrealised Fe source in glacial environments, and the export of this Fe-rich debris could be a contributor to overall glacial Fe export, which is known to fertilise extraglacial ecosystems.

Chapter 7 - Summary

Chapter 7: Summary

In this thesis, the main aim was to quantify the under-detection of supraglacial landslide frequencies and magnitudes, improve detections, and then assess their potential as sources of bioavailable Fe for extra-glacial environments. To achieve this objective, Glacier Bay National Park and Preserve in southeast Alaska was chosen as the study area, due to its history of large supraglacial rock avalanches (RAs), which were said to be increasing in magnitude with warming atmospheric temperatures (Coe, Bessette-Kirton and Geertsema, 2018). This area has received significant investigation over the past decade (Geertsema, 2012; Bessette-Kirton, Coe and Zhou, 2018; Coe, Bessette-Kirton and Geertsema, 2018; Dufresne *et al.*, 2019), and has one of the most complete inventories of supraglacial RAs to date (Bessette-Kirton and Coe, 2016).

To quantify any under-detection of events a new method was required (Objective 1), that could exploit entire satellite data archives, in a fraction of the time it would take a user to manually analyse these images. Chapter 3 presents the Google Earth Engine supRaglAciaL Debris INput dEtector (GERALDINE). This tool takes a user specified time and region of interest to return a map, from which supraglacial landslides can be clearly detected. To do this it utilises the entire Landsat Thematic Mapper data archive to collect every image that meets the user criteria, before masking cloud from each image, and then applying the normalised difference snow index to categorise the glacier area into two: ice or debris. It then creates a maximum debris mosaic of these images, which is subtracted from a maximum debris mosaic of the previous year, before clipping these mosaics to the Randolph Glacier Inventory v6.0 boundaries. This highlights where new supraglacial debris additions have occurred. A user can take this map of new debris additions, identify large supraglacial debris additions from rock-slope processes, verify them and undertake further analysis. This tool was verified against 48 known glacial RAs, with 92% event detection accuracy and 100% accuracy post-1991.

GERALDINE was run over Glacier Bay National Park and Preserve to quantify the under-detection of RAs in glacial environments (Objective 2). By analysing 1853 Landsat images between 1984-2020, identification of supraglacial RAs from annual GERALDINE outputs, determined that the existing inventory underestimated the number of RAs by 53%. The additional 27 RAs that occurred over the same period as the original inventory, were small (mean 0.49 km^2), indicating that current inventories have a size/volume bias that impacts our current understanding of magnitude-frequency relationships in glacial environments. In total, between 1984 and 2020 the area experienced 69 rock avalanches, with frequencies highest in the last three years. RAs clustered spatially at high elevations, on the boundary of modelled permafrost likelihood and around certain peaks and ridges. Temporally, there was only one multi-year period between 1989 and 1993 without RAs, and RAs clustered seasonally, between May and September. This seasonal triggering, in combination with analysis of monthly temperatures, indicated that rock-permafrost degradation is likely to be a key component in the triggering of slope failures in Glacier Bay National Park and Preserve. With increasing atmospheric temperatures likely to trigger more slope failures in the future, the impacts of this debris are important, so the first estimates of RA debris sequestration into the ice were calculated. In total, 58% of RA deposits were sequestered into the ice within two years, suggesting glaciers in the region are significant, unaccounted for debris stores.

The geochemical impacts of RA debris were investigated by looking at the iron (Fe) content of the largest supraglacial RA to have occurred in Glacier Bay National Park and Preserve; the Lamplugh glacier RA (Objective 3). Lithology controls the quantity of total Fe and extractable Fe, with grain size controlling the amount that is potentially bioavailable. Bioavailability is highest immediately after deposition due to the creation of substantial quantities of freshly comminuted sediment. However, the bioavailability of the Fe decreases over time as it ages and crystallises into more stable forms, that are not currently known to be bioavailable. Overall, the total Fe content of the RA debris was similar to other glacial and aeolian sources, but the extractable bioavailable Fe (oxyhydr)oxides were two orders of magnitude lower. This was due to debris exposure on the surface of the glacier resulting in aging, crystallisation and consequently depletion of the bioavailable fraction, a lack of pyrite available for oxidation within the source rock and potentially a lack of subglacial processing. Despite this, the rapid delivery and size of the Lamplugh RA means that it was a large supraglacial input of Fe into the glacial domain, with the bioavailable Fe quantity estimated at 34 tonnes, two years post-deposition.

To link our improved detections (Chapter 3 and 4) with the finding that deposits contain bioavailable Fe, but it degrades fast (Chapter 5), a conceptual model was created (Chapter 6). It is hypothesised that the initial delivery of RA debris onto the glacier surface, creates an abundance (70-90 kg m^2; Sosio, Crosta, Chen, & Hungr, 2012) of frictionally-produced meltwater. In the model presented, this frictionally-produced meltwater interacts with the freshly comminuted sediment, causing dissolution of bioavailable Fe, and also entrainment of large quantities of fine material that is rich in bioavailable Fe. This meltwater drains through moulins and crevasses and by percolating through the snowpack/ice. The fine-grained dust created during flow and deposition will also be distributed over a much larger area than the deposit, delivering this bioavailable fraction further afield. This initial meltwater and dust pulse will be the biggest pulse of bioavailable Fe into the glacial system, and if glacial conditions are optimum; the extraglacial environment. After deposition, the location of the deposit on a glacier determines its future ability to export Fe. A RA deposited in the accumulation zone will be rapidly sequestered, freezing the debris and subsequently slowing the crystallisation of bioavailable ferrihydrite, until it re-emerges in the ablation zone or during export. This may initiate a second Fe pulse. For a RA deposited in the accumulation zone, there is no second Fe pulse. Instead, the deposit will stay on the surface, subjected to weathering processes and seasonal snowmelt flushing, which will deplete the fine-grained fraction, whilst the bioavailable Fe stocks in the remaining deposit decrease due to crystallisation over time. Export of Fe from RAs is hypothesised to be dependent on the deposition month and the seasonal evolution of the glacier hydrological network. It is important to note that the conceptual model outlines the key processes of RA Fe delivery, transport and export, but these processes will be unique to each RA and its host glacier.

7.1 Future work

The under-estimation of RA frequencies and magnitudes, their likely increase in the future due to warming atmospheric temperatures, and their role in glacial Fe cycling all require further investigation. Here I outline a number of key areas:

1. Further development of the GERALDINE tool is required to further reduce the time it takes a user to identify supraglacial landslides. It would be useful for the tool to automatically identify landslide-like objects (rather than simply aiding identification) characterised by their lobate, elongated appearance from GERALDINE outputs and signal this to the user. In addition, instead of having to verify the deposits manually using GEEDiT, it would be beneficial for the images to be available within GERALDINE itself. Development of tools using different methodologies but for similar purposes would also be advantageous, such as a tool that uses synthetic aperture radar data, which would help alleviate the issues with clouds and reduced image frequency in the winter months, as well as narrowing the time window of occurrence. Nevertheless, the key to creating accurate

inventories of these events is the utilisation of all available data i.e., seismic, optical and radar.

2. As noted by Coe (2020) there is a need to create inventories of slope-failures in glacial environments on a global scale, to assess the rates of activity and improve our understanding of climate change impacts. It is recommended that GERALDINE is run in the five 'bellwether' sites he identifies, so standardised comparisons can be made between regions. This will allow assessment as to whether Glacier Bay National Park and Preserve is a 'hot spot' for large RAs, or whether this activity is normal in high mountain glacial environments.
3. The fate of RA sediment that has been sequestered into the ice and quantification of total RA debris volume locked up within ice masses. Ground-penetrating radar (GPR) has initially shown promise for tracking these deposits (Dunning *et al.*, 2015). In areas with frequent RA activity, it is recommended that GPR surveys are undertaken to track new RA deposits, in addition to image and track deposits that are known to have occurred over the last three decades. It would also be a useful tool to assess and quantify how much debris is locked up and travelling englacially, from slope failures that have occurred over the last few hundred years.
4. A number of research questions from the conceptual model presented here require more verification.
    a. The amounts of frictionally-produced meltwater created during RA debris delivery and whether the amounts vary between deposition on snow or ice. In situ observations would be impossible but instrumentation of glacial outflows from glaciers with frequent RAs would allow detection of meltwater pulses immediately following an event. This instrumentation could also measure and/or take samples to help determine changes in suspended sediment concentrations, and meltwater elemental composition, to detect sediment and Fe pulses.
    b. Characterising the finer debris fraction losses in the frictionally-produced meltwater. As RAs have a fractal grain size distribution (Dufresne and Dunning, 2017), it would be possible to determine whether the fine fraction is lost in meltwater, following transportation and deposition. This could be used in combination with instrumentation of glacial outflows to determine the lag times of sediment export.

   c. The crystallisation rates of bioavailable ferrihydrite for debris that travels either supraglacially, englacially and subglacially needs quantifying in glacial environments, to determine how long RA debris is a source of bioavailable Fe. This can be done in the laboratory, by freezing RA debris over a period of time, and then measuring the concentration in comparison to an unfrozen control sample. It would also be beneficial to sample RA debris that is re-emerging at the glacier surface following sequestration and englacial transportation, to assess its bioavailable Fe content. This sediment could be identified as RA debris by analysing for agglomerate particles (Reznichenko *et al.*, 2012).

5. Investigation of other biologically important nutrients a RA could input into the glacial domain such as phosphorous, silica and nitrogen. These are all exported from glacial sources (e.g. Hawkings et al., 2014, 2016; Wadham et al., 2016), so it is key to determine what percentage of this is from RA processes in areas of significant RA activity, such as Glacier Bay National Park and Preserve.
6. Analysis of ocean chlorophyll concentrations at the terminus of marine-terminating glaciers immediately before and after RA deposition, to determine any stimulation of phytoplankton communities, which could be attributed to pulses of nutrients from the rock avalanche.

In this thesis it has been shown that supraglacially deposited RAs are under-estimated and therefore more important than previously realised. In addition, they are important point-source inputs of Fe into the glacial domain, which will have fertilising effects both glacially and extra-glacially. Further study is needed to help validate the conceptual model presented here and determine the impact of these increasingly frequent slope processes on the sediment and nutrient cycles in both the glacial and extra-glacial environment.

Chapter S1: Supporting information for Chapter 3

S1.1. Randolph Glacier Inventory (RGI) v6.0 errors

The Randolph Glacier Inventory v6.0 (Pfeffer *et al.*, 2014) is a global dataset of digitised glacier outlines, excluding the ice sheets of Greenland and Antarctica. These outlines were digitised from images acquired between 1943 and 2014. This large temporal array of images introduces a variety of dataset errors, due to rapid glacial thinning and retreat, in response to climatic change over the last century. GERALDINE's delineation of new debris additions on glaciers is impacted by these discrepancies.

We run GERALDINE for the year 2018 over the Columbia glacier, a glacier which has undergone unprecedented retreat over the last three decades, to demonstrate RGI impacts (Figure S 1). RGI outlines in this region were digitised from imagery acquired in 2009 but the glacier has retreated ~8 km since then, losing 46.9 km^2 at its tongue. Clean ice is 'found' in the now ice-free area, owing to ice melange/icebergs, and debris is 'found' due to the dark, unreflective ocean surface. We advise caution with the delineation of new debris additions near the terminus of marine-terminating glaciers, if they have recently undergone substantial retreat. Glacial thinning/down-wasting can also cause discrepancies in GERALDINE outputs. All tributaries of the western trunk of the Columbia glacier have undergone down-wasting, exposing valley walls. GERALDINE delineates this down-wasting and subsequent valley wall exposure as surficial debris, represented by each glacier having thick lateral 'debris' bands (Figure S 1B). These are likely to expand with further glacial mass wastage, until RGI outlines are updated in v7.0.

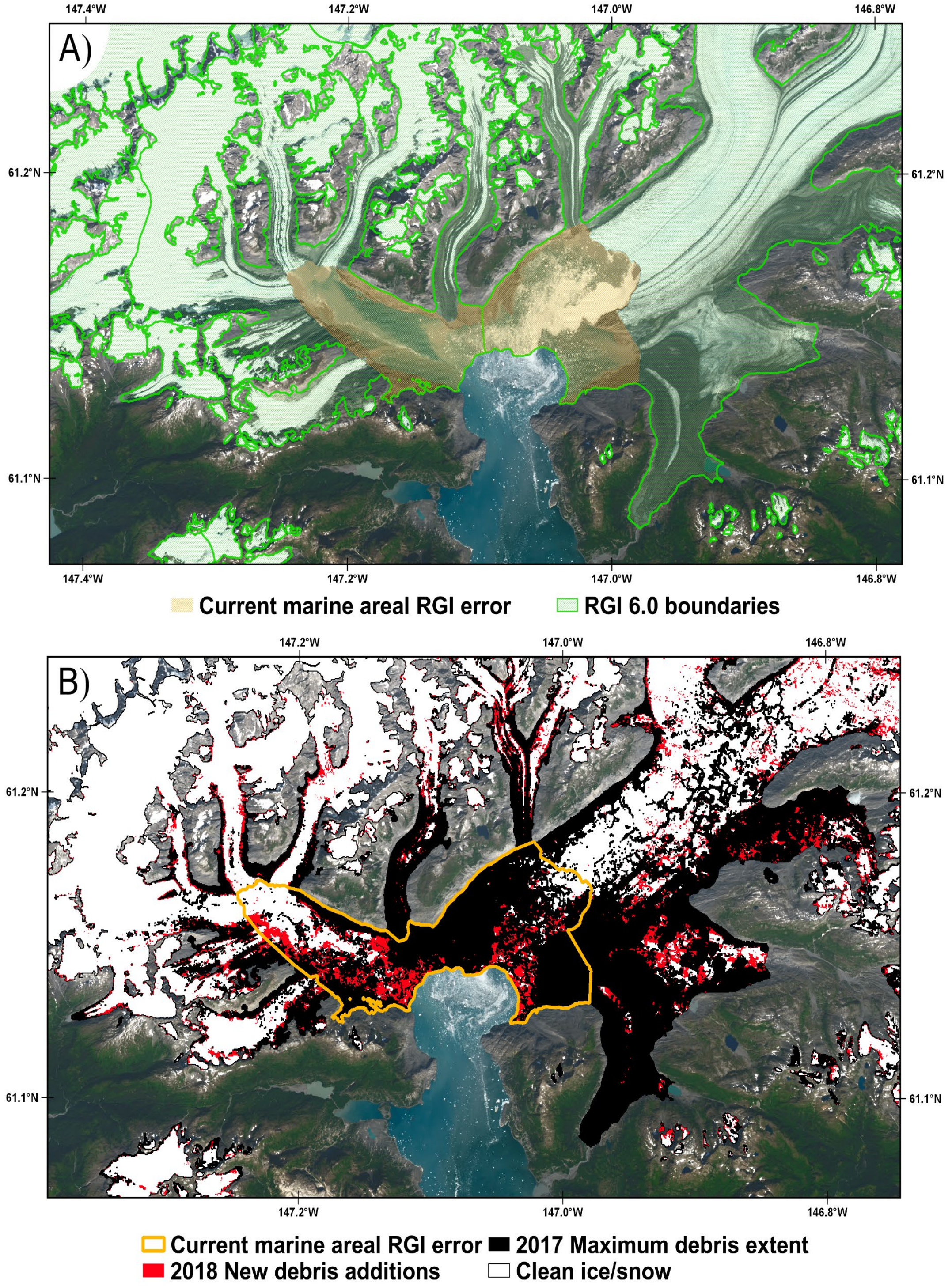

Figure S 1: Retreat of the Columbia Glacier, Alaska and the impact on RGI v6.0 outline accuracy. A) RGI v6.0 glacier outlines (green) and the area, which is no longer glaciated (orange). B) GERALDINE new debris results in this area for 2018. Landsat 8 background from 2019-08-20.

S1.2. Cloud mask threshold validation

To determine the optimum threshold for cloud masking we chose 13 rock avalanches (RA) from the validation dataset, to validate different thresholds against. The high prevalence of RAs in Alaska meant all events chosen for cloud mask threshold validation occurred in the region, with nine occurring in Glacier Bay National Park (Coe, Bessette-Kirton and Geertsema, 2018) and four occurring in the eastern Alaska Range, in particular the area around Mt Hayes (Jibson *et al.*, 2006) (Table S 1). This selection incorporated two areas with different climatic regimes (marine vs continental climate) and a wide temporal coverage incorporating all Landsat satellites, with particular focus on the current constellation, due to the tool's main use for aiding RA detection in the present day.

Table S 1: Rock avalanches (RA) used for cloud mask threshold validation.

RA Name	Region	Year	Latitude	Longitude	Satellite	Area (km^2)
2	Glacier Bay National Park	1986	58.794	-137.354	Landsat 4/5	0.025
10	Glacier Bay National Park	1986	58.830	-137.502	Landsat 4/5	1.371
14	Glacier Bay National Park	1986	58.647	-137.058	Landsat 4/5	0.544
Black Rapids Glacier W	Eastern Alaska Range (Mt Hayes)	2002	63.472	-146.263	Landsat 5/7	1.136
McGinnis Peak Glacier S	Eastern Alaska Range (Mt Hayes)	2002	63.547	-146.198	Landsat 5/7	1.321
Black Rapids Glacier E	Eastern Alaska Range (Mt Hayes)	2002	63.461	-146.167	Landsat 5/7	1.612
Black Rapids Glacier M	Eastern Alaska Range (Mt Hayes)	2002	63.466	-146.226	Landsat 5/7	1.950
7 - John Hopkins	Glacier Bay National Park	2015	58.769	-137.269	Landsat 7/8	3.375
11	Glacier Bay National Park	2015	58.626	-137.281	Landsat 7/8	1.223

23	Glacier Bay National Park	2015	58.622	-137.275	Landsat 7/8	0.586
24 - Lamplugh	Glacier Bay National Park	2016	58.779	-136.888	Landsat 7/8	19.174
26	Glacier Bay National Park	2016	58.635	-137.018	Landsat 7/8	0.231
27	Glacier Bay National Park	2016	58.852	-137.247	Landsat 7/8	0.146
28	Glacier Bay National Park	2016	58.844	-137.345	Landsat 7/8	0.707

Five different cloud thresholds were tested: 10%, 20%, 30%, 50% and 90%, to investigate their influence on highlighting new RA events. GERALDINE was run for the year of the event, or in the case of the eastern Alaska Range RAs, the year after the event, because these RAs occurred in November 2002 and therefore appeared in no Landsat imagery during that year. New debris layers generated by GERALDINE were downloaded, and the area of new debris detected in the location of RAs, was compared to digitised RA outlines from the same year. A cloud mask threshold of 20% highlighted the largest area of new RAs, delineating 60.6% of RA area (Figure S 2: Mean area of RA highlighted as new debris by GERALDINE, and mean area of each Landsat image available after cloud masking, for five different cloud thresholds. Error bars represent standard deviation of the mean.). The 10% cloud threshold masked too much of each image, inhibiting its ability to highlight new debris. Higher thresholds did not mask enough cloud discrepancies out of images resulting in misclassification of cloud as debris in previous year debris extents. This misclassification prevented GERALDINE from highlighting new debris because debris was already present in the previous year. GERALDINE therefore utilises a 20% cloud threshold by default.

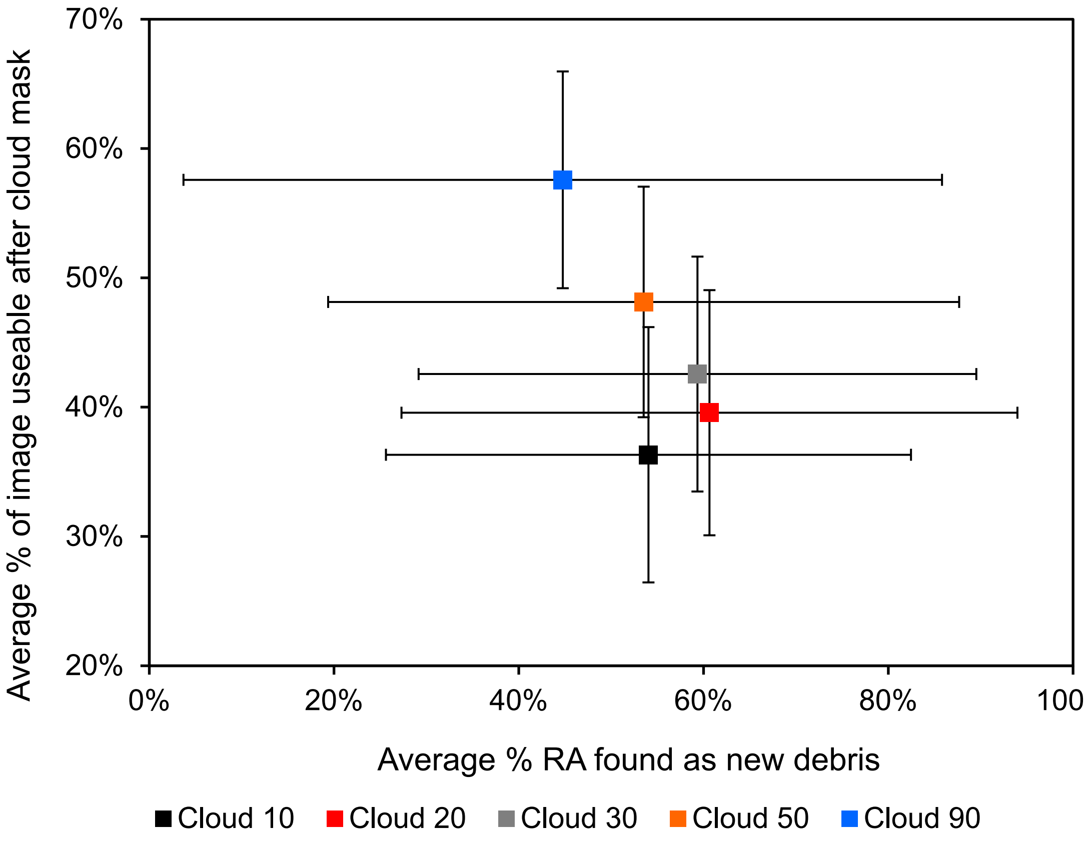

Figure S 2: Mean area of RA highlighted as new debris by GERALDINE, and mean area of each Landsat image available after cloud masking, for five different cloud thresholds. Error bars represent standard deviation of the mean.

We provide both good and bad examples of cloud mask performance on a single Landsat image in Figures S3 and S4, respectively. Figure S3 showcases the cloud masks ability to accurately mask cloud that is obscuring part of the Lamplugh RA, removing it from further analysis (Figure S 3). However, occasionally it can suffer over debris cover in some areas (Figure S 4), due to the optical and temperature similarities of the debris to cirrus clouds. This has similarly been found in Antarctica with sunlit rock misclassification as cloud (Burton-Johnson *et al.*, 2016). However, the image stack methodology used by GERALDINE helps to negate these cloud masking discrepancies.

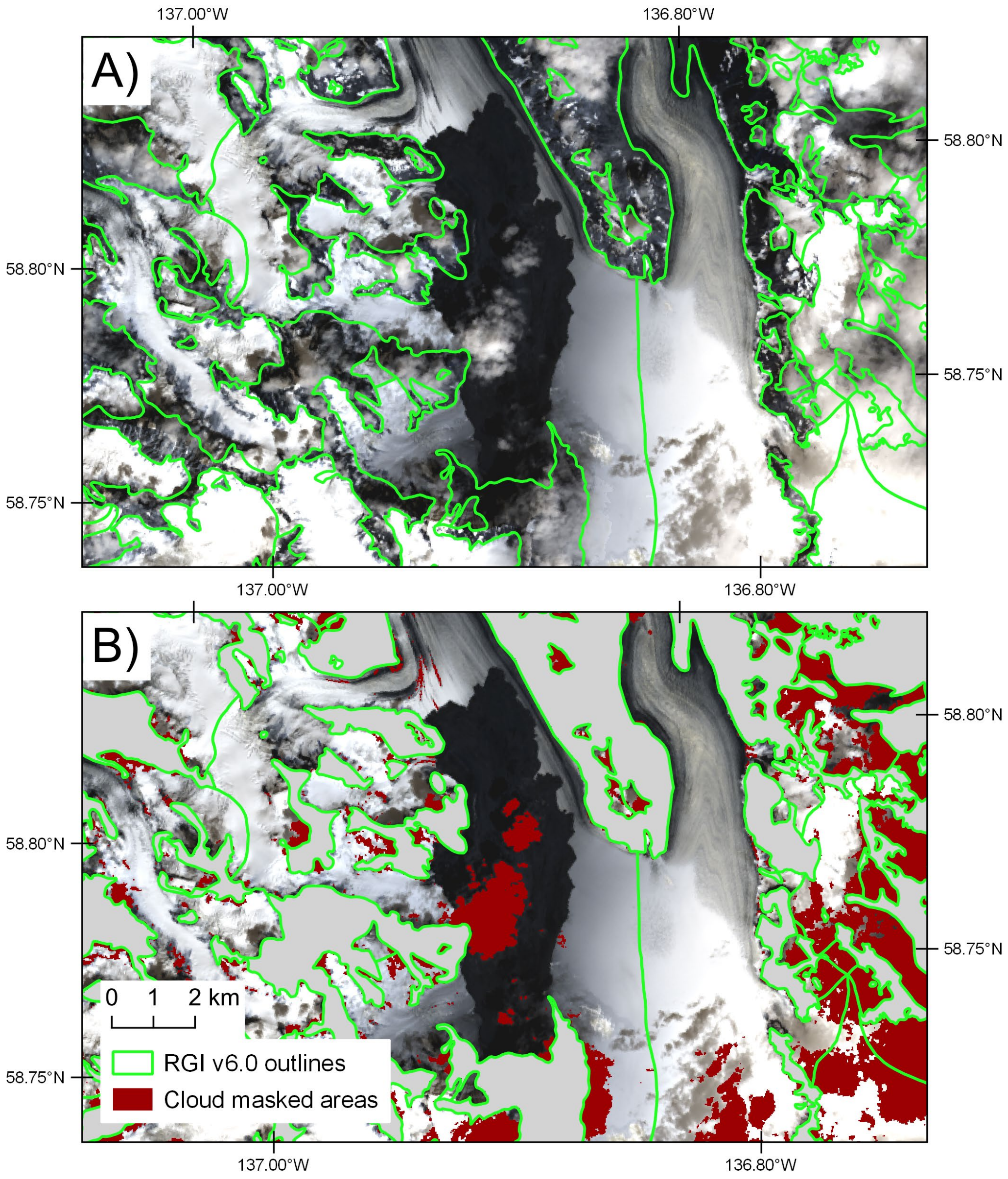

Figure S 3: A) Original Landsat image (LC08_060019_20160729), B) Cloud masked Landsat image. Masking shows good ability to eliminate cloud pixels from scenes.

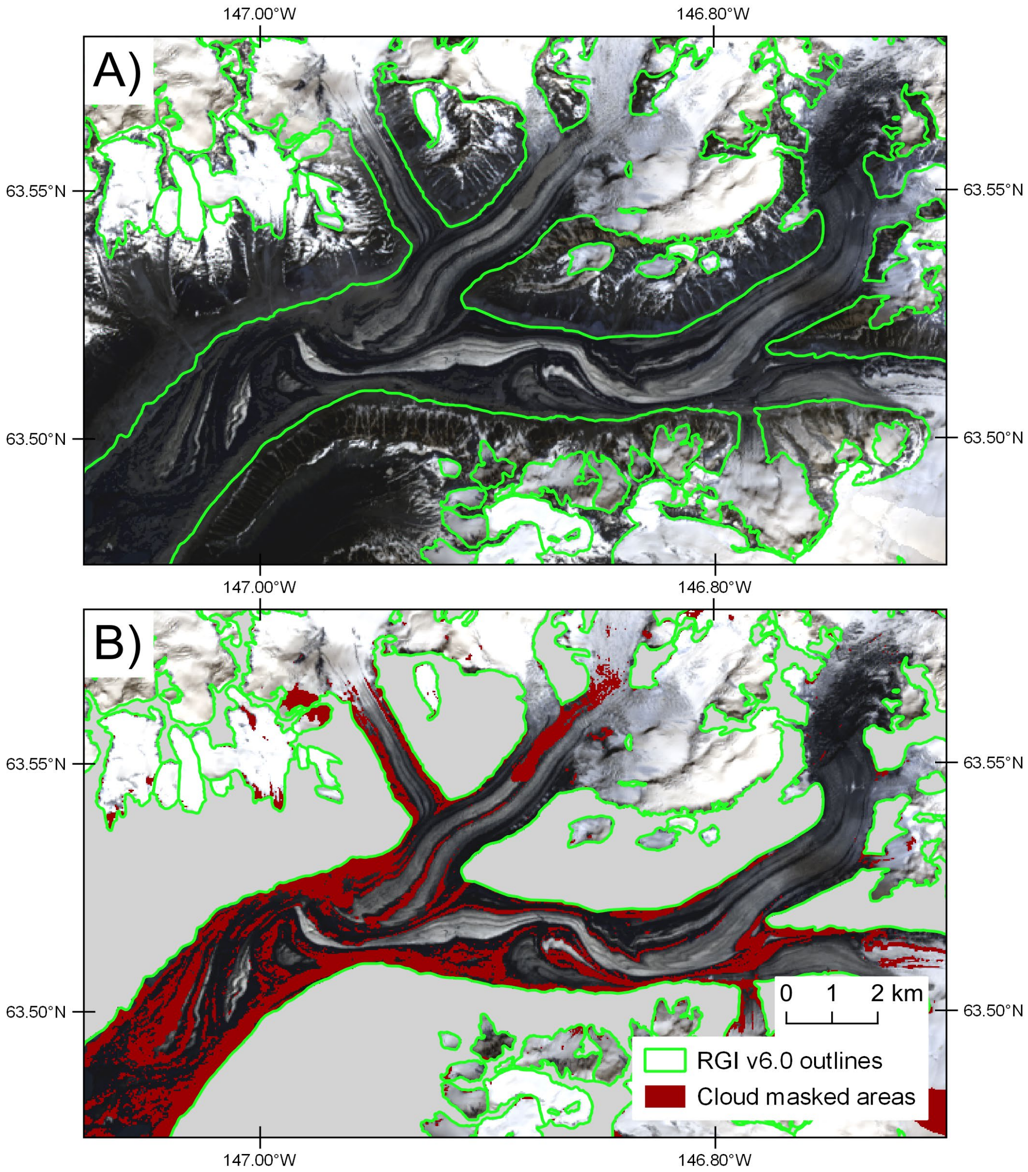

Figure S 4: A) Original Landsat image (LC08_067016_20180704), B) Cloud masked Landsat image. Masking shows poor ability to eliminate cloud pixels from scenes, with misclassification of lighter debris as cloud.

S1.3. Global distribution of validation RAs

Figure S 5: Global distribution of RAs used for GERALDINE validation (48 in total).

for GERALDINE validation (48 in total).

S1.4. GERALDINE user guide

The tool is freely available to use at (https://code.earthengine.google.com/87b7fdf47b8d550a7c6ed85a2ebd7ad8) but requires a Google account authorized to use Google Earth Engine (GEE), which is free of charge if used for research and educational purposes (sign up for Google account here: https://accounts.google.com/signup/v2/webcreateaccount?flowName=GlifWebSignIn&flowEntry=SignUp and register for GEE access here: https://earthengine.google.com/). Exporting of tool outputs requires a Google Drive account, which is complementary with the Gmail account required to sign up for GEE. The tool is open access and GUI (graphical user interface) driven. Tutorials on how to use Earth Engine are available at https://developers.google.com/earth-engine/ but here we will provide instructions on how to use our tool to detect supraglacial landslide deposits.

Step 1:

Open v1.1 of GERALDINE (the version described in the manuscript) by clicking on this link: https://code.earthengine.google.com/87b7fdf47b8d550a7c6ed85a2ebd7ad8 or access the latest version of GERALDINE at https://doi.org/10.5281/zenodo.3524414 (if using the latest version these instructions may differ slightly).

Step 2:

You will be greeted by the start page shown below. Click ‘New project’ to start analysis.

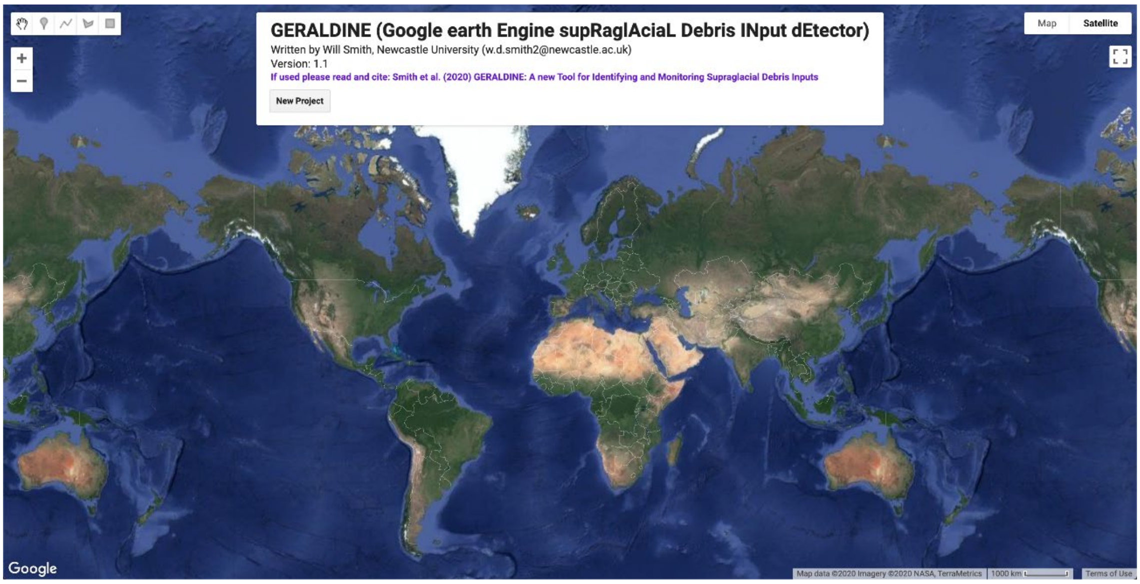

GERALDINE (Google earth Engine supRaglAciaL Debris INput dEtector)

Written by Will Smith, Newcastle University (w.d.smith2@newcastle.ac.uk)

Version: 1.1

If used please read and cite: Smith et al. (2020) GERALDINE: A new Tool for Identifying and Monitoring Supraglacial Debris Inputs

Step 3:

Draw region of interest (ROI) by zooming in and clicking around an area to draw a polygon (Note: large ROIs and time periods that involve >800 images can be slow to load as they are calculated 'on the fly' in the map window). Alternatively, upload a shapefile of your ROI to Google Earth Engine (see: https://developers.google.com/earth-engine/importing for more information) and specify the GEE file path, which can be found by sliding down the top panel and navigating to the ‘Assets’ tab in the top left hand panel (highlighted by red box in image below). Click OK button when your ROI is defined.

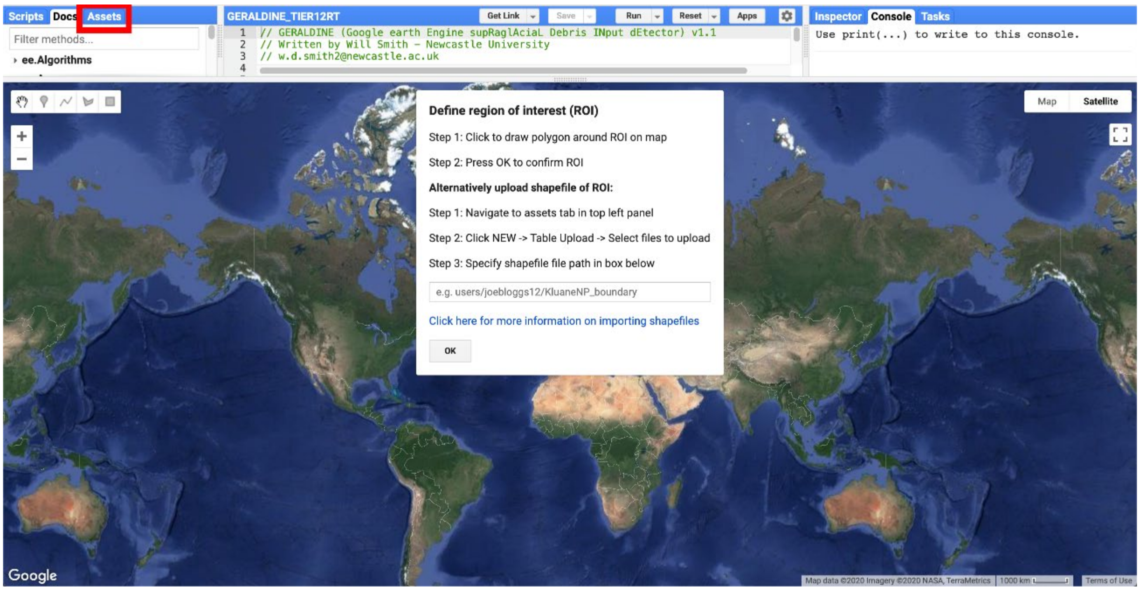

```
// GERALDINE (Google earth Engine supRaglAciaL Debris INput dEtector) v1.1
// Written by Will Smith - Newcastle University
// w.d.smith2@newcastle.ac.uk
```

```
Use print(...) to write to this console.
```

Define region of interest (ROI)

Step 1: Click to draw polygon around ROI on map

Step 2: Press OK to confirm ROI

Alternatively upload shapefile of ROI:

Step 1: Navigate to assets tab in top left panel

Step 2: Click NEW -> Table Upload -> Select files to upload

Step 3: Specify shapefile file path in box below

e.g. users/joebloggs12/KluaneNP_boundary

Click here for more information on importing shapefiles

OK

Step 4:

Specify date range from which you want the tool to detect new debris additions and select if you would like to use Tier 2 and/or Real Time Landsat imagery in addition to the default Tier 1 imagery. Tier 2 imagery is useful if minimal Tier 1 imagery is available i.e. in Antarctica, and Real Time imagery should only be used if the event has occurred in the

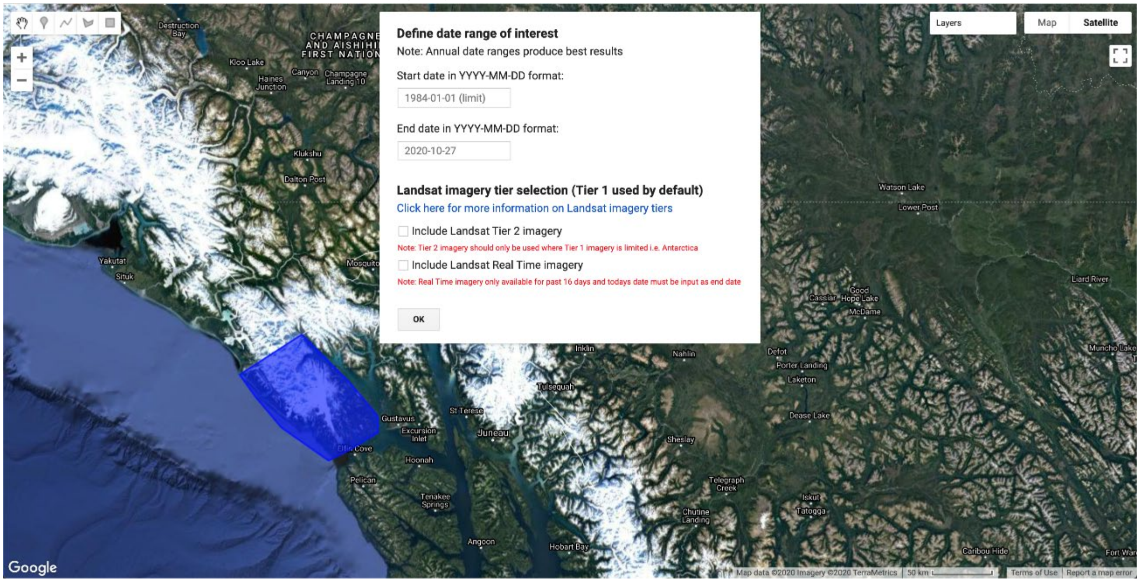

Define date range of interest

Note: Annual date ranges produce best results

Start date in YYYY-MM-DD format:

1984-01-01 (limit)

End date in YYYY-MM-DD format:

2020-10-27

Landsat imagery tier selection (Tier 1 used by default)

Click here for more information on Landsat imagery tiers

☐ Include Landsat Tier 2 imagery

Note: Tier 2 imagery should only be used where Tier 1 imagery is limited i.e. Antarctica

☐ Include Landsat Real Time imagery

Note: Real Time imagery only available for past 16 days and todays date must be input as end date

OK

previous 16 days (Note: for Real Time imagery ‘End date’ must be set as todays date). Tool accuracy and speed is optimum if date ranges are annual or sub-annual and only Tier 1 imagery is utilised. Date must be in the format of Year – Month – Day e.g. 2018-12-22. Press OK once start and end date are defined.

Step 5:

The tool should display results on the interactive web map (it can take up to 3 minutes for layers to load if analysis is being undertaken on >800 images). Two layers are created: a previous year maximum debris cover layer and a new debris additions layer. The user can view and toggle these layers by hovering the mouse over the ‘Layers’ button in the top right hand corner of the map viewer (highlighted by red rectangle in below image). To export the data click on the Export data button.

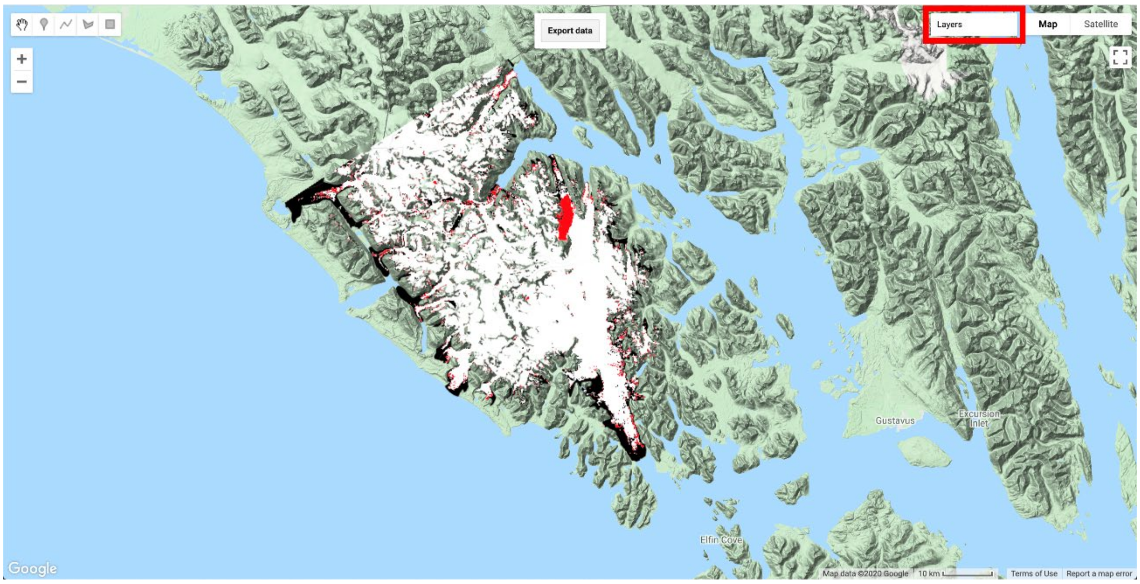

Step 6:

Instructions are displayed detailing how to export data from GEE. Once you have navigated to the Task tab in the top right hand panel and clicked ‘Run’ next to the layer you wish to download (note: you do not need to wait for layers to load within GEE before you export). The following window will be displayed (see image below), prompting the user to confirm or alter the filename, confirm the export format (GeoJSON is strongly recommended because it decreases export time), and confirm the save location. Once data is exported, it can be used in a GIS of your choice. Alternatively, you can save your files as an Earth Engine asset, this is particularly useful for your ROI, enabling you to call it in during Step 3, instead of redrawing it every time you use GERALDINE.

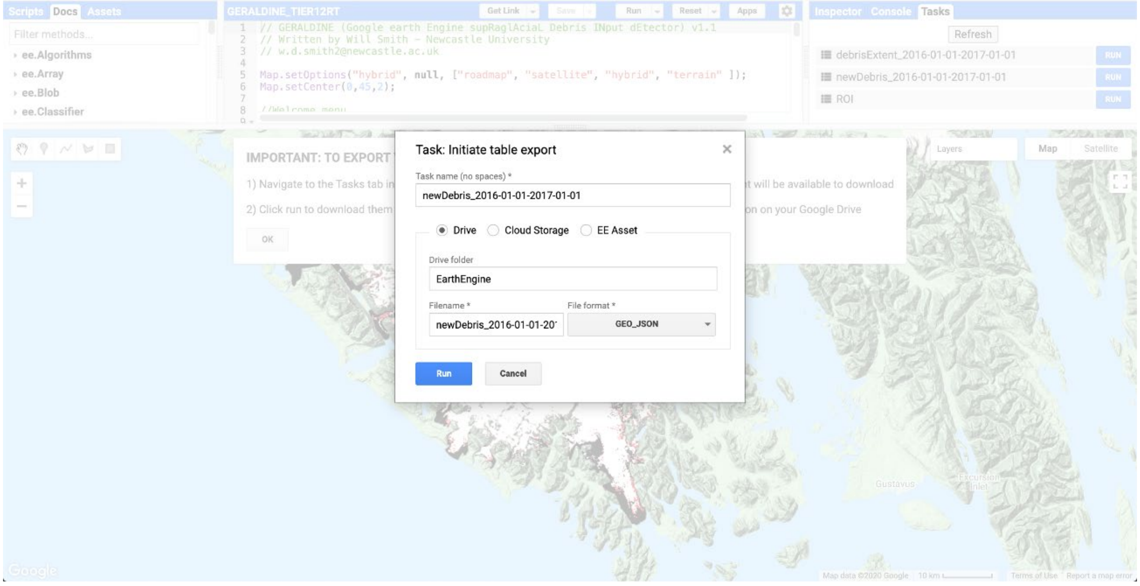

```
// GERALDINE (Google earth Engine supRaglAciaL Debris INput dEtector) v1.1
// Written by Will Smith - Newcastle University
// w.d.smith2@newcastle.ac.uk

Map.setOptions("hybrid", null, ["roadmap", "satellite", "hybrid", "terrain" ]);
Map.setCenter(0,45,2);

//Welcome menu
```

Task: Initiate table export

Task name (no spaces) *: newDebris_2016-01-01-2017-01-01

● Drive ○ Cloud Storage ○ EE Asset

Drive folder: EarthEngine

Filename *: newDebris_2016-01-01-20

File format *: GEO_JSON

Chapter S2: Supporting information for Chapter 4

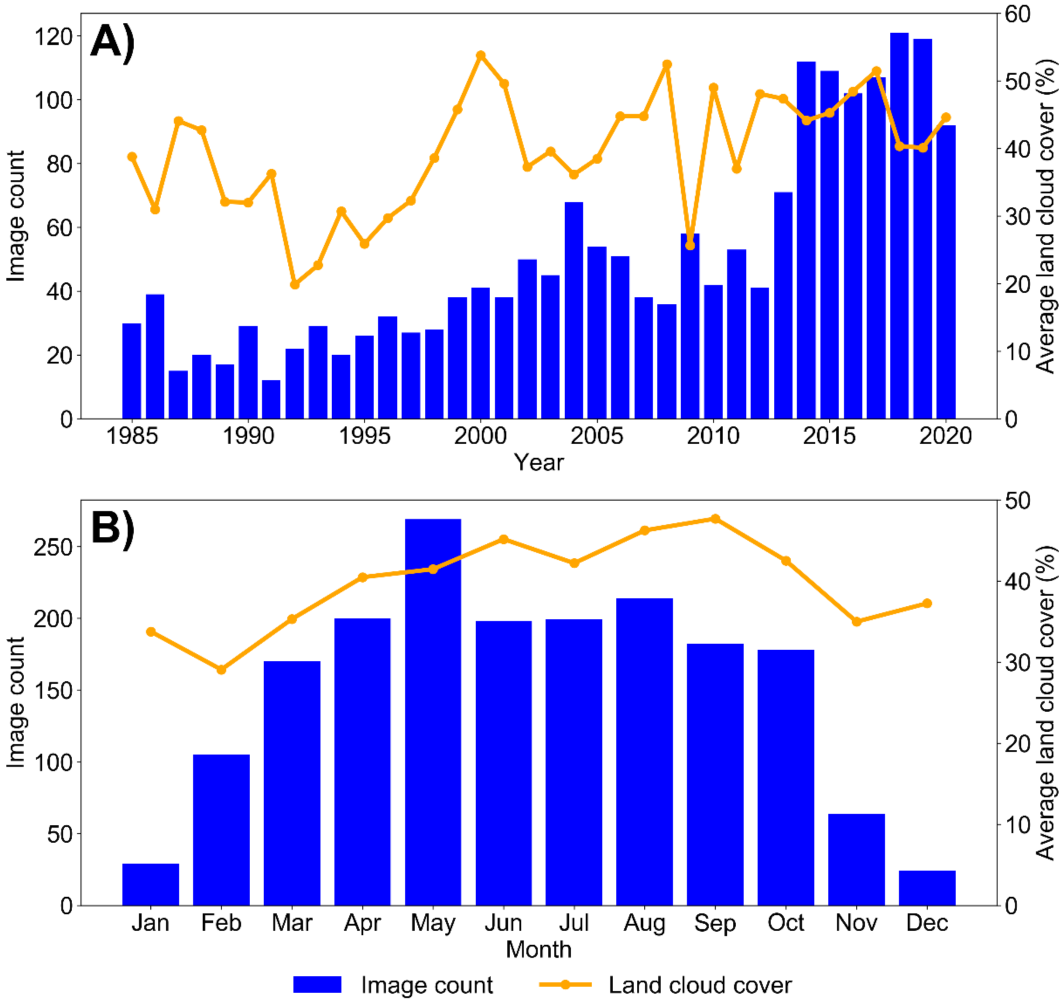

Figure S 6:A) Yearly, and B) monthly Landsat image frequency and average land cloud cover (see USGS (2021) for more information) for all 1853 Landsat images used to create GLBA RA inventory.

Table S 2: RA inventory basic information. [1]Occurrence Window Length (OWL) in days (the time between the RA not being visible and being visible in Landsat imagery), [2]RA deposit area, [3]Maximum headscarp elevation (m a.s.l.), [4]Sequestered Y=yes, P=partially, N=no, U=unknown

ID	Inventory	Longitude	Latitude	Not visible	Visible	OWL[1]	A[2] (km^2)	Z[3] (m)	H/L	S[4]
1	BK&C(2016)	-137.271	58.613	Pre 07/09/1984	Pre 07/09/1984	-	1.661	2532	0.43	U
2	BK&C(2016)	-137.296	58.747	21/05/1985	22/06/1985	32	3.736	2579	0.32	P
3	BK&C(2016)	-137.073	58.561	04/07/1986	20/07/1986	16	0.285	1377	0.33	Y
4	BK&C(2016)	-137.353	58.791	12/10/1985	25/06/1986	256	1.431	2511	0.47	U
5	BK&C(2016)	-137.443	58.794	04/07/1986	20/07/1986	16	0.681	2483	0.44	Y
6	BK&C(2016)	-137.081	58.648	20/04/1988	30/06/1988	71	0.360	1137	0.38	N
7	BK&C(2016)	-137.036	58.960	15/06/1994	11/08/1994	57	1.523	2318	0.24	Y
8	BK&C(2016)	-137.196	58.863	15/06/1994	02/08/1994	48	0.318	2161	0.63	Y
9	BK&C(2016)	-137.352	58.791	01/05/1995	27/06/1995	57	0.114	1343	0.40	Y
10	BK&C(2016)	-136.990	58.860	01/05/1995	27/06/1995	57	0.151	1713	0.61	Y
11	BK&C(2016)	-137.100	58.643	24/04/1995	01/05/1995	7	0.161	1213	0.63	N
12	BK&C(2016)	-137.372	58.744	31/05/2000	23/06/2000	23	0.261	1490	0.25	Y
13	BK&C(2016)	-137.277	58.823	09/06/2006	02/07/2006	23	0.693	1225	0.29	N
14	BK&C(2016)	-137.358	58.790	30/07/2010	14/08/2010	15	0.701	2515	0.45	Y
15	BK&C(2016)	-137.511	58.823	01/06/2012	24/06/2012	23	7.941	3325	0.27	P
16	BK&C(2016)	-137.081	58.647	12/06/2013	14/07/2013	32	0.595	1415	0.29	Y
17	BK&C(2016)	-137.599	58.888	07/02/2014	23/02/2014	16	5.455	2822	0.24	Y
18	BK&C(2016)	-137.511	58.823	02/08/2014	01/05/2015	272	3.600	1591	0.15	P
19	BK&C(2016)	-137.271	58.613	24/05/2015	04/07/2015	41	1.275	1950	0.30	N
20	BK&C(2016)	-136.894	58.731	01/05/2015	17/05/2015	16	0.640	1968	0.43	N
21	BK&C(2016)	-137.207	58.953	27/06/2016	06/07/2016	9	22.186	2165	0.16	N
22	BK&C(2016)	-137.025	58.631	26/05/2016	06/07/2016	41	0.253	1690	0.39	Y
23	BK&C(2016)	-137.247	58.857	26/05/2016	27/06/2016	32	0.245	1269	0.35	N
24	BK&C(2016)	-137.357	58.839	10/05/2016	19/05/2016	9	0.711	2576	0.33	Y
25	GERALDINE	-137.378	58.667	13/04/1997	22/05/1997	39	0.467	2021	0.56	N
26	GERALDINE	-137.185	58.739	07/06/1997	23/06/1997	16	0.357	1528	0.47	N
27	GERALDINE	-137.333	58.952	13/04/1997	02/07/1997	80	0.158	2265	0.68	Y
28	GERALDINE	-137.366	58.814	25/05/1998	26/06/1998	32	0.883	1462	0.21	Y
29	GERALDINE	-137.198	58.656	25/05/1998	26/06/1998	32	0.452	2774	0.61	Y
30	GERALDINE	-137.071	58.654	18/03/1999	31/07/1999	135	0.097	2310	0.65	Y
31	GERALDINE	-137.030	58.570	18/03/1999	09/09/1999	175	0.461	2055	0.40	Y
32	GERALDINE	-137.191	58.784	13/04/2000	31/05/2000	48	0.527	983	0.40	N
33	GERALDINE	-137.097	58.655	18/07/2000	03/08/2000	16	0.225	2493	0.62	Y
34	GERALDINE	-137.084	58.652	26/06/2001	13/08/2001	48	0.341	2718	0.53	Y
35	GERALDINE	-137.404	58.819	06/06/2002	08/07/2002	32	0.250	2995	0.82	Y
36	GERALDINE	-137.295	58.759	16/08/2002	25/08/2002	9	0.915	1250	0.17	P
37	GERALDINE	-137.077	58.655	18/07/2003	11/08/2003	24	0.829	2573	0.43	Y
38	GERALDINE	-137.076	58.654	18/07/2003	11/08/2003	24	1.006	2632	0.55	Y
39	GERALDINE	-137.068	58.643	18/07/2003	11/08/2003	24	0.263	2006	0.45	Y
40	GERALDINE	-136.951	58.739	28/08/2003	05/09/2003	8	0.337	1969	0.68	Y
41	GERALDINE	-137.086	58.650	18/06/2004	05/08/2004	48	1.490	2889	0.48	Y
42	GERALDINE	-137.025	58.668	14/08/2004	22/08/2004	8	0.286	2126	0.56	Y
43	GERALDINE	-137.279	58.731	05/06/2005	08/07/2005	33	0.146	2124	0.74	Y
44	GERALDINE	-137.086	58.652	08/07/2005	24/07/2005	16	0.325	2761	0.74	Y
45	GERALDINE	-137.306	58.789	06/06/2005	24/07/2005	48	0.231	2157	0.60	Y
46	GERALDINE	-137.033	58.567	02/07/2005	09/08/2005	38	0.303	2296	0.54	Y
47	GERALDINE	-137.189	58.784	20/05/2008	29/05/2008	9	0.499	982	0.41	N
48	GERALDINE	-137.089	58.654	24/06/2009	10/07/2009	16	0.454	2678	0.47	Y
49	GERALDINE	-137.378	58.816	03/07/2009	04/08/2009	32	0.637	1713	0.29	Y
50	GERALDINE	-137.256	58.830	10/07/2009	04/08/2009	25	1.245	1989	0.48	N
51	GERALDINE	-137.377	58.708	29/08/2015	06/09/2015	8	0.144	1710	0.66	Y
52	GERALDINE	-137.031	58.668	05/05/2017	23/06/2017	49	0.456	2120	0.39	Y
53	GERALDINE	-136.980	58.778	23/06/2017	09/08/2017	47	1.206	2023	0.37	N
54	GERALDINE	-137.534	58.880	15/04/2018	08/05/2018	23	3.378	3297	0.45	P
55	GERALDINE	-137.058	58.680	01/06/2018	26/06/2018	25	0.325	2172	0.50	Y
56	GERALDINE	-137.088	58.653	01/06/2018	26/06/2018	25	0.317	2742	0.72	Y
57	GERALDINE	-137.383	58.887	01/06/2018	26/06/2018	25	0.231	2593	0.45	Y
58	GERALDINE	-137.053	58.672	01/06/2018	26/06/2018	25	0.290	2173	0.43	Y
59	GERALDINE	-137.402	58.885	28/07/2018	05/09/2018	39	0.135	2597	0.43	Y
60	GERALDINE	-136.995	58.863	12/05/2019	28/05/2019	16	0.176	1816	0.66	N
61	GERALDINE	-137.470	58.773	12/05/2019	13/06/2019	32	0.381	2157	0.47	Y
62	GERALDINE	-137.062	58.627	14/05/2020	21/05/2020	7	0.783	2318	0.37	U
63	GERALDINE	-137.030	58.664	21/05/2020	06/06/2020	16	0.133	2066	0.63	U
64	GERALDINE	-136.982	58.703	06/06/2020	15/06/2020	9	0.190	1899	0.45	U
65	GERALDINE	-136.992	58.721	01/07/2020	08/07/2020	7	0.306	2145	0.52	U
66	GERALDINE	-137.091	58.508	30/07/2020	18/08/2020	19	1.225	2105	0.32	U
67	GERALDINE	-137.448	58.768	11/08/2020	10/09/2020	30	1.740	2342	0.35	U
68	GERALDINE	-137.053	58.563	10/09/2020	19/09/2020	9	0.220	2498	0.43	U
69	GERALDINE	-137.011	58.576	30/07/2020	22/09/2020	54	0.494	2087	0.47	U

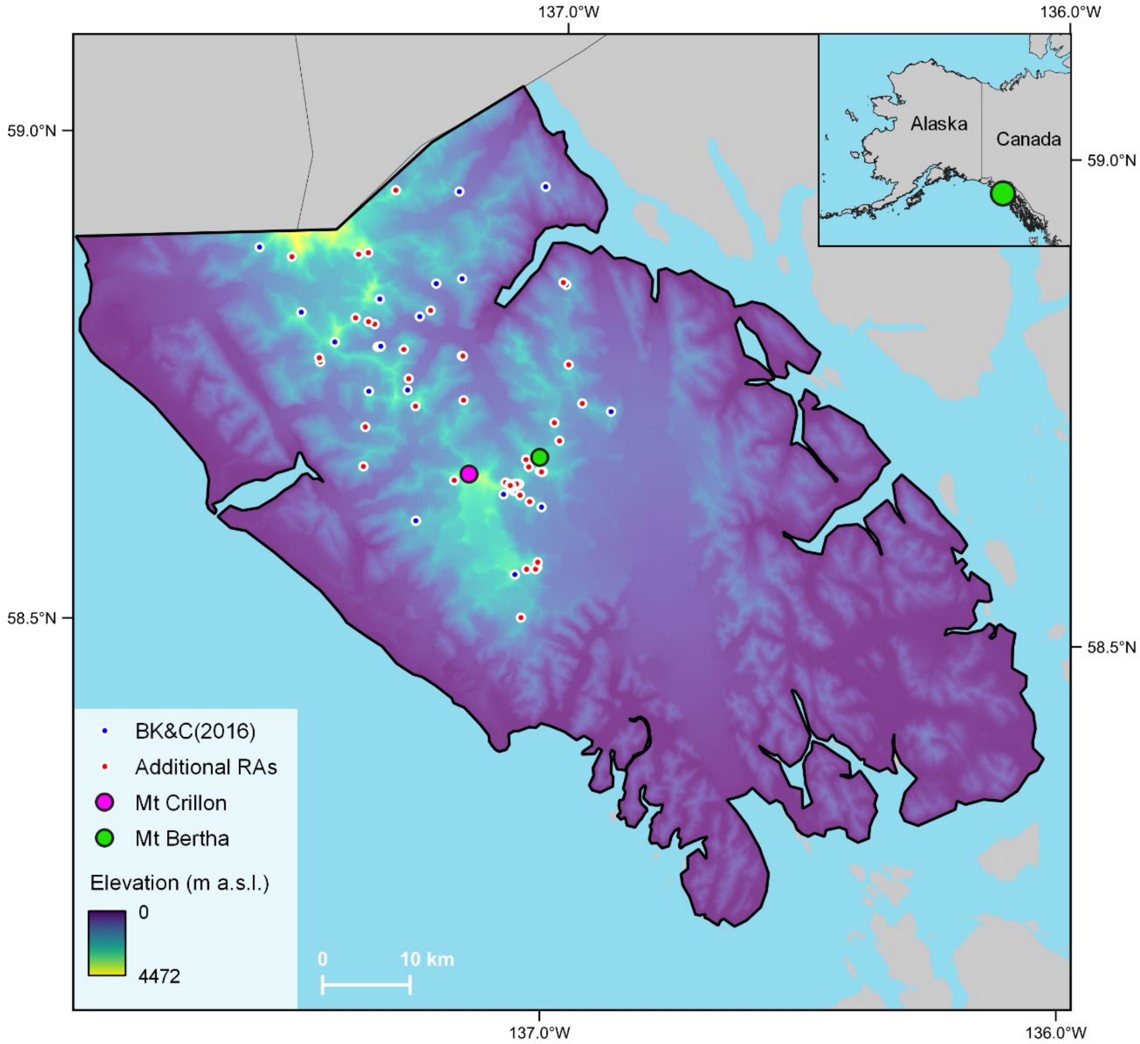

Figure S 7: Topography of Glacier Bay National Park and RA source locations

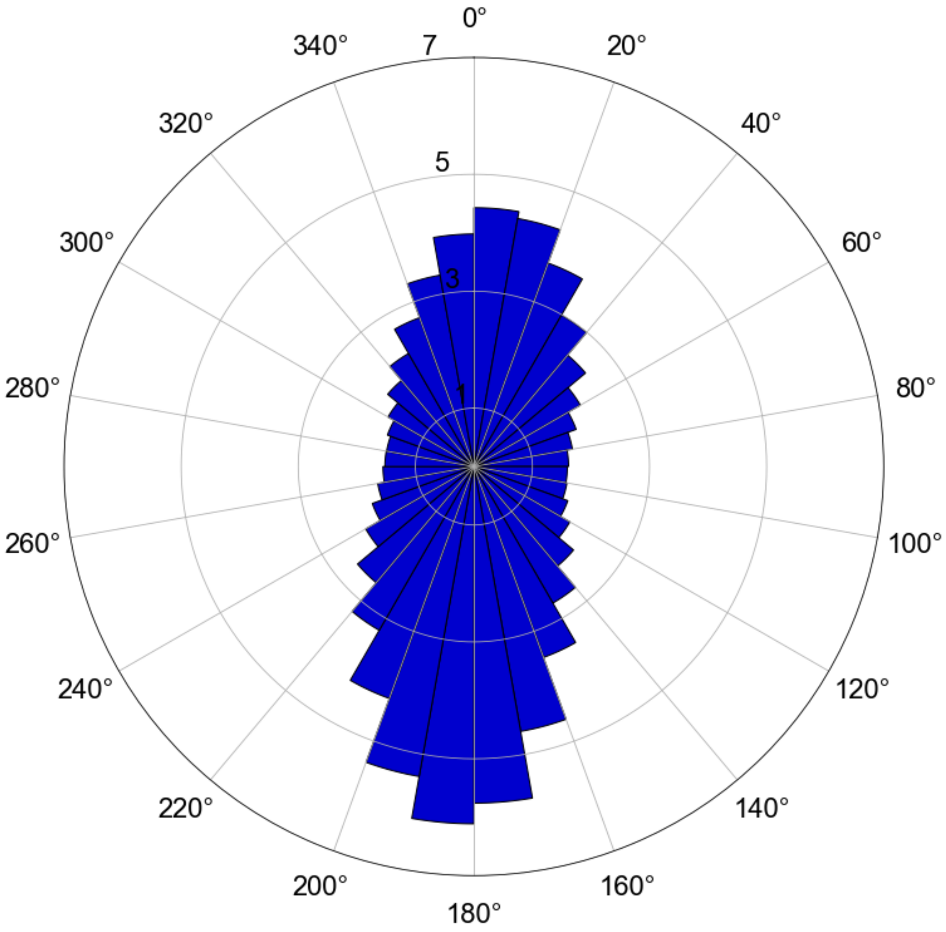

Figure S 8: Percentage aspect of all slopes in Glacier Bay National Park

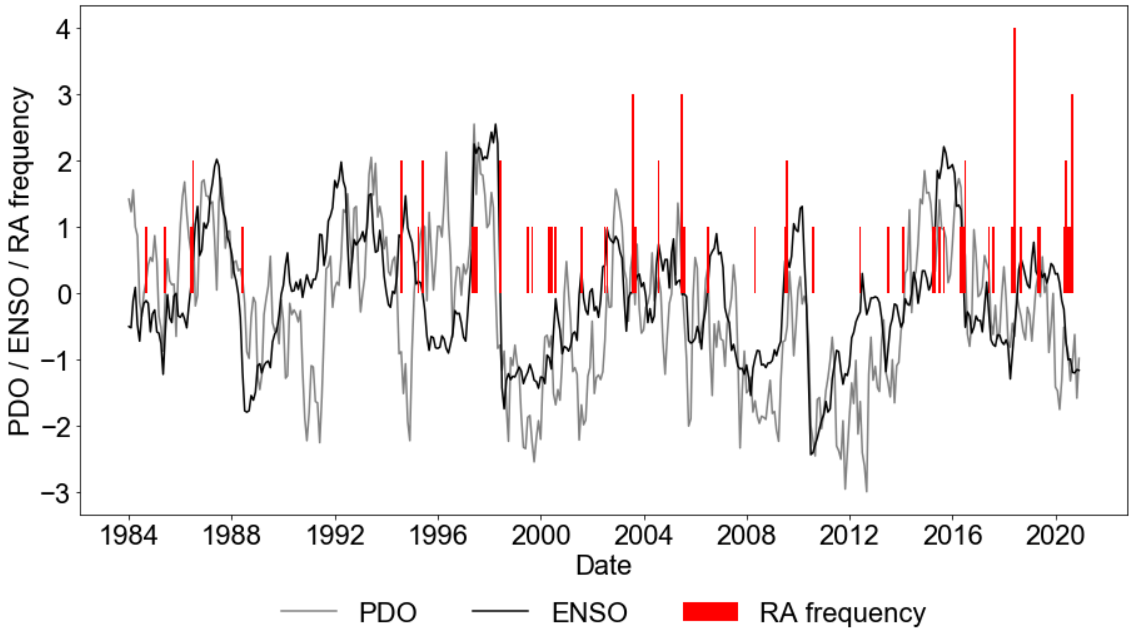

Figure S 9: Monthly Pacific Decadal Oscillation (PDO) index (NOAA, 2021) and Multivariate El-Nino Southern Oscillation (ENSO) index (MEI, Wolter and Timlin 2011), in comparison to rock avalanche (RA) monthly frequency in Glacier Bay National Park.

Chapter S3: Supporting information for Chapter 5

Table S 3: Grain size distribution statistics for rock avalanche fines and crushed rock

		Method of Moments Geometric (µm)			
Crushing	**Sample**	**Mean**	**Sorting**	**Skewness**	**Kurtosis**
N/A	Zone C	75.41	6.124	-0.498	2.278
	Zone D	71.48	6.559	-0.450	2.135
	Zone E	61.14	6.406	-0.327	2.023
	Zone F	104.6	6.620	-0.594	2.186
2 minutes	Sch	52.75	6.030	-0.234	1.911
	GSch	61.33	6.268	-0.445	2.101
	Q	136.7	4.950	-0.650	2.762
30 minutes	Sch	8.865	3.132	0.395	3.021
	GSch	13.70	4.574	-0.077	1.996
	Q	24.43	3.406	-0.432	2.521

Table S 4: Total Fe concentrations for each rock avalanche zone and each lithology sampled

	Total Fe (TFe)	
Sample	**µmol g^{-1}**	**wt%**
Zone C	1216.8 ± 1.3	6.8
Zone D	1113.1 ± 1.2	6.2
Zone E	988.1 ± 1.2	5.5
Zone F	966 ± 1.2	5.4
Schist	421.9 ± 0.6	2.4
Greenschist	1686.5 ± 2.3	9.4
Quartz	126.6 ± 0.3	0.7

S3.1. Lamplugh rock avalanche rock density calculations

Of the 25 clasts extracted from the Lamplugh RA deposit, 10 of the dominant lithology (schist) were selected for density calculations that varied between 55.9 g and 291.2 g (average 197.3 g). Clasts were weighed and then submerged in water to measure their displacement. Average rock density was 2.83 g cm^3 (Table S 5).

Table S 5: Weight, volume and density measurements for 10 clasts of dominant lithology (schist) extracted from the Lamplugh RA deposit.

Sample	Weight (g)	Volume (cm^3)	Density (g/cm^3)
ZES1_1	233.6	90	2.6
ZES1_2	244.2	85	2.87
ZES4_1	228.4	80	2.85
ZES4_2	286.3	100	2.86
ZES5_1	55.9	17	3.29
ZES5_2	162.4	60	2.71
ZFS1_1	291.2	100	2.91
ZFS4_1	175.9	65	2.71
ZFS4_2	100.7	35	2.88
ZFS4_3	140.5	50	2.81
ZFS5_1	251.2	95	2.64
Average	*197.2*	*70.64*	*2.83*

References

References

Aaron, J. and McDougall, S. (2019) ‘Rock avalanche mobility: The role of path material’, *Engineering Geology*, 257, p. 105126. doi: 10.1016/j.enggeo.2019.05.003.

Akhtar, M., Ahmad, N. and Booij, M. J. (2008) ‘The impact of climate change on the water resources of Hindukush-Karakorum-Himalaya region under different glacier coverage scenarios’, *Journal of Hydrology*, 355(1–4), pp. 148–163. doi: 10.1016/j.jhydrol.2008.03.015.

Alexander, D., Davies, T. and Shulmeister, J. (2014) ‘Formation of the Waiho Loop terminal moraine, New Zealand’, *Journal of Quaternary Science*, 29(4), pp. 361–369. doi: 10.1002/jqs.2707.

Allen, S. K., Cox, S. C. and Owens, I. F. (2011) ‘Rock avalanches and other landslides in the central Southern Alps of New Zealand: A regional study considering possible climate change impacts’, *Landslides*, 8(1), pp. 33–48. doi: 10.1007/s10346-010-0222-z.

Allen, S. K., Gruber, S. and Owens, I. F. (2009) ‘Exploring steep bedrock permafrost and its relationship with recent slope failures in the southern alps of New Zealand’, *Permafrost and Periglacial Processes*, 20(4), pp. 345–356. doi: 10.1002/ppp.658.

Andermann, C., Crave, A., *et al.* (2012) ‘Connecting source and transport: Suspended sediments in the Nepal Himalayas’, *Earth and Planetary Science Letters*, 351–352, pp. 158–170. doi: 10.1016/j.epsl.2012.06.059.

Andermann, C., Longuevergne, L., *et al.* (2012) ‘Impact of transient groundwater storage on the discharge of Himalayan rivers’, *Nature Geoscience*, 5(2), pp. 127–132. doi: 10.1038/ngeo1356.

Andermann, C., Bonnet, S., *et al.* (2012) ‘Sediment transfer and the hydrological cycle of Himalayan rivers in Nepal’, *Comptes Rendus - Geoscience*, 344(11–12), pp. 627–635. doi: 10.1016/j.crte.2012.10.009.

Anderson, J.B. (1999). *Antarctic Marine Geology*. Cambridge, UK: Cambridge University Press, 289pp.

Anderson, L. S. *et al.* (2021) ‘The Causes of Debris-Covered Glacier Thinning: Evidence for the Importance of Ice Dynamics From Kennicott Glacier, Alaska’, *Frontiers in Earth Science*, 9, p. 723. doi: 10.3389/feart.2021.680995.

Anderson, L. S. and Anderson, R. S. (2016) ‘Modeling debris-covered glaciers: response to steady debris deposition', *The Cryosphere*, 10, pp. 1105–1124. doi: 10.5194/tc-10-1105-2016.

Anderson, R. S. (2000) 'A model of ablation-dominated medial moraines and the generation of debris-mantled glacier snouts', *Journal of Glaciology*, 46(154), pp. 459–469. doi: 10.3189/172756500781833025.

Anesio, A. M. *et al.* (2017) 'The microbiome of glaciers and ice sheets', *npj Biofilms and Microbiomes*. Nature Publishing Group, pp. 1–11. doi: 10.1038/s41522-017-0019-0.

Antoniazza, G. and Lane, S. N. (2021) 'Sediment yield over glacial cycles: A conceptual model', *Progress in Physical Geography*, 45(6), pp. 842–865. doi: 10.1177/0309133321997292.

Armstrong, W. H. and Anderson, R. S. (2020) 'Ice-marginal lake hydrology and the seasonal dynamical evolution of Kennicott Glacier, Alaska', *Journal of Glaciology*, 66(259), pp. 699–713. doi: 10.1017/jog.2020.41.

Arp, C. D. *et al.* (2020) 'Recurring outburst floods from drained lakes: an emerging Arctic hazard', *Frontiers in Ecology and the Environment*, 18(7), pp. 384–390. doi: 10.1002/fee.2175.

Arrigo, K. R. *et al.* (2017) 'Melting glaciers stimulate large summer phytoplankton blooms in southwest Greenland waters', *Geophysical Research Letters*, 44(12), pp. 6278–6285. doi: 10.1002/2017GL073583.

Augustinus, P. (1995) 'Rock mass strength and the stability of some glacial valley slopes', *Zeitschrift fur Geomorphologie*, 39(1). doi: 10.1016/0148-9062(96)87568-1.

de Baar, H. J. W. *et al.* (1995) 'Importance of iron for plankton blooms and carbon dioxide drawdown in the Southern Ocean', *Nature*, pp. 412–415. doi: 10.1038/373412a0.

Ballantyne, C. K. (2002a) 'A general model of paraglacial landscape response', *Holocene*. Sage PublicationsSage CA: Thousand Oaks, CA, pp. 371–376. doi: 10.1191/0959683602hl553fa.

Ballantyne, C. K. (2002b) 'Paraglacial geomorphology', *Quaternary Science Reviews*. Elsevier Ltd, pp. 1935–2017. doi: 10.1016/S0277-3791(02)00005-7.

Ballantyne, C. K., Wilson, P., *et al.* (2014) 'Enhanced rock-slope failure following ice-sheet deglaciation: Timing and causes', *Earth Surface Processes and Landforms*, 39(7), pp. 900–913. doi: 10.1002/esp.3495.

Ballantyne, C. K., Sandeman, G. F., *et al.* (2014) ‘Rock-slope failure following Late Pleistocene deglaciation on tectonically stable mountainous terrain’, *Quaternary Science Reviews*, 86, pp. 144–157. doi: 10.1016/j.quascirev.2013.12.021.

Ballantyne, C. K. and Stone, J. O. (2013) ‘Timing and periodicity of paraglacial rock-slope failures in the Scottish Highlands’, *Geomorphology*, 186, pp. 150–161. doi: 10.1016/j.geomorph.2012.12.030.

Bamber, J. L. *et al.* (2018) ‘The land ice contribution to sea level during the satellite era’, *Environmental Research Letters*. Institute of Physics Publishing, p. 063008. doi: 10.1088/1748-9326/aac2f0.

Barkdull, N. S. *et al.* (2021) ‘Glaciers Control the Hydrogeochemistry of Proglacial Streams During Late Summer in the Wind River Range, Wyoming, United States’, *Frontiers in Earth Science*, 9, p. 977. doi: 10.3389/feart.2021.727575.

Barnes, P. and Tabor, D. (1966) ‘Plastic flow and pressure melting in the deformation of ice I’, *Nature*, 210(5039), pp. 878–882. doi: 10.1038/210878a0.

Barouillet, C. *et al.* (2019) ‘Influence of glacial flour on the primary and secondary production of sockeye salmon nursery lakes: A comparative modern and paleolimnological study’, *Canadian Journal of Fisheries and Aquatic Sciences*, 76(12), pp. 2303–2314. doi: 10.1139/cjfas-2018-0372.

Barry, R. G. (2011) ‘The cryosphere-past,present,and future: a review of the frozen water resources of the world’, *Polar Geography*. Taylor & Francis Group, pp. 219–227. doi: 10.1080/1088937X.2011.638146.

Barry, R. G. and Gan, T. Y. (2011) *The global cryosphere: Past, present, and future*, *The Global Cryosphere: Past, Present, and Future*. New York: Cambridge University Press. doi: 10.1017/CBO9780511977947.

Bartholomew, I. *et al.* (2011) ‘Supraglacial forcing of subglacial drainage in the ablation zone of the Greenland ice sheet’, *Geophysical Research Letters*, 38(8). doi: 10.1029/2011GL047063.

Belousov, A., Belousova, M. and Voight, B. (1999) ‘Multiple edifice failures, debris avalanches and associated eruptions in the Holocene history of Shiveluch volcano, Kamchatka, Russia', *Bulletin of Volcanology*, 61(5), pp. 324–342. doi: 10.1007/s004450050300.

Benn, D. *et al.* (2017) 'Structure and evolution of the drainage system of a Himalayan debris-covered glacier, and its relationship with patterns of mass loss', *Cryosphere*, 11(5), pp. 2247–2264. doi: 10.5194/tc-11-2247-2017.

Benn, D. I. (2009) 'Glacial sediments', in *Encyclopedia of Earth Sciences Series*. Springer Netherlands, pp. 1234–1236. doi: 10.1007/978-1-4020-4411-3_95.

Benn, D. I. *et al.* (2012) 'Response of debris-covered glaciers in the Mount Everest region to recent warming, and implications for outburst flood hazards', *Earth-Science Reviews*. Elsevier, pp. 156–174. doi: 10.1016/j.earscirev.2012.03.008.

Benn, D. I. *et al.* (2014) 'Glaciated valley landsystems', in *Glacial Landsystems*. doi: 10.4324/9780203784976.

Benn, D. I., Wiseman, S. and Hands, K. A. (2001) 'Growth and drainage of supraglacial lakes on debrismantled Ngozumpa Glacier, Khumbu Himal, Nepal', *Journal of Glaciology*, 47(159), pp. 626–638. doi: 10.3189/172756501781831729.

Berger, W. H., Smetacek, V. and Wefer, G. (1989) 'Ocean Productivity and Paleoproductivity - An Overview', *Productivity of the Ocean: Present and Past*. New York: Wiley, pp. 1–34.

Bergquist, B. A., Wu, J. and Boyle, E. A. (2007) 'Variability in oceanic dissolved iron is dominated by the colloidal fraction>', *Geochimica et Cosmochimica Acta*, 71(12), pp. 2960–2974. doi: 10.1016/j.gca.2007.03.013.

Berthier, E. *et al.* (2010) 'Contribution of Alaskan glaciers to sea-level rise derived from satellite imagery', *Nature Geoscience*, 3(2), pp. 92–95. doi: 10.1038/ngeo737.

Bessette-Kirton, E. and Coe, J. (2020) 'A 36-Year Record of Rock Avalanches in the Saint Elias Mountains of Alaska, With Implications for Future Hazards', *Frontiers in Earth Science*, 8, p. 293. doi: 10.3389/feart.2020.00293.

Bessette-Kirton, EK, Coe, JA. (2016) Inventory of rock avalanches in western Glacier Bay National Park and Preserve, Alaska, 1984–2016: a baseline data set for evaluating the impact of climate change on avalanche magnitude, mobility, and frequency. U.S. Geological Survey data release, https://doi.org/10.5066/F7C827F8

Bessette-Kirton, E. K., Coe, J. A. and Zhou, W. (2018) ‘Using Stereo Satellite Imagery to Account for Ablation, Entrainment, and Compaction in Volume Calculations for Rock Avalanches on Glaciers: Application to the 2016 Lamplugh Rock Avalanche in Glacier Bay National Park, Alaska’, *Journal of Geophysical Research: Earth Surface*, 123(4), pp. 622–641. doi: 10.1002/2017JF004512.

Bhardwaj, A. *et al.* (2015) ‘Applicability of Landsat 8 data for characterizing glacier facies and supraglacial debris’, *International Journal of Applied Earth Observation and Geoinformation*, 38, pp. 51–64. doi: 10.1016/j.jag.2014.12.011.

Bhatia, M. P. *et al.* (2013) ‘Greenland meltwater as a significant and potentially bioavailable source of iron to the ocean’, *Nature Geoscience*, 6(4), pp. 274–278. doi: 10.1038/ngeo1746.

Bhatt, M. P., Takeuchi, N. and Acevedo, M. F. (2016) ‘Chemistry of Supraglacial Ponds in the Debris-Covered Area of Lirung Glacier in Central Nepal Himalayas’, *Aquatic Geochemistry*, 22(1). doi: 10.1007/s10498-015-9276-9.

Bhutiyani, M. R. and Mahto, R. (2018) ‘Remote-sensing-based study of impact of a rock avalanche on North Terong Glacier in Karakorum Himalaya’, *International Journal of Remote Sensing*, 39(22), pp. 8076–8091. doi: 10.1080/01431161.2018.1480073.

Blain, S., Sarthou, G. and Laan, P. (2008) ‘Distribution of dissolved iron during the natural iron-fertilization experiment KEOPS (Kerguelen Plateau, Southern Ocean)’, *Deep Sea Research Part II: Topical Studies in Oceanography*, 55(5–7), pp. 594–605. doi: 10.1016/J.DSR2.2007.12.028.

De Blasio, F. V. (2014) ‘Friction and dynamics of rock avalanches travelling on glaciers’, *Geomorphology*, 213. doi: 10.1016/j.geomorph.2014.01.001.

Blöthe, J. H., Korup, O. and Schwanghart, W. (2015) ‘Large landslides lie low: Excess topography in the Himalaya-Karakoram ranges’, *Geology*, 43(6), pp. 523–526. doi: 10.1130/G36527.1.

Blott, S. J. and Pye, K. (2001) ‘GRADISTAT: a grain size distribution and statistics package for the analysis of unconsolidated sediments’, *Earth Surface Processes and Landforms*, 26(11), pp. 1237–1248. doi: 10.1002/ESP.261.

Bolt, B. A. *et al.* (1975) ‘Hazards from Landslides’, in *Geological Hazards*. Springer Berlin Heidelberg, pp. 148–197. doi: 10.1007/978-3-642-86820-7_4.

Booth, A. D. *et al.* (2013) ‘A comparison of seismic and radar methods to establish the thickness and density of glacier snow cover’, *Annals of Glaciology*, 54(64), pp. 73–82. doi: 10.3189/2013AoG64A044.

Boulton, G. S. (1970) ‘On the Deposition of Subglacial and Melt-Out tills at the Margins of Certain Svalbard Glaciers’, *Journal of Glaciology*, 9(56), pp. 231–245. doi: 10.3189/s0022143000023546.

Boyd, P. W. *et al.* (2004) ‘The decline and fate of an iron-induced subarctic phytoplankton bloom’, *Nature*, 428(6982), pp. 549–553. doi: 10.1038/nature02437.

Boyd, P. W. *et al.* (2007) ‘Mesoscale Iron Enrichment Experiments 1993-2005: Synthesis and Future Directions’, *Science*, 315(5812), pp. 612–617. doi: 10.1126/SCIENCE.1131669.

Boyd, P. W. and Ellwood, M. J. (2010) ‘The biogeochemical cycle of iron in the ocean’, *Nature Geoscience*, 3(10), pp. 675–682. doi: 10.1038/ngeo964.

Breitbarth, E. *et al.* (2009) ‘Dissolved iron (II) in the Baltic Sea surface water and implications for cyanobacterial bloom development’, *Biogeosciences*, 6(11), pp. 2397–2420. doi: 10.5194/bg-6-2397-2009.

Brock, B. W. *et al.* (2010) ‘Meteorology and surface energy fluxes in the 2005-2007 ablation seasons at the Miage debris-covered glacier, Mont Blanc Massif, Italian Alps’, *Journal of Geophysical Research Atmospheres*, 115(9), p. 9106. doi: 10.1029/2009JD013224.

Brykala, D. and Arazny, A. (2000) ‘Influence of meteorological conditions to the surface run-off on the Waldemar Glacier (NW Spitsbergen) in the summer of 1997’, *Problemy Klimatologii Polarnej*, 10, pp. 139–158. Available at: https://www.researchgate.net/publication/230583383_Influence_of_meteorological_conditions_to_the_surface_run-off_on_the_Waldemar_Glacier_NW_Spitsbergen_in_the_summer_of_1997 (Accessed: 14 December 2021).

Bullard, J. E. (2013) ‘Contemporary glacigenic inputs to the dust cycle’, *Earth Surface Processes and Landforms*, 38(1), pp. 71–89. doi: 10.1002/ESP.3315.

Burbank, D. W. and Anderson, R. S. (2011) *Tectonic Geomorphology: Second Edition*, *Tectonic Geomorphology: Second Edition*. doi: 10.1002/9781444345063.

Burgess, E. W., Forster, R. R. and Larsen, C. F. (2013) 'Flow velocities of Alaskan glaciers', *Nature Communications*, 4(1), p. 2146. doi: 10.1038/ncomms3146.

Buri, P. *et al.* (2016) 'A physically based 3-D model of ice cliff evolution over debris-covered glaciers', *Journal of Geophysical Research: Earth Surface*, 121(12), pp. 2471–2493. doi: 10.1002/2016JF004039.

Burns, P. and Nolin, A. (2014) 'Using atmospherically-corrected Landsat imagery to measure glacier area change in the Cordillera Blanca, Peru from 1987 to 2010', *Remote Sensing of Environment*, 140, pp. 165–178. doi: 10.1016/j.rse.2013.08.026.

Burt, T. P. and Allison, R. J. (2009) *Sediment Cascades: An Integrated Approach*, *Sediment Cascades: An Integrated Approach*. doi: 10.1002/9780470682876.

Burt, T. P. and Pinay, G. (2005) 'Linking hydrology and biogeochemistry in complex landscapes', *Progress in Physical Geography*, pp. 297–316. doi: 10.1191/0309133305pp450ra.

Burton-Johnson, A. *et al.* (2016) 'An automated methodology for differentiating rock from snow, clouds and sea in Antarctica from Landsat 8 imagery: A new rock outcrop map and area estimation for the entire Antarctic continent', *Cryosphere*, 10(4), pp. 1665–1677. doi: 10.5194/tc-10-1665-2016.

Carling, P. A. (2013) 'Freshwater megaflood sedimentation: What can we learn about generic processes?', *Earth-Science Reviews*, 125, pp. 87–113. doi: 10.1016/J.EARSCIREV.2013.06.002.

Carlson, D. F. *et al.* (2017) 'Bergy bit and melt water trajectories in Godthåbsfjord (SW Greenland) observed by the expendable ice tracker', *Frontiers in Marine Science*, 4(AUG). doi: 10.3389/fmars.2017.00276.

Carrivick, J. L. *et al.* (2013) 'Contemporary geomorphological activity throughout the proglacial area of an alpine catchment', *Geomorphology*, 188, pp. 83–95. doi: 10.1016/j.geomorph.2012.03.029.

Carrivick, J. L. and Heckmann, T. (2017) 'Short-term geomorphological evolution of proglacial systems', *Geomorphology*, 287, pp. 3–28. doi:

10.1016/j.geomorph.2017.01.037.

Carrivick, J. L. and Tweed, F. S. (2016) ‘A global assessment of the societal impacts of glacier outburst floods’, *Global and Planetary Change*, 144, pp. 1–16. doi: 10.1016/j.gloplacha.2016.07.001.

Chadburn, S. E. *et al.* (2017) ‘An observation-based constraint on permafrost loss as a function of global warming’, *Nature Climate Change*, 7(5), pp. 340–344. doi: 10.1038/nclimate3262.

Chander, G., Markham, B. L. and Helder, D. L. (2009) ‘Summary of current radiometric calibration coefficients for Landsat MSS, TM, ETM+, and EO-1 ALI sensors’, *Remote Sensing of Environment*, 113(5), pp. 893–903. doi: 10.1016/j.rse.2009.01.007.

Chen, T. *et al.* (2020) ‘Reactive iron isotope signatures of the East Asian dust particles: Implications for iron cycling in the deep North Pacific’, *Chemical Geology*, 531, p. 119342. doi: 10.1016/j.chemgeo.2019.119342.

Chiarle, M. *et al.* (2015) ‘High Elevation Rock Falls and Their Climatic Control: A Case Study in the Conca Di Cervinia (NW Italian Alps)’, in *Engineering Geology for Society and Territory - Volume 1: Climate Change and Engineering Geology*. Springer International Publishing, pp. 439–442. doi: 10.1007/978-3-319-09300-0_84.

Choi, Y. *et al.* (2021) ‘Ice dynamics will remain a primary driver of Greenland ice sheet mass loss over the next century’, *Communications Earth and Environment*, 2(1), pp. 1–9. doi: 10.1038/s43247-021-00092-z.

Clague, J. J. and O’Connor, J. E. (2015) ‘Glacier-Related Outburst Floods’, in *Snow and Ice-Related Hazards, Risks, and Disasters*. Elsevier Inc., pp. 487–519. doi: 10.1016/B978-0-12-394849-6.00014-7.

Clark, K. E. *et al.* (2016) ‘Storm-triggered landslides in the Peruvian Andes and implications for topography, carbon cycles, and biodiversity’, *Earth Surface Dynamics*, 4(1), pp. 47–70. doi: 10.5194/esurf-4-47-2016.

Clauset, A., Shalizi, C. R. and Newman, M. E. J. (2009) ‘Power-law distributions in empirical data’, *SIAM Review*. Society for Industrial and Applied Mathematics, pp. 661–703. doi: 10.1137/070710111.

Coe, J. A. (2020) ‘Bellwether sites for evaluating changes in landslide frequency and magnitude in cryospheric mountainous terrain: a call for systematic, long-term observations to decipher the impact of climate change', *Landslides*. Springer, pp. 2483–2501. doi: 10.1007/s10346-020-01462-y.

Coe, J. A., Bessette-Kirton, E. K. and Geertsema, M. (2018) 'Increasing rock-avalanche size and mobility in Glacier Bay National Park and Preserve, Alaska detected from 1984 to 2016 Landsat imagery', *Landslides*, 15(3), pp. 393–407. doi: 10.1007/s10346-017-0879-7.

Collier, E. *et al.* (2015) 'Impact of debris cover on glacier ablation and atmosphere-glacier feedbacks in the Karakoram', *Cryosphere*, 9(4), pp. 1617–1632. doi: 10.5194/tc-9-1617-2015.

Collins, G. S. and Melosh, H. J. (2003) 'Acoustic fluidization and the extraordinary mobility of sturzstroms', *Journal of Geophysical Research: Solid Earth*, 108(B10). doi: 10.1029/2003jb002465.

Connor, C. *et al.* (2009) 'The Neoglacial landscape and human history of Glacier Bay, Glacier Bay National Park and Preserve, southeast Alaska, USA', *The Holocene*, 19(3), pp. 381–393. doi: 10.1177/0959683608101389.

Conway, T. M. and John, S. G. (2014) 'Quantification of dissolved iron sources to the North Atlantic Ocean', *Nature*, 511(7508), pp. 212–215. doi: 10.1038/nature13482.

Cook, J. M., Hodson, A. J. and Irvine-Fynn, T. D. L. L. (2016) 'Supraglacial weathering crust dynamics inferred from cryoconite hole hydrology', *Hydrological Processes*. doi: 10.1002/hyp.10602.

Cook, S. J. and Swift, D. A. (2012) 'Subglacial basins: Their origin and importance in glacial systems and landscapes', *Earth-Science Reviews*, pp. 332–372. doi: 10.1016/j.earscirev.2012.09.009.

Cornell, R. M. and Schwertmann, U. (2003) *The Iron Oxides*, *The Iron Oxides*. New York: Wiley. doi: 10.1002/3527602097.

Cowan, E. A. *et al.* (2010) 'Fjords as temporary sediment traps: History of glacial erosion and deposition in Muir Inlet, Glacier Bay National Park, southeastern Alaska', *GSA Bulletin*, 122(7–8), pp. 1067–1080. doi: 10.1130/B26595.1.

Cowton, T. *et al.* (2013) 'Evolution of drainage system morphology at a land-terminating

Greenlandic outlet glacier', *Journal of Geophysical Research: Earth Surface*, 118(1), pp. 29–41. doi: 10.1029/2012JF002540.

Coyle, K. O., Hermann, A. J. and Hopcroft, R. R. (2019) 'Modeled spatial-temporal distribution of productivity, chlorophyll, iron and nitrate on the northern Gulf of Alaska shelf relative to field observations', *Deep Sea Research Part II: Topical Studies in Oceanography*, 165, pp. 163–191. doi: 10.1016/J.DSR2.2019.05.006.

Croissant, T. *et al.* (2021) 'Pulsed carbon export from mountains by earthquake-Triggered landslides explored in a reduced-complexity model', *Earth Surface Dynamics*, 9(4), pp. 823–844. doi: 10.5194/esurf-9-823-2021.

Crosta, G. B., Frattini, P. and Fusi, N. (2007) 'Fragmentation in the Val Pola rock avalanche, Italian Alps', *Journal of Geophysical Research: Earth Surface*, 112(F1), p. 1006. doi: 10.1029/2005JF000455.

Crozier, M. J. and Glade, T. (2005) 'The Nature of Landslide Hazard Impact', in Glade, T., Anderson, M., and Crozier, M. J. (eds) *Landslide Hazard and Risk*. 1st edn. Chichester: John Wiley & Sons, Ltd, pp. 43–74. doi: 10.1002/9780470012659.ch2.

Cruden D.M. and Varnes D.J. (1996) 'Landslide types and processes'. In: Turner AK, Schuster RL (eds) *Landslides investigation and mitigation*. Transportation research board, US National Research Council. Special Report 247, Washington, DC, Chapter 3, pp. 36–75.

Crumley, R. L. *et al.* (2019) 'Seasonal components of freshwater runoff in Glacier Bay, Alaska: Diverse spatial patterns and temporal change', *Cryosphere*, 13(6), pp. 1597–1619. doi: 10.5194/tc-13-1597-2019.

Crusius, J. *et al.* (2011) 'Glacial flour dust storms in the Gulf of Alaska: Hydrologic and meteorological controls and their importance as a source of bioavailable iron', *Geophysical Research Letters*, 38(6). doi: 10.1029/2010GL046573.

Dahlström, L.-O. (1992) *Rock mechanical consequences of refrigeration: a study based on a pilot scale rock cavern*. Chalmers University of Technology. Available at: https://research.chalmers.se/en/publication/1470 (Accessed: 10 May 2021).

Das, S., Hendry, M. J. and Essilfie-Dughan, J. (2011) 'Transformation of two-line ferrihydrite to goethite and hematite as a function of pH and temperature', *Environmental Science and Technology*, 45(1), pp. 268–275. doi: 10.1021/es101903y.

Davies, M. C. R., Hamza, O. and Harris, C. (2001) ‘The effect of rise in mean annual temperature on the stability of rock slopes containing ice-filled discontinuities’, *Permafrost and Periglacial Processes*, 12(1), pp. 137–144. doi: 10.1002/ppp.378.

Davies, T. and McSaveney, M. (2013) ‘Mobility of long-runout rock avalanches’, in Clague, J. J. and Stead, D. (eds) *Landslides*. New York: Cambridge University Press, pp. 50–58. doi: 10.1017/cbo9780511740367.006.

Davies, T. R. H. (1982) ‘Spreading of rock avalanche debris by mechanical fluidization’, *Rock Mechanics Felsmechanik Mécanique des Roches*, 15(1), pp. 9–24. doi: 10.1007/BF01239474.

Davies, T. R. and McSaveney, M. J. (1999) ‘Runout of dry granular avalanches’, *Canadian Geotechnical Journal*, 36(2), pp. 313–320. doi: 10.1139/t98-108.

Davies, T. R. and McSaveney, M. J. (2009) ‘The role of rock fragmentation in the motion of large landslides’, *Engineering Geology*, 109(1–2), pp. 67–79. doi: 10.1016/j.enggeo.2008.11.004.

Davison, B. J. *et al.* (2019) ‘The influence of hydrology on the dynamics of land-terminating sectors of the Greenland ice sheet’, *Frontiers in Earth Science*, 7, p. 10. doi: 10.3389/feart.2019.00010.

Death, R. *et al.* (2014) ‘Antarctic ice sheet fertilises the Southern Ocean’, *Biogeosciences*, 11(10), pp. 2635–2643. doi: 10.5194/bg-11-2635-2014.

DeConto, R. M. and Pollard, D. (2016) ‘Contribution of Antarctica to past and future sea-level rise’, *Nature*, 531(7596), pp. 591–597. doi: 10.1038/nature17145.

Delaney, I. and Anderson, L. S. (2022) ‘Debris Cover Limits Subglacial Erosion and Promotes Till Accumulation’, *Geophysical Research Letters*, 49(16), p. e2022GL099049. doi: 10.1029/2022gl099049.

Delaney, K. B. and Evans, S. G. (2014) ‘The 1997 Mount Munday landslide (British Columbia) and the behaviour of rock avalanches on glacier surfaces’, *Landslides*, 11(6), pp. 1019–1036. doi: 10.1007/s10346-013-0456-7.

Delannay, R. *et al.* (2017) ‘Granular and particle-laden flows: From laboratory experiments to field observations’, *Journal of Physics D: Applied Physics*. IOP Publishing, p. 053001. doi: 10.1088/1361-6463/50/5/053001.

Deline, P. (2001) ‘Recent Brenva rock avalanches (Valley of Aosta): new chapter in an old story?’, *Geografiska Annaler. Series A, Physical Geography*, (7), pp. 55–63.

Deline, P. (2005) ‘Change in surface debris cover on Mont Blanc massif glaciers after the “Little Ice Age” termination’, *Holocene*, 15(2), pp. 302–309. doi: 10.1191/0959683605hl809rr.

Deline, P. (2009) ‘Interactions between rock avalanches and glaciers in the Mont Blanc massif during the late Holocene’, *Quaternary Science Reviews*, 28(11–12), pp. 1070–1083. doi: 10.1016/J.QUASCIREV.2008.09.025.

Deline, P., Gruber, S., *et al.* (2014) ‘Ice Loss and Slope Stability in High-Mountain Regions’, in *Snow and Ice-Related Hazards, Risks, and Disasters*. doi: 10.1016/B978-0-12-394849-6.00015-9.

Deline, P., Hewitt, K., *et al.* (2014) ‘Rock Avalanches onto Glaciers’, in Davies, T. (ed.) *Landslide Hazards, Risks, and Disasters*. 1st edn. San Diego, CA: Elsevier, pp. 263–319. doi: 10.1016/B978-0-12-396452-6.00009-4.

Deprez, M. *et al.* (2020) ‘A review on freeze-thaw action and weathering of rocks’, *Earth-Science Reviews*. Elsevier B.V., p. 103143. doi: 10.1016/j.earscirev.2020.103143.

Ding, Y. *et al.* (2021) ‘Increasing cryospheric hazards in a warming climate’, *Earth-Science Reviews*, p. 103500. doi: 10.1016/j.earscirev.2020.103500.

Diolaiuti, G. A. *et al.* (2012) ‘The 1975-2005 glacier changes in Aosta Valley (Italy) and the relations with climate evolution’, *Progress in Physical Geography*, 36(6), pp. 764–785. doi: 10.1177/0309133312456413.

Domack, E. W. and Powell, R. (2018) ‘Modern Glaciomarine Environments and Sediments: An Antarctic Perspective’, in Menzies, J. and van der Meer, J. J. M. (eds) *Past Glacial Environments: Second Edition*. 2nd edn. Elsevier, pp. 181–272. doi: 10.1016/B978-0-08-100524-8.00030-0.

Domine, F., Taillandier, A. S. and Simpson, W. R. (2007) ‘A parameterization of the specific surface area of seasonal snow for field use and for models of snowpack evolution’, *Journal of Geophysical Research: Earth Surface*, 112(2), p. 2031. doi: 10.1029/2006JF000512.

Douglas, T. A. and Sturm, M. (2004) ‘Arctic haze, mercury and the chemical composition of snow across northwestern Alaska', *Atmospheric Environment*, 38(6), pp. 805–820. doi: 10.1016/j.atmosenv.2003.10.042.

Dow, C. F. *et al.* (2015) 'Modeling of subglacial hydrological development following rapid supraglacial lake drainage', *Journal of Geophysical Research: Earth Surface*, 120(6), pp. 1127–1147. doi: 10.1002/2014JF003333.

Dowdeswell, J. A. *et al.* (2015) 'Sediment-rich meltwater plumes and ice-proximal fans at the margins of modern and ancient tidewater glaciers: Observations and modeling', *Sedimentology*, 62(6), pp. 1665–1692. doi: 10.1111/sed.12198.

Dowdeswell, J. A. *et al.* (2016) 'The variety and distribution of submarine glacial landforms and implications for ice-sheet reconstruction', *Geological Society Memoir*, 46(1), pp. 519–552. doi: 10.1144/M46.183.

Draebing, D. and Krautblatter, M. (2012) 'P-wave velocity changes in freezing hard low-porosity rocks: A laboratory-based time-average model', *Cryosphere*, 6(5), pp. 1163–1174. doi: 10.5194/tc-6-1163-2012.

Duan, Y. *et al.* (2020) 'Accurate simulation of ice and snow runoff for the mountainous terrain of the Kunlun Mountains, China', *Remote Sensing*, 12(1), p. 179. doi: 10.3390/RS12010179.

Ducklow, H. W. (1999) 'The bacterial component of the oceanic euphotic zone', *FEMS Microbiology Ecology*, 30(1), pp. 1–10. doi: 10.1111/J.1574-6941.1999.TB00630.X.

Dufresne, A. (2017) 'Rock Avalanche Sedimentology—Recent Progress', *Advancing Culture of Living with Landslides*, pp. 117–122. doi: 10.1007/978-3-319-53498-5_14.

Dufresne, A. *et al.* (2019) 'The 2016 Lamplugh rock avalanche, Alaska: deposit structures and emplacement dynamics', *Landslides*, pp. 1–19. doi: 10.1007/s10346-019-01225-4.

Dufresne, A., Bösmeier, A. and Prager, C. (2016) 'Sedimentology of rock avalanche deposits – Case study and review', *Earth-Science Reviews*, 163, pp. 234–259. doi: 10.1016/J.EARSCIREV.2016.10.002.

Dufresne, A. and Davies, T. R. (2009) 'Longitudinal ridges in mass movement deposits', *Geomorphology*, 105(3–4), pp. 171–181. doi: 10.1016/j.geomorph.2008.09.009.

Dufresne, A. and Dunning, S. A. (2017) 'Process dependence of grain size distributions in rock avalanche deposits', *Landslides*, 14(5), pp. 1555–1563. doi: 10.1007/s10346-017-

0806-y.

Dufresne, A., Prager, C. and Bösmeier, A. (2016) ‘Insights into rock avalanche emplacement processes from detailed morpho-lithological studies of the Tschirgant deposit (Tyrol, Austria)’, *Earth Surface Processes and Landforms*, 41(5), pp. 587–602. doi: 10.1002/esp.3847.

Dunning, S. A. *et al.* (2015) ‘Rapid sequestration of rock avalanche deposits within glaciers’, *Nature Communications*, 6, p. 7964. doi: 10.1038/ncomms8964.

Duprat, L. P. A. M., Bigg, G. R. and Wilton, D. J. (2016) ‘Enhanced Southern Ocean marine productivity due to fertilization by giant icebergs’, *Nature Geoscience*, 9(3), pp. 219–221. doi: 10.1038/ngeo2633.

Dwivedi, R. D. *et al.* (1998) ‘Compressive strength and tensile strength of rocks at sub-zero temperature’, *Indian Journal of Engineering and Materials Sciences*, 5(1), pp. 43–48.

Eberhardt, E., Stead, D. and Coggan, J. S. (2004) ‘Numerical analysis of initiation and progressive failure in natural rock slopes-the 1991 Randa rockslide’, *International Journal of Rock Mechanics and Mining Sciences*, 41(1), pp. 69–87. doi: 10.1016/S1365-1609(03)00076-5.

Eisbacher, G.H., Clague, J.J. (1984) Destructive mass movements in high mountains: hazard and management. Geol. Surv. Can. Pap. 84-16, 230 pp.

Ekström, G. and Stark, C. P. (2013) ‘Simple scaling of catastrophic landslide dynamics’, *Science*, 339(6126), pp. 1416–1419. doi: 10.1126/science.1232887.

Elser, J. J. *et al.* (2009) ‘Shifts in lake N: P stoichiometry and nutrient limitation driven by atmospheric nitrogen deposition’, *Science*, 326(5954), pp. 835–837. doi: 10.1126/SCIENCE.1176199/SUPPL_FILE/ELSER.SOM.PDF.

Elser, J. J. *et al.* (2010) ‘Atmospheric nitrogen deposition is associated with elevated phosphorus limitation of lake zooplankton’, *Ecology Letters*, 13(10), pp. 1256–1261. doi: 10.1111/J.1461-0248.2010.01519.X.

Erismann, T. H. and Abele, G. (2001) *Dynamics of Rockslides and Rockfalls*, *Dynamics of Rockslides and Rockfalls*. doi: 10.1007/978-3-662-04639-5.

Etzelmüller, B. *et al.* (2022) ‘Permafrost in monitored unstable rock slopes in Norway-

New insights from temperature and surface velocity measurements, geophysical surveying, and ground temperature modelling', *Earth Surface Dynamics*, 10(1), pp. 97–129. doi: 10.5194/esurf-10-97-2022.

Evans, D. J. A. *et al.* (2006) 'Subglacial till: Formation, sedimentary characteristics and classification', *Earth-Science Reviews*, 78(1–2), pp. 115–176. doi: 10.1016/j.earscirev.2006.04.001.

Evans, S. G. *et al.* (2009) 'Catastrophic detachment and high-velocity long-runout flow of Kolka Glacier, Caucasus Mountains, Russia in 2002', *Geomorphology*, 105(3–4), pp. 314–321. doi: 10.1016/j.geomorph.2008.10.008.

Evans, S. G. and Clague, J. J. (1988) 'Catastrophic rock avalanches in glacial environments', *Landslides. Proc. 5th symposium, Lausanne, 1988. Vol. 2*. doi: 10.1016/0148-9062(89)91838-x.

Evans, S. G. and Delaney, K. B. (2015) 'Catastrophic Mass Flows in the Mountain Glacial Environment', in *Snow and Ice-Related Hazards, Risks, and Disasters*. Elsevier Inc., pp. 563–606. doi: 10.1016/B978-0-12-394849-6.00016-0.

Evans, S. G., Delaney, K. B. and Rana, N. M. (2021) 'The occurrence and mechanism of catastrophic mass flows in the mountain cryosphere', in *Snow and Ice-Related Hazards, Risks, and Disasters*. Elsevier, pp. 541–596. doi: 10.1016/b978-0-12-817129-5.00004-4.

Everdingen, R. O. van (1998) *Multi-language glossary of permafrost and related ground-ice terms in chinese, english, french, german..., Arctic Inst. of North America University of Calgary*.

Eyles, N. (1979) 'Facies of supraglacial sedimentation of Icelandic and Alpine temperate glaciers.', *Canadian Journal of Earth Sciences*, 16(7), pp. 1341–1361. doi: 10.1139/e79-121.

Faillettaz, J., Funk, M. and Vincent, C. (2015) 'Avalanching glacier instabilities: Review on processes and early warning perspectives', *Reviews of Geophysics*, 53(2), pp. 203–224. doi: 10.1002/2014RG000466.

Fegel, T. *et al.* (2019) 'Assessing the Chemistry and Bioavailability of Dissolved Organic Matter From Glaciers and Rock Glaciers', *Journal of Geophysical Research: Biogeosciences*, 124(7), pp. 1988–2004. doi: 10.1029/2018JG004874.

Fegel, T. S. *et al.* (2016) 'The differing biogeochemical and microbial signatures of glaciers and rock glaciers', *Journal of Geophysical Research G: Biogeosciences*, 121(3), pp. 919–932. doi: 10.1002/2015JG003236.

Ferguson, J. C. and Vieli, A. (2021) 'Modelling steady states and the transient response of debris-covered glaciers', *Cryosphere*, 15(7), pp. 3377–3399. doi: 10.5194/tc-15-3377-2021.

Finkel, Z. V *et al.* (2010) 'Phytoplankton in a changing world: Cell size and elemental stoichiometry', *Journal of Plankton Research*, 32(1), pp. 119–137. doi: 10.1093/plankt/fbp098.

Fischer, L. *et al.* (2012) 'On the influence of topographic, geological and cryospheric factors on rock avalanches and rockfalls in high-mountain areas', *Natural Hazards and Earth System Science*, 12(1), pp. 241–254. doi: 10.5194/nhess-12-241-2012.

Fleming, S. and Whitfield, P. (2010) 'Spatiotemporal mapping of ENSO and PDO surface meteorological signals in British Columbia, Yukon, and southeast Alaska', *Atmosphere - Ocean*, 48(2), pp. 122–131. doi: 10.3137/AO1107.2010.

Foreman, C. M. *et al.* (2007) 'Metabolic activity and diversity of cryoconites in the Taylor Valley, Antarctica', *Journal of Geophysical Research: Biogeosciences*, 112(4). doi: 10.1029/2006JG000358.

Fountain, A. G. *et al.* (2005) 'Fractures as the main pathways of water flow in temperate glaciers', *Nature*, 433(7026), pp. 618–621. doi: 10.1038/nature03296.

Fountain, A. G. and Walder, J. S. (1998) 'Water flow through temperate glaciers', *Reviews of Geophysics*, 36(3), pp. 299–328. doi: 10.1029/97RG03579.

Froude, M. J. and Petley, D. N. (2018) 'Global fatal landslide occurrence from 2004 to 2016', *Natural Hazards and Earth System Sciences*, 18(8), pp. 2161–2181. doi: 10.5194/nhess-18-2161-2018.

Fyffe, C. L. *et al.* (2019) 'Do debris-covered glaciers demonstrate distinctive hydrological behaviour compared to clean glaciers?', *Journal of Hydrology*, 570, pp. 584–597. doi: 10.1016/j.jhydrol.2018.12.069.

Fyffe, C. L. *et al.* (2020) 'Processes at the margins of supraglacial debris cover: Quantifying dirty ice ablation and debris redistribution', *Earth Surface Processes and*

Landforms, 45(10), pp. 2272–2290. doi: 10.1002/esp.4879.

Gaglioti, B. V. *et al.* (2019) 'Timing and Potential Causes of 19th-Century Glacier Advances in Coastal Alaska Based on Tree-Ring Dating and Historical Accounts', *Frontiers in Earth Science*, 0, p. 82. doi: 10.3389/FEART.2019.00082.

Gajjar, P. *et al.* (2021) 'Size segregation of irregular granular materials captured by time-resolved 3D imaging', *Scientific Reports 2021 11:1*, 11(1), pp. 1–6. doi: 10.1038/s41598-021-87280-1.

Gálvez, N., Barrón, V. and Torrent, J. (1999) 'Effect of phosphate on the crystallization of hematite, goethite, and lepidocrocite from ferrihydrite', *Clays and Clay Minerals*, 47(3), pp. 304–311. doi: 10.1346/CCMN.1999.0470306.

GAPHAZ (2017) Assessment of Glacier and Permafrost Hazards in Mountain Regions – Technical Guidance Document. Prepared by Allen, S., Frey, H., Huggel, C. et al. Standing Group on Glacier and Permafrost Hazards in Mountains (GAPHAZ) of the International Association of Cryospheric Sciences (IACS) and the International Permafrost Association (IPA). Zurich, Switzerland / Lima, Peru, 72 pp.

Gardner, A. S. *et al.* (2018) 'Increased West Antarctic and unchanged East Antarctic ice discharge over the last 7 years', *The Cryosphere*, 12(2), pp. 521–547. doi: 10.5194/tc-12-521-2018.

Gardner, A. S., Fahnestock, M. A. and Scambos, T. A. (2019) ITS_LIVE Regional Glacier and Ice Sheet Surface Velocities. Data archived at National Snow and Ice Data Center, doi:10.5067/6II6VW8LLWJ7.

Gardner, J. S. and Hewitt, K. (1990) 'A surge of Bualtar Glacier, Karakoram Range, Pakistan: a possible landslide trigger', *Journal of Glaciology*, 36(123), pp. 159–162. doi: 10.1017/S0022143000009394.

Garg, P. K. *et al.* (2022) 'Stagnation of the Pensilungpa glacier, western Himalaya, India: causes and implications', *Journal of Glaciology*, 68(268), pp. 221–235. doi: 10.1017/jog.2021.84.

Gariano, S. L. and Guzzetti, F. (2016) 'Landslides in a changing climate', *Earth-Science Reviews*. Elsevier B.V., pp. 227–252. doi: 10.1016/j.earscirev.2016.08.011.

Geertsema, M. *et al.* (2006) 'An overview of recent large catastrophic landslides in northern British Columbia, Canada', *Engineering Geology*, 83(1–3), pp. 120–143. doi: 10.1016/j.enggeo.2005.06.028.

Geertsema, M. (2012) 'Initial observations of the 11 June 2012 rock / ice avalanche , Lituya', in *The First Meeting of Cold Region Landslides Network, Harbin, China*, pp. 1–5. doi: 10.13140/2.1.2473.5682.

Geilhausen, M. *et al.* (2013) 'Sediment discharge from the proglacial zone of a retreating Alpine glacier', *Zeitschrift für Geomorphologie, Supplementary Issues*, 57(2), pp. 29–53. doi: 10.1127/0372-8854/2012/s-00122.

Gerringa, L. J. A. *et al.* (2012) 'Iron from melting glaciers fuels the phytoplankton blooms in Amundsen Sea (Southern Ocean): Iron biogeochemistry', *Deep-Sea Research Part II: Topical Studies in Oceanography*, 71–76, pp. 16–31. doi: 10.1016/j.dsr2.2012.03.007.

Giordan, D. *et al.* (2021) 'Classification and kinematics of the Planpincieux Glacier break-offs using photographic time-lapse analysis', *Journal of Glaciology*, 66(256), pp. 188–202. doi: 10.1017/jog.2019.99.

Girard, L. *et al.* (2013) 'Environmental controls of frost cracking revealed through in situ acoustic emission measurements in steep bedrock', *Geophysical Research Letters*, 40(9), pp. 1748–1753. doi: 10.1002/grl.50384.

Gjermundsen, E. F. *et al.* (2011) 'Assessment of multispectral glacier mapping methods and derivation of glacier area changes, 1978-2002, in the central Southern Alps, New Zealand, from ASTER satellite data, field survey and existing inventory data', *Journal of Glaciology*, 57(204), pp. 667–683. doi: 10.3189/002214311797409749.

Gledhill, M. and van den Berg, C. M. G. (1994) 'Determination of complexation of iron(III) with natural organic complexing ligands in seawater using cathodic stripping voltammetry', *Marine Chemistry*, 47(1), pp. 41–54. doi: 10.1016/0304-4203(94)90012-4.

Godio, A. and Rege, R. B. (2015) 'The mechanical properties of snow and ice of an alpine glacier inferred by integrating seismic and GPR methods', *Journal of Applied Geophysics*, 115, pp. 92–99. doi: 10.1016/j.jappgeo.2015.02.017.

Goodsell, B., Hambrey, M. J. and Classer, N. F. (2005) 'Debris transport in a temperate valley glacier: Haut Glacier d'Arolla, Valais, Switzerland', *Journal of Glaciology*, 51(172), pp. 139–146. doi: 10.3189/172756505781829647.

Goosse, H. *et al.* (2018) ‘Quantifying climate feedbacks in polar regions’, *Nature Communications*. doi: 10.1038/s41467-018-04173-0.

Gordon, J. E., Birnie, R. V. and Timmis, R. (1978) ‘A Major Rockfall and Debris Slide on the Lyell Glacier, South Georgia’, *Arctic and Alpine Research*, 10(1), p. 49. doi: 10.2307/1550656.

Gordon, R. M., Martin, J. H. and Knauer, G. A. (1982) ‘Iron in north-east Pacific waters’, *Nature 1982 299:5884*, 299(5884), pp. 611–612. doi: 10.1038/299611a0.

Gorelick, N. *et al.* (2017) ‘Google Earth Engine: Planetary-scale geospatial analysis for everyone’, *Remote Sensing of Environment*, 202, pp. 18–27. doi: 10.1016/j.rse.2017.06.031.

Graly, J. A. *et al.* (2014) ‘Chemical weathering under the Greenland ice sheet’, *Geology*, 42(6), pp. 551–554. doi: 10.1130/G35370.1.

Grämiger, L. M. *et al.* (2017) ‘Beyond debuttressing: Mechanics of paraglacial rock slope damage during repeat glacial cycles’, *Journal of Geophysical Research: Earth Surface*, 122(4), pp. 1004–1036. doi: 10.1002/2016JF003967.

Grämiger, L. M. *et al.* (2018) ‘Thermomechanical Stresses Drive Damage of Alpine Valley Rock Walls During Repeat Glacial Cycles’, *Journal of Geophysical Research: Earth Surface*, 123(10), pp. 2620–2646. doi: 10.1029/2018JF004626.

Grämiger, L. M. *et al.* (2020) ‘Hydromechanical Rock Slope Damage During Late Pleistocene and Holocene Glacial Cycles in an Alpine Valley’, *Journal of Geophysical Research: Earth Surface*, 125(8), p. e2019JF005494. doi: 10.1029/2019JF005494.

Gruber, S. (2012) ‘Derivation and analysis of a high-resolution estimate of global permafrost zonation’, *The Cryosphere*, 6(1), pp. 221–233. doi: 10.5194/tc-6-221-2012.

Gruber, S. and Haeberli, W. (2007) ‘Permafrost in steep bedrock slopes and its temperature-related destabilization following climate change’, *Journal of Geophysical Research*, 112(F2), p. F02S18. doi: 10.1029/2006JF000547.

Gruber, S., Hoelzle, M. and Haeberli, W. (2004) ‘Permafrost thaw and destabilization of Alpine rock walls in the hot summer of 2003’, *Geophysical Research Letters*, 31(13), p. L13504. doi: 10.1029/2004GL020051.

Gulley, J. D., Benn, D. I., Müller, D., *et al.* (2009) ‘A cut-and-closure origin for englacial conduits in uncrevassed regions of polythermal glaciers', *Journal of Glaciology*, 55(189), pp. 66–80. doi: 10.3189/002214309788608930.

Gulley, J. D., Benn, D. I., Screaton, E., *et al.* (2009) 'Mechanisms of englacial conduit formation and their implications for subglacial recharge', *Quaternary Science Reviews*, 28(19–20), pp. 1984–1999. doi: 10.1016/J.QUASCIREV.2009.04.002.

Guthrie, R. H. *et al.* (2012) 'The 6 August 2010 Mount Meager rock slide-debris flow, Coast Mountains, British Columbia: Characteristics, dynamics, and implications for hazard and risk assessment', *Natural Hazards and Earth System Science*, 12(5), pp. 1277–1294. doi: 10.5194/nhess-12-1277-2012.

Haeberli, W. *et al.* (2004) 'The Kolka-Karmadon rock/ice slide of 20 September 2002: an extraordinary event of historical dimensions in North Ossetia, Russian Caucasus', *Journal of Glaciology*, 50(171), pp. 533–546. doi: 10.3189/172756504781829710.

Haeberli, W., Schaub, Y. and Huggel, C. (2017) 'Increasing risks related to landslides from degrading permafrost into new lakes in de-glaciating mountain ranges', *Geomorphology*, 293, pp. 405–417. doi: 10.1016/j.geomorph.2016.02.009.

Haeberli, W., Wegmann, M. and Mühll, D. V. (1997) 'Slope stability problems related to glacier shrinkage and permafrost degradation in the Alps', *Eclogae Geologicae Helvetiae*, 90(3).

Hall, D. K., Riggs, G. A. and Salomonson, V. V. (1995) 'Development of methods for mapping global snow cover using moderate resolution imaging spectroradiometer data', *Remote Sensing of Environment*, 54(2), pp. 127–140. doi: 10.1016/0034-4257(95)00137-P.

Harris, C. *et al.* (2003) 'Warming permafrost in European mountains', *Global and Planetary Change*, 39(3–4). doi: 10.1016/j.gloplacha.2003.04.001.

Harrison, S. *et al.* (2018) 'Climate change and the global pattern of moraine-dammed glacial lake outburst floods', *The Cryosphere*, 12(4), pp. 1195–1209. doi: 10.5194/tc-12-1195-2018.

Hart, J. K. *et al.* (2022) 'The seasonal evolution of subglacial drainage pathways beneath a soft-bedded glacier', *Communications Earth and Environment*, 3(1), pp. 1–13. doi: 10.1038/s43247-022-00484-9.

Hartmeyer, I. *et al.* (2020) ‘A 6-year lidar survey reveals enhanced rockwall retreat and modified rockfall magnitudes/frequencies in deglaciating cirques’, *Earth Surface Dynamics*, 8(3), pp. 753–768. doi: 10.5194/esurf-8-753-2020.

Hasler, A. *et al.* (2011) ‘Advective Heat Transport in Frozen Rock Clefts: Conceptual Model, Laboratory Experiments and Numerical Simulation’, *Permafrost and Periglacial Processes*, 22(4), pp. 378–389. doi: 10.1002/ppp.737.

Havenith, H. B. *et al.* (2016) ‘A new classification of earthquake-induced landslide event sizes based on seismotectonic, topographic, climatic and geologic factors’, *Geoenvironmental Disasters*, 3(1), pp. 1–24. doi: 10.1186/s40677-016-0041-1.

Hawkings, J. R. *et al.* (2014) ‘Ice sheets as a significant source of highly reactive nanoparticulate iron to the oceans’, *Nature Communications*, 5(May), pp. 1–8. doi: 10.1038/ncomms4929.

Hawkings, J. R. *et al.* (2015) ‘The effect of warming climate on nutrient and solute export from the Greenland Ice Sheet’, *Geochemical Perspectives Letters*, 1(1), pp. 94–104. doi: 10.7185/GEOCHEMLET.1510.

Hawkings, J. R. *et al.* (2016) ‘The Greenland Ice Sheet as a hot spot of phosphorus weathering and export in the Arctic’, *Global Biogeochemical Cycles*, 30(2), pp. 191–210. doi: 10.1002/2015GB005237.

Hawkings, J. R. *et al.* (2017) ‘Ice sheets as a missing source of silica to the polar oceans’, *Nature Communications*, 8(1), p. 14198. doi: 10.1038/ncomms14198.

Hawkings, J. R. *et al.* (2018) ‘Biolabile ferrous iron bearing nanoparticles in glacial sediments’, *Earth and Planetary Science Letters*, 493, pp. 92–101. doi: 10.1016/j.epsl.2018.04.022.

Hawkings, J. R. *et al.* (2020) ‘Enhanced trace element mobilization by Earth’s ice sheets’, *Proceedings of the National Academy of Sciences of the United States of America*, 117(50), pp. 31648–31659. doi: 10.1073/pnas.2014378117.

Heim, A. (1932) ‘Bergsturz und Menschenleben’, *Naturforschenden Gesellschaft in Zürich*, 77(20), p. 218.

Helly, J. J. *et al.* (2011) ‘Cooling, dilution and mixing of ocean water by free-drifting icebergs in the Weddell Sea’, *Deep-Sea Research Part II: Topical Studies in*

Oceanography, 58(11–12), pp. 1346–1363. doi: 10.1016/j.dsr2.2010.11.010.

Henkel, S. *et al.* (2018) ‘Iron cycling and stable Fe isotope fractionation in Antarctic shelf sediments, King George Island’, *Geochimica et Cosmochimica Acta*, 237, pp. 320–338. doi: 10.1016/j.gca.2018.06.042.

Hergarten, S. (2003) ‘Landslides, sandpiles, and self-organized criticality’, *Natural Hazards and Earth System Science*, 3(6), pp. 505–514. doi: 10.5194/NHESS-3-505-2003.

Hernández-Henríquez, M. A., Déry, S. J. and Derksen, C. (2015) ‘Polar amplification and elevation-dependence in trends of Northern Hemisphere snow cover extent, 1971-2014’, *Environmental Research Letters*, 10(4), p. 044010. doi: 10.1088/1748-9326/10/4/044010.

Herreid, S. and Pellicciotti, F. (2020) ‘The state of rock debris covering Earth’s glaciers’, *Nature Geoscience*, 13(9), pp. 621–627. doi: 10.1038/s41561-020-0615-0.

Herreid, S. and Truffer, M. (2016) ‘Automated detection of unstable glacier flow and a spectrum of speedup behavior in the Alaska Range’, *Journal of Geophysical Research: Earth Surface*, 121(1), pp. 64–81. doi: 10.1002/2015JF003502.

Hersbach, H. *et al.* (2020) ‘The ERA5 global reanalysis’, *Quarterly Journal of the Royal Meteorological Society*, 146(730), pp. 1999–2049. doi: 10.1002/qj.3803.

Hewitt, K. (1988) ‘Catastrophic landslide deposits in the Karakoram Himalaya’, *Science*, 242(4875), pp. 64–67. doi: 10.1126/science.242.4875.64.

Hewitt, K. (1999) ‘Quaternary moraines vs catastrophic rock avalanches in the Karakoram Himalaya, Northern Pakistan’, *Quaternary Research*, 51(3), pp. 220–237. doi: 10.1006/qres.1999.2033.

Hewitt, K. (2002a) ‘Styles of rock-avalanche depositional complexes conditioned by very rugged terrain, Karakoram Himalaya, Pakistan’, *GSA Reviews in Engineering Geology*, 15. doi: 10.1130/REG15-p345.

Hewitt, K. (2002b) ‘Styles of rock-avalanche depositional complexes conditioned by very rugged terrain, Karakoram Himalaya, Pakistan’, *GSA Reviews in Engineering Geology*, 15, pp. 345–377. doi: 10.1130/REG15-p345.

Hewitt, K. (2009) ‘Rock avalanches that travel onto glaciers and related developments, Karakoram Himalaya, Inner Asia’, *Geomorphology*, 103(1), pp. 66–79. doi: 10.1016/j.geomorph.2007.10.017.

Hewitt, K., Clague, J. J. and Deline, P. (2011) ‘Catastrophic rock slope failures and mountain glaciers’, in *Encyclopedia of Earth Sciences Series*. Springer Netherlands, pp. 113–126. doi: 10.1007/978-90-481-2642-2_615.

von der Heyden, B. P. and Roychoudhury, A. N. (2015) ‘A review of colloidal iron partitioning and distribution in the open ocean’, *Marine Chemistry*, 177, pp. 9–19. doi: 10.1016/j.marchem.2015.05.010.

Hibert, C. *et al.* (2019) ‘Exploration of continuous seismic recordings with a machine learning approach to document 20 yr of landslide activity in Alaska’, *Geophysical Journal International*, 219(2), pp. 1138–1147. doi: 10.1093/gji/ggz354.

Higman, B. *et al.* (2018) ‘The 2015 landslide and tsunami in Taan Fiord, Alaska’, *Scientific Reports*, 8(1), pp. 1–12. doi: 10.1038/s41598-018-30475-w.

Hilger, P. *et al.* (2021) 'Permafrost as a first order control on long-term rock-slope deformation in (Sub-)Arctic Norway', *Quaternary Science Reviews*, 251, 106718 https://doi.org/10.1016/j.quascirev.2020.106718

Hilton, R. G., Galy, A. and Hovius, N. (2008) ‘Riverine particulate organic carbon from an active mountain belt: Importance of landslides’, *Global Biogeochemical Cycles*, 22(1). doi: 10.1029/2006GB002905.

Hilton, R. G. and West, A. J. (2020) ‘Mountains, erosion and the carbon cycle’, *Nature Reviews Earth and Environment*, pp. 284–299. doi: 10.1038/s43017-020-0058-6.

Hodgkins, R. (2001) ‘Seasonal evolution of meltwater generation, storage and discharge at a non-temperate glacier in Svalbard’, *Hydrological Processes*, 15(3), pp. 441–460. doi: 10.1002/hyp.160.

Hodson, A. *et al.* (2008) ‘Glacial Ecosystems’, *Ecological Monographs*, 78(1), pp. 41–67. doi: 10.1890/07-0187.1.

Hodson, A. *et al.* (2015) ‘Cryospheric ecosystems: a synthesis of snowpack and glacial research’, *Environmental Research Letters*, 10(11), p. 110201. doi: 10.1088/1748-9326/10/11/110201.

Hodson, A. *et al.* (2017) ‘Climatically sensitive transfer of iron to maritime Antarctic ecosystems by surface runoff’, *Nature Communications 2017 8:1*, 8(1), pp. 1–7. doi: 10.1038/ncomms14499.

Hodson, A., Mumford, P. and Lister, D. (2004) 'Suspended sediment and phosphorous in proglacial rivers: Bioavailability and potential impacts upon the P status of ice-marginal receiving waters', *Hydrological Processes*, 18(13), pp. 2409–2422. doi: 10.1002/HYP.1471.

Holm, K., Bovis, M. and Jakob, M. (2004) 'The landslide response of alpine basins to post-Little Ice Age glacial thinning and retreat in southwestern British Columbia', *Geomorphology*, 57(3–4), pp. 201–216. doi: 10.1016/S0169-555X(03)00103-X.

Hood, E. and Berner, L. (2009) 'Effects of changing glacial coverage on the physical and biogeochemical properties of coastal streams in southeastern Alaska', *Journal of Geophysical Research: Biogeosciences*, 114(G3), p. 3001. doi: 10.1029/2009JG000971.

Hood, E. and Scott, D. (2008) 'Riverine organic matter and nutrients insoutheast Alaska affected by glacial coverage', *Nature Geoscience*, 1(9), pp. 583–587. doi: 10.1038/ngeo280.

Hooke, R. L. (2019) 'The velocity field in a glacier', in *Principles of Glacier Mechanics*. Cambridge University Press, pp. 81–114. doi: 10.1017/9781108698207.008.

Hopwood, M. J. *et al.* (2014) 'Glacial flours as a potential source of Fe(II) and Fe(III) to polar waters', *Biogeochemistry 2014 118:1*, 118(1), pp. 443–452. doi: 10.1007/S10533-013-9945-Y.

Hopwood, M. J. *et al.* (2016) 'Seasonal changes in Fe along a glaciated Greenlandic fjord', *Frontiers in Earth Science*, 4, p. 15. doi: 10.3389/feart.2016.00015.

Hopwood, M. J. *et al.* (2017) 'The heterogeneous nature of Fe delivery from melting icebergs', *Geochemical Perspectives Letters*, 3(2), pp. 200–209. doi: 10.7185/geochemlet.1723.

Hopwood, M. J. *et al.* (2019) 'Highly variable iron content modulates iceberg-ocean fertilisation and potential carbon export', *Nature Communications*, 10(1), pp. 1–10. doi: 10.1038/s41467-019-13231-0.

Hopwood, M. J. *et al.* (2020) 'Review article: How does glacier discharge affect marine biogeochemistry and primary production in the Arctic?', *Cryosphere*, 14(4), pp. 1347–1383. doi: 10.5194/TC-14-1347-2020.

Horowitz, A. J. and Elrick, K. A. (1987) 'The relation of stream sediment surface area, grain size and composition to trace element chemistry’, *Applied Geochemistry*, 2(4), pp. 437–451. doi: 10.1016/0883-2927(87)90027-8.

Hossain, M. S. *et al.* (2015) ‘Assessment of Landsat 7 Scan Line Corrector-off data gap-filling methods for seagrass distribution mapping’, *International Journal of Remote Sensing*, 36(4), pp. 1188–1215. doi: 10.1080/01431161.2015.1007257.

Hotaling, S. *et al.* (2017) ‘Climate change and alpine stream biology: progress, challenges, and opportunities for the future’, *Biological Reviews*, 92(4), pp. 2024–2045. doi: 10.1111/brv.12319.

Housman, I. W., Chastain, R. A. and Finco, M. V. (2018) ‘An evaluation of forest health insect and disease survey data and satellite-based remote sensing forest change detection methods: Case studies in the United States’, *Remote Sensing*, 10(8), p. 1184. doi: 10.3390/rs10081184.

Hsü, K. J. (1975) ‘Catastrophic debris streams (sturzstroms) generated by rockfalls’, *Bulletin of the Geological Society of America*, 86(1), pp. 129–140. doi: 10.1130/0016-7606(1975)86<129:CDSSGB>2.0.CO;2.

Huang, Y., Tagliabue, A. and Cassar, N. (2022) ‘Data-Driven Modeling of Dissolved Iron in the Global Ocean’, *Frontiers in Marine Science*, 9, p. 612. doi: 10.3389/fmars.2022.837183.

Huggel, C. *et al.* (2005) ‘The 2002 rock/ice avalanche at Kolka/Karmadon, Russian Caucasus: Assessment of extraordinary avalanche formation and mobility, and application of QuickBird satellite imagery’, *Natural Hazards and Earth System Science*, 5(2), pp. 173–187. doi: 10.5194/nhess-5-173-2005.

Huggel, C. (2009) ‘Recent extreme slope failures in glacial environments: effects of thermal perturbation’, *Quaternary Science Reviews*, 28(11–12), pp. 1119–1130. doi: 10.1016/j.quascirev.2008.06.007.

Huggel, C., Clague, J. J. and Korup, O. (2012) ‘Is climate change responsible for changing landslide activity in high mountains?’, *Earth Surface Processes and Landforms*, 37(1), pp. 77–91. doi: 10.1002/esp.2223.

Hugonnet, R. *et al.* (2021) ‘Accelerated global glacier mass loss in the early twenty-first century’, *Nature*, 592(7856), pp. 726–731. doi: 10.1038/s41586-021-03436-z.

Hungr, O. (1981) *Dynamics of Rock Avalanches and Other Types of Mass Movements*. University of Alberta, Edmonton, Canada.

Hungr, O. *et al.* (2001) 'A review of the classification of landslides of the flow type', *Environmental and Engineering Geoscience*, 7(3), pp. 221–238. doi: 10.2113/gseegeosci.7.3.221.

Hungr, O., Leroueil, S. and Picarelli, L. (2014) 'The Varnes classification of landslide types, an update', *Landslides*. Springer Verlag, pp. 167–194. doi: 10.1007/s10346-013-0436-y.

Huo, D., Bishop, M. P. and Bush, A. B. G. (2021) 'Understanding Complex Debris-Covered Glaciers: Concepts, Issues, and Research Directions', *Frontiers in Earth Science*, 9, p. 358. doi: 10.3389/feart.2021.652279.

Ilyashuk, B. P. *et al.* (2014) 'Rock glacier outflows may adversely affect lakes: Lessons from the past and present of two neighboring water bodies in a crystalline-rock watershed', *Environmental Science and Technology*, 48(11), pp. 6192–6200. doi: 10.1021/es500180c.

IPCC, 2019: IPCC Special Report on the Ocean and Cryosphere in a Changing Climate [H.-O. Pörtner, D.C. Roberts, V. Masson-Delmotte, P. Zhai, M. Tignor, E. Poloczanska, K. Mintenbeck, A. Alegría, M. Nicolai, A. Okem, J. Petzold, B. Rama, N.M. Weyer (eds.)]. Cambridge University Press, Cambridge, UK and New York, NY, USA, 755 pp. https://doi.org/10.1017/9781009157964.

IRIS DMC (2017) Data Services Products: Exotic Seismic Events Catalog, doi:10.17611/DP/ESEC.1.

Irvine-Fynn, T. D. L. *et al.* (2011) 'Polythermal glacier hydrology: A review', *Reviews of Geophysics*. John Wiley & Sons, Ltd, p. 4002. doi: 10.1029/2010RG000350.

Irvine-Fynn, T. D. L. *et al.* (2017) 'Supraglacial Ponds Regulate Runoff From Himalayan Debris-Covered Glaciers', *Geophysical Research Letters*, 44(23), pp. 11,894-11,904. doi: 10.1002/2017GL075398.

Jakob, L. *et al.* (2021) 'Spatially and temporally resolved ice loss in High Mountain Asia and the Gulf of Alaska observed by CryoSat-2 swath altimetry between 2010 and 2019', *The Cryosphere*, 15(4), pp. 1845–1862. doi: 10.5194/tc-15-1845-2021.

Jamieson, S. S. R., Ewertowski, M. W. and Evans, D. J. A. (2015) ‘Rapid advance of two mountain glaciers in response to mine-related debris loading’, *Journal of Geophysical Research: Earth Surface*, 120(7), pp. 1418–1435. doi: 10.1002/2015JF003504.

Jarman, D. and Harrison, S. (2019) ‘Rock slope failure in the British mountains’, *Geomorphology*, 340, pp. 202–233. doi: 10.1016/j.geomorph.2019.03.002.

Jennings, S. J. A., Hambrey, M. J. and Glasser, N. F. (2014) ‘Ice flow-unit influence on glacier structure, debris entrainment and transport’, *Earth Surface Processes and Landforms*, 39(10), pp. 1279–1292. doi: 10.1002/esp.3521.

Jibson, R. W. *et al.* (2006) ‘Large rock avalanches triggered by the M 7.9 Denali Fault, Alaska, earthquake of 3 November 2002’, *Engineering Geology*, 83(1–3), pp. 144–160. doi: 10.1016/j.enggeo.2005.06.029.

Jibson, R. W. (2013) ‘Mass-Movement Causes: Earthquakes’, in *Treatise on Geomorphology*. Elsevier Inc., pp. 223–229. doi: 10.1016/B978-0-12-374739-6.00169-X.

Johnson, K. S., Michael Gordon, R. and Coale, K. H. (1997) ‘What controls dissolved iron concentrations in the world ocean?’, *Marine Chemistry*, pp. 137–161. doi: 10.1016/S0304-4203(97)00043-1.

Jones, A. M. *et al.* (2009) ‘The effect of silica and natural organic matter on the Fe(II)-catalysed transformation and reactivity of Fe(III) minerals’, *Geochimica et Cosmochimica Acta*, 73(15), pp. 4409–4422. doi: 10.1016/j.gca.2009.04.025.

Kääb, A. *et al.* (2018) ‘Massive collapse of two glaciers in western Tibet in 2016 after surge-like instability’, *Nature Geoscience*, 11(2), pp. 114–120. doi: 10.1038/s41561-017-0039-7.

Kääb, A. *et al.* (2021) ‘Sudden large-volume detachments of low-angle mountain glaciers - More frequent than thought?’, *Cryosphere*, 15(4), pp. 1751–1785. doi: 10.5194/tc-15-1751-2021.

Kalnay, E. *et al.* (1996) ‘The NCEP/NCAR 40-Year Reanalysis Project in: Bulletin of the American Meteorological Society Volume 77 Issue 3 (1996)’, *American Meterological Society*, 77(3), pp. 437–472. Available at: https://journals.ametsoc.org/view/journals/bams/77/3/1520-0477_1996_077_0437_tnyrp_2_0_co_2.xml (Accessed: 1 May 2022).

Kanna, N. *et al.* (2018) ‘Upwelling of Macronutrients and Dissolved Inorganic Carbon by a Subglacial Freshwater Driven Plume in Bowdoin Fjord, Northwestern Greenland’, *Journal of Geophysical Research: Biogeosciences*, 123(5), pp. 1666–1682. doi: 10.1029/2017JG004248.

Kavanaugh, J. L. and Clarke, G. K. C. (2001) ‘Abrupt glacier motion and reorganization of basal shear stress following the establishment of a connected drainage system’, *Journal of Glaciology*, 47(158), pp. 472–480. doi: 10.3189/172756501781831972.

Keefer, D. . (1984) ‘Landslides caused by earthquakes’, *Bulletin of the Geological Society of America*. GeoScienceWorld, pp. 406–421. doi: 10.1130/0016-7606(1985)96<1091:LCBEDA>2.0.CO;2.

Keefer, D. K. (2002) ‘Investigating landslides caused by earthquakes - A historical review’, *Surveys in Geophysics*, 23(6), pp. 473–510. doi: 10.1023/A:1021274710840.

Keshri, A. K., Shukla, A. and Gupta, R. P. (2009) ‘ASTER ratio indices for supraglacial terrain mapping’, *International Journal of Remote Sensing*, 30(2), pp. 519–524. doi: 10.1080/01431160802385459.

Kim, K. *et al.* (2010) ‘Photoreductive Dissolution of Iron Oxides Trapped in Ice and Its Environmental Implications’, *Environmental Science and Technology*, 44(11), pp. 4142–4148. doi: 10.1021/ES9037808.

Kirkbride, M. P. (2000) ‘Ice-marginal geomorphology and Holocene expansion of debris-covered Tasman Glacier, New Zealand’, in *IAHS-AISH Publication*, pp. 211–217.

Kirkbride, M. P. (2011) ‘Debris-Covered Glaciers’, in Singh, V. P., Singh, P., and Haritashya, U. K. (eds) *Encyclopedia of Snow, Ice and Glaciers*. Dordrecht: Springer Netherlands, pp. 190–192. doi: 10.1007/978-90-481-2642-2_622.

Kirkbride, M. P. and Deline, P. (2013) ‘The formation of supraglacial debris covers by primary dispersal from transverse englacial debris bands’, *Earth Surface Processes and Landforms*, 38(15), pp. 1779–1792. doi: 10.1002/esp.3416.

Knapp, S. and Krautblatter, M. (2020) ‘Conceptual Framework of Energy Dissipation During Disintegration in Rock Avalanches’, *Frontiers in Earth Science*, 0, p. 263. doi: 10.3389/FEART.2020.00263.

Kokelj, S. V. and Jorgenson, M. T. (2013) ‘Advances in thermokarst research’, *Permafrost and Periglacial Processes*, 24(2), pp. 108–119. doi: 10.1002/ppp.1779.

Korup, O. (2005) ‘Large landslides and their effect on sediment flux in South Westland, New Zealand’, *Earth Surface Processes and Landforms*, 30(3), pp. 305–323. doi: 10.1002/esp.1143.

Korup, O. (2012) ‘Earth’s portfolio of extreme sediment transport events’, *Earth-Science Reviews*. Elsevier, pp. 115–125. doi: 10.1016/j.earscirev.2012.02.006.

Korup, O. and Clague, J. J. (2009) ‘Natural hazards, extreme events, and mountain topography’, *Quaternary Science Reviews*, 28(11–12), pp. 977–990. doi: 10.1016/j.quascirev.2009.02.021.

Kotlyakov, V. M., Rototaeva, O. V. and Nosenko, G. A. (2004) ‘The September 2002 Kolka Glacier Catastrophe in North Ossetia, Russian Federation: Evidence and Analysis’, *Mountain Research and Development*, 24(1). doi: 10.1659/0276-4741(2004)024[0078:tskgci]2.0.co;2.

Kraaijenbrink, P. D. A. *et al.* (2017) ‘Impact of a global temperature rise of 1.5 degrees Celsius on Asia’s glaciers’, *Nature*, 549(7671), pp. 257–260. doi: 10.1038/nature23878.

Krautblatter, M. (2009) *Detection and quantification of permafrost change in alpine rock walls and implications for rock instability*. PhD Thesis. Universität Bonn. Available at: https://bonndoc.ulb.uni-bonn.de/xmlui/handle/20.500.11811/4117

Krautblatter, M. *et al.* (2010) ‘Temperature-calibrated imaging of seasonal changes in permafrost rock walls by quantitative electrical resistivity tomography (Zugspitze, German/Austrian Alps)’, *Journal of Geophysical Research: Earth Surface*, 115(2). doi: 10.1029/2008JF001209.

Krautblatter, M., Funk, D. and Günzel, F. K. (2013) ‘Why permafrost rocks become unstable: A rock-ice-mechanical model in time and space’, *Earth Surface Processes and Landforms*, 38(8), pp. 876–887. doi: 10.1002/esp.3374.

Kuma, K. and Matsunaga, K. (1995) ‘Availability of colloidal ferric oxides to coastal marine phytoplankton’, *Marine Biology*, 122(1), pp. 1–11. doi: 10.1007/BF00349272.

Larsen, C. F. *et al.* (2005) ‘Rapid viscoelastic uplift in southeast Alaska caused by post-Little Ice Age glacial retreat’, *Earth and Planetary Science Letters*, 237(3–4), pp. 548–560. doi: 10.1016/j.epsl.2005.06.032.

Laspoumaderes, C. *et al.* (2013) ‘Glacier melting and stoichiometric implications for lake community structure: Zooplankton species distributions across a natural light gradient’, *Global Change Biology*, 19(1), pp. 316–326. doi: 10.1111/gcb.12040.

Lawson, E. C. *et al.* (2014) ‘Continuous summer export of nitrogen-rich organic matter from the greenland ice sheet inferred by ultrahigh resolution mass spectrometry’, *Environmental Science and Technology*, 48(24), pp. 14248–14257. doi: 10.1021/es501732h.

Lea, J. M. (2018) ‘The Google Earth Engine Digitisation Tool (GEEDiT) and the Margin change Quantification Tool (MaQiT) - Simple tools for the rapid mapping and quantification of changing Earth surface margins’, *Earth Surface Dynamics*, 6(3), pp. 551–561. doi: 10.5194/esurf-6-551-2018.

Legay, A., Magnin, F. and Ravanel, L. (2021) ‘Rock temperature prior to failure: Analysis of 209 rockfall events in the Mont Blanc massif (Western European Alps)’, *Permafrost and Periglacial Processes*, pp. 1–17. doi: 10.1002/ppp.2110.

Legros, F. (2002) ‘The mobility of long-runout landslides’, *Engineering Geology*, 63(3–4), pp. 301–331. doi: 10.1016/S0013-7952(01)00090-4.

Li, K. *et al.* (2021) ‘Experiments on granular flow behavior and deposit characteristics: implications for rock avalanche kinematics’, *Landslides*, 18(5), pp. 1779–1799. doi: 10.1007/s10346-020-01607-z.

Lipovsky, P. S. *et al.* (2008) ‘The July 2007 rock and ice avalanches at Mount Steele, St. Elias Mountains, Yukon, Canada’, *Landslides*, 5(4), pp. 445–455. doi: 10.1007/s10346-008-0133-4.

Liu, J., Wu, Y. and Gao, X. (2021) ‘Increase in occurrence of large glacier-related landslides in the high mountains of Asia’, *Scientific reports*, 11(1), p. 1635. doi: 10.1038/s41598-021-81212-9.

Locat, P. *et al.* (2006) ‘Fragmentation energy in rock avalanches’, *Canadian Geotechnical Journal*, 43(8), pp. 830–851. doi: 10.1139/T06-045.

Lucas, A., Mangeney, A. and Ampuero, J. P. (2014) ‘Frictional velocity-weakening in landslides on Earth and on other planetary bodies’, *Nature Communications*, 5(1), pp. 1–9. doi: 10.1038/ncomms4417.

Luckman, B. H. (2013) ‘Processes, Transport, Deposition, and Landforms: Rockfall’, in *Treatise on Geomorphology*, pp. 174–182. doi: 10.1016/B978-0-12-374739-6.00162-7.

Mackay, S. L. *et al.* (2014) ‘Cold-based debris-covered glaciers: Evaluating their potential as climate archives through studies of ground-penetrating radar and surface morphology’, *Journal of Geophysical Research F: Earth Surface*, 119(11), pp. 2505–2540. doi: 10.1002/2014JF003178.

Magnin, F. *et al.* (2017) ‘Modelling rock wall permafrost degradation in the Mont Blanc massif from the LIA to the end of the 21st century’, *Cryosphere*, 11(4). doi: 10.5194/tc-11-1813-2017.

Mair, D. *et al.* (2002) ‘Influence of subglacial drainage system evolution on glacier surface motion: Haut Glacier d’Arolla, Switzerland’, *Journal of Geophysical Research: Solid Earth*, 107(B8), p. EPM 8-1. doi: 10.1029/2001JB000514.

Malamud, B. D. *et al.* (2004) ‘Landslide inventories and their statistical properties’, *Earth Surface Processes and Landforms*, 29(6), pp. 687–711. doi: 10.1002/esp.1064.

Mamot, P. *et al.* (2018) ‘A temperature-and stress-controlled failure criterion for ice-filled permafrost rock joints’, *Cryosphere*, 12(10), pp. 3333–3353. doi: 10.5194/TC-12-3333-2018.

Mamot, P. *et al.* (2021) 'A temperature-dependent mechanical model to assess the stability of degrading permafrost rock slopes', *Earth Surface Dynamics*, 9, pp. 1125-1151. https://doi.org/10.5194/esurf-9-1125-2021

Mann, D. H. and Streveler, G. P. (2008) ‘Post-glacial relative sea level, isostasy, and glacial history in Icy Strait, Southeast Alaska, USA’, *Quaternary Research*, 69(2), pp. 201–216. doi: 10.1016/J.YQRES.2007.12.005.

Marc, O., Turowski, J. M. and Meunier, P. (2021) ‘Controls on the grain size distribution of landslides in Taiwan: the influence of drop height, scar depth and bedrock strength’, *Earth Surface Dynamics*, 9(4), pp. 995–1011. doi: 10.5194/esurf-9-995-2021.

Markham, B. L. *et al.* (2004) ‘Landsat sensor performance: History and current status’, *IEEE Transactions on Geoscience and Remote Sensing*, pp. 2691–2694. doi: 10.1109/TGRS.2004.840720.

Martin, J. H. (1990) ‘Glacial-interglacial CO2 change: The Iron Hypothesis’, *Paleoceanography*, 5(1), pp. 1–13. doi: 10.1029/PA005i001p00001.

Martin, J. H. and Fitzwater, S. E. (1988) ‘Iron deficiency limits phytoplankton growth in the north-east pacific subarctic’, *Nature*, 331(6154), pp. 341–343. doi: 10.1038/331341a0.

Martino, S., Prestininzi, A. and Romeo, R. W. (2014) ‘Earthquake-induced ground failures in Italy from a reviewed database’, *Natural Hazards and Earth System Sciences*, 14(4), pp. 799–814. doi: 10.5194/nhess-14-799-2014.

Martyniuk, N., Modenutti, B. and Balseiro, E. G. (2014) ‘Can increased glacial melting resulting from global change provide attached algae with transient protection against high irradiance?’, *Freshwater Biology*, 59(11), pp. 2290–2302. doi: 10.1111/fwb.12431.

Matiu, M. *et al.* (2021) ‘Observed snow depth trends in the European Alps: 1971 to 2019’, *Cryosphere*, 15(3), pp. 1343–1382. doi: 10.5194/tc-15-1343-2021.

Matsuoka, N. *et al.* (1997) ‘Monitoring of Periglacial Slope Processes in the Swiss Alps: the First Two Years of Frost Shattering, Heave and Creep’, *Permafrost and Periglacial Processes*, 8(2), pp. 155–177. doi: 10.1002/(SICI)1099-1530(199732)8:2<155::AID-PPP248>3.0.CO;2-N.

Matsuoka, N. (2001) ‘Direct observation of frost wedging in alpine bedrock’, *Earth Surface Processes and Landforms*, 26(6), pp. 601–614. doi: 10.1002/esp.208.

Matsuoka, N. (2008) ‘Frost weathering and rockwall erosion in the southeastern Swiss Alps: Long-term (1994-2006) observations’, *Geomorphology*, 99(1–4), pp. 353–368. doi: 10.1016/j.geomorph.2007.11.013.

McColl, S., Davies, T. and McSaveney, M. (2010) ‘Glacier retreat and rock-slope stability: debunking debuttressing’, in *delegate papers 11th Congress of the International Association for Engineering Geology and the Environment*.

McColl, S. T. (2012) ‘Paraglacial rock-slope stability’, *Geomorphology*, 153–154, pp. 1–16. doi: 10.1016/j.geomorph.2012.02.015.

McColl, S. T. (2015) ‘Landslide Causes and Triggers’, in Davies, T. (ed.) *Landslide Hazards, Risks, and Disasters*. 1st edn. Amsterdam: Elsevier, pp. 17–42. doi: 10.1016/B978-0-12-396452-6.00002-1.

McColl, S. T., Davies, T. R. H. and McSaveney, M. J. (2012) ‘The effect of glaciation on the intensity of seismic ground motion', *Earth Surface Processes and Landforms*, 37(12), pp. 1290–1301. doi: 10.1002/esp.3251.

McColl, S. T. and Draebing, D. (2019) 'Rock Slope Instability in the Proglacial Zone: State of the Art', in *Geomorphology of Proglacial Systems*. Springer, Cham, pp. 119–141. doi: 10.1007/978-3-319-94184-4_8.

McCutcheon, J. *et al.* (2021) 'Mineral phosphorus drives glacier algal blooms on the Greenland Ice Sheet', *Nature Communications*, 12(1), pp. 1–11. doi: 10.1038/s41467-020-20627-w.

McSaveney, M. and Davies, T. (2007) 'Rockslides and their motion', in *Progress in Landslide Science*, pp. 113–133. doi: 10.1007/978-3-540-70965-7_8.

McSaveney, M. J. (1975) *The Sherman Glacier Rock Avalanche of 1964: Its Emplacement and Subsequent Effects on the Glacier Beneath it*. Ohio State University, Columbus, OH.

McSaveney, M. J. (1978) 'Sherman Glacier Rock Avalanche, Alaska, U.S.A.', *Developments in Geotechnical Engineering*, 14(PA), pp. 197–258. doi: 10.1016/B978-0-444-41507-3.50014-3.

McSaveney, M. J. (2002) 'Recent rockfalls and rock avalanches in Mount Cook National Park, New Zealand', *GSA Reviews in Engineering Geology*, 15, pp. 35–70. doi: 10.1130/REG15-p35.

Measures, C. I. *et al.* (2008) 'High-resolution Al and Fe data from the Atlantic Ocean CLIVAR-CO2 Repeat Hydrography A16N transect: Extensive linkages between atmospheric dust and upper ocean geochemistry', *Global Biogeochemical Cycles*, 22(1). doi: 10.1029/2007GB003042.

Meire, L. *et al.* (2016) 'High export of dissolved silica from the Greenland Ice Sheet', *Geophysical Research Letters*, 43(17), pp. 9173–9182. doi: 10.1002/2016GL070191.

Meire, L. *et al.* (2017) 'Marine-terminating glaciers sustain high productivity in Greenland fjords', *Global Change Biology*, 23(12), pp. 5344–5357. doi: 10.1111/gcb.13801.

Mellor, M. (1973) 'Mechanical properties of rocks at low temperatures', in *Permafrost: Second International Conference*. Washington D.C.: National Academy of Sciences, pp.

334–344.

Meunier, P., Hovius, N. and Haines, J. A. (2008) ‘Topographic site effects and the location of earthquake induced landslides’, *Earth and Planetary Science Letters*, 275(3–4), pp. 221–232. doi: 10.1016/j.epsl.2008.07.020.

Mihalcea, C., Mayer, C., *et al.* (2008) ‘Spatial distribution of debris thickness and melting from remote-sensing and meteorological data, at debris-covered Baltoro glacier, Karakoram, Pakistan’, in *Annals of Glaciology*. Cambridge University Press, pp. 49–57. doi: 10.3189/172756408784700680.

Mihalcea, C., Brock, B. W., *et al.* (2008) ‘Using ASTER satellite and ground-based surface temperature measurements to derive supraglacial debris cover and thickness patterns on Miage Glacier (Mont Blanc Massif, Italy)’, *Cold Regions Science and Technology*, 52(3), pp. 341–354. doi: 10.1016/j.coldregions.2007.03.004.

Mikucki, J. A. *et al.* (2009) ‘A contemporary microbially maintained subglacial ferrous “Ocean”’, *Science*, 324(5925), pp. 397–400. doi: 10.1126/science.1167350.

Miles, E. S. *et al.* (2017) ‘Pond dynamics and supraglacial-englacial connectivity on debris-covered Lirung Glacier, Nepal’, *Frontiers in Earth Science*, 5, p. 69. doi: 10.3389/feart.2017.00069.

Miles, K. E. *et al.* (2019) ‘Surface and subsurface hydrology of debris-covered Khumbu Glacier, Nepal, revealed by dye tracing’, *Earth and Planetary Science Letters*, 513, pp. 176–186. doi: 10.1016/j.epsl.2019.02.020.

Miles, K. E. *et al.* (2020) ‘Hydrology of debris-covered glaciers in High Mountain Asia’, *Earth-Science Reviews*. Elsevier, p. 103212. doi: 10.1016/j.earscirev.2020.103212.

Mindl, B. *et al.* (2007) ‘Factors influencing bacterial dynamics along a transect from supraglacial runoff to proglacial lakes of a high Arctic glacieri’, in *FEMS Microbiology Ecology*. doi: 10.1111/j.1574-6941.2006.00262.x.

Mitchell, T. D. *et al.* (2004) ‘A comprehensive set of high-resolution grids of monthly climate for Europe and the globe : the observed record (1901-2000) and 16 scenarios (2001-2100).’, *Geography*, 55(July), p. 30. Available at: https://www.researchgate.net/publication/242274942_A_Comprehensive_Set_of_High-Resolution_Grids_of_Monthly_Climate_for_Europe_and_the_Globe_The_Observed_Record_1901-2000_and_16_Scenarios_2001-2100 (Accessed: 1 May 2022).

Monien, D. *et al.* (2017) ‘Meltwater as a source of potentially bioavailable iron to Antarctica waters’, *Antarctic Science*, 29(3), pp. 277–291. doi: 10.1017/S095410201600064X.

Montgomery, D. R. and Brandon, M. T. (2002) ‘Topographic controls on erosion rates in tectonically active mountain ranges’, *Earth and Planetary Science Letters*, 201(3–4), pp. 481–489. doi: 10.1016/S0012-821X(02)00725-2.

Moore, C. M. *et al.* (2013) ‘Processes and patterns of oceanic nutrient limitation’, *Nature Geoscience*. Nature Publishing Group, pp. 701–710. doi: 10.1038/ngeo1765.

Moore, J. K. *et al.* (2001) ‘Iron cycling and nutrient-limitation patterns in surface waters of the world ocean’, *Deep-Sea Research Part II: Topical Studies in Oceanography*, 49(1–3), pp. 463–507. doi: 10.1016/S0967-0645(01)00109-6.

Moore, J. R. *et al.* (2012) ‘Earthquake-triggered rock slope failures: Damage and site effects’, in *Landslides and Engineered Slopes: Protecting Society through Improved Understanding - Proceedings of the 11th International and 2nd North American Symposium on Landslides and Engineered Slopes, 2012*.

Moore, P. L. (2021) ‘Numerical Simulation of Supraglacial Debris Mobility: Implications for Ablation and Landform Genesis’, *Frontiers in Earth Science*, 9, p. 595. doi: 10.3389/feart.2021.710131.

Muñoz-Sabater, J., (2019): ERA5-Land hourly data from 1981 to present. Copernicus Climate Change Service (C3S) Climate Data Store (CDS). (Accessed on 08-03-2021), 10.24381/cds.e2161bac

Muñoz-Sabater, J. *et al.* (2021) ‘ERA5-Land: A state-of-the-art global reanalysis dataset for land applications’, *Earth System Science Data Discussions*, pp. 1–50. doi: 10.5194/ESSD-2021-82.

Murton, J. B., Peterson, R. and Ozouf, J. C. (2006) ‘Bedrock fracture by ice segregation in cold regions’, *Science*, 314(5802), pp. 1127–1129. doi: 10.1126/science.1132127.

Nagai, H. *et al.* (2013) ‘Southwest-facing slopes control the formation of debris-covered glaciers in the Bhutan Himalaya’, *Cryosphere*, 7(4), pp. 1303–1314. doi: 10.5194/tc-7-1303-2013.

Narama, C. *et al.* (2017) ‘Seasonal drainage of supraglacial lakes on debris-covered glaciers in the Tien Shan Mountains, Central Asia', *Geomorphology*, 286, pp. 133–142. doi: 10.1016/j.geomorph.2017.03.002.

Neupane, R., Chen, H. and Cao, C. (2019) 'Review of moraine dam failure mechanism', *Geomatics, Natural Hazards and Risk*. Taylor & Francis, pp. 1948–1966. doi: 10.1080/19475705.2019.1652210.

Nicholson, L. and Benn, D. I. (2006) 'Calculating ice melt beneath a debris layer using meteorological data', *Journal of Glaciology*, 52(178), pp. 463–470. doi: 10.3189/172756506781828584.

Nielsen, L. E. and Stockton, F. D. (1956) 'Flow patterns in glacier ice', *Journal of Applied Physics*, 27(5), pp. 448–453. doi: 10.1063/1.1722400.

Ning, L. *et al.* (2003) 'Fatigue properties of cracked, saturated and frozen sandstone samples under cyclic loading', *International Journal of Rock Mechanics and Mining Sciences*, 40(1), pp. 145–150. doi: 10.1016/S1365-1609(02)00111-9.

Nixon, S. L. *et al.* (2017) 'Viable cold-tolerant iron-reducing microorganisms in geographically diverse subglacial environments', *Biogeosciences*, 14(6), pp. 1445–1455. doi: 10.5194/bg-14-1445-2017.

NOAA (2021) Pacific Decadal Oscillation (PDO). Available at: https://www.ncdc.noaa.gov/teleconnections/pdo/ (Accessed: 07/05/2021).

Nodwell, L. M. and Price, N. M. (2001) 'Direct use of inorganic colloidal iron by marine mixotrophic phytoplankton', *Limnology and Oceanography*, 46(4), pp. 765–777. doi: 10.4319/lo.2001.46.4.0765.

Noetzli, J. *et al.* (2007) 'Three-dimensional distribution and evolution of permafrost temperatures in idealized high-mountain topography', *Journal of Geophysical Research: Earth Surface*, 112(2). doi: 10.1029/2006JF000545.

Noetzli, J. (2008) *Modeling transient three-dimensional temperature fields in mountain permafrost*, *Modeling Transient Three-dimensional Temperature Fields in Mountain Permafrost*.

Normandeau, A. *et al.* (2019) 'Retreat Pattern of Glaciers Controls the Occurrence of Turbidity Currents on High-Latitude Fjord Deltas (Eastern Baffin Island)', *Journal of Geophysical Research: Earth Surface*, 124(6), pp. 1559–1571. doi:

10.1029/2018JF004970.

Østrem, G. (1959) ‘Ice Melting under a Thin Layer of Moraine, and the Existence of Ice Cores in Moraine Ridges’, *Geografiska Annaler*, 41(4), pp. 228–230. Available at: http://www.jstor.org/stable/4626805.

Ott, R. F. (2020) ‘How Lithology Impacts Global Topography, Vegetation, and Animal Biodiversity: A Global-Scale Analysis of Mountainous Regions’, *Geophysical Research Letters*, 47(20), p. e2020GL088649. doi: 10.1029/2020GL088649.

Paguican, E. M. R., van Wyk de Vries, B. and Lagmay, A. M. F. (2014) ‘Hummocks: How they form and how they evolve in rockslide-debris avalanches’, *Landslides*, 11(1), pp. 67–80. doi: 10.1007/s10346-012-0368-y.

Pánek, T. *et al.* (2017) ‘Late Quaternary sackungen in the highest mountains of the Carpathians’, *Quaternary Science Reviews*, 159, pp. 47–62. doi: 10.1016/j.quascirev.2017.01.008.

Pánek, T. (2019) ‘Landslides and Quaternary climate changes—The state of the art’, *Earth-Science Reviews*, 196, p. 102871. doi: 10.1016/j.earscirev.2019.05.015.

Papineau, J. M. (2001) ‘Wintertime temperature anomalies in Alaska correlated with ENSO and PDO’, *International Journal of Climatology*, 21(13), pp. 1577–1592. doi: 10.1002/joc.686.

Paranunzio, R. *et al.* (2016) ‘Climate anomalies associated with the occurrence of rockfalls at high-elevation in the Italian Alps’, *Natural Hazards and Earth System Sciences*, 16(9), pp. 2085–2106. doi: 10.5194/nhess-16-2085-2016.

Patton, A. I., Rathburn, S. L. and Capps, D. M. (2019) ‘Landslide response to climate change in permafrost regions’, *Geomorphology*. Elsevier B.V., pp. 116–128. doi: 10.1016/j.geomorph.2019.04.029.

Van Pelt, W. J. J., Pohjola, V. A. and Reijmer, C. H. (2016) ‘The changing impact of snow conditions and refreezing on the mass balance of an idealized svalbard glacier’, *Frontiers in Earth Science*, 4, p. 102. doi: 10.3389/feart.2016.00102.

Pelto, M. *et al.* (2013) ‘Rising ELA and expanding proglacial lakes indicate impending rapid retreat of Brady Glacier, Alaska’, *Hydrological Processes*, 27(21), pp. 3075–3082. doi: 10.1002/hyp.9913.

Pepin, N. *et al.* (2015) ‘Elevation-dependent warming in mountain regions of the world’, *Nature Climate Change*. Nature Publishing Group, pp. 424–430. doi: 10.1038/nclimate2563.

Perovich, D. K. and Polashenski, C. (2012) ‘Albedo evolution of seasonal Arctic sea ice’, *Geophysical Research Letters*, 39(8). doi: 10.1029/2012GL051432.

Petley D (2022) The 17 September 2022 rock avalanche at Lamplugh Glacier in Alaska. Available at: https://blogs.agu.org/landslideblog/2022/09/23/lamplugh-glacier-1/ (Accessed: 09/01/2023)

Pfeffer, W. T. *et al.* (2014) ‘The Randolph Glacier Inventory: a globally complete inventory of glaciers’, *Journal of Glaciology*, 60(221), pp. 537–552. doi: 10.3189/2014jog13j176.

Pfeffer, W. T., Meier, M. F. and Illangasekare, T. H. (1991) ‘Retention of Greenland runoff by refreezing: implications for projected future sea level change’, *Journal of Geophysical Research*, 96(C12), pp. 22117–22124. doi: 10.1029/91jc02502.

Pierre, K. A. St. *et al.* (2019) ‘Proglacial freshwaters are significant and previously unrecognized sinks of atmospheric CO2’, *Proceedings of the National Academy of Sciences*, 116(36), pp. 17690–17695. doi: 10.1073/PNAS.1904241116.

Pithan, F. and Mauritsen, T. (2014) ‘Arctic amplification dominated by temperature feedbacks in contemporary climate models’, *Nature Geoscience*, 7(3), pp. 181–184. doi: 10.1038/ngeo2071.

Pollet, N. and Schneider, J. L. M. (2004) ‘Dynamic disintegration processes accompanying transport of the Holocene Flims sturzstrom (Swiss Alps)’, *Earth and Planetary Science Letters*, 221(1–4), pp. 433–448. doi: 10.1016/S0012-821X(04)00071-8.

Porter, P. R. *et al.* (2010) ‘Ice-marginal sediment delivery to the surface of a high-arctic glacier: Austre brøggerbreen, svalbard’, *Geografiska Annaler, Series A: Physical Geography*, 92(4), pp. 437–449. doi: 10.1111/j.1468-0459.2010.00406.x.

Porter, P. R., Smart, M. J. and Irvine-Fynn, T. D. L. (2019) ‘Glacial Sediment Stores and Their Reworking’, in Heckmann, T. and Morche, D. (eds) *Geomorphology of Proglacial Systems*. Springer, Cham, pp. 157–176. doi: 10.1007/978-3-319-94184-4_10.

Poulton, S. W. and Raiswell, R. (2002) ‘The low-temperature geochemical cycle of iron: From continental fluxes to marine sediment deposition’, *American Journal of Science*, 302(9), pp. 774–805. doi: 10.2475/ajs.302.9.774.

Prospero, J. M., Bullard, J. E. and Hodgkins, R. (2012) ‘High-Latitude Dust Over the North Atlantic: Inputs from Icelandic Proglacial Dust Storms’, *Science*, 335(6072), pp. 1078–1082. doi: 10.1126/SCIENCE.1217447.

Pudasaini, S. P. and Krautblatter, M. (2014) ‘A two-phasemechanicalmodel for rock-ice avalanches’, *Journal of Geophysical Research: Earth Surface*, 119(10), pp. 2272–2290. doi: 10.1002/2014JF003183.

Pudasaini, S. P. and Mergili, M. (2019) ‘A Multi-Phase Mass Flow Model’, *Journal of Geophysical Research: Earth Surface*, 124(12), pp. 2920–2942. doi: 10.1029/2019JF005204.

Racoviteanu, A. E. *et al.* (2008) ‘Decadal changes in glacier parameters in the Cordillera Blanca, Peru, derived from remote sensing’, *Journal of Glaciology*, 54(186), pp. 499–510. doi: 10.3189/002214308785836922.

Rada, C. and Schoof, C. (2018) ‘Channelized, distributed, and disconnected: Subglacial drainage under a valley glacier in the Yukon’, *Cryosphere*, 12(8), pp. 2609–2636. doi: 10.5194/tc-12-2609-2018.

Raiswell, R. *et al.* (2006) ‘Contributions from glacially derived sediment to the global iron (oxyhydr)oxide cycle: Implications for iron delivery to the oceans’, *Geochimica et Cosmochimica Acta*, 70(11), pp. 2765–2780. doi: 10.1016/j.gca.2005.12.027.

Raiswell, R., Benning, L. G., Tranter, M., *et al.* (2008) ‘Bioavailable iron in the Southern Ocean: The significance of the iceberg conveyor belt’, *Geochemical Transactions*, 9(1), p. 7. doi: 10.1186/1467-4866-9-7.

Raiswell, R., Benning, L. G., Davidson, L., *et al.* (2008) ‘Nanoparticulate bioavailable iron minerals in icebergs and glaciers’, *Mineralogical Magazine*, 72(1), pp. 345–348. doi: 10.1180/minmag.2008.072.1.345.

Raiswell, R. *et al.* (2010) ‘The determination of labile Fe in ferrihydrite by ascorbic acid extraction: Methodology, dissolution kinetics and loss of solubility with age and de-watering’, *Chemical Geology*, 278(1–2), pp. 70–79. doi: 10.1016/j.chemgeo.2010.09.002.

Raiswell, R. (2011) ‘Iceberg-hosted nanoparticulate Fe in the Southern Ocean: Mineralogy, origin, dissolution kinetics and source of bioavailable Fe’, *Deep-Sea Research Part II: Topical Studies in Oceanography*, 58(11–12), pp. 1364–1375. doi: 10.1016/j.dsr2.2010.11.011.

Raiswell, R. *et al.* (2016) ‘Potentially bioavailable iron delivery by iceberg-hosted sediments and atmospheric dust to the polar oceans’, *Biogeosciences*, 13(13), pp. 3887–3900. doi: 10.5194/bg-13-3887-2016.

Raiswell, R. *et al.* (2018) ‘Iron in Glacial Systems: Speciation, Reactivity, Freezing Behavior, and Alteration During Transport’, *Frontiers in Earth Science*, 6(11), p. 222. doi: 10.3389/feart.2018.00222.

Raiswell, R. and Canfield, D. E. (2012) ‘The iron biogeochemical cycle past and present’, *Geochemical Perspectives*, 1(1), pp. 1–232. doi: 10.7185/geochempersp.1.1.

Raiswell, R., Canfield, D. E. and Berner, R. A. (1994) ‘A comparison of iron extraction methods for the determination of degree of pyritisation and the recognition of iron-limited pyrite formation’, *Chemical Geology*, 111(1–4), pp. 101–110. doi: 10.1016/0009-2541(94)90084-1.

Rangwala, I. and Miller, J. R. (2012) ‘Climate change in mountains: A review of elevation-dependent warming and its possible causes’, *Climatic Change*, 114(3–4). doi: 10.1007/s10584-012-0419-3.

Ravanel, L. and Deline, P. (2011) ‘Climate influence on rockfalls in high-Alpine steep rockwalls: The north side of the Aiguilles de Chamonix (Mont Blanc massif) since the end of the “Little Ice Age”’, *The Holocene*, 21(2), pp. 357–365. doi: 10.1177/0959683610374887.

Ravanel, L. and Deline, P. (2015) ‘Rockfall Hazard in the Mont Blanc Massif Increased by the Current Atmospheric Warming’, in *Engineering Geology for Society and Territory - Volume 1: Climate Change and Engineering Geology*. Springer International Publishing, pp. 425–428. doi: 10.1007/978-3-319-09300-0_81.

Ravanel, L., Magnin, F. and Deline, P. (2017) ‘Impacts of the 2003 and 2015 summer heatwaves on permafrost-affected rock-walls in the Mont Blanc massif’, *Science of The Total Environment*, 609, pp. 132–143. doi: 10.1016/J.SCITOTENV.2017.07.055.

Reisdorph, S. C. and Mathis, J. T. (2015) ‘Assessing net community production in a glaciated Alaskan fjord', *Biogeosciences*, 12, pp. 5185–5198. doi: 10.5194/bg-12-5185-2015.

Ren, Z. *et al.* (2019) 'Ecological stoichiometry of the mountain cryosphere', *Frontiers in Ecology and Evolution*, 7(SEP), p. 360. doi: 10.3389/fevo.2019.00360.

Reznichenko, N. *et al.* (2010) 'Effects of debris on ice-surface melting rates: An experimental study', *Journal of Glaciology*, 56(197), pp. 384–394. doi: 10.3189/002214310792447725.

Reznichenko, N. V. *et al.* (2012) 'A new technique for identifying rock avalanche-sourced sediment in moraines and some paleoclimatic implications', *Geology*, 40(4), pp. 319–322. doi: 10.1130/G32684.1.

Reznichenko, N. V., Davies, T. R. H. and Alexander, D. J. (2011) 'Effects of rock avalanches on glacier behaviour and moraine formation', *Geomorphology*, 132(3–4), pp. 327–338. doi: 10.1016/j.geomorph.2011.05.019.

RGI Consortium (2017) Randolph Glacier Inventory – A Dataset of Global Glacier Outlines: Version 6.0: Technical Report, Global Land Ice Measurements from Space, Colorado, USA. Digital Media. doi:10.7265/N5-RGI-60.

Rich, H. W. and Morel, F. M. M. (1990) 'Availability of well-defined iron colloids to the marine diatom Thalassiosira weissflogii', *Limnology and Oceanography*, 35(3), pp. 652–662. doi: 10.4319/lo.1990.35.3.0652.

Riihelä, A., Manninen, T. and Laine, V. (2013) 'Observed changes in the albedo of the Arctic sea-ice zone for the period 1982-2009', *Nature Climate Change*, 3(10), pp. 895–898. doi: 10.1038/nclimate1963.

Rose, K. C. *et al.* (2014) 'Light attenuation characteristics of glacially-fed lakes', *Journal of Geophysical Research: Biogeosciences*, 119(7), pp. 1446–1457. doi: 10.1002/2014JG002674.

Rosser, B. *et al.* (2017) 'New Zealand's National Landslide Database', *Landslides*, 14(6), pp. 1949–1959. doi: 10.1007/s10346-017-0843-6.

Rue, E. L. and Bruland, K. W. (1995) 'Complexation of iron(III) by natural organic ligands in the Central North Pacific as determined by a new competitive ligand equilibration/adsorptive cathodic stripping voltammetric method', *Marine Chemistry*, 50(1–4), pp. 117–138. doi: 10.1016/0304-4203(95)00031-L.

Salzmann, N. *et al.* (2007) 'Ground surface temperature scenarios in complex high-mountain topography based on regional climate model results', *Journal of Geophysical Research*, 112(F2), p. F02S12. doi: 10.1029/2006JF000527.

Sam, L. *et al.* (2015) 'Remote sensing flow velocity of debris-covered glaciers using Landsat 8 data', *Progress in Physical Geography*, 40(2), pp. 305–321. doi: 10.1177/0309133315593894.

Samimi, S. and Marshall, S. J. (2017) 'Diurnal cycles of meltwater percolation, refreezing, and drainage in the supraglacial snowpack of Haig Glacier, Canadian Rocky Mountains', *Frontiers in Earth Science*, 5, p. 6. doi: 10.3389/feart.2017.00006.

Sanhueza-Pino, K. *et al.* (2011) 'Glacial advances constrained by 10Be exposure dating of bedrock landslides, Kyrgyz Tien Shan', *Quaternary Research*, 76(3), pp. 295–304. doi: 10.1016/j.yqres.2011.06.013.

Sansone, S., Zugliani, D. and Rosatti, G. (2021) 'A mathematical framework for modelling rock-ice avalanches', *Journal of Fluid Mechanics*, 919, p. 8. doi: 10.1017/jfm.2021.348.

Sato, Y. *et al.* (2021) 'Ice Cliff Dynamics of Debris-Covered Trakarding Glacier in the Rolwaling Region, Nepal Himalaya', *Frontiers in Earth Science*, 9. doi: 10.3389/feart.2021.623623.

Scambos, T. A. *et al.* (2004) 'Glacier acceleration and thinning after ice shelf collapse in the Larsen B embayment, Antarctica', *Geophysical Research Letters*, 31(18). doi: 10.1029/2004GL020670.

Scherler, D., Bookhagen, B. and Strecker, M. R. (2011a) 'Hillslope-glacier coupling: The interplay of topography and glacial dynamics in High Asia', *Journal of Geophysical Research: Earth Surface*, 116(2). doi: 10.1029/2010JF001751.

Scherler, D., Bookhagen, B. and Strecker, M. R. (2011b) 'Spatially variable response of Himalayan glaciers to climate change affected by debris cover', *Nature Geoscience*, 4(3), pp. 156–159. doi: 10.1038/ngeo1068.

Scherler, D., Wulf, H. and Gorelick, N. (2018) 'Global Assessment of Supraglacial Debris-Cover Extents', *Geophysical Research Letters*, 45(21), pp. 11,798-11,805. doi:

10.1029/2018GL080158.

Schlögel, R. *et al.* (2011) ‘Evidence of a changing size–frequency distribution of landslides in the Kyrgyz Tien Shan, Central Asia’, *Earth Surface Processes and Landforms*, 36(12), pp. 1658–1669. doi: 10.1002/ESP.2184.

Schneider, D. *et al.* (2011) ‘Unraveling driving factors for large rock–ice avalanche mobility’, *Earth Surface Processes and Landforms*, 36(14), pp. 1948–1966. doi: 10.1002/ESP.2218.

Schomacker, A. (2008) ‘What controls dead-ice melting under different climate conditions? A discussion’, *Earth-Science Reviews*, 90(3–4), pp. 103–113. doi: 10.1016/j.earscirev.2008.08.003.

Schroth, A. W. *et al.* (2011) ‘Glacial influence on the geochemistry of riverine iron fluxes to the Gulf of Alaska and effects of deglaciation’, *Geophysical Research Letters*, 38(16). doi: 10.1029/2011GL048367.

Schroth, A. W. *et al.* (2014) ‘Estuarine removal of glacial iron and implications for iron fluxes to the ocean’, *Geophysical Research Letters*, 41(11), pp. 3951–3958. doi: 10.1002/2014GL060199.

Schuur, E. A. G. *et al.* (2015) ‘Climate change and the permafrost carbon feedback’, *Nature*. Nature Publishing Group, pp. 171–179. doi: 10.1038/nature14338.

Schwarz, J. N. and Schodlok, M. P. (2009) ‘Impact of drifting icebergs on surface phytoplankton biomass in the Southern Ocean: Ocean colour remote sensing and in situ iceberg tracking’, *Deep-Sea Research Part I: Oceanographic Research Papers*, 56(10), pp. 1727–1741. doi: 10.1016/j.dsr.2009.05.003.

Schwertmann, U. and Fischer, W. R. (1973) ‘Natural “amorphous” ferric hydroxide’, *Geoderma*, 10(3). doi: 10.1016/0016-7061(73)90066-9.

Schwertmann, U., Stanjek, H. and Becher, H.-H. (2004) ‘Long-term in vitro transformation of 2-line ferrihydrite to goethite/hematite at 4, 10, 15 and 25°C’, *Clay Minerals*, 39(4), pp. 433–438. doi: 10.1180/0009855043940145.

Schwertmann, U. and Taylor, R. M. (1972) ‘The transformation of lepidocrocite to goethite’, *Clays and Clay Minerals*, 20(3). doi: 10.1346/CCMN.1972.0200306.

Seaberg, S. Z. *et al.* (1988) ‘Character of the Englacial and Subglacial Drainage System in the Lower Part of the Ablation Area of Storglaciären, Sweden, as Revealed by Dye-Trace Studies', *Journal of Glaciology*, 34(117), pp. 217–227. doi: 10.3189/S0022143000032263.

Seip, H. M. (1980) 'Acid Snow - Snowpack Chemistry and Snowmelt', in *Effects of Acid Precipitation on Terrestrial Ecosystems*. Springer, Boston, MA, pp. 77–94. doi: 10.1007/978-1-4613-3033-2_8.

Sharp, M. and Tranter, M. (2017) 'Glacier biogeochemistry', *Geochemical Perspectives*, 6(2), pp. 1–177. doi: 10.7185/geochempersp.6.2.

Shaw, S. *et al.* (2005) 'The kinetics and mechanisms of goethite and hematite crystallization under alkaline conditions, and in the presence of phosphate', *American Mineralogist*, 90(11–12). doi: 10.2138/am.2005.1757.

Shoenfelt, E. M. *et al.* (2017) 'High particulate iron(II) content in glacially sourced dusts enhances productivity of a model diatom', *Science Advances*, 3(6). doi: 10.1126/sciadv.1700314.

Shreve, R. L. (1968) 'Leakage and fluidization in air-layer lubricated avalanches', *Bulletin of the Geological Society of America*, 79(5), pp. 653–658. doi: 10.1130/0016-7606(1968)79[653:LAFIAL]2.0.CO;2.

Shugar, D. H. *et al.* (2012) 'The response of Black Rapids Glacier, Alaska, to the Denali earthquake rock avalanches', *Journal of Geophysical Research: Earth Surface*, 117, p. F01006. doi: 10.1029/2011JF002011.

Shugar, D. H. and Clague, J. J. (2011) 'The sedimentology and geomorphology of rock avalanche deposits on glaciers', *Sedimentology*, 58(7), pp. 1762–1783. doi: 10.1111/j.1365-3091.2011.01238.x.

Shugar, D. H., Clague, J. J. and McSaveney, M. J. (2018) 'Late Holocene activity of Sherman and Sheridan glaciers, Prince William Sound, Alaska', *Quaternary Science Reviews*, 194, pp. 116–127. doi: 10.1016/j.quascirev.2018.07.016.

Shugar, D. H., Rabus, B. T. and Clague, J. J. (2010) 'Elevation changes (1949-1995) of Black Rapids Glacier, Alaska, derived from a multi-baseline InSAR DEM and historical maps', *Journal of Glaciology*, 56(198), pp. 625–634. doi: 10.3189/002214310793146278.

Shulmeister, J. *et al.* (2009) ‘Catastrophic landslides, glacier behaviour and moraine formation - A view from an active plate margin’, *Quaternary Science Reviews*, 28(11–12), pp. 1085–1096. doi: 10.1016/j.quascirev.2008.11.015.

Simon, Q., St-Onge, G. and Hillaire-Marcel, C. (2012) ‘Late Quaternary chronostratigraphic framework of deep Baffin Bay glaciomarine sediments from high-resolution paleomagnetic data’, *Geochemistry, Geophysics, Geosystems*, 13(1). doi: 10.1029/2012GC004272.

Singer, G. A. *et al.* (2012) ‘Biogeochemically diverse organic matter in Alpine glaciers and its downstream fate’, *Nature Geoscience*, 5(10), pp. 710–714. doi: 10.1038/ngeo1581.

Slemmons, K. E. H. and Saros, J. E. (2012) ‘Implications of nitrogen-rich glacial meltwater for phytoplankton diversity and productivity in alpine lakes’, *Limnology and Oceanography*, 57(6), pp. 1651–1663. doi: 10.4319/LO.2012.57.6.1651.

Smith, K. L. *et al.* (2007) ‘Free-drifting icebergs: Hot spots of chemical and biological enrichment in the Weddell Sea’, *Science*, 317(5837), pp. 478–482. doi: 10.1126/science.1142834.

Smith, K. L. *et al.* (2013) ‘Icebergs as unique lagrangian ecosystems in polar seas’, *Annual Review of Marine Science*, 5, pp. 269–287. doi: 10.1146/annurev-marine-121211-172317.

Smith, W. D. *et al.* (2020) ‘GERALDINE (Google Earth Engine supRaglAciaL Debris INput dEtector): A new tool for identifying and monitoring supraglacial landslide inputs’, *Earth Surface Dynamics*, 8(4), pp. 1053–1065. doi: 10.5194/esurf-8-1053-2020.

Sommaruga, R. (2014) ‘When glaciers and ice sheets melt: Consequences for planktonic organisms’, *Journal of Plankton Research*, 37(3), pp. 509–518. doi: 10.1093/plankt/fbv027.

Sommaruga, R. and Kandolf, G. (2014) ‘Negative consequences of glacial turbidity for the survival of freshwater planktonic heterotrophic flagellates’, *Scientific Reports 2014 4:1*, 4(1), pp. 1–5. doi: 10.1038/srep04113.

Sommer, C. *et al.* (2020) ‘Rapid glacier retreat and downwasting throughout the European Alps in the early 21st century’, *Nature Communications*, 11(1), pp. 1–10. doi: 10.1038/s41467-020-16818-0.

Sosio, R. *et al.* (2012) 'Modelling rock avalanche propagation onto glaciers', *Quaternary Science Reviews*, 47, pp. 23–40. doi: 10.1016/j.quascirev.2012.05.010.

St-Laurent, P. *et al.* (2017) 'Pathways and supply of dissolved iron in the Amundsen Sea (Antarctica)', *Journal of Geophysical Research: Oceans*, 122(9), pp. 7135–7162. doi: 10.1002/2017JC013162.

Stanjek, H. and Weidler, P. G. (1992) 'The effect of dry heating on the chemistry, surface area, and oxalate solubility of synthetic 2-line and 6-line ferrihydrites', *Clay Minerals*, 27(4), pp. 397–411. doi: 10.1180/claymin.1992.027.4.01.

Statham, P. J., Skidmore, M. and Tranter, M. (2008) 'Inputs of glacially derived dissolved and colloidal iron to the coastal ocean and implications for primary productivity', *Global Biogeochemical Cycles*, 22(3). doi: 10.1029/2007GB003106.

Stjern, C. W. *et al.* (2019) 'Arctic Amplification Response to Individual Climate Drivers', *Journal of Geophysical Research: Atmospheres*, 124(13), pp. 6698–6717. doi: 10.1029/2018JD029726.

Stoffel, M., Tiranti, D. and Huggel, C. (2014) 'Climate change impacts on mass movements - Case studies from the European Alps', *Science of the Total Environment*, 493, pp. 1255–1266. doi: 10.1016/j.scitotenv.2014.02.102.

Stroeve, J. C. *et al.* (2012) 'The Arctic's rapidly shrinking sea ice cover: A research synthesis', *Climatic Change*, 110(3–4), pp. 1005–1027. doi: 10.1007/s10584-011-0101-1.

Stuecker, M. F. *et al.* (2018) 'Polar amplification dominated by local forcing and feedbacks', *Nature Climate Change*, 8(12). doi: 10.1038/s41558-018-0339-y.

Sunda, W. G., Swift, D. G. and Huntsman, S. A. (1991) 'Low iron requirement for growth in oceanic phytoplankton', *Nature 1991 351:6321*, 351(6321), pp. 55–57. doi: 10.1038/351055a0.

Tanyaş, H. *et al.* (2017) 'Presentation and Analysis of a Worldwide Database of Earthquake-Induced Landslide Inventories', *Journal of Geophysical Research: Earth Surface*, 122(10), pp. 1991–2015. doi: 10.1002/2017JF004236.

Tanyaş, H., Allstadt, K. E. and van Westen, C. J. (2018) 'An updated method for estimating landslide-event magnitude', *Earth Surface Processes and Landforms*, 43(9), pp. 1836–1847. doi: 10.1002/esp.4359.

Tebbens, S. F. (2020) ‘Landslide Scaling: A Review’, *Earth and Space Science*. Wiley-Blackwell Publishing Ltd, p. e2019EA000662. doi: 10.1029/2019EA000662.

Thies, H. *et al.* (2013) ‘Evidence of rock glacier melt impacts on water chemistry and diatoms in high mountain streams’, *Cold Regions Science and Technology*, 96, pp. 77–85. doi: 10.1016/j.coldregions.2013.06.006.

Thompson, S. *et al.* (2016) ‘Stagnation and mass loss on a Himalayan debris-covered glacier: Processes, patterns and rates’, *Journal of Glaciology*, 62(233), pp. 467–485. doi: 10.1017/jog.2016.37.

Tielidze, L. G. *et al.* (2020) ‘Supra-glacial debris cover changes in the Greater Caucasus from 1986 to 2014’, *The Cryosphere*, 14(2), pp. 585–598. doi: 10.5194/tc-14-585-2020.

Timmermans, K. R. *et al.* (2001) ‘Co-limitation by iron and light of Chaetoceros brevis, C. dichaeta and C. calcitrans (Bacillariophyceae)’, *Marine Ecology Progress Series*, 217, pp. 287–297. doi: 10.3354/MEPS217287.

Timmermans, K. R. *et al.* (2005) ‘Physiological responses of three species of marine pico-phytoplankton to ammonium, phosphate, iron and light limitation’, *Journal of Sea Research*, 53(1–2), pp. 109–120. doi: 10.1016/J.SEARES.2004.05.003.

Torrent, J., Guzman, R. and Parra, M. A. (1982) ‘Influence of relative humidity on the crystallization of Fe(III) oxides from ferrihydrite.’, *Clays & Clay Minerals*, 30(5), pp. 337–340. doi: 10.1346/CCMN.1982.0300503.

Torsvik, T. *et al.* (2019) ‘Impact of tidewater glacier retreat on the fjord system: Modeling present and future circulation in Kongsfjorden, Svalbard’, *Estuarine, Coastal and Shelf Science*, 220, pp. 152–165. doi: 10.1016/j.ecss.2019.02.005.

Tortell, P. D. *et al.* (1999) ‘Marine bacteria and biogeochemical cycling of iron in the oceans’, *FEMS Microbiology Ecology*, 29(1), pp. 1–11. doi: 10.1111/J.1574-6941.1999.TB00593.X.

Tovar, D. S., Shulmeister, J. and Davies, T. R. (2008) ‘Evidence for a landslide origin of New Zealand’s Waiho Loop moraine’, *Nature Geoscience*, 1(8), pp. 524–526. doi: 10.1038/ngeo249.

Tranter, M. *et al.* (2002) ‘Geochemical weathering at the bed of Haut glacier d’Arolla, Switzerland - A new model', *Hydrological Processes*. doi: 10.1002/hyp.309.

Turcotte, D. L. (1986) 'Fractals and fragmentation.', *Journal of Geophysical Research*, 91(B2), pp. 1921–1926. doi: 10.1029/JB091iB02p01921.

Turetsky, M. R. *et al.* (2020) 'Carbon release through abrupt permafrost thaw', *Nature Geoscience*, 13(2). doi: 10.1038/s41561-019-0526-0.

Turnbull, J. M. and Davies, T. R. H. (2006) 'A mass movement origin for cirques', *Earth Surface Processes and Landforms*, 31(9), pp. 1129–1148. doi: 10.1002/esp.1324.

Uhlmann, M. *et al.* (2013) 'Supra-glacial deposition and flux of catastrophic rock-slope failure debris, south-central Alaska', *Earth Surface Processes and Landforms*, 38(7), pp. 675–682. doi: 10.1002/esp.3311.

Vacco, D. A., Alley, R. B. and Pollard, D. (2010) 'Glacial advance and stagnation caused by rock avalanches', *Earth and Planetary Science Letters*, 294(1–2), pp. 123–130. doi: 10.1016/j.epsl.2010.03.019.

Varnes, D. J. (1978) 'Slope movement types and processes. Analysis and control, special report 176', *Transportation and Road Research Board*, 176(National Academy of Sciences), pp. 11–33.

Del Vecchio, J. *et al.* (2018) 'Storage and weathering of landslide debris in the eastern San Gabriel Mountains, California, USA: Implications for mountain solute flux', *Earth Surface Processes and Landforms*, 43(13), pp. 2724–2737. doi: 10.1002/esp.4427.

de Vente, J. *et al.* (2007) 'The sediment delivery problem revisited', *Progress in Physical Geography*. Sage PublicationsSage UK: London, England, pp. 155–178. doi: 10.1177/0309133307076485.

Viles, H. A. (2013) 'Linking weathering and rock slope instability: non-linear perspectives', *Earth Surface Processes and Landforms*, 38(1), pp. 62–70. doi: 10.1002/esp.3294.

Wadham, J. L. *et al.* (2010) 'Biogeochemical weathering under ice: Size matters', *Global Biogeochemical Cycles*, 24(3), p. 3025. doi: 10.1029/2009GB003688.

Wadham, J. L. *et al.* (2016) 'Sources, cycling and export of nitrogen on the Greenland Ice Sheet', *Biogeosciences*, 13(22), pp. 6339–6352. doi: 10.5194/bg-13-6339-2016.

Wadham, J. L. *et al.* (2019) 'Ice sheets matter for the global carbon cycle', *Nature*

Communications. Nature Publishing Group, pp. 1–17. doi: 10.1038/s41467-019-11394-4.

Wakahama, G. *et al.* (1976) ‘Field Observations and Experimental and Theoretical Studies on the Superimposed Ice of McCall Glacier, Alaska’, *Journal of Glaciology*, 16(74), pp. 135–149. doi: 10.3189/s0022143000031488.

Warburton, J. (1990) ‘An alpine proglacial fluvial sediment budget’, *Geografiska Annaler, Series A*, 72 A(3–4), pp. 261–272. doi: 10.1080/04353676.1990.11880322.

Waychunas, G. A., Kim, C. S. and Banfield, J. F. (2005) ‘Nanoparticulate Iron Oxide Minerals in Soils and Sediments: Unique Properties and Contaminant Scavenging Mechanisms’, *Journal of Nanoparticle Research 2005 7:4*, 7(4), pp. 409–433. doi: 10.1007/S11051-005-6931-X.

Wells, M. L. and Mayer, L. M. (1991) ‘The photoconversion of colloidal iron oxyhydroxides in seawater’, *Deep Sea Research Part A, Oceanographic Research Papers*, 38(11), pp. 1379–1395. doi: 10.1016/0198-0149(91)90012-5.

Wells, M. L., Zorkin, N. G. and Lewis, A. G. (1983) ‘The role of colloid chemistry in providing a source of iron to phytoplankton.’, *Journal of Marine Research*, 41(4), pp. 731–746. doi: 10.1357/002224083788520478.

Wendler, G., Gordon, T. and Stuefer, M. (2017) ‘On the precipitation and precipitation change in Alaska’, *Atmosphere*. MDPI AG, p. 253. doi: 10.3390/atmos8120253.

Wessels, R. L., Kargel, J. S. and Kieffer, H. H. (2002) ‘ASTER measurement of supraglacial lakes in the Mount Everest region of the Himalaya’, *Annals of Glaciology*, 34, pp. 399–408. doi: 10.3189/172756402781817545.

Westoby, M. J. *et al.* (2020) ‘Geomorphological evolution of a debris-covered glacier surface’, *Earth Surface Processes and Landforms*, 45(14), pp. 3431–3448. doi: 10.1002/ESP.4973.

Whitehouse, I. E. and Griffiths, G. A. (1983) ‘Frequency and hazard of large rock avalanches in the central Southern Alps, New Zealand.’, *Geology*, 11(6), pp. 331–334. doi: 10.1130/0091-7613(1983)11<331:FAHOLR>2.0.CO;2.

Williams, H. B. and Koppes, M. N. (2019) ‘A comparison of glacial and paraglacial denudation responses to rapid glacial retreat’, *Annals of Glaciology*, 60(80), pp. 151–164.

doi: 10.1017/aog.2020.1.

Willis, I. C., Sharp, M. J. and Richards, K. S. (1990) 'Configuration of the Drainage System of Midtdalsbreen, Norway, as Indicated by Dye-Tracing Experiments', *Journal of Glaciology*, 36(122), pp. 89–101. doi: 10.3189/S0022143000005608.

Winter, K. *et al.* (2019) 'Radar-Detected Englacial Debris in the West Antarctic Ice Sheet', *Geophysical Research Letters*, 46(17–18), pp. 10454–10462. doi: 10.1029/2019GL084012.

Wirbel, A., Jarosch, A. H. and Nicholson, L. (2018) 'Modelling debris transport within glaciers by advection in a full-Stokes ice flow model', *Cryosphere*, 12(1), pp. 189–204. doi: 10.5194/tc-12-189-2018.

Van Woerkom, T. *et al.* (2019) 'Sediment supply from lateral moraines to a debris-covered glacier in the Himalaya', *Earth Surface Dynamics*, 7(2), pp. 411–427. doi: 10.5194/esurf-7-411-2019.

Voight, B. (1978) *Rockslides and Avalanches, 1. Natural Phenomena*. Elsevier, Amsterdam, 843 pp.

Wilson, F.H., Hults, C.P., Mull, C.G, and Karl, S.M. (2015) Geologic map of Alaska: U.S. Geological Survey Scientific Investigations Map 3340, pamphlet 196 p., 2 sheets, scale 1:1,584,000, http://dx.doi.org/10.3133/sim3340.

Wolter, K. and Timlin, M. S. (2011) 'El Niño/Southern Oscillation behaviour since 1871 as diagnosed in an extended multivariate ENSO index (MEI.ext)', *International Journal of Climatology*, 31(7), pp. 1074–1087. doi: 10.1002/joc.2336.

Woo, M. K. (2012) *Permafrost hydrology*, *Permafrost Hydrology*. doi: 10.1007/978-3-642-23462-0.

Wu, J. *et al.* (2001) 'Soluble and colloidal iron in the oligotrophic North Atlantic and North Pacific', *Science*, 293(5531), pp. 847–849. doi: 10.1126/science.1059251.

Wu, J. and Luther, G. W. (1995) 'Complexation of Fe(III) by natural organic ligands in the Northwest Atlantic Ocean by a competitive ligand equilibration method and a kinetic approach', *Marine Chemistry*, 50(1–4), pp. 159–177. doi: 10.1016/0304-4203(95)00033-N.

Wu, S. Y. and Hou, S. (2017) 'Impact of icebergs on net primary productivity in the

Southern Ocean', *Cryosphere*, 11(2), pp. 707–722. doi: 10.5194/tc-11-707-2017.

Wu, Y. hong *et al.* (2013) 'Phosphorus biogeochemical cycle research in mountainous ecosystems', *Journal of Mountain Science*, 10(1), pp. 43–53. doi: 10.1007/s11629-013-2386-1.

Wu, Z. *et al.* (2019) 'Fluctuation analysis in the dynamic characteristics of continental glacier based on Full-Stokes model', *Scientific Reports*, 9(1), pp. 1–17. doi: 10.1038/s41598-019-56864-3.

Wulder, M. A. *et al.* (2019) 'Current status of Landsat program, science, and applications', *Remote Sensing of Environment*, 225, pp. 127–147. doi: 10.1016/j.rse.2019.02.015.

Yang, M. *et al.* (2021) 'Ferrihydrite Transformation Impacted by Adsorption and Structural Incorporation of Rare Earth Elements', *ACS Earth and Space Chemistry*, 5(10), pp. 2768–2777. doi: 10.1021/acsearthspacechem.1c00159.

Yang, Q. *et al.* (2019) 'High mobility of rock-ice avalanches: Insights from small flume tests of gravel-ice mixtures', *Engineering Geology*, 260, p. 105260. doi: 10.1016/j.enggeo.2019.105260.

Yee, N. *et al.* (2006) 'The rate of ferrihydrite transformation to goethite via the Fe(II) pathway', *American Mineralogist*, 91(1). doi: 10.2138/am.2006.1860.

Yu, J. Y. *et al.* (1999) 'Apparent solubilities of schwertmannite and ferrihydrite in natural stream waters polluted by mine drainage', *Geochimica et Cosmochimica Acta*, 63(19–20), pp. 3407–3416. doi: 10.1016/S0016-7037(99)00261-6.

Zhang, J. *et al.* (2019) 'Glacier Facies Mapping Using a Machine-Learning Algorithm: The Parlung Zangbo Basin Case Study', *Remote Sensing*, 11(4), p. 452. doi: 10.3390/rs11040452.

Zhang, R. *et al.* (2015) 'Transport and reaction of iron and iron stable isotopes in glacial meltwaters on Svalbard near Kongsfjorden: From rivers to estuary to ocean', *Earth and Planetary Science Letters*, 424, pp. 201–211. doi: 10.1016/j.epsl.2015.05.031.

Appendix

Supraglacial rock avalanches, Alaska

Aim: Sample supraglacially deposited rock avalanches to understand their influence on glacial biogeochemistry

William Smith, Stuart Dunning, Richard Smith

21st June – 2nd July 2018

ACKNOWLEDGEMENTS

Mount Everest Foundation (18-22)

Gino Watkins Memorial fund

Newcastle University

Expedition Foods

This trip would not have been possible without the financial support of the Mount Everest Foundation, the Gino Watkins Memorial fund awarded by the Scott Polar Research Institute, and Newcastle University. We would also like to thank Expedition Foods for their support and for keeping us well fuelled in the mountains. In addition, a big thank you is given to our pilot Drake Olson of Fly Drake, who safely flew us to one of the remotest parts of North America and helped us with his exceptional knowledge of the area.

CONTENTS

1.0 MEET THE TEAM

EXPEDITION LEADER: WILL SMITH

Will is a PhD student at Newcastle University, investigating how supraglacially deposited rock avalanches can affect glacial biogeochemistry. This expedition was the first fieldwork of his current PhD research, which is focussing on Alaskan glaciers, due to the prevalence of rock avalanches in the region. During Will's time in academia (BSc Geography at Northumbria University and MSc Polar and Alpine Change at the University of Sheffield) he has undertaken glaciological fieldwork in the European Alps and Svalbard. In his spare time, he is also a keen rock climber and mountaineer, spending the majority of his time climbing / fell running / cycling in the Lake District and Northumberland.

STUART DUNNING

Stuart is a Senior Lecturer in Physical Geography at Newcastle University and Will's PhD supervisor. His main research focus centres on hillslope processes, often in cryospheric systems. He has undertaken fieldwork all over the world, including Greenland, Antarctica, Himalaya, New Zealand and the European Alps.

RICHARD SMITH

Richard is an aspiring mountain guide having recently completed a BA in Outdoor Leadership at the University of Cumbria. His aim, now he has finished university, is to undertake his walking, climbing and mountaineering awards to become a certified guide. He therefore spends the majority of his time in the Lake District, climbing and fell running, honing his skills in preparation. He has previous mountaineering and climbing experience in Scotland (winter) and the European Alps.

2.0 SCIENCE BACKGROUND / INTENTIONS

Slope processes are a critical control on sediment delivery onto ice masses, which is becoming increasingly important as glacial environments transition to deglacierized (e.g. Porter *et al*., 2010). During large rock slope failures (>10^6 m^3) rapid transport of this sediment promotes rock comminution, creating rare aggregates formed under intense pressure and heat (Weidinger *et al*., 2014). The delivery of this sediment onto ice masses causes large extensive deposits, covering larger areas than their non-glacial counterpart (Hewitt, 2009). This is due to the friction between the rock avalanche material and the ice, creating vast amounts of meltwater, lubricating the debris, promoting additional expansion. However, it is currently unknown how this meltwater interacting with fresh rock substrates affects meltwater geochemistry and subsequently the biogeochemistry of the glacier. For example, rock comminution is known to increase the bioavailability of certain compounds in glacial environments (Telling *et al*., 2015), but the impacts of these potentially nutrient-rich sediment inputs on fertilising supra-, sub-, and extra-glacial environments are unknown. Substantial nutrient delivery may stimulate autotrophic activity, creating a negative climate feedback loop. This project aims to quantify the biogeochemical effects of supraglacially deposited rock avalanches by sampling large fresh deposits in Glacier Bay National Park, Alaska, before laboratory analysis of these samples in the UK. Alaska is the ideal place to study these deposits because they are well documented, with known event dates and volumes. We hope to understand how initial rock avalanche deposition modifies glacial biogeochemistry through analogue experiments, but also understand how supraglacial deposits effect glacial biogeochemistry over time, through seasonal interaction with snowpacks and subsequently snowmelt.

This work will form part of the PhD thesis of William Smith titled “Effects of supraglacially deposited rock avalanches on glacial biogeochemistry”, undertaken at Newcastle University.

3.0 EXPEDITION SUMMARY

The team set off to Glacier Bay National Park, Alaska to investigate two large rock avalanches (RA): the La Perouse RA deposit and the Lamplugh RA deposit, both of which were deposited on outlet glaciers of the Brady Icefield in 2014 and 2016, respectively. This huge icefield is one of the remotest parts of North America, and a region with some of the highest terrain, with peaks rising over 4000 m straight out of the Pacific Ocean. The areas proximity to the Pacific Ocean is also the reason for its reputation as having unforgiveable weather conditions.

We had a very short 10-day period in which to get in, get samples and get them back to the lab. This was always going to be a difficult task because a certain amount of snow was needed for ski plane landing, but we needed the rock avalanche debris to be relatively snow-free so we could extract samples. Our plan to land at one deposit, traverse the icefield to access the next deposit, before sampling and flying back to the main town, was ultimately unfeasible due to snowpack conditions. Instead, we were dropped on a higher tributary of the icefield, due to the better snow for ski-plane landing and from here, we traversed the width of the icefield each day to extract samples from the Lamplugh RA. Luckily, we had an excellent 5-day weather window and did not experience any of the rainfall described as 'too heavy for Gore-Tex'.

The expedition gave us a chance to learn and experience proper self-sufficiency in the field and any limitations of our methodology, which will be invaluable for future work in other remote areas of Alaska. We were determined to get a large amount of samples for analysis, but also to enjoy the experience of being so isolated from civilisation – we succeeded in this and will hopefully be able to share some exciting new data from this expedition in the near future.

4.0 PLANNING

4.1 GLACIER BAY NATIONAL PARK

Glacier Bay National Park is a globally significant marine and terrestrial wilderness sanctuary. As the name suggests it is heavily glaciated, featuring large tidewater glaciers, valley glaciers and icefields. The area is particularly remote with only a few settlements within close proximity to the main glaciated peninsula. Access is only by boat or ski plane making it difficult to visit for tourists, who typically see the area on large cruise-ships. The area has some phenomenal peaks, the highest being Mount Fairweather at 4671 m, but numerous peaks remain unclimbed and numerous areas unexplored, due to harsh weather and accessibility issues.

4.2 OUR PLAN

The overarching aim of this project is to determine how rock avalanches deposited onto the surface of glaciers influence their biogeochemistry, and how this could modify extra-glacial ecosystems.

The main objective of this fieldwork was to visit two of the largest glacial rock avalanches (RA): Lamplugh and Le Perouse (Coe *et al*., 2017) (Figure 1), which occurred in 2016 and 2014, respectively. To do this, we planned to be flown onto the Lamplugh glacier by Fly Drake, from their base in Haines. Once onto the glacier we planned to camp overnight at a suitable location, before walking up the Lamplugh RA deposit the following day, to extract multiple samples in the six different deposit zones, outlined in the MSc thesis of Bessette-Kirton (2017). Once sampling was complete, we would begin an 18-mile traverse of the Brady Icefield, to access the Le Perouse glacial RA (58°33'40.81"N, 137° 4'24.19"W). Due to this being planned as a late June traverse of the icefield, climatic conditions are typically at their most stable, theoretically giving us larger weather windows for our research. The main issue we envisioned to encounter was snowpack conditions. For a ski plane to land on the icefield, snow needed to be of a suitable depth and have undergone compaction to ensure a solid landing platform; however, for the team to sample RA debris, the deposit needed to be relatively snow-free. Late June is typically a time when this small window of opportunity is available.

Depending on climatic conditions, time constraints and current accessibility, three other RA deposits were to be investigated on the way between Lamplugh and Le Perouse RA deposits (58°38'35.38"N, 137°6'0.82"W; 58°37'52.53"N, 137°1'30.36"W; 58°38'51.10"N, 137°4'52.47"W). These occurred in 2016, 2010, and 1994, allowing collection of samples from deposits, which have existed on the surface for multiple years, potentially reducing their ability to affect glacial geochemistry. Once the Le Perouse RA deposit had been reached, we planned to sample the deposit in a similar way to that of the Lamplugh RA deposit. After completing all sampling, we would be extracted from the icefield by Fly Drake, back to their base in Haines.

All RA sampling would involve extracting at least four 500 g samples of RA material, at different locations within each RA deposit zone, to investigate spatial variation in deposit chemistry. Samples would consist of material from depths of 0-10 cm and sampling would be undertaken using sterile sampling apparatus i.e. hand trowel, and pre-sterilised bottles. All samples would be frozen in the field using a portable freezer connected to solar panels.

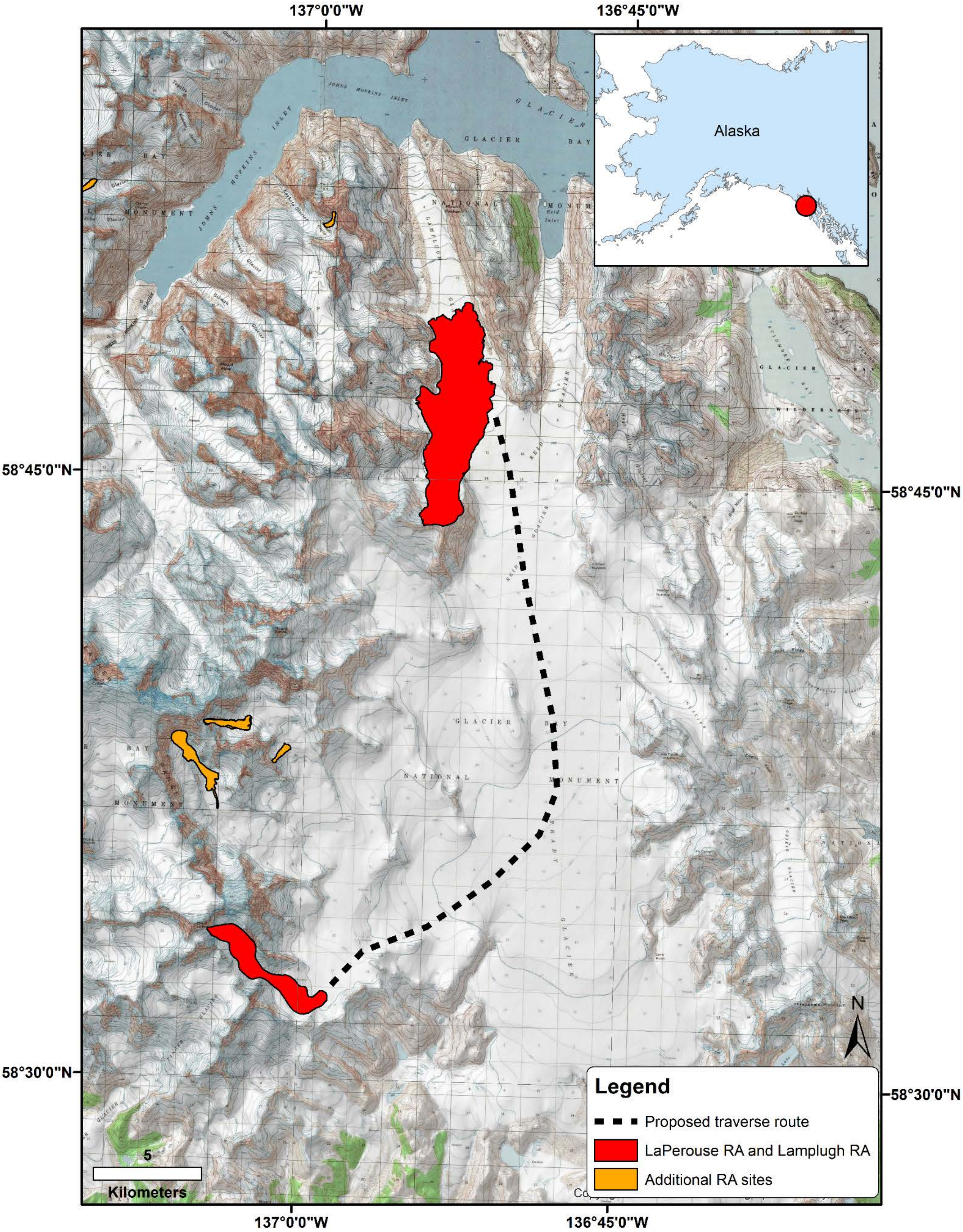

Figure 1: The planned traverse of the Brady Icefield to attain samples of the two largest glacial rock avalanches (RA). Red RA deposits depict primary objectives (Lamplugh the larger deposit towards the north of the figure, and La Perouse the smaller deposit in the south); orange RA deposits depict secondary objectives.

5.0 DIARY

PART 1 – GETTING TO HAINES

We set off from Newcastle University at 5 am on the 21st June to drive to Manchester airport, where we would get the first flight of our journey at 12:55 pm to Seattle Tacoma. This gave us plenty of time to sort out our 130 kg of baggage… or so we thought. We had booked enough excess baggage for all of our gear but because a portable freezer is apparently not something people usually carry in hold luggage, we had a couple of issues. This freezer was integral to our project, because samples would be useless if they were not frozen immediately after their extraction (it would prevent any chemical/biological changes to the debris before laboratory analysis), and therefore we needed it to come to Alaska with us. After a lot of persuasion, the freezer finally went off on its long journey down the baggage conveyor belt – we all let out a sigh of relief. Once arriving in Seattle we caught our next flight to Juneau, where we stayed the night in the airport. Check out our luxurious sleeping quarters below:

Awaking the next morning we caught the 4.5-hour ferry from Juneau to Haines, on board the Le Conte ship, where we got some stunning views of the Lynn Canal and its surroundings.

PART 2 - PREPARATION

After arriving in Haines we were taxied into town by John of Haines Shuttle (the only taxi service in Haines), stopping off at a hardware store to collect some science essentials e.g. gaffer tape and zip ties. Looking at the weather forecast for the next few days, it looked as if we would have a 5-day weather window, so had to ensure we were fully prepared for departing the next day. This involved some unconventional crevasse rescue practice using a hotel balcony, and a trip to buy a battery to power the freezer while in the field. The next day we got the call from Drake to say he could get us out there, after he had picked up another expedition who were attempting to summit Mt Bertha.

PART 3 – THE GRAND DEPARTURE

We arrived at the airstrip, cooked some lunch on the runway – an interesting place to eat, and Drake arrived. Due to the plane size, it was decided that two trips would be necessary: firstly one person with all the kit, and then the other two people with the remaining kit. Stuart volunteered and before we knew it, he was in the air and on his way. One hour later and we were loading up the plane ready for departure. Drake had scouted around multiple landing sites on the icefield during the first flight, deciding that our optimum-landing site next to the Lamplugh deposit was too dangerous. This was due to the hummocky snow surface, caused by differential ablation of the snowpack. The snowpack was also very wet at this altitude, potentially causing the skis to dig in and flip the plane on landing. Drake settled for a landing spot on a tributary of the Reid glacier, about five miles from the Lamplugh deposit (58.73, -136.776). After all team members and kit were on the glacier, we were left alone in the National Park for the next 4 days.

PART 4 – THE SCIENCE

During our first night on the ice, there was heavy rain, but we awoke to much calmer weather conditions. We kitted up and headed on over to the descent off the Reid tributary glacier, which was a 200 m snow and gravel slope with a gradient of ~50 %. For the first day, we decided to go light and take only one pulk and all sampling apparatus, to assess the conditions. Once down the descent, we negotiated a large amount of crevasses, which generally turned out to be a maximum of 20 cm wide, before traversing the icefield over a very wet snowpack. Even with a light pulk and snowshoes, there was considerable resistance from the snowpack, something that could have potentially been eradicated with the use of skis.

Sampling commenced once we arrived at the Lamplugh deposit, and after we had filled up on some excellent vegetable tikkas provided by Expedition Foods. Luckily, the majority of the deposit was snow free and therefore easy to sample, and in areas of snow cover, there were visible debris patches that were accessible. On the first day, we collected half of the samples needed. Once back at base camp we discussed the logistics of getting to the La Perouse deposit and concluded that if was unfeasible to sample. The two main reasons for this included: it was unknown if Drake would be able to collect us from the La Perouse deposit because snow conditions were unknown in that area, and the weather window was now only 3 days long. In addition, the steep descent would have been dangerous with 80 kg + of freezer, battery and solar panels and the snow conditions would have made dragging all equipment difficult and unfeasible in such a short amount of time. It was decided that Lamplugh would become the main objective, with more samples taken of the Lamplugh deposit than originally intended to counteract the lack of La Perouse samples. The second day was much like the first day, collecting the remaining samples and getting back to camp. In total, 20 sediment samples, 2 water samples, 12 snow samples and 10 clasts were collected for laboratory analysis.

PART 5 – THE ‘DAY OFF’

After sampling was complete, we were contacted by Drake to inform us of weather conditions. The weather window allowed one more day on the ice, we therefore used this day to explore the area and attempt an ascent of Contact Nunatak. Cloud rolled in and out of camp frequently throughout the day, with visibility varying between 2 m and 20 km. We approached the base of Contact Nunatak and assessed the snow: it was similarly wet and unstable and the ascent required continuing up a corniced snow ridge, which looked inherently unstable. It was at this point that we decided the risk was too great, and although it would have been an excellent way to finish the trip, we had already been successful in sampling. We walked back to camp and relaxed for the rest of the evening.

PART 6 – DEPARTURE DAY

Awaking early, we got the call from Drake that he would pick us up around 11 am, so camp was packed up and we awaited his arrival. The weather looked unnerving with low cloud frequently reducing visibility to only a few metres. Luckily, Drake managed to land, so Will and Stuart went first with the intention to collect Richard, and all the gear, after he had dropped those two back at base. On the first flight, the weather looked very unfavourable for another pick up, and everyone was unsure as to whether Richard would have to spend another day or two on the icefield alone. Drake was quick to drop kit and refuel before flying back out almost immediately, to try collecting Richard and the remaining gear. When he landed,

the conditions were perfect and while we were waiting back at the airstrip, wondering what was happening, Drake and Richard were walking around on the icefield, taking in the stunning views once more. While waiting we managed to persuade one of the local airlines to let us use some electricity to power the freezer and keep samples frozen. Richard and Drake finally arrived back and we headed into Haines, for the remaining two days of the trip. We were lucky to have excellent weather and a successful sampling campaign. It was unfortunate we could not sample all objectives, but we successfully negated this by taking more samples of the Lamplugh RA deposit.

6.0 THE FINAL ROUTE

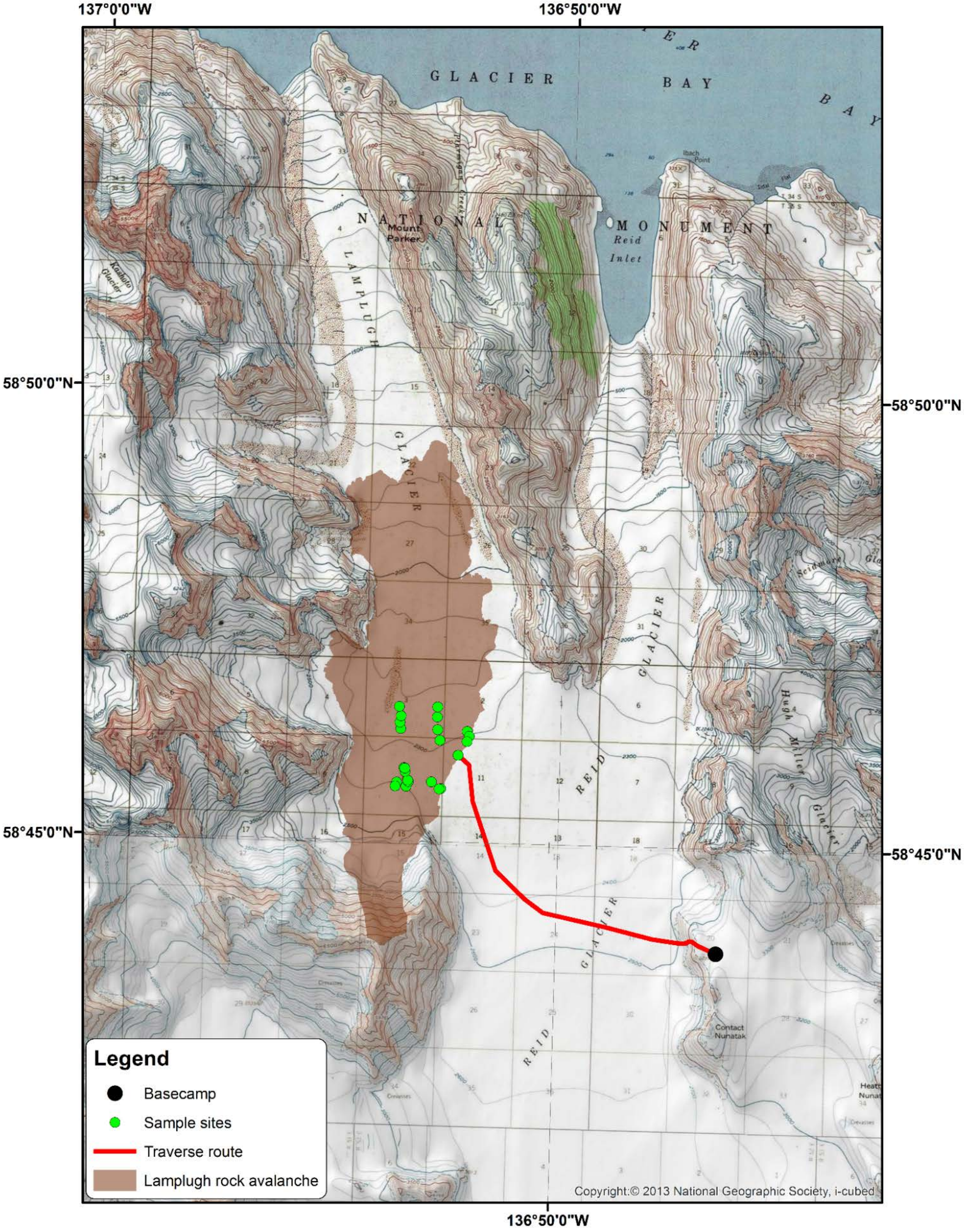

Figure 2: Map displaying basecamp, sample sites and the traverse route undertook on both days. Contact Nunatak is 1 km south of basecamp.

7.0 FUTURE WORK

Samples were successfully transported frozen back to the UK. Laboratory analysis has not yet been undertaken but is due to commence in the first quarter of 2019.

8.0 GLACIER BAY NATIONAL PARK SPECIFICS

PERMITS

A permit was obtained from the US National Park Service, with liaison primarily through Lewis Sharman. A permit should be applied for at least 3 months prior to fieldwork commencement.

MAPS

Google Earth and topo maps accessible through the USGS, were used for expedition planning.

EQUIPMENT TRANSPORTATION

All expedition equipment was taken as excess baggage on Thomas Cook Airlines and Alaska Airlines. A duplicate list was used to export and re-import equipment from the UK. If equipment were more valuable, a carnet would have been obtained.

FOOD AND ADDITIONAL EQUIPMENT

All food for the trip was bought from Expedition Foods and transported to the US as excess baggage. Freeze-dried food was available to buy in Alaska Sport Shop. Any outdoor equipment required (i.e. fuel, clothing etc.) was also available to buy at Alaska Sport Shop or Alaska Backcountry Outfitter.

COMMUNICATION

An Iridium satellite phone was used for all communication while in the field. Haines is not a big town but they had numerous cafes and a public library with free WiFi.

RISKS

The main risks were glacier travel i.e. crevasses, but weather was also known to be highly changeable in the area. Bears were also a risk, so we were advised to take an air horn for additional safety. A full risk assessment was undertaken and approved by Newcastle University.

MEDICAL ARRANGEMENTS

In case of small emergencies, we would contact Drake of Fly Drake. For any severe emergencies, our satellite phone had an SOS button, which would immediately put us in contact with local emergency services, which in our case would be the US Coast Guard.

9.0 MEF SPECIFIC QUESTIONS

OBSERVATIONS ON THE ACCURACY, OR OTHERWISE, OF GOOGLE EARTH IMAGES.

Google Earth images generally represented the area well and were sufficient for initial investigation of the study area and planning.

SUGGESTIONS FOR NEW ROUTES OR NEW SUBJECTS FOR STUDY IN THE AREA.

The icefield is generally poorly understood because of harsh conditions and accessibility issues. Snowpack evolution research would be particularly useful in this area due to the amount of snow deposited over the year and the hummocky topography it is characterised by, due to differential ablation. Simple melt rate research would also be valuable, providing mass balance estimates and estimates of discharge.

NOTES ON ACCESS, PORTERS, OR OTHER ISSUES OF INTEREST TO FUTURE VISITORS.

Fly Drake was an excellent pilot with exceptional knowledge of the area; this was invaluable for us during our time there.

DETAILS OF ANY INJURY OR ILLNESS TO EXPEDITION MEMBERS AND/OR PORTERS.

No injuries or illnesses during the expedition.

DETAILS OF WASTE DISPOSAL.

All human waste was buried in deep trenches, with all non-human waste brought back to be disposed of properly in Haines.

A SUMMARY OF EXPEDITION ACCOUNTS, INCLUDING INCOME AND EXPENDITURE.

Income

Source	Amount
Mount Everest Foundation (18-22)	£2,000
Gino Watkins Memorial Fund	£1,500
Newcastle University Research Training Support Grant	£6,300
Total	£9,800

Outgoings

Expenditure	Amount
Flights, Charter flight and in country travel	£5,593
Science and safety equipment	£3,454
Food	£458
Accomodation	£295
Total	£9,800

10.0 REFERENCES

Bisette-Kirton, E.K. (2017) *An analysis of landslide volume, structures, and kinematics from satellite imagery of the 2016 Lamplugh rock avalanche, Glacier Bay National Park and Preserve, Alaska.* MSc. Colorado School of Mines. (Available at: https://dspace.library.colostate.edu/handle/11124/171181).

Coe, J.A., Bessette-Kirton, E.K. and Geertsema, M. (2017) 'Increasing rock-avalanche size and mobility in Glacier Bay National Park and Preserve, Alaska detected from 1984 to 2016 Landsat imagery', Landslides, https://doi.org/10.1007/s10346-017- 0879-7.

Hewitt, K. (2009) 'Rock avalanches that travel onto glaciers and related developments, Karakoram Himalaya, Inner Asia', *Geomorphology*, 103(1), pp. 66-79.

Porter, P.R., Vatne, G., Ng, F. and Irvine-Fynn, T.D.L. (2010) 'Ice marginal sediment delivery to the surface of a high-arctic glacier: Austre Brøggerbreen, Svalbard', *Geografiska Annaler: Series A, Physical Geography*, 92(4), pp. 437-449.

Telling, J., Boyd, E.S., Bone, N. and 11 others. (2015) 'Rock comminution as a source of hydrogen for subglacial ecosystems', *Nature Geoscience*, 8, pp. 851-855.

Weidinger, J.T., Korup, O., Munack, H. and 4 others. (2014) 'Giant rockslides from the inside', *Earth and Planetary Science Letters*, 389, pp. 62-73.